

CLASSIFICATION OF RIPENESS LEVELS AND PREDICTION OF PHYSICOCHEMICAL
PROPERTIES OF DURIAN INTACT FRUIT AND PULP BY NEAR-INFRARED HYPERSPECTRAL
IMAGING



A THESIS SUBMITTED IN PARTIAL FULFILLMENT
OF THE REQUIREMENTS FOR THE DEGREE OF
DOCTOR OF ENGINEERING IN AGRICULTURAL ENGINEERING
SCHOOL OF ENGINEERING
KING MONGKUT'S INSTITUTE OF TECHNOLOGY LADKRABANG
2021
KMITL-2022-EN-D-108-075

This material is reserved for educational use only, not allowed for commercial use.

Forbidden to modify the content, and cite the document when use.

การจำแนกระดับความสุขและการทำนายสมบัติทางเคมีกายภาพของผลและเนื้อทุเรียนโดย
การถ่ายภาพไฮเปอร์สเปกตรัลอินฟราเรดย่านใกล้



วิทยานิพนธ์นี้เป็นส่วนหนึ่งของการศึกษาตามหลักสูตรปริญญาวิศวกรรมศาสตรดุษฎีบัณฑิต
สาขาวิชาวิศวกรรมเกษตร
คณะวิศวกรรมศาสตร์
สถาบันเทคโนโลยีพระจอมเกล้าเจ้าคุณทหารลาดกระบัง
พ.ศ.2565
KMITL-2022-EN-D-108-075

This material is reserved for educational use only, not allowed for commercial use.

Forbidden to modify the content, and cite the document when use.



COPYRIGHT 2022

SCHOOL OF ENGINEERING

KING MONGKUT'S INSTITUTE OF TECHNOLOGY LADKRABANG

This material is reserved for educational use only, not allowed for commercial use.

Forbidden to modify the content, and cite the document when use.

วิทยานิพนธ์	การจำแนกระดับความสุขและการทำนายสมบัติทางเคมี กายภาพของผลและเนื้อทุเรียนโดยการถ่ายภาพไฮเปอร์ สเปกตรัลอินฟราเรดย่านใกล้
รหัสนักศึกษา	Ms. Sneha Sharma
รหัสประจำตัว	61601170
ปริญญา	วิศวกรรมศาสตรดุษฎีบัณฑิต สาขาวิศวกรรมเกษตร
สาขาวิชา	วิศวกรรมเกษตร
พ.ศ.	2022
อาจารย์ที่ปรึกษาวิทยานิพนธ์	ศาสตราจารย์ ดร. ปานมนัส ศิริสมบุรณ์

บทคัดย่อ

ทุเรียนเป็นผลไม้เมืองร้อนที่ได้รับความนิยมและมีความสำคัญชนิดหนึ่งในเอเชียตะวันออกเฉียงใต้ ประเทศไทยเป็นหนึ่งในผู้ผลิตและส่งออกทุเรียนรายใหญ่ มาตรการจัดการก่อนและหลังการเก็บเกี่ยวเป็นหนึ่งในความท้าทายที่ผู้ปลูกทุเรียนในประเทศไทยต้องเผชิญเกษตรกรส่วนใหญ่ต้องอาศัยการตรวจสอบด้วยสายตาและการเคาะเพื่อระบุความ สมบูรณ์ของการเก็บเกี่ยว วิธีการแบบดั้งเดิมนั้นได้ผล อย่างไรก็ตาม การเลือกทุเรียนตามคุณภาพการส่งออกนั้นท้าทายวิธีการแบบใหม่ๆ เช่น เซอร์และ เทคโนโลยีแบบไม่ทำลายพร้อมสำหรับการตรวจสอบระดับความสุข และ สมบัติทางเคมีกายภาพของทุเรียนแบบเรียลไทม์ ด้วยความก้าวหน้าในเทคโนโลยีแบบไม่ทำลายด้วยภาพไฮเปอร์สเปกตรัม (HSI) ได้รับการพัฒนาให้เป็นการผลิตที่มีประสิทธิภาพของเทคนิคการถ่ายภาพและสเปกโตรสโกปีการถ่ายภาพด้วยคลื่น ความถี่ย่านใกล้อินฟราเรด (NIR-HSI) ถือเป็นแนวทางที่มีแนวโน้มดีสำหรับการตรวจสอบคุณภาพของผลิตผลทางเกษตร

วิทยานิพนธ์นี้ ได้มีการศึกษาความเป็นไปได้ของการใช้ระบบ NIR-HSI แบบพหุขบวนการ หรือที่เรียกว่าการสแกนแบบเส้น สำหรับการจำแนกระดับความสุขและการทำนายสมบัติทางเคมีกายภาพของทุเรียน โดยใช้ระบบ NIR-HSI แบบพหุขบวนการ ในช่วงความยาวคลื่น 900-1600 นาโนเมตร สร้างไฮเปอร์คิวบสามมิติด้วยการสแกนตัวอย่างบนพื้นเคลื่อนด้วยความเร็ว 10 มม.ต่อวินาที วิทยานิพนธ์นี้แบ่งออกเป็นสี่ส่วน ส่วนแรก มีการวิเคราะห์เบื้องต้นในการจำแนกระดับความสุข (ยังไม่สุก สุก และสุกเกินไป) ของเนื้อทุเรียนโดยอัลกอริธึมการเรียนรู้ของเครื่องโดยวิธีปรับให้เหมาะสมแบบ Bayesian ในส่วนนี้ มีการใช้เทคนิคการเพิ่มประสิทธิภาพการเลือกไฮเปอร์พารามิเตอร์อย่างเหมาะสมยอดนิยมวิธีหนึ่งที่รู้จักกันคือวิธี Bayesian เพื่อประยุกต์กับข้อมูล NIR-HSI เพื่อพัฒนาโมเดลการจำแนกระดับหรือประเภทด้วยการเรียนรู้ด้วยเครื่องสามแบบ คือ support vector machine (SVM), random forest (RF) และ k-nearest neighbor (kNN) โดย SVM ให้ความแม่นยำในการจำแนกระดับความสุขสูงสุด

และค่าสัมประสิทธิ์ค้ำป้า คือ 88.5% และ 0.83 ตามลำดับ ผลการวิจัยพบว่าวิธีการเพิ่มประสิทธิภาพ มีผลต่อความถูกต้องของแบบจำลองซึ่งสร้างโดยวิธีจำแนกประเภท ในส่วนที่สอง ศึกษาสมรรถนะของการเรียนรู้ของเครื่องเพื่อจำแนกประเภททหวิธีสำหรับการจำแนกระดับความสุกของผลและเนื้อทุเรียนตามวันเก็บเกี่ยว วิธีจำแนกประเภทการเรียนรู้ของเครื่อง 6 วิธี ได้แก่ การวิเคราะห์การจำแนกประเภทเชิงเส้น (LDA) การวิเคราะห์จำแนกประเภทแบบถดถอยกำลังสองน้อยที่สุดบางส่วน (PLS-DA) โคจรข่ายประสาทเทียม (ANN) SVM RF และ KNN การเพิ่มประสิทธิภาพการเลือกไฮเปอร์พารามิเตอร์ให้เหมาะสมใช้วิธี grid search เพื่อนำมาพัฒนาโมเดลการจำแนกระดับ การเปรียบเทียบความแม่นยำของโมเดลแสดงเป็นเมตริกการจำแนกประเภทระหว่างแต่ละวิธีทั้งโดยใช้ความยาวคลื่นเต็มและความยาวคลื่นสำคัญของคุณลักษณะซึ่งศึกษาโดยอัลกอริธึมทางพันธุกรรม (GA) และ การวิเคราะห์องค์ประกอบหลัก (PCA) ผลการวิจัยพบว่าแบบจำลองการจำแนกประเภท LDA โดยพิจารณาจากความยาวคลื่นเต็มและความยาวคลื่นสำคัญของคุณลักษณะสปีดความยาวคลื่นซึ่งจำแนกผลและเนื้อผลทุเรียนโดยไม่ทำลายได้ด้วยความแม่นยำ 100% ส่วน SVM, PLS-DA และ RF มีความแม่นยำปานกลาง อย่างไรก็ตาม KNN ให้ความแม่นยำต่ำสุด

ในส่วนที่สาม แบบจำลองการถดถอยได้รับการพัฒนาเพื่อทำนายสมบัติทางเคมีกายภาพ ได้แก่ เนื้อแห้ง (DM) ปริมาณของแข็งที่ละลายได้ทั้งหมด (TSS) และปริมาณไขมัน (FC) ในเนื้อทุเรียน โมเดลการถดถอยกำลังสองน้อยที่สุดบางส่วน (PLSR), SVM, RF และโคจรข่ายประสาทเทียมระดับซับซ้อนแบบ 1 มิติ (1-D CNN) ชนิดกำหนดเอง (custom) U-Net และ VGG-19 ได้รับการพัฒนาความยาวคลื่นสำคัญของคุณลักษณะซึ่งศึกษาโดยอัลกอริธึมการฉายต่อเนื่อง (SPA) และอัลกอริธึมทางพันธุกรรม (GA) โมเดลการทำนาย DM แม่นยำที่สุด โดยได้ค่าสัมประสิทธิ์การพิจารณาชุดทดสอบ (r^2) รากที่สองของความคลาดเคลื่อนกำลังสองเฉลี่ยของการทำนาย (RMSEP) และอัตราส่วนการทำนายต่อการเบี่ยงเบน (RPD) ในช่วง 0.87-0.95, 1.42-2.28 % และ 2.7-4.4% โมเดลที่โดดเด่นสำหรับการทำนาย DM คือ โมเดล GA-PLSR ส่วนโมเดล GA-SVM มีความแม่นยำสูงสุดในการทำนายค่า TSS โดยรวมได้สมรรถนะการทำนายปานกลางด้วย r^2 , RMSEP และ RPD ที่ 0.87, 3.05% และ 2.8 ตามลำดับ สำหรับการทำนาย FC ได้จากโมเดล GA-PLSR โดยมีความแม่นยำสูงสุด ให้ r^2 และ RMSEP เท่ากับ 0.81 และ 0.65% ตามลำดับ โมเดล 1-D CNN เป็นไปได้สำหรับการทำนาย DM เท่านั้น โมเดล CNN สำหรับ TSS และ FC ให้ผลลัพธ์ไม่น่าเชื่อถือ ไม่สามารถนำไปประยุกต์ใช้ได้ จากวิทยานิพนธ์ส่วนนี้ ได้มีการแสดงโมเดลที่ดีที่สุดสำหรับ DM TSS และ FC ซึ่งสามารถนำไปใช้กับการตรวจสอบเนื้อทุเรียนแบบเรียลไทม์ ในส่วนสุดท้าย ภาพแผนที่การกระจายเชิงพื้นที่ของ DM TSS และ FC ถูกแสดงสำหรับการแสดงภาพการเปลี่ยนแปลงภายในและระหว่างเนื้อทุเรียนที่เก็บเกี่ยวในวันต่างๆ หลังดอกบาน (DAA) ภาพแผนที่การกระจายเชิงพื้นที่แสดงการเปลี่ยนแปลงของสมบัติที่ศึกษาที่เกิดขึ้นระหว่างทุเรียนสุก

จากผลการวิจัยของวิทยานิพนธ์ฉบับนี้ ยืนยันได้ว่าระบบ NIR-HSI สามารถนำไปใช้ในการจำแนกระดับการสุกและการทำนายคุณภาพภายในของเนื้อทุเรียนได้ ระบบ NIR-HSI แบบพหุขบวนการได้เปรียบในการติดตั้งเพื่อการสแกนทุเรียนออนไลน์ในบริษัทบรรจุภัณฑ์ขนาดใหญ่ ความยาวคลื่นสำคัญของสมบัติซึ่งเลือกจาก PCA และ SPA สามารถใช้เพิ่มเติมเพื่อพัฒนากล้องถ่ายภาพแบบมัลติส

เปกตรัลหรือแบบถ่ายครั้งเดียวแบบพกพาได้ ระบบ NIR-HIS สามารถให้ข้อมูลซึ่งมีพลังจากแต่ละพิกเซลของภาพ ข้อมูลนี้สามารถนำไปใช้ในการพัฒนาโมเดลซึ่งมีความครอบคลุมเมื่อกับเทคนิคการเรียนรู้ของเครื่องขั้นสูงพร้อมกับการเลือกความยาวคลื่นสำคัญของสมบัติซึ่งศึกษา ระบบติดตามผลแบบเรียลไทม์สามารถพัฒนาได้โดยใช้ข้อมูลซึ่งได้จากวิทยานิพนธ์นี้เพื่อการจำแนกระดับคุณภาพและการตรวจสอบคุณภาพทุเรียน



Thesis	Classification of ripeness levels and prediction of physicochemical properties of durian fruit and pulp by near-infrared hyperspectral imaging
Student	Ms. Sneha Sharma
Student ID	61601170
Degree	Doctor of Engineering
Program	Agricultural Engineering
Year	2022
Thesis Advisor	Prof. Dr. Panmanas Sirisomboon

ABSTRACT

Durian is one of the popular and important tropical fruit in South-East Asia. Thailand is one of the main producers and exporters of durian. Pre and post-harvest handling measures are one of the challenging aspects being encountered by the durian growers in Thailand. Farmers mostly depend on visual inspection and tapping to identify the harvest maturity. Traditional approaches are effective, however, selecting the export quality of durian is challenging the traditional methods. Non-destructive sensors and technology are ready to be implemented for the real-time monitoring of the ripening stage and physicochemical properties of the durian. With the advancement in non-destructive technologies, hyperspectral imaging (HSI) has been developed as a powerful integration of imaging and spectroscopic techniques. Near-infrared hyperspectral imaging (NIR-HSI) has been considered a promising approach for the quality inspection of agricultural products.

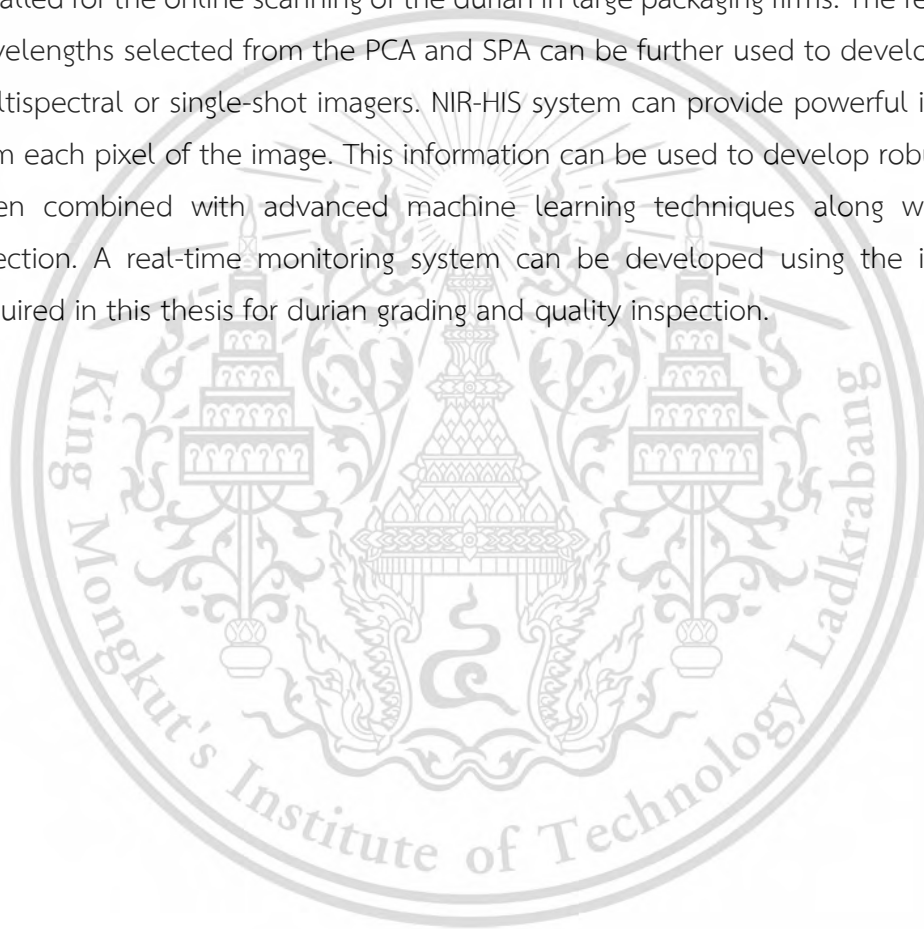
In this thesis, the possibility of using the pushbroom NIR-HSI system to classify the ripening stage and predict physicochemical properties has been established. The pushbroom NIR-HSI system (900-1600 nm), also known as line-scanning, generates the 3-D hypercube by scanning the sample on a transition stage at 10 mm s^{-1} . This thesis has been divided into mainly four sections. Firstly, the preliminary analysis was done for the ripening stages (unripe, ripe, and overripe) classification of durian pulp by Bayesian optimized machine learning algorithms. In this section, one of the popular hyperparameter optimization techniques known as the Bayesian method was

implemented on the NIR-HSI data to develop three machine learning classification models: support vector machine (SVM), random forest (RF), and k-nearest neighbour (kNN). Using Bayesian optimization, the highest classification accuracy and kappa coefficient obtained were 88.5% and 0.83, respectively, by the SVM classifier. The result showed that the optimization method influences the model accuracy of the classifiers. In the second section, the performance of the six machine learning classifiers for the ripening stage classification of intact fruit and pulp was performed. Six machine learning classifiers selected for the classification model development were linear discriminant analysis (LDA), partial least squares discriminant analysis (PLS-DA), artificial neural network (ANN), SVM, RF, and kNN. Grid search hyperparameter optimization was used to develop the model for classification. Accuracy comparison was made according to the classification metrics between the classifiers using full wavelengths and featured wavelengths selected by genetic algorithm (GA) and principal component analysis (PCA). The results showed that LDA classification models based on the full wavelengths and eleven feature wavelengths classified the durian intact fruit and pulp successfully with 100% accuracy. The performance of SVM, PLS-DA, and RF attained fair classification results; however, in comparison, the kNN classifier showed the lowest accuracy.

In the third section, the regression models were developed to predict the physicochemical properties: dry matter (DM), total soluble solids (TSS), and fat content (FC); in durian pulp. Partial least squares regression (PLSR), SVM, RF, and 1-dimensional convolution neural network (1-D CNN) models were developed: custom, U-Net, and VGG-19. Feature wavelengths were selected by successive projection algorithm (SPA) and genetic algorithm (GA). DM prediction model was the most accurate, showing coefficient of determination of test set (r^2), root mean square error of prediction (RMSEP), and the ratio of prediction to deviation (RPD) in the range from 0.87-0.95, 1.42-2.28%, and 2.7-4.4%. The outstanding performance for DM prediction was obtained from the GA-PLSR model. GA-SVM model attained the highest accuracy for TSS prediction. The overall model shows a fair result with the r^2 , RMSEP, and RPD of 0.87, 3.05%, and 2.8, respectively. For the FC prediction, the best accuracy was attained from the GA-PLSR model. GA-PLSR model for FC prediction exhibits the r^2 and RMSEP of 0.81 and 0.65%, respectively. The 1-D CNN models were only feasible for DM prediction. The CNN models for TSS and FC did not provide convincing results for further application. This part of the thesis identified the best model for the DM, TSS, and FC,

which can be applied for the real-time monitoring of durian pulp. In the final section, the spatial distribution of DM, TSS, and FC was represented for the visualization of changes within and between the durian pulp harvested on different days after anthesis (DAA). The spatial mapping of durian pulp shows the changes in physicochemical properties that occurred during the ripening stages.

Based on the findings of this thesis, it was confirmed that the NIR-HSI system could be implemented for ripening stage classification and the internal quality prediction of durian pulp. The pushbroom NIR-HSI system offers an advantage to be installed for the online scanning of the durian in large packaging firms. The few featured wavelengths selected from the PCA and SPA can be further used to develop portable multispectral or single-shot imagers. NIR-HIS system can provide powerful information from each pixel of the image. This information can be used to develop robust models when combined with advanced machine learning techniques along with feature selection. A real-time monitoring system can be developed using the information acquired in this thesis for durian grading and quality inspection.



Acknowledgements

I would like to acknowledge all the sources of assistance and contribution for the successful completion of this thesis. Firstly, I would like to express my deepest and sincere gratitude to my advisor, Professor Dr. Panmanas Sirisomboon for her continuous support, supervision, and encouragement throughout my course of study and research. This endeavor would not have been possible without her invaluable time, help, constant motivation, and immense knowledge to achieve the objectives of this thesis. I would like to thank King Mongkut's Institute of Technology Ladkrabang (KMITL) doctoral scholarship (KDS 2019/002) program for granting me with the scholarship which included tuition fee, research expenses, and monthly expenses and agricultural research development agency (ARDA) for the research grant (CRP6405031580).

I wish to thank the Near Infrared Spectroscopy Research Center for Agricultural Products and Food (www.nirsresearch.com) at King Mongkut's Institute of Technology Ladkrabang, Bangkok, Thailand and the Department of Agricultural Engineering, Faculty of Engineering, Kasetsart University Kamphaengsaen Campus for providing the necessary equipment for experiments. I would like to thank Prof. Dr. Anupun Terdwongworakul, and his lab members for helping me during the experiment. I would like to thank Dr. Lampan Khurnpoon for the sample collection. I would like to extend my gratitude to all my friends, seniors, and juniors from KMITL for their direct and indirect support in my thesis completion.

I am so grateful to all the faculties of the department of agricultural engineering at King Mongkut's Institute of Technology Ladkrabang (KMITL), for welcoming me in the department since my graduate studies and giving me the essential support during my course work and research activities.

Special thanks to my dear husband Mr. Sumesh K.C. for assisting me to conduct experiments and sharing his knowledge to guide me during the research. I could not have undertaken this journey without the encouragement and support of my parents. Finally, I would like to dedicate this thesis in loving memory of my grandfather Mr. Yogananda Sharma.

Sneha Sharma

Table of contents

Abstract (Thai).....	I
Abstract (English).....	IV
Acknowledgements.....	VII
Table of contents.....	VIII
List of tables.....	XIV
List of figures.....	XV
Abbreviations.....	XVIII
Chapter 1.....	1
Introduction.....	1
1.1 Background.....	1
1.2 Research problem.....	4
1.3 Research hypothesis.....	5
1.4 Research aim.....	6
1.5 Research questions.....	6
1.6 Research objective.....	6
1.7 Navigation of the thesis.....	6
Chapter 2.....	8
Theories and Literature Review.....	8
2.1 Durian.....	8
2.1.1 Botany, origin and structure of durian.....	8
2.1.2 Durian production in Thailand.....	10
2.1.3 Postharvest handling factors affecting the quality.....	12
2.1.4 Harvest operation.....	12
2.2 Fruit ripening and maturity.....	13

Table of contents (Continued)

2.2.1 Physicochemical properties in fruits	15
2.2.1.1 Fruit growth	16
2.2.1.2 Color.....	17
2.2.1.3 Texture	19
2.2.1.4 Flavour and aroma.....	20
2.2.2 Maturity of Durian	22
2.2.2.1 Important maturity indices.....	23
<i>Total soluble solids (TSS)</i>	23
<i>Dry matter (DM)</i>	24
2.3 Hyperspectral imaging (HSI).....	26
2.3.1 Components of Hyperspectral Imaging.....	27
2.3.1.1 Light source and interaction	27
2.3.1.2 Spectrograph	30
2.3.1.3 Filters	30
2.3.1.4 Area detector (Camera).....	31
2.3.2 Generating of hyperspectral image.....	31
2.3.2.1 Principle of hyperspectral imaging (HSI) system	33
2.3.2.2 Application.....	34
2.4 Hyperspectral image processing	35
2.4.1 Digital Image.....	36
2.4.2 Image Processing.....	38
2.4.2.1 Image acquisition.....	38
2.4.2.2 Calibration.....	39
2.4.2.3 Image preprocessing	39
2.4.2.4 Region of Interest (ROI) Extraction	41

Table of contents (Continued)

2.4.2.5 Feature Extraction	41
2.4.2.6 Spectral Preprocessing	42
2.4.3 Image Analysis	44
2.5 Classification and regression model.....	45
2.5.1 Feature selection.....	45
2.5.1.1 Principal component analysis (PCA).....	45
2.5.1.2 Successive projection algorithm (SPA)	47
2.5.1.3 Genetic algorithm (GA)	48
2.5.2 Machine learning.....	48
2.5.2.1 Partial least squares (PLS) regression	48
2.5.2.2 Support Vector Machine	50
2.5.2.3 Random forest (RF)	51
2.5.2.4 Linear discriminant analysis (LDA).....	52
2.5.2.5 Partial least squares discriminant analysis (PLS-DA).....	52
2.5.2.6 K-nearest neighbor	53
2.5.3 Deep learning.....	53
2.5.3.1 Artificial neural network (ANN).....	54
2.5.3.2 Convolution neural network (CNN).....	54
Chapter 3	56
Hyperspectral imaging system for maturity stage classification of durian pulp using Bayesian optimized machine learning algorithms	56
3.1 Introduction.....	58
3.2 Materials and methods.....	59
3.3 Results and discussions	63
3.4 Conclusion.....	68

Table of contents (Continued)

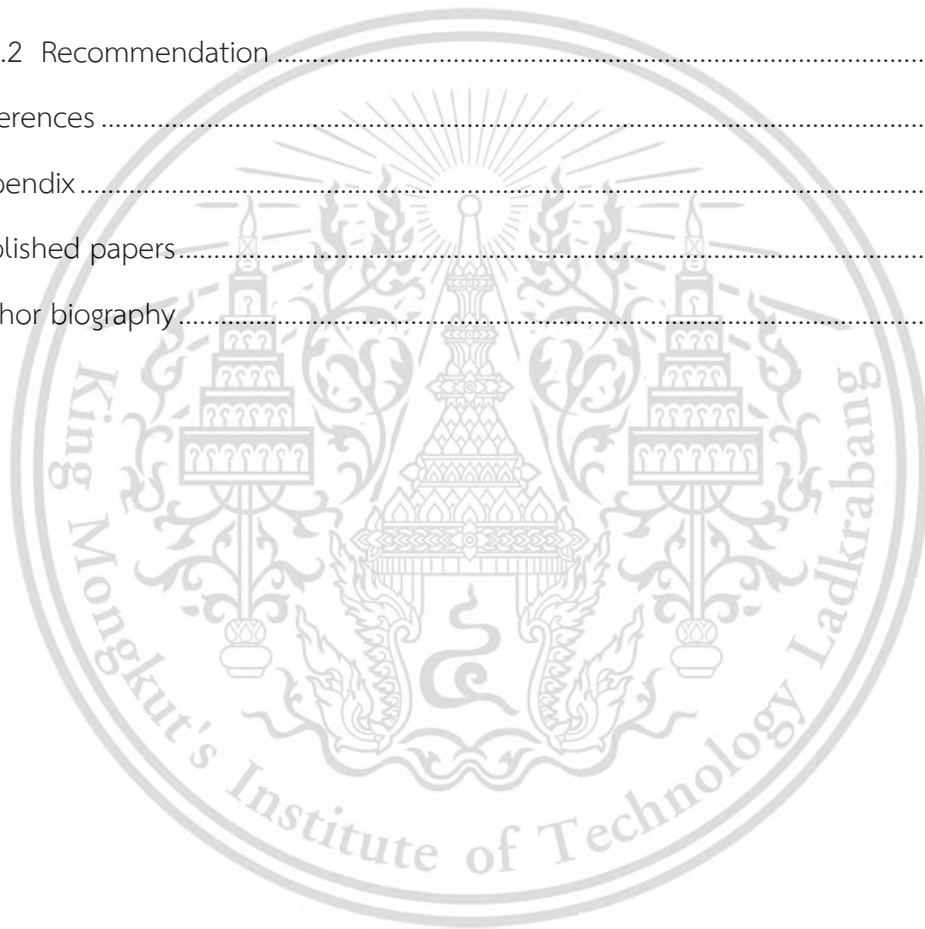
Chapter 4	69
Rapid ripening stage classification and dry matter prediction of durian intact fruit and pulp using a pushbroom near infrared hyperspectral imaging system.....	69
4.1 Introduction.....	70
4.2. Materials and methods.....	74
4.2.1 Sample collection	74
4.2.2 HSI system configuration.....	75
4.2.3 HSI radiometric calibration.....	76
4.2.4 Extracting area of interest (AOI)	77
4.2.5 DM content measurement	78
4.2.6 Spectral preprocessing.....	78
4.2.7 Classification model development.....	79
4.2.7.1 Support vector machine (SVM).....	79
4.2.7.2 Random forest (RF).....	80
4.2.7.3 Linear discriminant analysis (LDA).....	80
4.2.7.4 Partial least squares discriminant analysis (PLS-DA).....	80
4.2.7.5 k nearest neighbors (kNN).....	81
4.2.8 Selection of optimal wavelength.....	82
4.2.8.1 Principal component analysis (PCA).....	82
4.2.8.2 Genetic Algorithm (GA).....	83
4.2.9 DM prediction model and spatial distribution.....	84
4.3 Results and Discussion.....	85
4.3.1 Spectral profile of durian pulp	85
4.3.2 Classification model performance for durian pulp.....	87
4.3.2.1 Full wavelength	87

Table of contents (Continued)

4.3.2.2 GA selected wavelength	90
4.3.2.3 PCA selected wavelength	92
4.3.3 Classification model performance for intact fruit	96
4.3.4 PLSR model and spatial distribution of DM	100
4.4. Conclusion	105
Chapter 5	107
Physicochemical properties prediction and spatial mapping of durian pulp C.V Monthong for quality evaluation using near-infrared hyperspectral imaging	107
5.1 Introduction	108
5.2 Materials and methods	108
5.2.1 Sample preparation	110
5.2.2 NIR-HSI image acquisition and radiometric correction	111
5.2.3 Extraction of the area of interest (AOI)	112
5.2.4 Physicochemical properties measurement	112
5.2.4.1 DM content	112
5.2.4.2 Total soluble solids (TSS)	112
5.2.4.3 Fat content (FC)	113
5.2.5 Data analysis	113
5.2.6 Deep learning models	115
5.3 Results and discussion	117
5.3.1 Spectral profile	117
5.3.2 Statistical analysis of DM, TSS, and FC	118
5.3.3 DM prediction model performance	120
5.3.4 TSS prediction models performance	123
5.3.5 FC prediction models performance	125

Table of contents (Continued)

5.3.6 Deep learning model performance.....	128
5.3.7 Visualization of concentration distribution.....	130
5.4 Conclusion.....	132
Chapter 6	134
Conclusion and recommendations	134
6.1 Conclusion.....	134
6.2 Recommendation	135
References	136
Appendix.....	166
Published papers.....	166
Author biography.....	167



List of tables

Table	Page
2.1 Application of HSI on internal and external quality evaluation.....	35
3.1 Selection of hyperparameters for SVM, RF, and kNN using Bayesian optimization.....	64
3.2 Performance of machine learning classifiers using Bayesian optimization.....	65
3.3 Precision, recall and kappa coefficient obtained from the classification model by different machine learning classifiers.....	66
4.1 Classification of ripening with respect to the DAA and maturity percentage according to Siriphanich (2011).....	71
4.2 Confusion matrix of actual versus predicted classes.....	82
4.3 Accuracy comparison among the classification models using the full wavelength.....	88
4.4 Accuracy comparison among the classification models using the GA selected wavelength.....	91
4.5 Classification metrics obtained from each classifier using the selected wavelength by PCA.....	95
4.6 Performance of each classifier for ripeness classification of durian intact fruit.....	97
4.7 Performance of classifiers using PCA selected wavelengths for ripeness classification of durian intact fruit.....	98
4.8 PLSR model results obtained using raw and preprocessed spectra from the full wavelength and selected wavelengths by genetic algorithm and principal component analysis.....	103
5.1 Statistical parameters calculated for DM, TSS, and FC.....	118
5.2 Performance of regression model for DM prediction in durian pulp.....	121
5.3 Performance of regression model for TSS prediction in durian pulp.....	123
5.4 Performance of regression models for FC prediction in durian pulp.....	125
5.5 Performance of 1-D CNN models for DM, TSS, and FC prediction.....	129

List of figures

Figure		Page
2.1	Durian fruits after harvested from the orchard.....	9
2.2	Main parts and structure of durian (Monthong).....	10
2.3	Global fresh durian export quantity (Tons) from Thailand from 2010 to 2022.....	11
2.4	Fresh durian export value in a million USD from 2010 to 2022	11
2.5	The pattern of growth, respiration, and ethylene production during fruit development.....	15
2.6	Fruit growth curve.....	17
2.7	Change in aril color during ripening stage Chanee (a) and Monthong (b) during fruit growth and ripening.....	18
2.8	Main components and illustration of hyperspectral imaging system.....	30
2.9	Three different approaches to generating a hyperspectral image. (a) The point-scan method. (b) The line-scan method. (c) The area-scan method.....	33
2.10	Schematic representation of a hypercube showing the relationship between spatial and spectral dimension.....	34
2.11	An example of the process for creation of a digital image.....	38
2.12	Steps for hyperspectral image processing.....	38
2.13	Structure of biological and artificial neural network.....	54
2.14	1-D convolution neural network structure consisting of convolution and pooling layers.....	55
3.1	Overall methodology for the durian ripening stage classification model development using Bayesian optimized machine learning algorithms...	57
3.2	Pushbroom NIR-HSI system configuration for scanning durian pulp.....	60
3.3	Raw image acquired from hyperspectral imaging (a) Masked image by binary masking and morphological filter.....	61
3.4	Confusion matrix.....	62
3.5	Average raw spectra of durian pulp.....	63
3.6	SNV pretreated spectra of durian pulp.....	64
3.7	Confusion matrix from classification model of support vector machine (a), random forest (b), and k nearest neighbors (c).....	66

Figure	List of figures (Continued)	Page
4.1	Overall research methodology to classify the ripening level of durian intact fruit and pulp using hyperspectral imaging.....	70
4.2	Flowchart for the overall methodology from image acquisition to classification model development and validation.....	76
4.3	Near Infrared hyperspectral image after radiometric calibration pulp (a) and spectral profile of the section of durian pulp, guiding bar, and the translation stage (b), erosion applied to a binary image (c), dilation followed erosion (d), erosion followed dilation (e), contour extracted durian pulp (f).....	78
4.4	Flowchart representing the methodology for the dry matter prediction model and spatial mapping.....	85
4.5	Raw mean spectra of durian pulp (a), standard normal variate pretreated spectra (b), and average spectra of each ripening stage (c), and average spectra of intact durian fruit at each ripening stage.....	86
4.6	Precision, recall, specificity, and F1 score obtained for each ripening stage from the test set using the full wavelength.....	89
4.7	Precision, recall, specificity, and F1 score obtained for each ripening stage from the test set using the selected wavelengths by genetic algorithm.....	92
4.8	Loading weight plot of the first three principal components.....	93
4.9	Linear discriminant analysis score plot showing two components (LD1 and LD2) with explained variance to classify three ripening stages using full and selected wavelength by genetic algorithm and principal component analysis.....	96
4.10	Average full wavelength spectra pretreated by standard normal variate and 93 selected wavelengths by genetic algorithm.....	102
4.11	Dry matter spatial distribution from the optimum partial least squares regression model developed using the full wavelength and selected wavelengths by genetic algorithm and principal component analysis.....	104
4.12	Box plot representing a change in dry matter predicted by the optimum partial least squares regression model developed using full and selected wavelengths from 99-127 days after anthesis of the durian pulps.....	105

Figure	List of figures (Continued)	Page
5.1	Flowchart demonstrating the methodology used for the regression model development and spatial mapping.....	108
5.2	Deep network architecture of 1-D CNN and VGG 19.....	116
5.3	Transformation of raw to standard normal variate (SNV) pretreated spectral profile of durian pulp.....	118
5.4	Changes of dry matter (a), total soluble solids (b), and fat content (c) of durian pulp at different DAA.....	120
5.5	Average spectrum of durian pulp showing selected wavelengths by GA for DM prediction.....	122
5.6	Scatter plot showing the actual versus predicted dry matter from GA-PLSR (a) and SPA-PLSR with elimination (b) regression model.....	122
5.7	Average spectrum of durian pulp showing selected wavelengths by GA for TSS prediction.....	124
5.8	Scatter plot showing the actual versus predicted total soluble solids from GA-SVM (a) and SPA-PLSR with elimination (b) regression models....	124
5.9	Average spectrum of durian pulp showing selected wavelengths by GA for FC prediction.....	126
5.10	Scatter plot showing the actual versus predicted fat content from the GA-PLSR model.....	127
5.11	Spatial mapping of dry matter (DM), total soluble solids (TSS), and fat content (FC) in durian pulp on different days after anthesis (DAA).....	130

Abbreviations

ANN	Artificial neural networks
Bias	Average error
CNN	Convolutional neural network
CV	Cross validation
DAA	Days after anthesis
DM	Dry matter
FC	Fat content
FN	Number of false negatives
FP	Number of false positives
GA	Genetic algorithm
HSI	Hyperspectral imaging
kNN	k nearest neighbour
LDA	Linear discriminant analysis
MLR	Multiple linear regressions
MSC	Multiple scatter correlation
NIR	Near Infrared
PC	Principal components
PCA	Principal component analysis
PLS-DA	Partial least squares discriminant analysis
PLSR	Partial least squares regression
R ²	Coefficient of determination
ReLU	Rectified linear unit
RF	Random forest
RMSEC	Root mean square error of calibration

Abbreviations

RMSECV	Root mean square error of cross validation
RMSEP	Root mean square error of prediction
ROI	Regions of interest
RPD	Standard deviation to standard error of prediction
SD	Standard deviation
SEC	Standard deviation of error of calibration
SEP	standard deviation of error of prediction
SIMCA	Soft independent modeling of class analogies
SNV	Standard normal Variate
SPA	Successive projection algorithm
SVM	Support vector machines
TN	Number of true negatives
TP	Number of true positives
TSS	Total soluble solids

Chapter 1

Introduction

1.1 Background

Agricultural products are the main source of nutrients required for the human existence. The relative contribution of each agricultural product to human health and wellness depends upon its consumption of nutritive value, which is greatly influenced by consumer preferences and satisfaction from eating the fruit or vegetable (Kader, 2008). Fruits are essential commodity enriched with nutrition and high economic value. Fruits can be categorized into several varieties based on their unique characteristics, shapes, flavour, colors, etc. Citrus fruits, stone fruits, tropical fruits, and berries are some well-known categories of fruit. The fruits are usually grown in areas that constantly remain warm and do not have significant differences in the day length are known as tropical fruits (Yahia, 2011). In Southeast Asian countries; tropical fruits such as durian, mangosteen, rambutan, longan, jackfruit, and citrus fruits are considered important and have a significant impact on the lives, health, and overall economy (Yahia, 2011). Among the tropical fruits, Durian (*Durio zibethinus*) is the King of Fruits in Southeast Asia. According to the statistics in Thailand from January to December 2021, 875097 metric ton of fresh durian fruit worth approximately 330 million USD were exported from Thailand (*Thai Customs*, n.d.). In an article by Kasikorn Research Center (*Kasikorn Res. Inst.*, 2021), it was reported that from the year 2014, the export value for durian had surpassed all other fruits in Thailand; it recorded the highest value of USD 934.9 million in May 2021, with an increase of 95.3%. The price of durian has risen continuously due to the surging demand for durian in the Chinese market, because of which many ASEAN countries had expressed their interest in competing in China's durian market that eventually pose bigger challenge to Thai durian exporters in future (*Kasikorn Res. Inst.*, 2021). Vietnam and Cambodia are considered as the strong competitors for Thailand in term of high-quality durian exporters in the global market (Datepumee et al., 2019). The report shows the demand of durian in several countries is increasing annually and improving the quality of Thai durian is very important as it has the significant impact on the overall economy of the country.

Thailand durian farmers are facing major problems related to toxic residue, chemical or biological contamination, early maturity durian harvesting (Datepumee et al., 2019). These problems affect the export quality of durian and increase the

production cost for the farmers. To have the better-quality fruit acceptable in national and international markets in terms of food safety and export promotion, the Ministry of Agriculture and Cooperatives of Thailand has established a standard for the durian fruit (*Thai Agricultural Standard*, n.d.). Thai agricultural standard (TAS 3-2003), applies for durian which contains several provisions concerning quality, sizing, tolerances, packaging, presentation, marking and labelling, and contaminants (*Thai Agricultural Standard*, n.d.). If the product from the farmers does not meet the standard, the farmers are forced to sell their products in a local market with low profit. After harvesting, the fruits are transferred to the packing firms for the proper packaging and distribution in local and regional markets. During the period of harvesting durian, there occurs difficult for the farmer to identify the correct maturity or ripening stages.

Durian farmers perform visual inspections to determine the maturity and harvest period. Most of the standard methods to specify the harvest period is counting days after anthesis/flowering (DAA), characteristic of the fruit spines, tapping the fruit, and shape and color (Saichol Ketsa, 2018a). If the immature durian is harvested, it will not ripen properly or ripen with substantially less flavour and taste, leading to a poor eating experience. Conversely, an over-ripe one will decay rapidly after harvest (Lizada et al., 1998). Consumers' perception of quality is influenced by the product's intrinsic attributes and extrinsic indicators and indications provided by the seller of the product (Caswell and Noelke, 2002; Moser et al., 2011). The quality of agricultural produce incorporates sensory properties: texture, taste, aroma, and appearance; nutritive values; internal constituents; functional and mechanical properties and defects (Abbott, 1999). Internal attributes such as total soluble solids (TSS), acidity, moisture content, DM, and antioxidants have a high correlation with product aroma and taste (Rajkumar et al., 2012a), implicating a predominant role in quality assessment (Pu et al., n.d.).

Traditional manual and noninvasive methods can be applied for the ripening stage classification and the internal properties prediction of fruits. Traditional methods are considered time-consuming, laborious, and destructive for the classification and prediction of maturity and other parameters. Destructive methods are not desirable for the packaging industry as they will damage the external structure, and tissue evaluation cannot be done for a whole lot (Chauhan et al., 2017). Non-destructive or noninvasive techniques are widely used for the quality inspection of fruits and other agricultural products. Non-destructive techniques can be classified as mechanical (Manivel-Chávez et al., 2011), optical (Tian, 2022), electromagnetic and dynamic methods (Chauhan et al., 2017). The spectroscopic technique has been used extensively for quantitative and qualitative product composition and properties analysis. Xie et al. (2016) explained the

broad application of near-infrared spectroscopy (NIRS) for real-time, rapid online analysis, monitoring and inspection of fruits' physical and chemical composition (Xie et al., 2016). Imaging technology is another method for analyzing the surface and textural characteristics of the products plays. Since the external parameters and appearance also determine the quality of the product, imaging technology is widely used in the inspection, monitoring, and grading of agricultural products based on color, size, and texture during post-harvest handling, processing, and packaging (Davies, 2009).

Imaging and spectroscopy are widely used techniques for the quality inspection of agricultural products. The imaging techniques can acquire spatial characteristics such as texture, shape, size, and other physical properties, but they cannot provide information regarding the internal properties. On the other hand, spectroscopy can provide information regarding the internal properties of fruits and vegetables, but this technique lacks spatial information. Both methods have limitations as they cannot simultaneously acquire information regarding external and internal composition. Over the past 15 years, hyperspectral imaging has emerged as a new generation of sensing technology for non-destructive food quality and safety evaluation because it integrates the significant features of imaging and spectroscopy, thus enabling the acquisition of both spectral and spatial information from an object simultaneously (Lu et al., n.d.). The hyperspectral imagery is three-dimensional with two spatial and one spectral dimension providing continuity of data stored in the wavelength domain that captures images with a significant number of continuous wavebands enabling a full spectrum to be extracted from each pixel captured (Qin et al., 2013). Hyperspectral imaging has been widely researched and developed by integrating spectroscopy and imaging techniques into a system that can obtain a spatial map of spectral variation resulting in many successful applications in the quality assessment of fruits and vegetables (Li et al., 2017). The technology integrates or bridges spectroscopy and imaging to simultaneously acquire spectral and spatial information from a product (Park and Lu, 2015a). With the rapid evolution in hardware and software, hyperspectral imaging is expected to be increasingly used by the food and agricultural industries for quality and safety inspection of food and agricultural products in the coming years (Lu et al., n.d.).

Near-Infrared hyperspectral imaging (NIR-HSI) was applied to predict multiple quality attributes of apple fruit (Ma et al., 2017; D. Zhang et al., 2019). NIR-HSI was used to evaluate and visualize the distribution of the quality attributes such as SSC, DM, and total sugar content in apples (Lan et al., 2021). SSC and moisture content of bananas were determined using the short wave visible NIR HSI system (Rajkumar et al., 2012a). Prediction mapping of physicochemical properties in mango was done using visible NIR-HSI (450-998 nm) by (Rungpichayapichet et al., 2017). The physicochemical properties

of mango, such as soluble solids content (SSC), titratable acidity (TA) and firmness, were determined, and the spatial variability of the properties was used for visualizing the changes in properties during ripening. HSI imaging was applied for several other fruits such as pear (Khodabakhshian and Emadi, 2018), peach (Cen et al., 2011), and berries (Elmasry et al., 2007), avocado (Diaz et al., 2021) and many more. However, this state-of-the-art has not yet been applied for the ripening stage classification and DM prediction of durian fruit or pulp.

1.2 Research problem

In the ASEAN countries, the market value of fresh durian keeps fluctuating every year depending on the supply and quality. Durian pulp is consumed fresh and in several durian products such as minimally processed durian, frozen durian, powder, chips, ice cream, candy, milkshakes, jams, rolls, tarts, and pies. Consumers enjoy fresh durian but do not want a whole fruit as it is too big, and the rind (outer part) is difficult to cut. Therefore, the packaging house minimally processes the durian, which contains one or two pulps held in a polystyrene tray wrapped with plastic film. Durian consumers prefer the ripening stage; in Taiwan and Hongkong, people like the edible and soft ripe pulp with a mild aroma; in Singapore, they like it overripe with a strong smell. After harvesting, the farm's fruits are transferred to the packaging house for the maturity check. The maturity is determined with several criteria such as husk color, abscission layer, sap, grooves, stalk, tapping, and DM of pulp. However, these criteria cannot be applied to the large volume of durian that must be exported. The non-destructive maturity classification model of durian based on non-destructive approaches was done, and the results are very promising (Chuenatsadongkot et al., 2018; Rutpralom et al., 2002; Somton et al., 2015; Timkhum and Terdwongworakul, 2012). However, Ketsa, 2020 reported that the non-destructive approaches using NIR spectroscopy and other methods are carried out intensively for maturity identification. Still, none of these methods has been adopted for commercial practice.

DM, TSS and fat content are the important physicochemical properties directly related to the quality of durian pulp. The fruit packaging firm's durian pulp is graded based on its quality attributes. The traditional method of grading the fruit is time-consuming and laborious. Spectroscopic techniques were applied to predict DM and soluble solids content of durian by several researchers (Kuson and Terdwongworakul, 2013; Onsawai et al., 2021; Somton et al., 2015). Spectroscopic techniques are done in point scanning. The information from the spectroscopy does not provide information related to the overall changes within some fruit. Online measurement of the durian

quality parameters is possible using NIR spectroscopy, but it can only give information about the scanned part of the fruit. Computer vision and image processing were applied by (M. G. Lim and Chuah, 2019) using deep learning approaches to classify the type of durian. However, computer vision or imaging is unsuitable for determining the internal properties of a biological substance. Therefore, an advanced system must be installed in the production process at the packaging house and can give the overall visualization of internal attributes in a single fruit before it is exported or transferred to the market.

1.3 Research hypothesis

The concept of hyperspectral imaging is based upon the spectroscopy theory, which ideally connects to the concept of dispersion of light. Fruits and vegetables are biological substances containing molecular bonds like C-H, N-H or O-H. Spectroscopy uses the interaction of electromagnetic radiation with the biological substance and provides the chemical and physical information within the wavelength range that is either absorbed or reflected. The interaction of radiation and biological substance gives rise to the spectrum due to the transition in the energy level of molecules occurring from the overtones and combinational bands. This basic concept of spectroscopy is applied in the NIR-HSI system. The internal constituents in fruits are mainly organic compounds such as moisture (O-H), carbohydrate (C-H), and fat (C-H) organic compounds. NIR moisture absorption comprises five bands with maxima at 760, 970, 1190, 1450 and 1940 nm (Osborne et al., 1993). The bands at 1450, 970 and 760 nm are due to the O-H stretch's first, second and third overtone, respectively (Osborne et al., 1993). The absorption band of carbohydrate constituent rises at 990, 1440, 1450, 1528, 15840, 1580, 1900, 2000, 2100, 2252, 2276, 2461, 2488, and 2500 nm for starch; 1490, 1780, 1820, 2336, and 2352 nm for cellulose; 1440 and 2080 nm for sucrose and 1480 and 1580 nm for glucose, respectively (Osborne et al., 1993). These absorption bands of carbohydrate constituents are due to the overtone and combination band of C-H and O-H bonds. NIR absorption bands of fat or oil give rise to a CH_2 second overtone at 1200 and first overtone in 1734 and 1765 nm; and stretch bend combination at 2310 and 2345 nm, respectively (Osborne et al., 1993). The NIR range (700-2500 nm) can be applied for fruit's quantitative and qualitative analysis.

In the climacteric fruit, several changes occur within the fruit during the ripening stages. The breakdown of starch into carbohydrate, sucrose and fat brings gradual changes in the appearance and taste of durian. NIR-HSI can be used to monitor these changes and identify the ripening stages. The research hypothesis can be divided into two parts:

1. Durian ripening stages can be classified using the image and signal processing obtained from the NIR-HSI system
2. During the ripening stages of the durian, the DM, TSS and fat content change significantly.

1.4 Research aim

The research aims to:

- Develop a suitable method for the ripening stage classification of the durian pulp and intact fruit.
- Develop a robust prediction model for DM, TSS and fat content in durian pulp.

1.5 Research questions

The following research questions have been identified based on the literature review and existing research gaps.

- a) Can the HSI system be applicable in the ripening stage classification of durian?
- b) Compared to spectroscopy and imaging techniques, is there an improvement in the accuracy of ripening stage classification when we use HSI techniques in durian?
- c) Can the NIR-HSI technique improve the accuracy of DM, TSS and fat content prediction in durian pulp compared to the other methods?
- d) Will the spatial mapping of the physicochemical properties be helpful for the qualitative analysis?

1.6 Research objective

The main objectives of this doctoral research are:

- 1) To explore the possibility of using the NIR-HSI system for ripening stages classification of durian.
- 2) To apply the feature selection and compare the machine learning algorithm's performance for the ripening stage classification
- 3) To develop the regression model for predicting the physicochemical properties: DM, TSS and fat content in durian pulp.
- 4) To improve the accuracy of the regression model using deep learning and feature selection and visualize the distribution of the physicochemical properties by spatial mapping

1.7 Navigation of the thesis

This material is reserved for educational use only, not allowed for commercial use.

Forbidden to modify the content, and cite the document when use.

This thesis is organized into seven chapters. A brief discussion of every chapter is presented below.

Chapter 1 presents the research background, problem, hypothesis, research question and objective initiating this thesis.

Chapter 2 involves theories and literature reviews, beginning with an overview of the durian and its importance in the overall economy, durian botany, current harvesting practices, quality measurement, introduction of the NIR-HSI system, principal, and application in the quantitative and qualitative analysis of fruits. It also briefly introduces image processing techniques, machine learning, deep learning, and feature selection approaches.

Chapter 3 focuses on the Bayesian hyperparameter optimization method for the durian pulp ripening stage classification. It includes the methodology, results and discussion and conclusion of the approach.

Chapter 4 focuses on five machine learning algorithms and their accuracy assessment using the selected wavelength and full wavelength to classify durian pulp and intact fruit ripening stages.

Chapter 5 contains the physicochemical properties prediction model of durian pulp and spatial mapping of the DM, TSS and fat content to visualize the changes occurring within the fruit. It also includes some algorithms for the wavelength selection and regression model accuracy assessment using full wavelength and selected wavelength.

Chapter 6 summarizes the main conclusions and recommends further studies.

Chapter 2

Theories and Literature Review

2.1 Durian

Durian (*Durio zibethinus Murray*) belongs to the genus *Durio* and the Malvaceae family. The name “Durian” is derived from the Malay word *Duri*, meaning “thorn”, and the species name “zibethinus” is derived from the Italian word ‘zibetto’ meaning the strong aroma (Ketsa, 2018). Durian is known as “the king of fruits” in the Southeast Asian market. Thailand is one of the largest producers, followed by Indonesia, Malaysia and Philippines. Durian is mainly characterized by its unique appearance and aroma. The fruit is highly prized in the markets of Southeast Asia. Most durian lovers choose the firmer, ripen and less-volatile cultivars, while some consumers prefer the cultivars with strong flavour and overripe fruit.

2.1.1 Botany, origin and structure of durian

Durian is in the order Malvales, family Bombacaceae and genus *Durio* (Siriphanich, 2011). The genus *Durio* is native to the island of Borneo, the largest island in Asia (Siriphanich, 2011). This genus have 28 species, out of which only six are edible including *D. kutejensis*, *D. oxleyanus*, *D. graveolens*, *D. ducis*, *D. grandiflorus* and *D. zibethinus* (Siriphanich, 2011). The species differ in fruit size, pulp/aryl, color, and leaf area (Ketsa et al., 2020). Among the six species, *Durio zibethinus* (Durian) is one of the most famous and domesticated species cultivated commercially in large orchards throughout Southeast Asia (Yaacob, 1983). Channee, Kob, Kampan, Kan Yao, Kradum, Luang and Monthong are the most popular cultivars in Thailand (Ketsa et al., 2020). Fertile soil or clay loam with high organic matter and good drainage are well suited to grow durian (Ketsa et al., 2020). Durian trees are primarily grown in lowland tropics with an elevation of approximately 800 meters above sea level, an optimum temperature of 25-35°C and 80% relative humidity (“Durian Production Guide,” 2021). The fruit is a loculicidal capsule with a round, cylindrical or ellipsoidal shape generally consisting of five to six segments (locules) (Siriphanich, 2011).

The size of one fruit is approximately 15 to 30 cm long, 12.5 to 15 cm wide and weight from 1–6 kg. The fruit is attached to the stem. There are two parts of the stem, the part from the abscission zone to the meeting point on the branch is the upper part, and the part from the fruit to the abscission zone is the lower part, as shown in Figure 2.1. The lower parts are developed from the flower pedicel, and the upper part is developed from the flower peduncle (Siriphanich, 2011), as shown in Figure 2.2. One

fruit is formed from one flower with one ovary; however, among several flowers on an inflorescence emerging from main branches, 1-3 fruits selected by the farmers develop into mature fruit (Siriphanich, 2011). The fruits drop off from the tree at the abscission zone after ripening. The outer cover, known as the fruit's rind, is thorny and spiny. It is comparatively tough to peel and requires a special technique to handle and peel the rind off. In the dehiscence zone, at the early flower development stage, the ovary wall of each carpel joins to form a locule (Siriphanich, 2011). At the dehiscence zone, the fruits eventually split (Siriphanich, 2011). Inside each fruit are five to six pulp or aril units, known as locules. The aril consists of seeds that are 3–4 cm wide and 6-7 cm long. The seeds are hard and covered with the thin, light brown-colored skin known as a testa. The testa color turns brown gradually when the fruit matures (Siriphanich, 2011). The aril, the dark yellow colored pulp, starts to develop from the funiculus of each seed (Siriphanich, 2011). As the fruit develops, the aril outwardly covers the whole seed in each locule (Siriphanich, 2011). The fruit is big, and at least 30% of the total portion is edible (Ketsa et al., 2020; Lim and Luders, 1997; Yaacob, 1983). Each fruit is composed of three main components rind (50-60%), aril (20-30%) and seeds (5-10%). Basically, the fruit is symmetrical in shape; only if the fruit is poorly pollinated or fertilized the shapes will be twisted or odd in structure (Figure 2.1).



Figure. 2.1 Durian fruits after harvested from the orchard.

Monthong is the most popular variety of durian in Thailand. Monthong durian trees are 10-12 m in height and 8-10 m in the canopy (Ketsa et al., 2020). This variety is large, elongated, and oval-cylindrical in shape (Figure 2.2). The weight of each fruit can range from 4 to 6 kg. Each fruit can contain up to 10 arils, many of which are small,

shrunken, and under-developed. However, at least one fruit contains three fully developed, large, thick creamy and smooth arils (Ketsa et al., 2020; Lim and Luders, 1997; Yaacob, 1983). The color of the mature arils is golden, therefore this variety is also known as “Golden Pillow” (Ketsa et al., 2020).

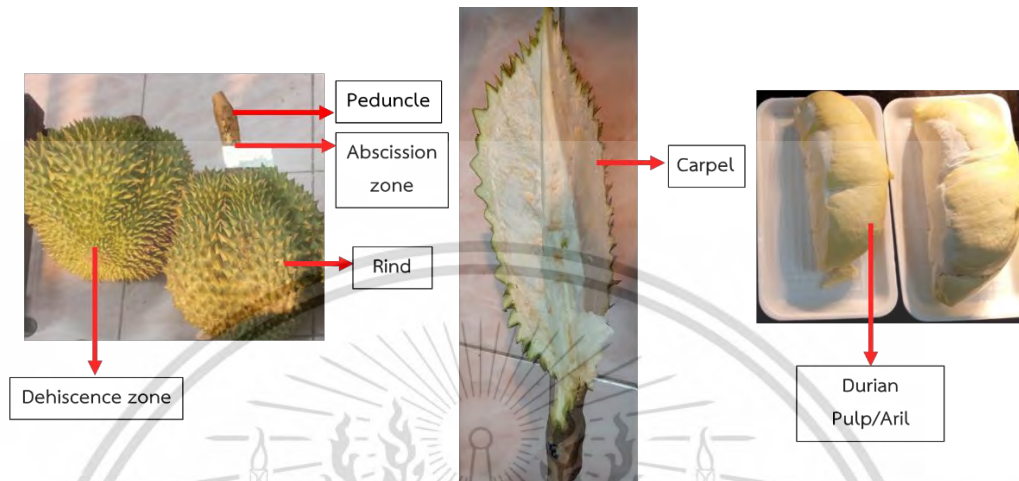


Figure. 2.2 Main parts and structure of durian (Monthong).

2.1.2 Durian production in Thailand

Durian is mainly cultivated in Thailand, Cambodia, Malaysia, Vietnam, South India, Southern Burma, Indonesia, Brunei, Philippines, and Papua New Guinea. Thailand is one of the important exporters of Durian for Southeast Asian countries. From January 2021 to 2022, 8732.4 tons of durian fruit worth approximately 52.8 million USD have been exported from Thailand (*Thai Customs*, n.d.). Figure 2.3 and 2.4 shows the fresh durian export quantity and export value between 2010 and 2022, respectively. Figure 2.3 shows that in 2013 the export of fresh durian was 26050.6 tons, the highest until this year. After 2013, the export rate is fluctuating. The worth value of fresh durian has been increasing since the year 2017.

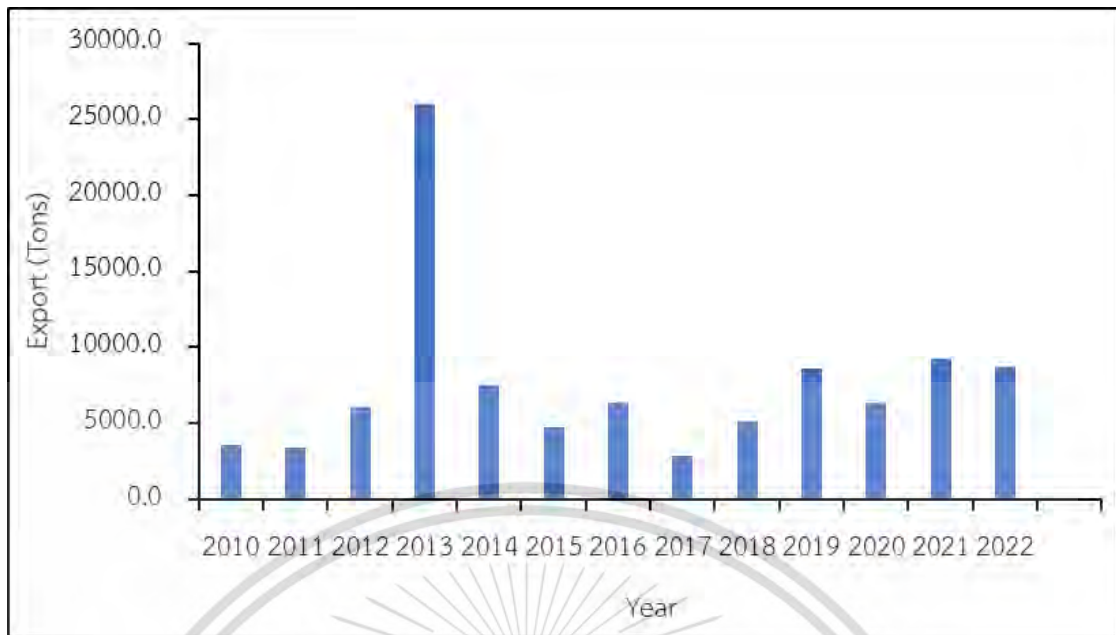


Figure. 2.3 Global fresh durian export quantity (Tons) from Thailand from 2010 to 2022 (Thai Customs, n.d.).

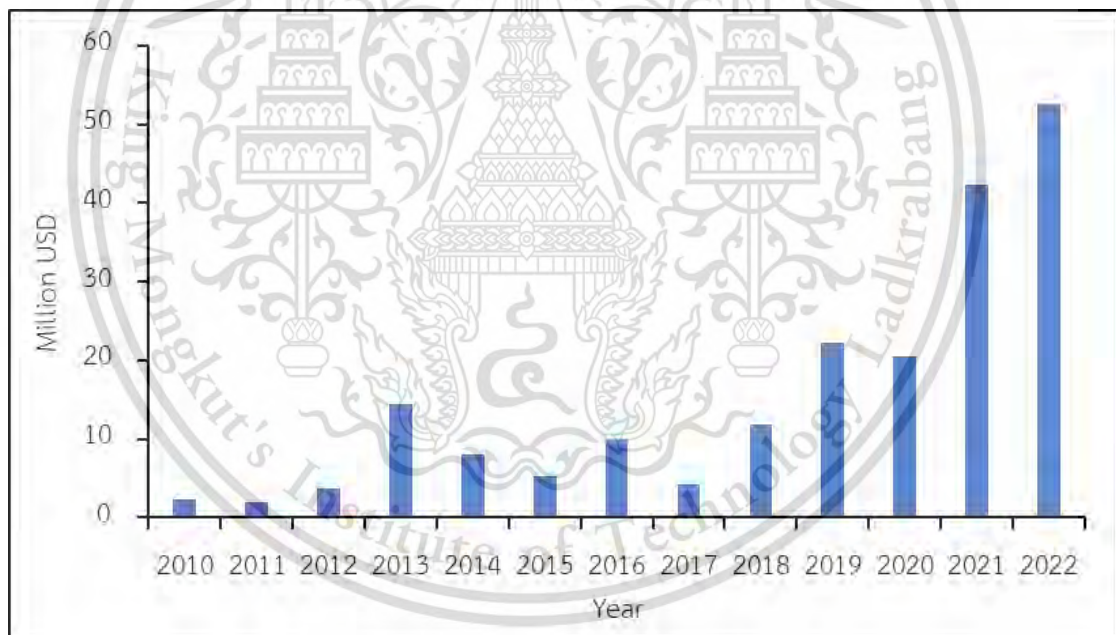


Figure. 2.4 Fresh durian export value in a million USD from 2010 to 2022 (Thai Customs, n.d.).

Durian is a climacteric fruit, available mainly between April and October in Thailand (Siriphanich, 2011). However, consumers can obtain early crops as early as mid-March, and late crops may be available in October (Siriphanich, 2011). Nowadays, durian production is possible throughout the year in Thailand using plant growth regulators, particularly Paclobutrazol (Siriphanich, 2011). The wide varieties are

categorized according to the duration from days after anthesis (DAA), size, variation of seedlings, and quality. Recently, the demand for processed durian products has increased in local and global markets. The processed products include chips, paste, flour, cake, ice cream, and juice (Mohd Ali et al., 2020).

2.1.3 Postharvest handling factors affecting the quality

Some postharvest handling factors affect the durian quality significantly. Physical damage due to a fractured or injured stem occurs when the fruit is accidentally dropped during harvesting, resulting in bruising and rotting around the rind (Siriphanich, 2011). Therefore, the fruits are separated by visual inspection. Chilling injury occurs in the durian when the fruit is exposed to low temperatures. On the other hand, humidity is another factor that affects the ripening behavior of durian. It has been observed that ripening at lower humidity will yield better-eating quality (Siriphanich, 2011); however, Ketsa and Pangkool, 1994 reported similar durian aril quality after ripening at 75 and 93% relative humidity. Due to high humidity, the ripening will take longer, and too much water loss will occur during the development (Siriphanich, 2011). This phenomenon may limit the dehiscence process, making it difficult to split open the fruit after harvesting (Ketsa, 2018). The atmosphere also plays an essential role in maintaining the quality of the fruit. Several of these factors leads to the common physiological disorder that can be detected in the case of durians, such as chilling injury, uneven ripeness, water-soaked core and aril tip browning (Ketsa et al., 2020). Durian is not an easy fruit to grow, and it requires full attention before and after harvesting to maintain excellent quality and increase the customer's demand. Uneven ripeness is one of the factors that is needed to be addressed. Identifying the ripening level and generating the index is helpful for the durian producers. Non-destructive sensors can be applied in the packaging firms to identify the ripeness level and internal attributes of fresh intact fruits and pulps.

2.1.4 Harvest operation

The fruits are harvested manually at the correct harvesting indices in Thailand (Ketsa et al., 2020). After harvesting, the durian is preliminarily sorted by the farmers. The defective, infected, immature or over mature, under or over size durians are removed. After that, the preliminary sorted fruit is loaded into a pick-up truck to be taken to the commercial vendor or exporter (Siriphanich, 2011). For the export of quality fruits, the durians are selected from clean and well-managed orchards. Trees should be healthy with dark green leaves and without infected bark or wounds. In addition, fungicides should be applied to the tree (Siriphanich, 2011). These are important criteria since unhealthy trees can produce poor quality fruit, including those with uneven fruit

ripening characteristics (Siriphanich, 2011). Finally, at the packinghouse, the fruits are sorted by an expert to determine their proper maturity and other minimum requirements. The fruits which do not meet the criteria are then rejected and returned to the farmers.

2.2 Fruit ripening and maturity

Fruit development starts from dry seed capsules to large fleshy structures with bright colors and aroma that can attract animals for seed dispersion. Generally, after the fertilization, fruits are formed from a fertilized ovary. Other parts of the flower, such as receptacle tissue and sepals, can also contribute to the fruit formation (Valero and Serrano, 2010). However, there are few species known as parthenocarpic fruits in which the fruits are set and mature without fertilization and seed development. Fruits such as pear, apple, peach, cherry, table grape, banana, and citrus are parthenocarpic fruits (Valero and Serrano, 2010). In fleshy fruit, it involves three stages: fruit set, fruit development, and fruit ripening.

Maturation refers to the processes that lead to ripening; in many cases, maturation and ripening overlap in time (Giovannoni, 2001). Maturation is the time between final fruit growth and the beginning of ripening and senescence. The ripening process corresponds to those modifications that allow the fruit to become edible and attractive for consumption. The ripening process is regulated by thousands of genes and molecular activities that control progressive softening and lignification of pericarp layers, accumulation of sugars, acids, pigments, and release of volatiles (Valero and Serrano, 2010). The key to crop or fruit improvement is a deeper understanding of fruit ripening processes at different maturity levels (Valero and Serrano, 2010). Most fruits show gradual changes in color, texture, flavour, and pathogen susceptibility during maturation (Valero and Serrano, 2010). Two major classifications of fruit, climacteric and non-climacteric, have been utilized to distinguish fruit based on respiration and ethylene biosynthesis rates.

Climacteric fruits inclusive of avocado, apple, banana, durian, peach, plum etc., are characterized via way of means of growth in the respiratory with a concomitant and fast manufacturing of ethylene on the initiation of ripening; the produced ethylene, that is a plant hormone, hurries up the ripening process. (Pech et al., 2012). In contrast, these changes do not occur in non-climacteric fruits such as grape, strawberry, and citrus; therefore the maturation proceeds relatively slowly. Ethylene production in unripe fruit could be deficient; however, as fruit develop, they produce immense quantities that accelerate the ripening technique or the degree of ripening. The range of ethylene production in the climacteric fruits during the growing period is low ($0.1\text{--}0.2 \mu\text{L kg}^{-1} \text{h}^{-1}$)

¹); however, this rate can increase up to 1000 folds during the ripening process (Valero and Serrano, 2010). Once the ripening process starts, the ethylene synthesis will lead to over-ripening and low shelf life, causing decay (Valero and Serrano, 2010). Therefore, postharvest storage conditions are vital to regulating ethylene effects, both in fruits and vegetables and crops, to ensure their quality and enlarge storage prospects (Valero and Serrano, 2010).

The ripening process requires the synthesis of novel proteins and mRNAs, as well as new pigments and flavour compounds (Seymour et al., 1993). The increase in respiration coincides with the physical, chemical and biological changes during ripening (Ketsa et al., 2020). Valero and Serrano, 2010 describe the respiration process as the oxidative breakdown of complicated substrate molecules commonly available in plant cells, such as starch, sugars, and organic acids, to fewer complex molecules such as carbon dioxide and water. These anabolic activities need energy and a supply of carbon skeleton building blocks (Seymour et al., 1993). These are provided in fruit, even as in alternative tissues by respiration (Seymour et al., 1993). Respiration maintains an adequate amount of Adenosine triphosphate (ATP). ATP is the energy carrier molecule inside the cells and an intermediate molecule required to endure the continuous chain of anabolic reactions (Valero and Serrano, 2010). These reactions are essential to maintaining living cells' cellular organization and membrane integrity (Valero and Serrano, 2010). The components of the anabolic responses are stored in different sources and destinations. Glucose, as one of the main components, proceeds from stored simple sugars or polysaccharides, such as starch (Valero and Serrano, 2010). Oxygen (O₂) circulates into the tissue from the encompassing atmosphere and is employed to oxidize glucose. In contrast, carbon dioxide (CO₂) diffuses out of the tissue; therefore, the water formed is solely incorporated into the aqueous solution of the cell (Valero and Serrano, 2010). The respiration rates are higher in the early growth stages, and the decline in respiration rate can be observed during maturation in the case of both climacteric and non-climacteric fruits (Figure 2.5). However, climacteric produces the rise in respiration that overlaps with the ripening and maturation stages, as observed in Figure 2.5 (Yang and Hoffman, 2003). Zuzunaga et al., 2001, described the typical behaviour in plums, the respiration rate is usually high during starting stage of fruit development and the rate decreases as it proceeds to maturity. Similar characteristics have been identified for tomatoes (Preedy, 2008), in which the respiration rate reaches the maximum at the pink stage (early development stage in tomato) and decrease gradually as it reaches maturity from light red to red fruits (Valero and Serrano, 2010).

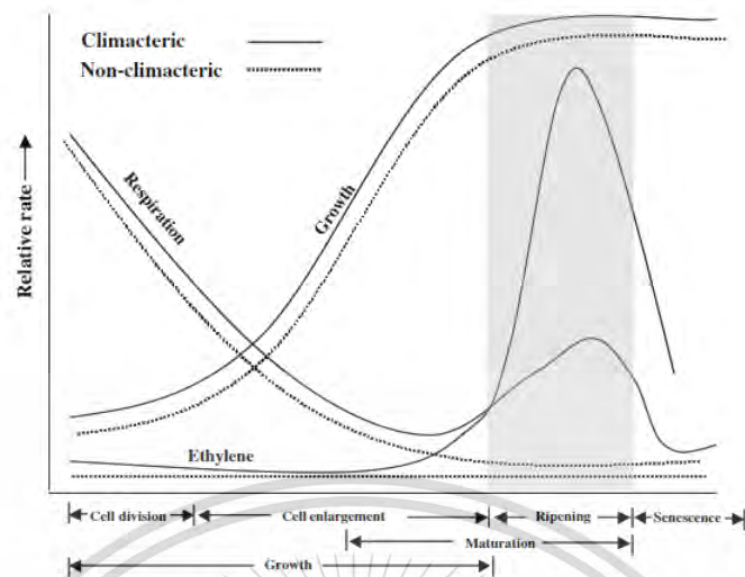


Figure. 2.5 The pattern of growth, respiration, and ethylene production during fruit development (Paul et al., n.d.) Source: (RBH and Golding, 2016).

As climacteric fruit, the ripening of durian fruit also coincides with the respiration rate. The significant factors influencing the durian's respiration rate are temperature, cultivar and maturity (Ketsa and Pangkool, 1995b; Ketsa and Pangkool, 1995a; Tongdee et al., 1988). An increase in temperature enhances the respiration rate, while a decrease in the temperature slows down the respiration rate. Fruit harvested at different maturity also had different respiration rates. The rind or husk of durian continues the respiration process for a few days before declining. Durian fruit cv. Monthong harvested at 95% maturity reach the climacteric respiration peak earlier than the fruit harvested at 80% maturity (Tongdee et al., 1988). Similarly, ethylene production also overlaps with the rise in respiration rate. In the durian, the rind produces most of the ethylene (Ketsa et al., 2020). As a result, ethylene synthesis after harvest continues to increase for some days before declining. Durian cultivars with high ethylene production tend to ripen earlier than those with lower ethylene production rates (Ketsa et al., 2020). Thai exporters treat durian for some hours with 1- Methylcyclopropene (1-MCP), which is an ethylene receptor inhibitor (Blankenship and Dole, 2003) that prevents ethylene production and slows down the ripening, which eventually increases the shelf life and storage after durian harvesting (Pareek, 2016).

2.2.1 Physicochemical properties in fruits

During the ripening process, changes undergo within the fruit, and it is important to understand how the changes impact the overall chemical or physical properties of fruits. Physicochemical properties are the properties that are dependent on the joint

action of both chemical and physical processes within the fruits. The fundamental changes related to ripening include firmness or texture, color, taste, and flavour. Changes in these properties are due to the different phenomena occurring within the fruit during the ripening phases. Textural changes occur due to cell wall degradation activities and modification in the cuticle properties (Seymour et al., 1993). The loss of green color and increased non-photosynthetic pigments during ripening lead to color alteration Seymour et al., 1993). During ripening, there is an increase in sugar and a decrease in the organic acids, which leads to changes in the taste (Seymour et al., 1993). Similarly, the flavour is related to the production of the volatile compounds providing a unique aroma (Seymour et al., 1993). These characteristics change throughout from unripe to fully ripe stage in fruits. The changes in physical and chemical properties occur from the late fruit growth stage to the initial senescence stage.

2.2.1.1 Fruit growth

The average fruit growth after blooming or days after anthesis (DAA) depends on the species or genotype. It can range from 3 weeks to 60 weeks, but in most fruits, it takes about 15 weeks (Valero and Serrano, 2010). After the flower is successfully pollinated, the fruit growth involves cell division, and cell expansion becomes an active carbohydrate sink (Valero and Serrano, 2010). In some fruits, such as blackberries, cell division is completed by the time of pollination, whereas, in some fruits, such as avocado, cell division continues throughout the development (Valero and Serrano, 2010). Fruit growth on the plant is a physical measurement such as weight, length, width, and volume. Generally, the fruit growth curve can be divided into double-sigmoid and single-sigmoid curves. The double sigmoid characteristics are determined in stone fruits such as peach, apricot, olive, and plum, and some nonstone fruits such as grape and currant. In double sigmoid growth, there are different phases from the first exponential phase characterized by growth due to cell enlargement, the second phase does not involve significant change except pit hardening or endocarp hardening, and the third phase is the second exponential growth due to cell enlargement (Valero and Serrano, 2010). Finally, the fruit growth rate decreases in the fourth phase, and ripening occurs (Valero and Serrano, 2010). During the cell division phase, the growth is low in a single sigmoid growth curve. It is followed by the second phase of pit hardening of fast growth due to cell expansion and finally the third phase with reduced growth until reaching the maximum fruit size. The comparison between single sigmoid (Apple and Pear) and double sigmoid (pear) is shown in Figure 2.6 (Din et al., 2019). Durian is climacteric fruit with a sigmoid growth pattern (Janick and Paull, 2008). In the durian, from fruit set to 57 days is slow growth or cell division stage followed by the rapid

growth stage, which starts between 57-85 and 57-92 days after anthesis (DAA), respectively (Sangwanangkul and Siriphanich, 2000).

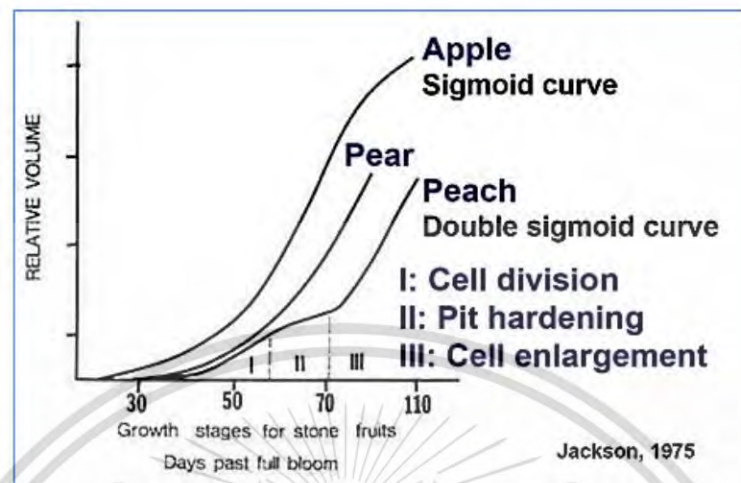


Figure. 2.6 Fruit growth curve (Din et al., 2019).

2.2.1.2 Color

Color change in fruits is highly associated with ripening and is an important attribute representing fruit quality. Most fruit changes color during maturation; however, some varieties of apple or pear remain green even after ripening. The color change is mainly related to the degradation of chlorophyll content and the biosynthesis of anthocyanins, carotenoids, or other pigments (Artés et al., 2002). Anthocyanins are confined within the vacuole of the plant cells, and these are a very diverse range of pigments (Timberlake, 1981). Although due to the presence of chlorophyll, the unripe fruits are usually green in color, as they proceed towards ripening, the chlorophyll breaks down. The anthocyanins and carotenoids replace it. These compounds are antioxidants that prevent the fruit from spoiling too quickly in the air (Seymour et al., 1993).

Anthocyanin and anthocyanidin are in the form of glycoside and aglycone (Khoo et al., 2017). Anthocyanins are in the form of anthocyanidin glycosides and acylated anthocyanins (Khoo et al., 2017). Anthocyanins are broad in the range from blue to red pigments, usually found in plants' flowers, fruits, and tubers (Khoo et al., 2017). The most common anthocyanidins are cyanidin, delphinidin, pelargonidin, peonidin, petunidin, and malvidin (Khoo et al., 2017). Carotenoids are another pigment responsible for color change which can be classified into two groups based on the functional group. Two groups are xanthophylls, which contain oxygen as an active group, including lutein and zeaxanthin, and carotenes, which include only a parent

hydrocarbon chain without any functional group, such as α -carotene, β -carotene, and lycopene (Saini et al., 2015). Their colors can predict the type and availability of carotenoids in fruits and vegetables. For example, the yellow-orange vegetables and fruits are generally rich in β -carotene and the α -carotene (Seymour et al., 1993). Similarly, in the orange fruits, α -Cryptoxanthin and zeinoxanthin can be found (Seymour et al., 1993). Likewise, lycopene pigment (responsible for the bright red) is the principal constituent of tomatoes and tomato products (Saini et al., 2015).

In the durian, a change in aril color after anthesis is due to the increase in β -carotene content (Sangwanangkul, 1998). During maturation and ripening, the aril changes from light to dark yellow depending on the cultivar, as shown in Figure 2.7 (Ketsa and Pangkool, 1995b; Wisutiamonkul et al., 2017; Wisutiamonkul et al., 2015). Wisutiamonkul et al., 2017 observed that the durian aril is a light cream color after harvest. After storing the aril for four days at 25°C, the aril color gradually changes to dark yellow. In the aril of durian, the powerful carotenoids found are β -carotene and α -carotene, with some minor carotenoids lutein and zeaxanthin (Wisutiamonkul et al., 2017; Wisutiamonkul et al., 2015). Among most cultivars, significant differences in β -carotene and α -carotene concentrations were detected (Wisutiamonkul et al., 2017; Wisutiamonkul et al., 2015). It was observed that both α -carotene and β -carotene, contents gradually increase with maturity (Wisutiamonkul et al., 2017; Wisutiamonkul et al., 2015). During ripening, the concentration of β -carotene increases five times higher than α -carotene (Isabelle et al. 2010). The concentration of carotenoids in ripe fruit is associated with the yellow color of the aril that develops during ripening (Wisutiamonkul., 2015).

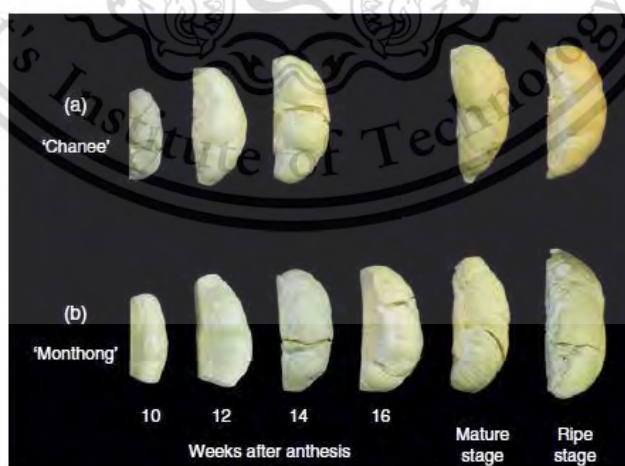


Figure. 2.7. Change in aril color during ripening stage Chanee (a) and Monthong (b) during fruit growth and ripening (Wisutiamonkul et al., 2017; Wisutiamonkul., 2015).

2.2.1.3 Texture

The textural change leading to the softening of fruits during the maturation and ripening is primarily due to three mechanisms: loss of turgor, degradation of starch, or modification of cell wall (Valero and Serrano, 2010). Turgor loss is principally a non-physiological process connected with the fruit's postharvest dehydration and will intrinsically assume commercial importance throughout storage (Seymour et al., 1993). The loss of water, approximately 5-10% of a fruit's fresh weight, has a negligible effect on the fruit's biochemistry but can make the fruit commercially unacceptable (Seymour et al., 1993). The degradation of starch results in significant textural changes in fruits like bananas because bananas' fresh weight contains a high percentage of starch. However, in the case of most fruits, the textural changes during the ripening phase are mainly due to cell wall degradation. More than ninety per cent of the cell wall structure is composed of carbohydrate polymer, and the rest is hydroxyproline-rich glycoprotein (HPRG) (Seymour et al., 1993). Carbohydrate polymer includes cellulose, hemicellulose, or pectin (Seymour et al., 1993).

According to the softening or changes in textural behaviour, fruits can be divided into two categories. The first category includes those that soften significantly to a melting texture due to swelling of the cell as they ripen, such as tomato, peach, strawberry, and kiwifruit (Valero and Serrano, 2010). The second category includes those that soften moderately, without cell swelling, and are characterized by a crisp fracturable texture, such as apple or cranberry (Valero and Serrano, 2010). The time when the softening starts can be before (avocado and strawberry) or after (pome fruits) fruit growth; it depends on the type of fruit. The changes in texture can be preceded by several mechanisms in the fruits, and the mechanism can be different among the fruit species and cultivars belonging to the same species (Valero and Serrano, 2010).

The softening of the aril in durian is due to cell wall degradation. The aril declines rapidly during ripening, associated with increased water-soluble pectin content (Ketsa and Daengkanit, 1998; Ketsa and Daengkanit, 1998). Mature aril has a greater water-soluble pectin concentration, rising faster than less ripe durian aril. Therefore, mature aril has a greater cell wall softening enzyme activity that helps in the degradation of cell wall pectin (Ahmad et al., 2013; Barrett and Gonzalez, 1994; Goulao and Oliveira, 2008). In some cultivars, if the aril firmness is higher at the unripe stage, it shows a slower decline in firmness than other cultivars that attain a lower aril firmness during ripening; however, at the fully ripe stage, the aril firmness for all cultivars is similar (Ketsa and Pangkool, 1995b; Wisutiamonkul et al., 2017; Wisutiamonkul, Promdang, Ketsa, and Van Doorn, 2015).

2.2.1.4 Flavour and aroma

The flavour of the fruit depends upon its taste and smell. The flavour of the fruit depends on the complex interaction of sugars, organic acids, phenolic and more specialized flavour compounds, including a wide range of volatiles.

Sugar and organic acid

Fruits differ in their contents of sugar and organic acid. Sugar and organic acids are respiratory substrates, but they usually are present in slightly higher amounts than required for energy generation (Seymour et al., 1993). The common sugars are fructose, glucose and sucrose, and most organic acid is malate and citrate (Seymour et al., 1993). Fruits assimilate sugar and organic acids during the ripening or development phase, but they differ in how the fruits accumulate (Valero and Serrano, 2010). For example, some fruits, such as bananas, mango, kiwifruit etc., collect the bulk of their carbohydrate before ripening, which is hydrolysed either as starch or as sugar (Valero and Serrano, 2010). And these fruits can be harvested at the mature green stage and still attain good flavor on ripening.

On the other hand, fruits such as berries, cherries, grapes, etc., accumulate the sugar from the plant during the ripening, accounting for a more significant part of their flavour. The hydrolysis of sucrose into fructose and glucose intensifies during the fruit ripening stage, depending upon the species (Valero and Serrano, 2010). For example, grapes contain primary sugar as glucose, while fructose is the major sugar in berries, mango, and citrus fruits. In contrast, apricot, plum, peach, and nectarine have sucrose as the primary sugar. The proportions of fructose, glucose, and sucrose are substantial in taste perception since fructose is 80% sweeter than sucrose, while glucose is only 60% sweeter than sucrose (Yamaguchi et al., 1970).

The fruits at the initial developing stage are highly acidic due to the accumulation of many organic acids. However, when it reaches maturity, the sour taste reduces because large amounts of accumulated sugars and decreased total acids (TA) occur during ripening. Another factor determining fruit acidity is the type of organic acids, the most important being malic, citric, tartaric, quinic, oxalic, fumaric, and succinic acid, which have a unique taste that contributes to the overall flavour of fruits (Valero and Serrano, 2010). Malic acid is the leading organic acid of fruits belonging to the Rosaceae family for *Prunus* (plum, apricot, peach, nectarine, sweet cherry) and *Malus* (apple, pear) genera. In these fruits concentration of TA is higher with the accumulation of malic acid during the cell division stage. Later at the maturation and ripening (Diaz-Mula et al., 2009; Serrano et al., 2005). TA starts to decline except for the sweet cherry, for which

the acidity continues to increase throughout on-tree ripening (Diaz-Mula et al., 2009; Serrano et al., 2005).

Like mango and banana, durian also tends to accumulate high levels of starch during growth on the tree. Mature and unripe durian aril contains about 23-26% starch that reaches a maximum and gradually declines during ripening with the significant increase in the soluble solids and total sugar (Ketsa and Pangkool, 1995a; Ketsa and Pongkool, 2001; Ketsa and Daengkanit, 1998). Reducing sugars (glucose and fructose) and non-reducing sugars (sucrose) rapidly increases with ripening. Non-reducing sugars comprised 70–80% of the total sugars and contributed to aril sweetness (Sutthaphan, 1993). The range of malic acid in durian aril is from 1.66-to 12.86%, with a significant amount of citric, tartaric and succinic acids (Ketsa et al., 2020).

Volatile compounds

Fruit volatile composition includes various chemicals from various classes, such as alcohols, aldehydes, esters, ketones, and terpenes (Seymour et al., 1993). It is fundamental to any fruit's consumer preference and market success. A particular fruit's characteristic aroma and flavour are usually absent in the early stage of its development. However, it acquires during the ripening process due to volatile accumulation (Valero and Serrano, 2010). Major volatiles accountable for the fruit aroma can be classified as primary or secondary based on the presence in intact fruit tissue or produced due to tissue disruption (Seymour et al., 1993). Among several complex flavour compounds responsible for fruit aroma, most are relatively simple, volatile molecules. An analysis of the volatiles present in apple and orange fruit indicates at least 230 and 330 different compounds, respectively (Straten et al., 1977).

In fresh durian, sulphur-containing compounds and esters significantly impact the characteristic aroma and flavour (Ketsa et al., 2020). Propane-1-thiol (C_3H_7SH) and ethyl α -methyl butyrate ($C_7H_{14}O_2$) are the predominant constituents of the odor (Maninang et al., 2011a). Ketsa et al., 2020 reported that 38 major volatile compounds are responsible for fresh durian's unique aroma, including eleven esters, ten alcohols, six carboxylic acids, six sulfurous and nitrogenous, and five hydrocarbons compounds. During aril development into fruit leather, most of the aroma components of fresh durian fruit retain (Jaswir et al., 2008). At post-harvest storage, the concentration of acids in the fruit increased, and the aldehydes, ester, and alcohols decreased, whereas sulfurous and nitrogenous compounds, hydrocarbons, and phenolic compounds fluctuated (Jaswir et al., 2008). The number of volatile compounds varies with the maturity stage and species. Maninang et al. (2011) distinguished one hundred thirty-seven volatile compounds in ripe durian that differed in both cultivar and maturity. Seventeen and thirteen volatile compounds were found at the fully and partially

matured stage, most of which were the ester compounds (Ketsa et al., 2020). This finding satisfies the fact that in durian, the aroma is weaker in immature fruits, and it intensifies with the increase in maturity level.

2.2.2 Maturity of Durian

There are several criteria to judge durian fruit maturity. Some of the durian maturity identification methods are: counting the number of days from full bloom (DAA), the color of the spine tip, elasticity and disposition of the spines, the intensity of the odour emitted, changes in the fruit stalk, aril dry matter percentage, and tapping (Pascua and Cantila, 1992). Maturity is a critical factor in influencing eating quality. Several researchers and growers are working to relate the number of days from full bloom (anthesis) to eating quality and flavour attributes. Durian fruit development pattern is simple sigmoid, and the total duration from days after anthesis (DAA) to harvest varies among cultivars, ranging from 90 to 150 days (Siriphanich, 2011). Specifically, for the Monthong variety, the fruit matures around 120 days after anthesis (DDA) (Siriphanich, 2011). According to Siriphanich, 2011, farmers use the maturity percentage from 70 to 100% for harvesting. Farmers refer 100% maturity to the stage when the fruit is already ripe (130 DAA), 90% maturity to the fully mature fruit (120–125 DAA), 80% maturity to the mature green stage durian (110–115 DAA), and 70% maturity is the minimum maturity (95-105 DAA) at which durian can be harvested with acceptable eating quality. When the durian fruit starts to mature, the aril color develops and becomes cream, yellow or deep orange, depending on the cultivars. The growth in the length of monthong fruit is faster than the width resulting in the oblong-shaped fruit (Koksungnoen and Siriphanich, 2008). During ripening, the rind and fruit axis follows the whole fruit. The aril of the monthong variety continues to overgrow from 35-84 DAA. Monthong durian takes 4 to 6 days to ripen after harvest, depending on maturity. Considering that the fruit at 85% maturity, based on DAA (110-120 DAA) and rind characteristics, ripens to excellent quality in under one week at an optimum temperature of 28 to 31 °C (82 to 88 °F) (Paull and Ketsa, 2014). Fruits harvested around the 95% maturity have commenced ripening, while harvested at 75% may mature with inferior quality. The shelf life of the fruits collected from the ground after falling is usually shorter than the hand-picked fruits. The reason behind this is the disease, fractures and injuries subjected to the fruits falling from the tree. Those fruits need special attention and proper handling after collecting it from the orchards.

In Thailand, durian harvesting with the stem (peduncle) attached and wrapped in either leaf or paper to reduce withering and maintain the fresh appearance of the stem (Siriphanich, 2011). The stem's freshness is one indicator of harvested durian

freshness. Factors like crop load on the tree and fruit position on the branch also impact the durian fruit maturity. The stem remains flexible and bendable during the early fruit growth stage; however, as the fruit develops, the fruit stem's phloem fibre increases, making the stem resistant to a bending force (Siriphanich, 2011). The elastic modulus of fruit stem can be measured using a firmness tester integrated with multiple plunger-head or other types of equipment available; however, to date, no equipment has been implemented on-field testing at durian orchards (Chattavongsin and Siriphanich, 1990; Siriphanich, 2011; Wattanawichian et al., 2002). There is variation in durian trees and cultivars in orchards, due to which the traditional methods such as visual inspection and tapping are preferable maturity index by durian experts.

2.2.2.1 Important maturity indices

During the ripening process, it is essential to understand how these changes impact the overall chemical or physical properties of fruits. Physicochemical properties are the properties that are dependent on the combined action of both chemical and physical processes within the fruits. The ripening in durian can be indicated by the soft, yellow and creamy aril, sweetness, strength of the odor, and flavour. The changes occur due to several physical and chemical reactions from anthesis to ripening (Ketsa, 2018b). As a result, durian aril softens rapidly during development and becomes mushy and unfit for fresh consumption. The food accumulation in aril, which can be determined in terms of sugar, starch, lipid and dry matter contents, takes place only after the fruit growth is slow (Siriphanich, 2011). These properties in the aril change during the ripening stages. Durian is consumed at different ripening stages according to the cultivar; however, the difference in the quality and nutritional values within the pulp at different ripening phases are practically unknown (Arancibia-Avila et al., 2008). Some critical physicochemical properties of durian pulp are total soluble solids (TSS), dry matter (DM) and fat content (FC).

Total soluble solids (TSS)

The combination of sugars and acids, with a small number of dissolved vitamins, fructans, proteins, pigments, phenolics, and minerals, are known as soluble solids (Chope et al., 2006; Ito et al., 1997; Kader, 2008; Tadeo et al., 1987). TSS indicate the sweetness of fresh and processed horticultural food products, mainly in the laboratories for research and by industries (Magwaza and Opara, 2015). TSS is reported as degrees Brix ($^{\circ}\text{Brix}$), equivalent to a percentage (%) (Magwaza and Opara, 2015). Theoretically, the unit $^{\circ}\text{Brix}$, represents the dry substance content of solutions comprising mainly sucrose (Dongare et al., 2014; Echeverria and Ismail, 1987; Wardowski et al., 1979), which means that if a juice sample has 25 $^{\circ}\text{Brix}$ then it implies that the juice contains 25 g of

sugar per 100 g (Ball, 2006). The above theory is unappropriated for the fruit and vegetable samples because TSS consists not only of sugar but also several other components (Magwaza and Opara, 2015). However, sugar components (sucrose, glucose, and fructose) and sugar alcohol (sorbitol and mannitol) represent approximately 85% of TSS in many fruits; therefore, the term °Brix has become a synonym with TSS (Magwaza and Opara, 2015). In the case of lime, sugar constitutes only 25% of TSS, but in another type of citrus fruit, 75-85% of TSS of juice is made up of sugars (Wardowski et al., 1979). The higher values of TSS (°Brix or %) correspond with higher sweetness in fruits (Magwaza and Opara, 2015). TSS can be quantified in laboratories for research or by industries using a hydrometer, refractometer or spectrophotometer. A refractometer is an instrument that utilizes light power to detect the concentration of liquid, whereas the spectrophotometer measures the absorbance value of the solution (Li et al., 2016).

In the case of durian, there is a significant change in TSS and total sugar content in the aril during the ripening stages. As a result, there is an increment in total sugar from 5–10% to 20–30%, while reducing sugars (glucose and fructose) increase from 1–3% to 2–6% (Karichiappan et al., 2000). A previous study indicated that minimally processed durian pulp SSC ranged from 17.5 to 36.88% (Karichiappan et al., 2000). Onsawai et al., 2021 identified that TSS increased more than twofold from 13.2% at 80 DAA to 24.9% at 100 DAA, and later decreased to 19.3% at 110 DAA and reached a maximum of 34.9% at 120 DAA. The TSS value changes with the ripening stage and is directly related to the eating quality; therefore, monitoring the TSS of durian is desirable.

Dry matter (DM)

Dry matter (DM) in fruits indicates the weight of all tissue components, excluding water (Anderson et al., 2017). It is a valuable index representing the accumulation of soluble and insoluble carbohydrate content, i.e. sugars and starch in climacteric fruits (Anderson et al., 2017). Studies have revealed that DM can determine the post-harvest quality and indicate the maturity stage of fruit (Ncama et al., 2018). Fruits harvested at an immature stage will have a long shelf life but lower DM content, leading to consumer dissatisfaction (Anderson et al., 2017). Crisosto et al., 2012 and McGlone et al., 2003 investigated a positive correlation between DM content at harvest with TSS and titratable acidity (TA) after storage in kiwi and apple, respectively. Furthermore, DM content at harvest and flesh firmness has a positive correlation (Palmer et al., 2010; Saei et al., 2011). Literature suggests that DM content determination can be a measure complementary to harvest maturity for determining fruit storage potential. The measurement of DM is done by the destructive method. The hot oven drying technique is widely used to measure the DM percentage in agricultural products. However, several

non-destructive methods have been developed for decades to replace destructive ways to determine DM.

In the durian, the average DM content was affected by maturity between 97 DAA to 104 DAA (Somton et al., 2015). The DM content increased at a higher rate from 97 DAA to 111 DAA and then levelled off toward 132 DAA (Somton et al., 2015). However, (Onsawai et al., 2021) found that the DM increased from 12.55% to 39.50 % from 80 DAA to 127 DAA, respectively. In particular, the Monthong durian cultivar usually reaches minimum maturity at 106 to 110 DAA (Onsawai et al., 2021; Sangwanangkul and Siriphanich, 2000). The rate of DM accumulation in durian pulp is higher between 110-120 DAA (Onsawai et al., 2020). Durian fruit with minimum maturity at 106 DAA was reported to experience uneven ripening and higher variation in pulp firmness than fully mature fruit (Pakcharoen et al., 2013). Therefore, durian should not be harvested until 106 DAA and should contain at least 32 per cent DM (Sangwanangkul and Siriphanich, 2000). The durian with low DM content than the optimum percentage was observed to have poor eating quality with no odor (Siriphanich and Khurnpoon, 2003). Therefore, monitoring the DM in the ripening stages can assist in grading durian pulp quality. The percentage of DM content was calculated from equation (2.1).

$$DM = 100 \times \frac{W_2}{W_1} \quad (2.1)$$

Where, W_1 is the initial durian weight and W_2 is the final durian weight after dried in constant weight.

Fat content (FC)

Fat content (FC) is one of the important components that add up to the unique flavour of durian. The index of flavor quality of fruits is correlated with their acid and sugar contents. Lipids contribute to the mouthfeel and modify the taste and flavour of other food compounds (Berry, 1981). Furthermore, the chemical composition of the lipid is a crucial factor in determining the textural and rheological properties of high-fat foods. This may also apply to fruits- particularly those with relatively higher proportions of lipids (Berry, 1981). Lipids are a class of organic molecules that are insoluble in water and soluble in organic solvents. Fats are large molecules composed of three fatty acid molecules bonded to a glycerol molecule (Bidlack, 1998). The fatty acid molecule is a long chain of covalently bonded carbon atoms with nonpolar bonds to hydrogen atoms all along the carbon chain with a carboxyl group attached to one end (Bidlack, 1998).

The fresh arils of durian contain fat of about 3.10-5.29 g per 100 g fresh weight (Aziz and Jalil, 2019). The fatty acid composition of durian lipid is mostly unsaturated (Berry, 1981; Koksungnoen and Siriphanich, 2008; Sangwanangkul and Siriphanich, 2000).

The aril of the durian was first analyzed using gas chromatography (Aspiras and Tocino, 1971), but no conclusions about its constituents were made. Later Greve, 1974 conducted an analysis of the fatty acid composition of durian seeds, arils and husks collected from two locations in Thailand. The experiment noted that not only does the fatty acid make-up differ between these three tissues, but it also differed markedly between the two varieties of durian. DM and lipid content in durian pulp rapidly increased from the end of the rapid growth phase to the early stationary phase (Sangwanangkul and Siriphanich, 2000). Monitoring the changes in fat content at different ripening stages can be an important aspect in case of durian.

2.3 Hyperspectral imaging (HSI)

Most of the research nowadays is focused on sensing technology since the technologies have provided convincing results in measuring, sorting, inspecting, or grading food products effectively and efficiently. Recently, the research has focused more on real-time and non-destructive analysis. The spectroscopic technique has been used extensively for quantitative and qualitative product composition and properties analysis. Nicolai et al., 2008 explained the broad application of near-infrared (NIR) spectroscopy for real-time, rapid online analysis, monitoring, and inspection of the physical and chemical composition of several agricultural products and food. Imaging technology is another method for analyzing horticultural products' surface and textural characteristics. Since the external parameters and appearance also determine the quality of the product, imaging technology is being widely used in the inspection, monitoring and grading the agricultural products based on color, size, and texture during post-harvest handling, processing, and packaging (Davies, 2009; Ruiz-Altisent et al., 2010).

Park and Lu, 2015 emphasized that spectroscopic and imaging technology have drawbacks. For example, the spectroscopic technique lacks spatially resolved information about the product and the information about the sample is confined to a small area. In contrast, the imaging technique is unsuitable for detecting the products' physical and chemical characteristics. Therefore, many researchers have used the emerging and new generation optical technology, hyperspectral imaging (HSI), to solve the shortcoming of spectroscopic and imaging technology. HSI is the combination of spectroscopy and imaging techniques to acquire the object or sample's spectral and spatial information. It provides the physical and geometrical features of a product, such as size, shape, appearance, and color, along with the chemical composition of product through the spectral analysis (Vadivambal and Jayas, 2015). Hyperspectral images consist of a two-dimensional vector array representing the spectrum at each pixel

location. The three-dimensional dataset containing two-dimensional spatial information and one-dimensional spectral information, also known as a hypercube or data cube, is obtained from each image.

Several advantages and disadvantages of HSI over other spectroscopic and imaging techniques are explained by Sun, 2010. There are several advantages to using HSI, such as no sample preparation and a chemical-free assessment method that is environment friendly. It is a non-invasive and non-destructive method, making the sample reusable for other purposes. HSI acquires a spectral volume consisting complete spectrum of every location (pixels) in the sample, unlike in the spectroscopic techniques where a single spectrum represents a sample (ElMasry and Sun, 2010). HSI has the advantage to choose any region of interest (ROI) in the image even after image acquisition (ElMasry and Sun, 2010). When an object or an ROI in the object is selected, its spectrum is saved in a spectral library, and we can determine several constituents simultaneously in the same sample (ElMasry and Sun, 2010). HSI allows the visualization of different biochemical constituents presented in a sample, separated into particular areas of the image through chemical mapping (Gowen et al., 2007). The region of samples should have a similar chemical composition, which can be visualized using HSI (Gowen et al., 2007). Therefore, a detailed sample study is more accessible using HSI. The high dimensional data set from HSI can be simplified by choosing the feature wavelength. These optimal wavelengths can be used further to construct multispectral imaging that can be installed for process monitoring and real-time inspections.

Along with the advantages, there are some disadvantages of this technology, such as image acquisition and analysis being time-consuming, which limits the direct implementation of this system in an online system for quality evaluation. Furthermore, HSI data suffer from multicollinearity, although several multivariate analysis and feature selection techniques are employed to overcome these issues. Feature selection has the upper hand on the HSI data as it can improve the predictive power of the training model and avoid irrelevant variables and redundancy. This way, the data can be effectively reduced, and the processing time will speed up. Another drawback of HSI is that it is not suitable for liquids or homogenous samples because the value of HSI lies in the ability to resolve spatial heterogeneities in samples (ElMasry and Sun, 2010).

2.3.1 Components of Hyperspectral Imaging

HSI is mainly consisted of 4 parts: light source or illumination, spectrograph, filter, and an area detector (camera). The configuration of NIR-HSI system is shown in Figure 2.8.

2.3.1.1 Light source and interaction

Active HSI systems are equipped with a functional light source, while passive HSI systems depend on ambient radiation, e.g., sunlight. Either way, illumination is an important component of HSI acquisition. Broadband lights are generally used as the illumination sources for reflectance and transmittance, while narrowband lights are commonly used as an excitation source (Li et al., 2017). The illumination device generates light that irradiates the target object. Thus, the performance of the illumination system can significantly influence the image quality, overall efficiency and accuracy of the HSI system (D. Liu et al., 2015). The commonly used light source are halogen lamps (400-2500 nm) (Vadivambal and Jayas, 2015), light-emitting diodes (LED) (range from UV-Visible-IR, depending on the material used), and lasers (narrowband) (Sun, 2010).

Interaction of radiation to generate the spectrum is an important phenomenon; for better understanding, several theories have been explained by (Osborne et al., 1993). Electromagnetic radiation can be considered simple harmonic waves as it gives rise to the spectrum when interacting with the sample. Each radiation interacts with the object in different ways. Light can be absorbed, transmitted, or reflected from objects. As per the law of conservation of energy, the total radiation incident on the sample must be equal to the sum of radiant power absorbed, transmitted, or reflected. In the transmission of radiation, when the radiation crosses the boundary between two media of two different refractive indices, refraction occurs, which changes the direction of propagation. This deviation is thus explained by Snells's law (Osborne et al., 1993).

$$\frac{\sin \theta_1}{\sin \theta_2} = \frac{n_2}{n_1} \quad (2.2)$$

Where, n_1 is the refractive index of less dense medium, n_2 is the refractive index of denser medium and θ_1 and θ_2 are the angles of the beam from the normal in each medium. The Beer-Lambert law describes the attenuation of transmitted radiation by an absorption sample. It states that the infinitesimal thickness of the sample absorbs the fraction $\frac{dP}{P}$ of radiant energy P is proportional to the number of molecules dn in that thickness.

$$-\frac{dP}{P} = kdn \quad (2.3)$$

Integrating through the samples give, equation (4)

$$-\int_{P_0}^{P_T} \frac{dP}{P} = k \int_0^n n$$

$$-\ln(P_T - P_0) = k(n - 0)$$

$$\ln P_0 - \ln P_T = kn$$

$$\ln(P_0/P_T) = kn$$

When the transmittance, P was P_T/P_0 , where P_0 is the power of incident and P_T is transmitted radiation and n is the number of molecules in the path of the radiation, therefore

$$\ln \frac{1}{T} = kn \quad (2.4)$$

However, absorbance (A) is written by logarithm using base 10, therefore,

$$\frac{1}{T} = e^{kn}$$

Taking log on both sides,

$$\log \frac{1}{T} = \log e^{kn}$$

$$\log \frac{1}{T} = kn \log e = 0.434 kn$$

$$A = \log \frac{1}{T} = kn \quad (2.5)$$

In equation 2.5, $k \approx 0.434 k$, n proportional to the concentration (c) of molecules in the sample and the thickness (b) through which the radiation passes, a is the absorptivity constant.

$$A = \log \frac{1}{T} = \log(P_0/P_T) = abc \quad (2.6)$$

therefore,

$$A = abc \quad (2.7)$$

But Beer Lambert law does not explain the scattering effect that can occur if the radiation emerging from the surface becomes diffused by random reflection, refraction and scatter at further interface inside the sample. In this case new theory known as Kubelka-Munk is developed. This theory states that the power of reflected radiation could be described by mean of scattering and absorption constant.

$$\text{Log} \left(\frac{1}{R} \right) = \frac{ac}{s} \quad (2.8)$$

Equation 2.8 represents the Kubelka-Munk theory and the mathematical model upon which the spectroscopic analysis is based. When the radiation from the light source interacts with the sample, certain characteristic frequencies of radiation are absorbed by each kind of matter. These frequencies are thus missing from the spectrum of radiation reflected from the sample.

2.3.1.2 Spectrograph

The spectrograph is an optical device that can disperse the incident light into different wavelengths instantaneously for different spatial regions from the target surface (Sun, 2010). Spectrographs are an optical component that converts the camera to an HSI device with high spectral resolution (Vadivambal and Jayas, 2015). Spectrographs carry the spatial information of the object along with the spectral data. Generally, spectrographs are used for line scanning mode; therefore, it is one of the important parts of the pushbroom HSI system (Sun, 2010). The spectral resolution depends on the spectrograph's ability to analyse the spectrum's features. For example, the spectrograph slit width and size of entry and exit apertures determine the magnitude of the spectral resolution (ElMasry et al., 2012). The configuration of HSI system has been shown in Figure 2.8.

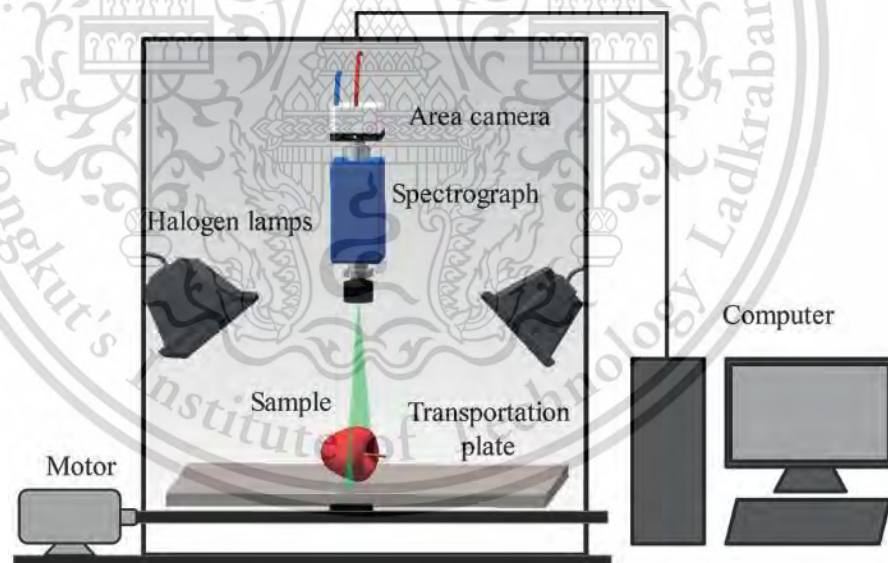


Figure. 2.8 Main components and illustration of hyperspectral imaging system (Li et al., 2017).

2.3.1.3 Filters

Filters are used in the multispectral imaging system, whereas the HSI system uses prism and grating to disperse the light (Li et al., 2017). The selection of wavelength

is made by dispersing the incident radiation into its wavelength or blocking the radiation so that only the desired wavelength reaches the detector (Park and Lu, 2015b). There are two types of dispersive optical components used in HIS system; one is the grating instruments such as diffraction grating, prism and mirror that are installed behind the detector, and another type includes liquid crystal tunable filters (LCTF) and, acousto-optic tunable filters (AOTF) (Park and Lu, 2015b). Grating devices are used mostly for line scanning mode as in pushbroom HSI, and the tunable filters are used mostly for the area scanning mode (Sun, 2010).

2.3.1.4 Area detector (Camera)

The detector records the reflectance or transmittance spectra in the hyperspectral system. An array of detectors called focal plane arrays (FPAs) are widely used in HSI systems (Vadivambal and Jayas, 2015). FPA detectors have advantages such as obtaining uniform or constant background, high signal-to-noise ratio, decreased scanning time and less image distortion (Vadivambal and Jayas, 2015). Some of the commercially available FPA is indium gallium arsenide (InGaAs), platinum silicide (PtSi), mercury cadmium telluride (HgCdTe), indium antimonide (InSb), germanium (Ge) and quantum well infrared photodetectors (QWIPs) (Vadivambal and Jayas, 2015). InGaAs detectors are widely used in 900-1700 nm wavelength range and are best suited for monitoring the quality of agricultural and food materials (Vadivambal and Jayas, 2015). In addition, other image acquisition devices such as computed tomography (CT), magnetic resonance imaging (MRI), ultrasound and electrical tomography are used in food applications (Du and Sun, 2004). Charge-coupled device (CCD) and complementary metal oxide semiconductor (CMOS) image sensors are two different means to generate the image digitally (Zhang et al., 2014). CCD is used to move the electrical charge from within the device to an area where the charge can be manipulated (Li et al., 2017). In the CMOS image sensor, pixels are represented by P-doped metal oxide semiconductor (MOS) capacitors. Generally, the CMOS image sensor is used in applications with less demand; in contrast, CCD image sensors are widely used where a high-quality data is required, such as in the medical, scientific, and professional research and many other applications (Li et al., 2017).

2.3.2 Generating of hyperspectral image

Hyperspectral images consist of hundreds of spectral bands and spatial resolution, and every pixel in an image provides an individual spectrum. There are three approaches to generating the hyperspectral image: whiskbroom (point) imaging, pushbroom (line) imaging and tunable filter (area) imaging, as illustrated in Figure 2.9. In point scanning or whiskbroom, a single spectrum is obtained by scanning at a single

point or pixel at a time, and then the sample is moved to acquire another pixel (spectrum) (Vadivambal and Jayas, 2015). Thus, simultaneously a 3-D hypercube generated from point scanning is stored in a band interleaved by pixel (BIP) format (ElMasry and Sun, 2010). The point-scan method is similar to the basic spectroscopic approach, where a single point is scanned along two spatial dimensions by moving the sample or the detector (Li et al., 2017). In line scanning, or pushbroom the whole line of an image is recorded at once using 2-D dispersing elements and a 2-D detector array (Vadivambal and Jayas, 2015). For each spatial point in the linear field of view, a line of complete spatial and spectral information can be acquired in pushbroom configuration (Li et al., 2017). The hypercube in this configuration is stored in band interleaved by line (BIL) format (ElMasry and Sun, 2010). Line scanning acquires the hypercube as the sample moves linearly along the linear translation stage, making this configuration more appropriate for online inspection of agricultural products (Qin et al., 2013). Similarly, for area scanning or wavelength scanning, the sample is kept fixed and images are obtained one object after another for the whole object. A tunable filter is required to acquire the image at a different wavelength. In area scanning (tunable filter) configuration, the 3-D hypercube is stored in a band sequential (BSQ) format. Area scanning is different from single-shot imagers such as computed tomography imaging spectrometer (CTIS). In single-shot imagers multiplexed spatial and spectral data are collected simultaneously to complete the 3D hypercube using one exposure of an area detector (Qin, 2010). The single-shot scanner has advantages over the scanning imager (area scanning or line scanning) as it can capture the 3-D images in milliseconds which is helpful for real-time HSI applications (Qin, 2010).

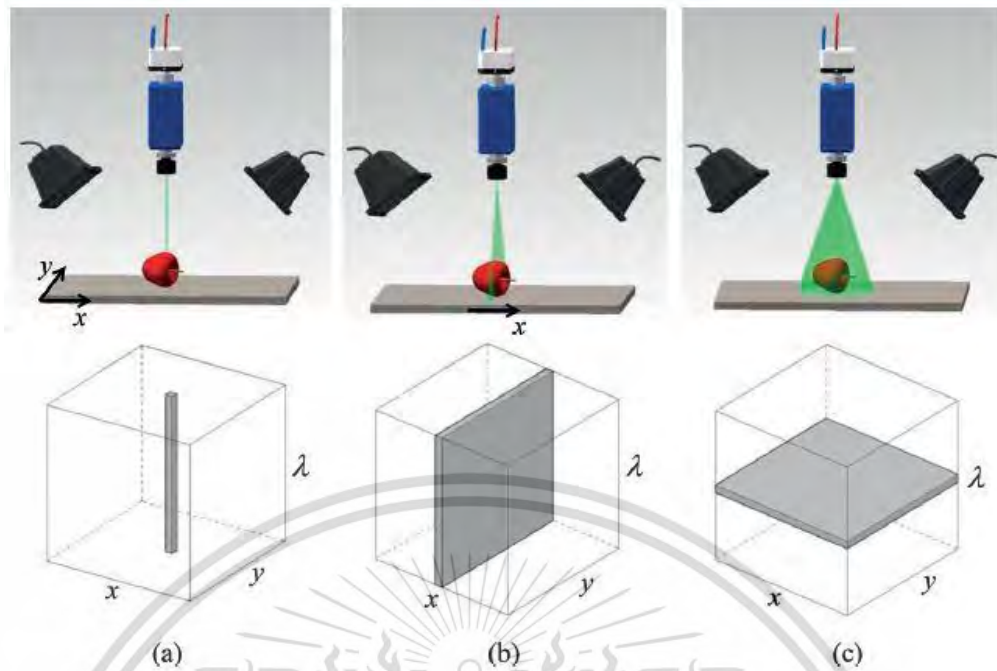


Figure. 2.9 Three different approaches to generating a hyperspectral image. (a) The point-scan method. (b) The line-scan method. (c) The area-scan method (Li et al., 2017)

2.3.2.1 Principle of hyperspectral imaging (HSI) system

ElMasry and Sun, 2010 explained the basic working principle of the pushbroom HSI. As the radiation from light sources illuminates the object, it is transmitted through, reflected, or absorbed (ElMasry et al., 2012). The radiation is collected from the camera lens and focused on the entrance slit of the imaging spectrograph. The light is then collimated and dispersed by the wavelength dispersion unit. The wavelength dispersion unit in HSI is mainly grating spectrograph with a 2D detector array (ElMasry and Sun, 2010). As the light beam enters the spectrograph, it is dispersed in different directions according to wavelength while keeping spatial information. The dispersed light is then plotted onto the detector array, resulting in a 2D image (x, y), one dimension representing the spectral axis (λ) and the other containing the spatial information for the scanning line. Scanning the specimen's entire surface creates a complete 3D hyperspectral image cube, as shown in Figure 2.10, where two dimensions represent the spatial information and the third represents the spectral information (Lu, 2003).

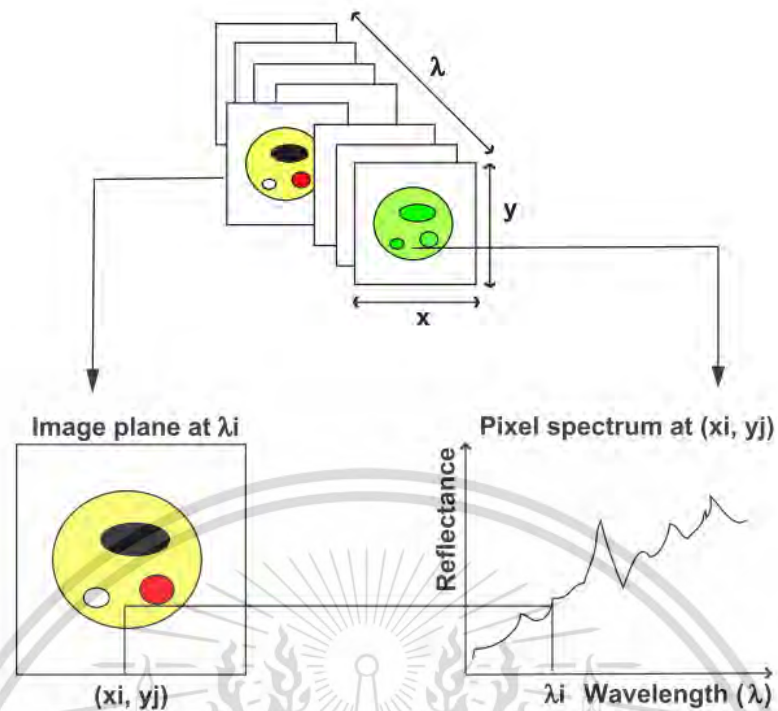


Figure. 2.10 Schematic representation of a hypercube showing the relationship between spatial and spectral dimension (Gowen et al., 2007).

2.3.2.2 Application

HSI was first used in satellite remote sensing for geographical search, vegetation growth and monitoring, geological search, or mineral mapping (Moran et al., 1997). The research and development of this technique for quality and safety inspection of agricultural products began in the late 1990s (Martinsen and Schaare, 1998; Park and Lu, 2015a). Many research-based on spatial image and spectral image processing and analysis have been done, showing the strong possibility of using HSI technique in the quality assessment of fruits and vegetables (Li et al., 2017). The internal and external quality of fruits and vegetables has been identified in several agricultural products using HSI techniques. Estimating moisture content, TSS, acidity, firmness, as well as fruit contaminants and defect detection in a fast and accurate way are the basic application of HSI in agricultural products.

The summary of research conducted on different types of fruits to develop the model for quality detection and classification using HSI system of various wavelength range are listed in Table 2.1.

Table. 2.1 Application of HSI on internal and external quality evaluation.

Fruits	Parameter	Wavelength range	References
Apple	Sugar content and firmness	400-1000 nm	(Chen et al., 2017)
	Bruise detection	400-1000 nm	(Lu, 2003)
Banana	Moisture content TSS and Firmness	400-1000 nm	(Rajkumar et al., 2012b)
Blueberries	Firmness and SSC	500-1000 nm	(Leiva-Valenzuela et al., 2013)
Mango	Firmness, TSS and TA	450-998 nm	(Rungpichayapich et al., 2017)
	Ripeness classification	390-890 nm	(Gutiérrez et al., 2019)
Pear	Maturity classification and firmness prediction	425-1000 nm	(Khodabakhshian and Emadi, 2018)
	Soluble solids content and firmness	400-1000 nm	(Fan et al., 2015)
Strawberries	Moisture content (MC), TSS, and acidity (expressed as pH)	400-1000 nm	(Elmasry et al., 2007)
	Ripeness	380-1030 nm 874-1734 nm	(Zhang et al., 2016a)
Orange	TSS, TA, (TSS/TA), color component and color index	400-1000 nm	(Aredo et al., 2019)
Peach	Firmness, SSC, color, and maturity	515-1000 nm	(Cen et al., 2011)
Cherry	Maturity, SSC, pH	874-1734 nm	(Li et al., 2018)

2.4 Hyperspectral image processing

HSI is the combination of two mature technologies, i.e. spectroscopy and imaging. Hyperspectral images are volumetric image cubes that consist of hundreds of spatial images. Each spatial image, or spectral band, captures the responses of ground

objects at a particular wavelength (Cheung and Ortega, 2009). A single hyperspectral image of a sample can contain more extensive information than a single monochromatic or a conventional RGB image (Lorente et al., 2012). Many images are combined to form a 3D hypercube with pixels, and each pixel represents a spectrum in the HSI system. It can be complicated to extract the valuable information from hyperspectral images since the data can be redundant and could not be useful to distinguish between the regions with a similar profile. The image files generated are large and multidimensional, making visual interpretation difficult. Many digital image processing techniques are applied to the multidimensional image to extract relevant and adequate information (Sun, 2010). Image analysis has been used in many fields of science and technology to assess or quantify the external characteristics of food products, such as color, texture, shape, size, and internal characteristics (Park and Lu, 2015a). Hyperspectral image processing refers to using computer algorithms to extract, store and manipulate the information from visible NIR or NIR hyperspectral images for various information processing and data mining tasks such as analysis, classification, regression, target detection and pattern recognition (Chang, 2003; Eismann, n.d.; Gowen et al., 2007; Landgrebe, 2003; Plaza et al., 2009; Shaw and Manolakis, 2002; Sun, 2010; Thenkabail and Lyon, 2016). Thus, a combination of developed techniques and tools is required to process the hyperspectral images.

2.4.1 Digital Image

The basic of image analysis starts with the formation of the digital image. Mendoza and Lu, 2015, explains the fundamentals of digital image and the creation of a digital image with an example. A digital image is a numerical 2D or 3D representation of the actual physical object or scene (Mendoza and Lu, 2015). From this, we can obtain an accurate spatial (geometric) and spectral representation with sufficient detail or resolution for processing, compression, storage, printing, and display (Mendoza and Lu, 2015). A digital image may be vector or raster type. Raster images are electronic files that consist of discrete picture elements called pixels. Vector graphics represent the images based on mathematical expression, as are typically used in computer graphics for images made up of vectors (arrows of direction, points, and lines) that define shapes compared to the individual pixels used to represent the raster image (Mendoza and Lu, 2015). There are three basic measures of digital image: spatial resolution, pixel bit depth and colors (Sitts, 2000). The higher the values are within these measures, the more data will be captured, representing a more significant amount of photographic detail from the original. Spatial resolution is defined as the rate or number of times an image is sampled during the acquisition or image processing. Quantitatively, spatial frequency or

spatial resolution (i.e. the number of pixels in an image) can be described as dpi (dots per inch), ppi (pixels per inch), and lpi (lines per inch) (Gonzalez and Woods, 2008). Pixel bit depth is the number of shades that can be represented by the amount of information saved for each pixel. A string of binary digits represents each pixel in the raster image and the number of digits is known as the bit depth. One bit image can assign only one of two values to a single-pixel: 0 or 1 (black or white). There are several different systems to represent color image such as RGB (additive color system), CMYK (subtractive color image), HSV and the CIELAB color space.

A hyperspectral image is a raster image. According to Mendoza and Lu, 2015, the most used raster images are digital photography with a CCD camera in a process called digitization. Digitization converts an analog signal to the digital signal by mapping the image on a grid and quantising the intensity level (Mendoza and Lu, 2015). Digitization converts an image into a series of a pixel that is either black or white (binary) or a specific shade of grey (greyscale) or color (Mendoza and Lu, 2015). Each pixel is represented by a single or series of binary digits, either 0 or 1 (Mendoza and Lu, 2015). By measuring the color of an image at a large number of points, a digital approximation of an image from can be constructed (Mendoza and Lu, 2015). Figure 2.11 shows the process of creating a digital image. Radiation from an illuminating source has been reflected from a sample element (Mendoza and Lu, 2015). Thus, the imaging system collects incoming energy and focuses on the image plane (Mendoza and Lu, 2015). The front side of the imaging system is the optical lens, which projects the viewed scene onto the focal length. The camera sensor is an array detector that does not directly recognize the color of incoming light (Mendoza and Lu, 2015). Still, the dispersive elements separate the light into three color channel red (R), green (G) and blue (B) (Mendoza and Lu, 2015). The response of each sensor, which coincides with the focal plane, is proportional to the integral of light energy projected onto the sensor's surface (Mendoza and Lu, 2015). Once a digital image is created, digital to analog conversion allows the computer to present the image in human-readable format (Mendoza and Lu, 2015). Digitization is done to process and analyze the images on a computer (Mendoza and Lu, 2015).

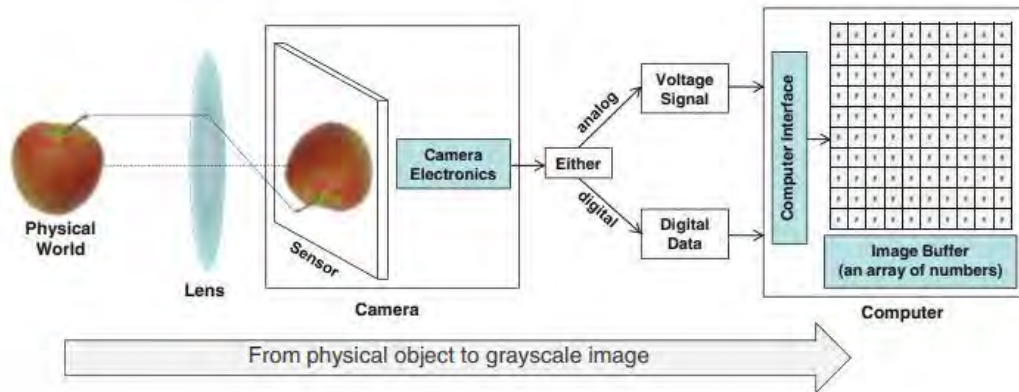


Figure. 2.11 An example of the process for creation of a digital image (Sitts, 2000).

2.4.2 Image Processing

Figure 2.12 shows the basic steps involved in hyperspectral image processing.

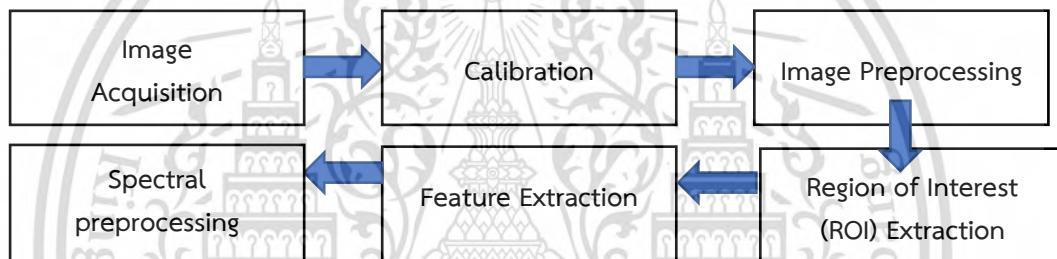


Figure. 2.12 Steps for hyperspectral image processing.

2.4.2.1 Image acquisition

Hyperspectral images are typically made up of hundreds of contiguous wavebands for each spatial position of a target studied. Consequently, each pixel in a hyperspectral image contains the spectrum of that specific position (Gowen et al., 2007). The detector commonly used as 2D device such as charged couple device (CCD) and image sensor complementary metal oxide semi-conductor (CMOS), thus, resulting 3D datacubes or hypercubes with xyz coordinate where x and y are the spatial coordinate and z is the spectral coordinate (Yoon and Park, 2015). HSI system uses two types of dispersive elements either grating, prism or mirrors or electro optical filters such as AOTF and LCTF. There are basically three techniques to generate the hyperspectral image i.e. whiskbroom (point scanning), pushbroom (line scanning) and tunable filter (area scanning). Depending upon the configuration of the system the hypercubes are generated. Hypercube is constructed in either BSQ, BIL or BIP) format (Balram, 2003). BSQ format stores each band as a separate file, allowing each band to be analyzed as a separate and individual entity (Bossler et al., 2010). BIP stores all data layers of one

pixel as adjacent data set members. BIL format compromise between BSQ and BIP, as rows from each band are stored adjacent to each other and thus different features of a row that correspond to one another are located near each other in the data set (Bossler et al., 2010). Typically tunable filter configuration save image in BSQ format, whiskbroom scanning and pushbroom scanning saves images in BIP and BIL format, respectively.

2.4.2.2 Calibration

HSI image calibration, also known as radiometric calibration, is a mandatory step to ensure the efficiency and reliability of the result produced from the HSI system (Yoon and Park, 2015). Radiometric calibration converts the measured digital numbers to per cent reflectance (or transmittance) values with spectrally flat and spatially homogenous standard (known) materials (Yoon and Park, 2015). The reflectance calibration calculates relative (per cent) reflectance values at each pixel with a known diffuse reflectance material (white or gray) in the field of view, such as Spectralon (Labsphere) and Teflon (Yoon and Park, 2015). After hyperspectral image acquisition, the raw cube was calibrated using Equation 2.9.

$$R = \frac{(I_0 - D)}{(W - D)} \quad (2.9)$$

where R is the relative reflectance image, I_0 is the raw reflectance image, D is the dark reference image, and W is the white reference image. Radiometric calibration accounts for the instrument's background spectral response and the “dark current” camera response (Gowen et al., 2007). However, since absorbance is directly proportional to concentration according to the Beer–Lambert law (Swinehart, 1962), the analysis of NIR hyperspectral image data often involves a conversion to absorbance values (Equation 2.10), where the logarithm of reflectance is taken (ElMasry et al., 2012).

$$\text{Absorbance} = \text{Log}_{10} \left(\frac{W - D}{I_0 - D} \right) \quad (2.10)$$

After the radiometric calibration, pre-processing can be applied to the data to improve the signal-to-noise ratio, reduce scattering and minimize the effect of physical inconsistencies due to non-uniform illumination (Basantia et al., 2018).

2.4.2.3 Image preprocessing

Spatial preprocessing

An image can be affected by noise due to several factors that affect the sensor leading to blurring and distortion of the image. According to Ngadi and Liu, 2010, the process of enhancing or manipulating the information in the spatial image domain is spatial processing. Image enhancement improves the visibility of specific image features for subsequent analysis or display by pseudo coloring, sharpening, contrast and edge enhancement, noise filtering, and magnifying (Ngadi and Liu, 2010). The spatial processing can be operated on an entire image or a local region of an image (Ngadi and Liu, 2010). Some spatial domain techniques, such as convolution and histogram equalization, are widely applicable (Ngadi and Liu, 2010). In addition, transfer domain techniques such as discrete Fourier and wavelet transforms can manipulate the information in an image in the transfer domain (Ngadi and Liu, 2010).

Histogram equalization

Image histogram primarily describes the image's global description (Ngadi and Liu, 2010). The histogram of a gray level image is the relative frequency of occurrence of each gray level in the image (Ngadi and Liu, 2010). Histogram equalization or linearization (Stark and Fitzgerald, 1996) reorganises the image gray levels by reallocating the pixel's brightness values based on the image histogram (Ngadi and Liu, 2010). This preprocessing method has been found to be a powerful method of enhancing low-contrast images (Ngadi and Liu, 2010).

Convolution and spatial filtering

Spatial filtering refers to the convolution of an image with a specific filter mask (Castleman, 1996). The process consists simply of moving the filter mask from point to point in an image (Ngadi and Liu, 2010). At each point, the filter's response is the weighted average of neighbouring pixels that fall within the mask's window (Ngadi and Liu, 2010). In the continuous form, the output image $g(x, y)$ is obtained as the convolution of the image $f(x, y)$ with the filter mask $w(x, y)$ as follows in equation (2.11) (Ngadi and Liu, 2010):

$$g(x, y) = f(x, y) * w(x, y) \quad (2.11)$$

where, the convolution is performed over all values of (x, y) in the defined region of the image. In the discrete form, convolution denotes $(g_{i,j} = f_{i,j} * w_{i,j})$, and the spatial filter $w_{i,j}$ takes the form of a weight mask. Some commonly used discrete filters are smoothing linear filtering, median filtering and derivative filtering. The response of a smoothing linear spatial filter is the weighted average of the pixels in the filter mask's neighbourhood (Ngadi and Liu, 2010). Smoothing filters are widely used for minimizing noise and blurring in the image (Ngadi and Liu, 2010). Likewise, a median filter is one of

the popular nonlinear spatial filters that gives an excellent performance to reduce noise with noticeably fewer blurring edges in the image (Jain, 1989; Ngadi and Liu, 2010). A median filter replaces the value of a pixel with the median of the gray levels in a specified neighbourhood of that pixel (Ngadi and Liu, 2010). There are two factors responsible for reducing the noise effect by median filter: (1) the number of noise pixels involved in the median calculation and (2) the spatial extent of its neighbourhood (Ngadi and Liu, 2010). A sharpening operation is applied to an image to highlight or enhance fine details such as edges and lines that have been blurred (Ngadi and Liu, 2010). Generally, an image can be enhanced by the following sharpening operation,

$$z(x,y) = f(x,y) + \lambda e(x,y) \quad (2.12)$$

where, $\lambda > 0$ and $e(x, y)$ is a high-pass filtered version of the image, which usually corresponds to some form of the derivative of an image (Ngadi and Liu, 2010).

2.4.2.4 Region of Interest (ROI) Extraction

In image processing, region of interest extraction or segmentation is a significant step and nontrivial image segmentation is one of the most challenging tasks (Ngadi and Liu, 2010). The accuracy of image segmentation eventually determines the success or failure of processing and analysis procedures (Ngadi and Liu, 2010). Generally, segmentation algorithms are based on one of two different but complementary perspectives by seeking to identify either the similarity of regions or the discontinuity of object boundaries in an image (Castleman, 1996). Image segmentation or ROI extraction is typically used to locate objects and boundaries (lines, curves, etc.) in images (Li et al., 2017). Therefore, the accuracy of image segmentation plays a vital role in subsequent image processing (Li et al., 2017). Threshold-based segmentation, edge-based segmentation, region-based segmentation, and classification-based segmentation are four major types of segmentation methods (Kamila, 2015; Narendra and Hareesha, 2010; Teena et al., 2013).

2.4.2.5 Feature Extraction

Hyperspectral images carry much redundant information in the spatial and spectral domains (Yoon and Park, 2015). Feature extraction transforms the high dimensional data to low dimension (dimensionality reduction) by the linear or non-linear process to reduce multicollinearity and redundancy in the spatial and spectral domain (Yoon and Park, 2015). It is a key step in connecting image processing and analysis, which converts image data or segmented regions into feature vectors (Li et al., 2017). Feature extraction builds informative and non-redundant features that facilitate

subsequent learning, simplifying further steps and modelling to achieve the desired classification or regression goals (Kamila, 2015). Therefore, feature extraction process should be carefully designed to extract only the information relevant to desired classification and regression application (Yoon and Park, 2015) An important thing for finding the best features is to extract features specific to the desired application, which involves the domain knowledge about the data (Yoon and Park, 2015). In case the domain knowledge is unavailable, general feature extraction methods such as principal component analysis (PCA), independent component analysis (ICA) (Comon, 1994), partial least square (PLS) (Wold et al., 2001), kernel PCA (Schölkopf et al., 1998), and spatial image processing to detect spatial features edges, corners, blobs and shapes, can be applied.

2.4.2.6 Spectral Preprocessing

After obtaining the spectra from ROI, spectral preprocessing should be applied. Some of the suitable preprocessing techniques used are listed below:

Smoothing

Smoothing is a method to reduce the noise in the spectrum. There are two types of smoothing: running mean or moving average smoothing and Savitzky-Goley. Savitzky-Goley is based on principle to fit the spectrum in a wavelength interval with a polynomial by the least square method, and the parameters are the degree of the polynomial and the number of points to fit (Hruschka, 1990). Equation (12) expresses the calculation of this method for Savitzky-Goley (Varmuza and Filzmoser, 2016).

$$\mathbf{x}_j^* = \frac{1}{N} \sum_{h=-k}^k c_h \mathbf{x}_{j+h} \quad (2.13)$$

where \mathbf{x}_j^* is the smoothed value, N is the normalization factor, k is the number of adjacent values at each side of j , c_h are the filter coefficients depending on the used polynomial degree.

The moving average relies on running along with the spaced data or spectrum of a pre-defined window in which the filter width is defined. Calculation of filtering raw signal or raw spectral data is expressed as the following equation (13):

$$\mathbf{y}_k^* = \frac{1}{2m+1} \sum_{j=-m}^m \mathbf{y}_{k+j} \quad (2.14)$$

where \mathbf{y}_k^* is filtered value, k is the index for the actual data point, $2m + 1$ identifies the window size or filter width, and m is the number of variables used to set the window size.

Derivatives

Derivatives are applied to the spectral data to enhance the appearance and improve calibration for the constituents (Hruschka, 1990). It simply calculates the first and second derivatives of the spectrum. The first derivative, the signals with steep edges, will emphasise more than those with relatively flat bands. But with the second derivative, even more, flat bands can be evaluated (Conzen, 2006). The main drawback of this derivative pretreatment is the enhancement of spectral noise after using this preprocessing.

$$X'_i = X_i - X_{i-1} \quad (2.15)$$

$$X''_i = X'_i - X'_{i-1} \quad (2.16)$$

Where X'_i denotes the first derivative and X''_i the second derivative at point wavelength (i) (Rinnan et al., 2009).

Normalization

Normalization suppresses the unwanted sources of variability by making a group of spectra have more standard features. For example, normalization eliminates the influence of different optical path lengths in the case of transmission measurement. Similarly, for diffuse reflectance, the interfering influence of varying material densities or particle sizes can be minimized by Normalization (Conzen, 2006). There are different types of normalization, such as Mean Normalization, Max Normalization and Range Normalization.

Mean Normalization

In Mean Normalization, each row in data matrix ($X_{i,k}$) is divided by its average value \bar{X} (Camo, 2022).

$$X_{i,k} = \frac{X_{i,k}}{|\bar{X}|} \quad (2.17)$$

Maximum Normalization

In this normalization, each row in the data matrix $X_{i,k}$ is divided by its maximum absolute value $\text{Max}|X_i|$ (Camo, 2022).

$$X_{i,k} = \frac{X_{i,k}}{\text{Max}|X_i|} \quad (2.18)$$

Range Normalization

In this normalization, each row in the data matrix is divided by the range of the total value (max value –min value) (Camo, 2022).

$$X_{i,k} = \frac{X_{i,k}}{\text{Max}(X_j) - \text{Min}(X_j)} \quad (2.19)$$

Multiple Scatter Correction (MSC)

Multiple scatter correction is applied to remove the spectra' scattering effect and baseline correction. The technique to calculate MSC is explained by (Buddenbaum and Steffens, 2012); in this preprocessing the mean spectrum $X(i)$ is considered the ideal spectrum. This spectrum represents mean scattering and offset. Each spectrum $X(i)'$ is then fit to the mean spectrum using the least square method (Buddenbaum and Steffens, 2012).

$$X(i)' = u + v X(i) \quad (2.20)$$

where, $X(i)'$ is the transformed spectra, $X(i)$ is the mean spectra and u and v are chosen such that the difference between the mean and transformed spectra is minimum. Hence, the MSC spectrum is calculated by determining the coefficients for each spectrum and then transforming the spectrum as (Buddenbaum and Steffens, 2012),

$$\text{MSC} = \frac{X(i)' - u}{v} \quad (2.21)$$

Standard Normal Variate (SNV)

SNV is a transformation usually applied to spectroscopic data to center and scale each individual spectrum. SNV is sometime used with De-trending to reduce multicollinearity, baseline shifting and curvature in the spectrum (Barnes et al., 1989).

$$\text{SNV} = \frac{X - \bar{X}}{\text{SD}(X)} \quad (2.22)$$

where, X is the individual value in a row, \bar{X} is the mean value of the row.

2.4.3 Image Analysis

Image analysis is a nondestructive method of calculating measurements and statistics based on the interesting values of images' pixels and their corresponding spatial location (Li et al., 2017). Image analysis uses the feature extracted images to analyze and interpret the data. Visual measurement and classification are the two main parts of image analysis (Li et al., 2017). Visual measurement is the process of quantitative measurement of interest parameters based on the characteristics extracted from the image. Visible measurements include the size, colors, and texture.

Classification is a qualitative analysis which means to organize or decide in which group the object fits the most. Pattern recognition is the building of a classification procedure for a given set of data on its characteristics and forming into a group or pattern. However, the quantitative measurement for providing the numerical prediction is based on modelling. Determining the concentration of chemical and biological components in an image is the quantitative analysis. Regression such as partial least square regression, linear regression, logistic regression is employed for the image quantitative analysis. Classification and regression methods can be divided into supervised methods and unsupervised methods. The significant difference between these two classes is the presence of labels in the training data. Supervised algorithms develop a prediction or classification model according to the corresponding characteristics of a predefined dataset (Li et al., 2017). Support vector machine (SVM), random forest (RF), and AdaBoost are a few examples of supervised methods. In contrast, unsupervised algorithms use raw and unlabelled data to identify the similarity between the selected features using clustering algorithms (Li et al., 2017).

2.5 Classification and regression model

HSI technology provides a large amount of spectral information, and a practical approach for data analysis, data mining, and pattern classification is necessary to extract the desired information (Jiang et al., 2010). Supervised and unsupervised machine learning methods and deep learning are used for regression and classification model development. Feature selection plays a significant role in identifying the optimum features before HSI model development. Some feature selection, machine learning, and deep learning algorithms are described below.

2.5.1 Feature selection

2.5.1.1 Principal component analysis (PCA)

As a classical projection-based method, PCA is often used for feature selection and data dimension reduction problems (Campbell and Wynne, 2011; Fukunaga, 2013). The advantage of PCA compared with other methods is that PCA is an unsupervised learning method. Principal components analysis is a data transformation technique. If, for a series of sites, or objects, or persons, several variables is measured, then each variable will have a variance (a measure of the dispersion of values around the mean), and usually the variables will be associated with each other, i.e., there will be covariance between pairs of variables (Daultrey, 1976). The data set will have a total variance, the sum of the individual variances. Each variable measured is an axis, or dimension, of variability (Daultrey, 1976). In principal components analysis is that the data are transformed to describe the same amount of variability, the total variance,

with the same number of axes, the number of variables, but in such a way that: the first axis accounts for as much of the total variance as possible, the second axis accounts for as much of the remaining variance as possible whilst being uncorrelated with the first axis and the third axis accounts for as much of the total variance remaining after accounted for by the first two axes, whilst being uncorrelated with either; and so on (Daultrey, 1976).

The entire principal components transformation can be divided into three steps (Richards, 1984).

1. Derivative of covariance matrix.
2. Computation of eigenvectors and
3. Linear transformation of the data

Mathematically, given an N-dimensional variable X with mean vector M and variance-covariance matrix C, C_x can be estimated as,

$$C_X = \frac{1}{K-1} \sum_{i=1}^K (X_i - M)(X_i - M)^T \quad (2.23)$$

where K is the number of pixels. Each principal component is Y_j is expressed as

$$Y_j = a_{1j} X_1 + a_{2j} X_2 + \dots + a_{Nj} X_N$$

$$Y_j = a_j^T X \quad (2.24)$$

where a_j^T is the transpose of the normalized eigenvectors of the variance-covariance matrix C, of X. Thus, the entire transformation can be written as:

$$Y = A^T X \quad (2.25)$$

where A is the matrix of eigenvectors which diagonalizes the covariance matrix C, of X such that the covariance matrix C_y of Y is

$$C_Y = A C_X A^T \quad (2.26)$$

whose diagonal elements are the eigenvalues λ_N of C_x i.e.,

$$C_Y = \begin{bmatrix} \lambda_1 & & 0 \\ & \lambda_2 & \\ 0 & & \lambda_N \end{bmatrix} \quad (2.27)$$

where λ₁ > λ₂ >.. > λ_N

In the computational procedure, the covariance matrix C_x of the original data set X can be the covariance matrix of the total number of pixels or an estimate of the matrix from a sample of pixels. In PCA the projection A_{opt} is chosen to maximize the determinant of the covariance matrix of the projected samples.

That is:
$$A_{opt} = \arg \max |A C_x A^T| = [a_1 a_2 \dots a_k] \quad (2.28)$$

where, a_i ($i=1, 2, \dots, k$) is the set of N -dimensional eigenvector of covariance matrix corresponding to the k largest eigenvalues (Fukunaga, 2013). In general, the eigenvectors of covariance matrix corresponding to the first three largest eigenvalues will explain more than 90% variance of the whole dataset. However, the selection of the parameter k is still a significant problem because the performance of the classifier becomes better as the principal components increase to some extent; on the other hand, the computation time also increases as the principal components increase. As a result, there is a balance among the number of selected principal components, the classifier's performance and the computation time. A cross-validation method could be used to select optimal k in PCA analysis (Goutte, 1997).

2.5.1.2 Successive projection algorithm (SPA)

A successive projection algorithm (SPA) is a variable selection technique that is widely used in spectroscopic data. SPA is a forward-selection method which applies simple operation in a vector space to reduce multicollinearity (Araújo et al., 2001). SPA operation initially starts with one variable or wavelength and then combines with another wavelength at each iteration until a desired number of wavelengths, feature or variables are selected (Cheng et al., 2016). As explained by Brown et al. (2009), there are three main steps in SPA algorithm. The first step is to construct the subsets of variables according to a sequence of vector projection operations applied to the column of the predictor or independent data (X) matrix. The dependent variables (Y) are not involved in this step. The second step is to choose the best candidate subset according to the criteria that evaluate the prediction ability of the resulting multiple linear regression (MLR) model. This criterion is based on the prediction error of each subset, known as the predicted residual error sum of square (PRESS) of either validation or cross-validation. The last step is optional in which the elimination procedure is subjected. This step determines whether any variable can be further removed without significant loss of prediction ability. The detailed explanation and calculation of all the steps are provided by Brown et al. (2009).

2.5.1.3 Genetic algorithm (GA)

Genetic algorithms are popular feature selection algorithms based on the mechanics of natural selection theory and an evolutionary computing algorithm for solving optimization problems (Hassanat et al., 2019). The basic idea of GA is based on the theory of evolution: the best individuals have a greater chance to survive and there is a greater probability of getting better offspring from mating two good individuals. GA performs a random search method to find the optimal solution by simulating the natural selection and evolution processes (Ying and Liu, 2008), which mainly consists of the following five steps (Li et al., 2018): 1) variable coding, 2) creation of the initial chromosome which is a collection of values of the variables to be optimized, the variables themselves are called genes (Ying and Liu, 2008), 3) fitness evaluation (response evaluation), 4) reproduction (crossover) and 5) mutation (Ying and Liu, 2008). After one loop is completed, steps 3 to 5 are executed until the criteria are satisfied (Li et al., 2018). Crossover operations recombine the part of two parental solutions to create a new chromosome which can provide a better solution and the mutation can occur randomly (Shorman and Pitchay, 2015). GA searches a population of points in parallel dimensions not only in a single point, which implicitly evaluates many schemas at once (Gandhi, 2015; Shorman and Pitchay, 2015). GA does not require prior knowledge of the problem, as it can produce the random changes through the crossover and mutation in their solution genes and then use the objective function to determine whether the applied changes are positive or negative to the overall search problem (Gandhi, 2015). Most of the algorithms can only explore the solution area to a problem in trend at a time, if the solution found is suboptimal the whole process must be restarted (Gandhi, 2015). However, if one path turns out to be suboptimal, it can change the path and continue to work, providing a greater chance in each run to find the optimal solution, which saves the computational time. Therefore, it is a well-suited optimization method to interrogate a large search in HSI high dimensional space where many wavelength combinations are possible (Ying and Liu, 2008).

2.5.2 Machine learning

2.5.2.1 Partial least squares (PLS) regression

The multivariate regression model builds a relationship between an object's desired physical, chemical, or biological attribute and its spectrum response. The most widely used multivariate regression methods in the quantitative analysis are multiple linear regression (MLR), partial component regression (PCR), and partial least squares regression (PLSR) (ElMasry et al., 2012). As a bilinear modelling method, PLSR is used to predict a set of dependent variables (concentrations of chemical attributes) from a large

set of independent variables (predictors or wavelengths) (ElMasry et al., 2012). In X-block (spectra) Let $u_1 =$ any y (reference value). Calculating the weight of X-block using the score of Y-block (Andrade-Garda, 2013),

$$w_1^T = \frac{u_1^T X}{u_1^T u_1} \quad (2.29)$$

$$w_1^T = \frac{w_1^T}{\|w_1\|} \text{ (normalizing)} \quad (2.30)$$

defining the X-score using original X-data

$$t_1 = Xw_1 \quad (2.31)$$

in Y-block, using X-score to calculate the Y-loading

$$q_1^T = \frac{t_1^T Y}{t_1^T t_1} \quad (2.32)$$

Calculating Y score,

$$u_{1, \text{new}} = \frac{Y q_1}{q_1^T q_1} \quad (2.33)$$

the inner relation is given as

$$\hat{u}_1 = b_1 t_1 \quad (2.34)$$

The inner regression coefficient is

$$b = \frac{u_1^T t_1}{t_1^T t_1} \quad (2.35)$$

calculating X-block loading,

$$p_1^T = \frac{t_1^T X}{t_1^T t_1} \quad (2.36)$$

Calculation of residual

$$E = X - t_1^T p_1 \quad (2.37)$$

$$F = Y - b t_1^T q_1 \quad (2.38)$$

Finally, regression coefficient vector is

$$b = W(P^T W)^{-1} q \quad (2.39)$$

$$q = (T^T T)^{-1} T^T y \quad (2.40)$$

The quality of the calibration models is then evaluated by the following statistical parameters: standard error of calibration (SEC), standard error of prediction (SEP), the correlation coefficient for calibration and prediction R , coefficient of determination (R^2), and root mean square error estimated by cross-validation (RMSECV), calibration (RMSEC) and prediction (RMSEP). A good model should have a lower value of SEC, SEP, and RMSECV and a higher value of R and a small difference between SEC and SEP (ElMasry et al., 2012).

2.5.2.2 Support Vector Machine

As a statistical learning method in data mining (Fukunaga, 2013; Hart et al., 2000), Support Vector Machine (SVM) (Burgess, 1998) has been used in applications such as object recognition (Guo et al., 2014) and face detection (Osuna et al., 1997), ripening stage classification in fruits (Zhang et al., 2016b), internal properties prediction of fruits (Munera et al., 2017). A support vector machine (SVM) is a supervised learning algorithm that classifies or predicts unknown data by using training data as an input and creating a decision function as an output (Vadivambal and Jayas, 2015). The SVM consists of linear and nonlinear classifiers (Pouladzadeh et al., 2012; Titova et al., 2013). Vadivambal and Jayas (2015) explains that SVM classifies a group of samples into two different classes separated by a hyperplane defined in a suitable space. It constructs a decision line known as a hyperplane that separates one class from another in a binary classification. However, some other strategies can be carried out for multiclass problems (Vapnik, 1999). When using a hyperplane to classify two possible classes, the objects nearer to the margin make a vector referred to as the support vector (Vadivambal and Jayas, 2015). These support vectors make the optimization of the hyperplane margin convenient (Vadivambal and Jayas, 2015). The hyperplane position corresponds to any changes in the support vector; however, the hyperplane remains unaffected by the changes occurred in any item which is not a support vector (Vadivambal and Jayas, 2015; Vapnik, 1999). The main aim of the SVM method is to determine an optimum kernel function that can represent the data in multidimensional feature space (Hassan and Al-Saqer, 2011). The optimal hyperplane, h , that is searched in the input space can be defined by the following equation (2.41):

$$h = w^T x + b \quad (2.41)$$

where, x is the input hyperspectral image pixel vector, w is the adaptable weight vector, b is the bias, and T is the transverse operator.

SVM can model non-linear boundaries and avoid overfitting by controlling the computational complexity and error (Vadivambal and Jayas, 2015). The SVM models use a kernel function such as linear, polynomial, and RBF and act as an alternate method of training for classifiers in which the network weights are determined by solving a quadratic programming problem with linear constraints, instead of solving the unconstrained minimization problem as in neural network training (Kaur and Singh, 2013; Palmieri and Fiore, 2010).

2.5.2.3 Random forest (RF)

The random forests (RF) are an extension of Breiman's bagging idea which was initially implemented as the decision tree. RF can be very advantageous in several ways such as, it can handle both regression and multiclass classification, less data processing time for train and to predict, less hyperparameter tuning parameters, can be used for high-dimensional problems, and it can estimate error in the process (Cutler and Cutler, 2012). RF solves the overfitting problem and develops the simple and interpretable models. RF is a binary tree constructed using the recursive partitioning in which RF tree base learner is grown using the classification and regression tree (Chen and Ishwaran, 2012). A binary split recursively splits pushes the data from a parent tree-node to its daughter tree nodes in such a way that the homogeneity in the daughter nodes is improved from the root or parent node (Chen and Ishwaran, 2012). Bagging or bootstrap aggregation is one of the features used in RF. The training data can be divided into subsets of data randomly with replacement. These subsets can be known as bootstrap samples. RF is dense and it is collection of several trees, each tree is grown using a bootstrap sample of the original data and the randomization is introduced in each level starting from the original data and to the node level when developing the tree (Chen and Ishwaran, 2012). To find the best split for a node, RF select a random subset of variables rather than splitting a tree node using all variables. This step is important as its purpose is to decorrelate trees so that the forest ensemble will have low variance, which is a bagging phenomenon (Chen and Ishwaran, 2012).

Steps for the RF construction has been explained by Chen and Ishwaran, 2012

1. Draw n bootstrap samples from the original data.
2. Grow a tree for each bootstrap data set. At each node of the tree, randomly select m variables for splitting. Grow the tree so that each terminal node has no fewer than n_{size} cases.
3. Aggregate information from the n trees for new data prediction such as majority voting for classification.

4. Compute an out-of-bag (OOB) error rate by using the data not in the bootstrap sample.

2.5.2.4 Linear discriminant analysis (LDA)

Linear discriminant analysis (LDA) is one of the popular machine learning techniques used for dimensionality reduction and pattern classification. The main principle behind the method is to determine a subspace of lower dimension, compared to the original data sample dimension (Zaki and Meira, Jr, 2020). The data points of the original problem are separable, and the separability is mainly defined by the mean and variance (Zaki and Meira, Jr, 2020). The LDA technique is developed to transform the features into a lower dimensional space, which maximizes the ratio of the between-class variance to the within-class variance, thereby guaranteeing maximum class separability (Pan et al., 2014; Tharwat et al., 2017; Welling, 2005). There are three main steps to construct the lower dimensional space. First step is to calculate the distance between the means of different classes, i.e., between-class variance, second step is to calculate the distance between the mean and the samples of each class, i.e., within-class variance (Tharwat et al., 2017). The final step is to construct the lower dimensional space in such a way that maximizes the between class variance and minimizes the within-class variance (Tharwat et al., 2017).

2.5.2.5 Partial least squares discriminant analysis (PLS-DA)

PLS Discriminant Analysis (PLS-DA) is a classification method based on modelling the differences between several classes with PLS. It is a supervised chemometric method for classification problems developed from the two-block PLS algorithms used in multivariate calibration to model the relationship between two matrices (Barker and Rayens, 2003). PLS-DA establishes a relationship between one or several dependent variables in a y vector or Y matrix where each column represents a class and the independent variable (X) by PLS regression (Andries and Vander Heyden, 2021). Based on principal component analysis (PCA), the matrix X and Y are decomposed into the product of two matrices, scores, and loadings (Marquetti et al., 2016; Wold et al., 2001). In the PLS and PLS-DA methods, there is a slight rotation on the principal component axis, seeking X 's maximum covariance with Y (Marquetti et al., 2016). The main difference between PLS and PLS-DA is the Y matrix. The Y matrix in PLS contains the values of the property of interest, while in PLS-DA, the matrix y or Y includes information on the sample's classes (Marquetti et al., 2016). For binary class, the value of y is assumed to be 0 or 1, depending on whether it belongs to the class represented for that column (Barker and Rayens, 2003). However, for multiclass Y matrix is converted into a dummy

$(N \times G)$, where N is the number of samples and G is the number of classes (Lee et al., 2018).

2.5.2.6 K-nearest neighbor

The K-nearest neighbor (KNN) classification separates the data into test and training sets. For every row of the test set data, the K-nearest training set objects are determined and classified based on the majority rule (Vadivambal and Jayas, 2015). The KNN is a conventional nonparametric classifier that provides good classification performance for optimum k values. KNN classifies a pattern x by allocating it to the class that is very frequently represented among its k nearest patterns (Joshi and Bapna, 2011).

Typically, the object is classified based on the labels of its k nearest neighbors by majority vote. If $k=1$, the object is classified as the class of the object closest to it. When there are only two classes, k must be an odd integer. However, there can still be tie between the classes when k is an odd integer when performing multiclass classification (Kim et al., 2012). After converting each image to a vector of fixed length with real numbers, we used the most common distance function for KNN, Euclidean distance. If $x = (x_1, x_2 \dots x_n)$ and $y = (y_1, y_2 \dots y_n)$ are two points in Euclidian space, then the distance between x to y or y to x can be given by

$$d(x, y) = \sqrt{\sum_{i=1}^n (x_i - y_i)^2} \quad (2.42)$$

The KNN classifier is a simple and efficient classifier based on distance. It does not require any training computations, but its testing time increases linearly with the size of the training set (Satti et al., 2013).

2.5.3 Deep learning

Deep learning, or deep structured learning, is a new form of machine learning that allows computational models composed of multiple processing layers to learn representations of data with various levels of abstraction (Lecun et al., 2015). The deep learning model consists of multiple layers or stages of nonlinear information which enables supervised or unsupervised learning of feature representation at successively higher, more abstract layers (Deng and Yu, 2013). This brings to the greater advantage of using deep learning as it has the potential to exploit complex, nonlinear compositional functions, learn distributed and hierarchical feature representation and make efficient use of both categorized and uncategorized data (Deng and Yu, 2013). Artificial neural networks (ANN) and convolution neural networks (CNN) are some deep structures that have been widely used for data processing.

2.5.3.1 Artificial neural network (ANN)

ANN works in a structure that is similar to the human nervous system. ANN is a nonlinear statistical model used for pattern recognition and classification tasks. Neurons are the fundamental working unit of ANN (Porwal et al., 2013). ANN consists of an input layer, hidden layers, and an output layer. Each neuron in a particular layer relates to all the neurons in the next layer. First, the weight and bias provided by each neuron in the input layers are added. Once the input value is calculated, the processing element uses a transfer function to produce its output. This transformation in the input layers is done using a sigmoid, hyperbolic-tangent, or other nonlinear function (Walczak and Cerpa, 2003).

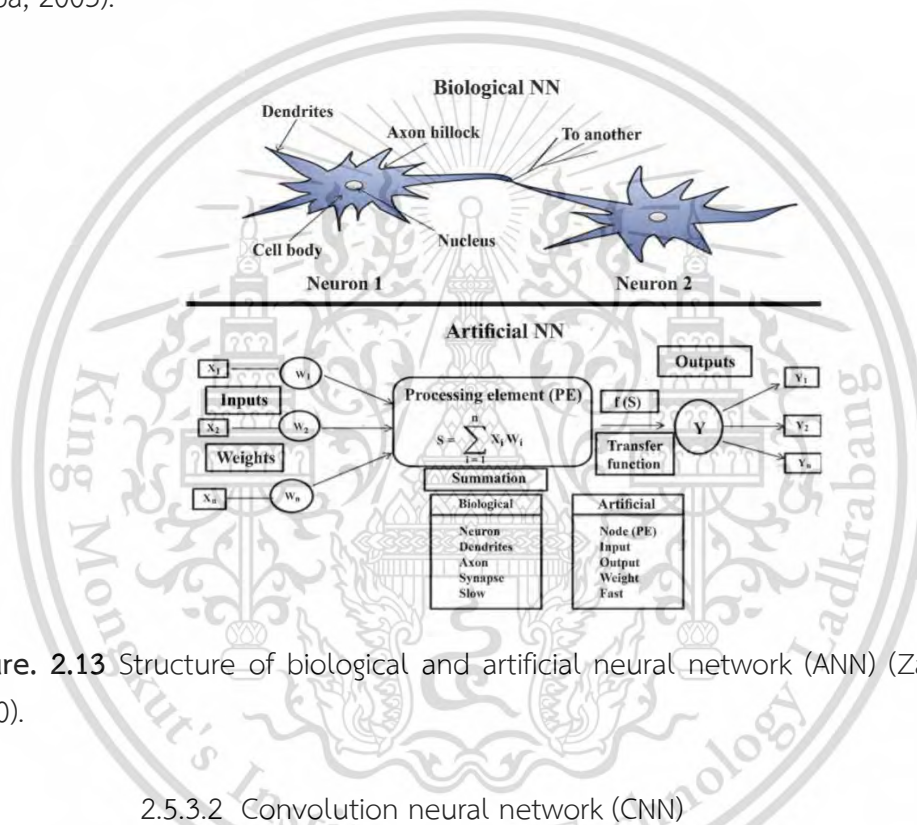


Figure. 2.13 Structure of biological and artificial neural network (ANN) (Zareef et al., 2020).

2.5.3.2 Convolution neural network (CNN)

Convolution neural network (CNN) was first introduced as a method applied to handwritten character recognition by LeCun et al., 1998 as a class of deep feedforward ANN. There is a broad application of CNN in 2-D and 3-D data, but nowadays, much research shows the potential of CNN in 1-D data (Chen and Wang, 2019). The 1-D CNN unit can aggregate local features and reduce data dimensions through convolutional learning and spatial pooling operation (Yang et al., 2019). Unlike in ANN, where the hidden layer is fully connected, in 1-D CNN, the network structure alternates between convolution and pooling ply. Yang et al. (2019) explained the 1-D CNN network with the convolution and pooling layers. The portion of the input layer is connected to the convolution unit, i.e. each unit of the convolution layer is a feature extracted from the

corresponding portion of the input layers. The unit of the convolution layer can be organized as a feature signal, and all unit of the feature share the same weight vector but receives the input from different parts. The pooling ply is formed after the convolution operation. The aim of pooling is for dimensional reduction of the feature signal unit and to increase the signal-to-noise ratio. A pooling function is applied to the multiple convolution feature signal units wherein the number of input feature signal units of the operation is referred to as the pooling size (Yang et al., 2019).

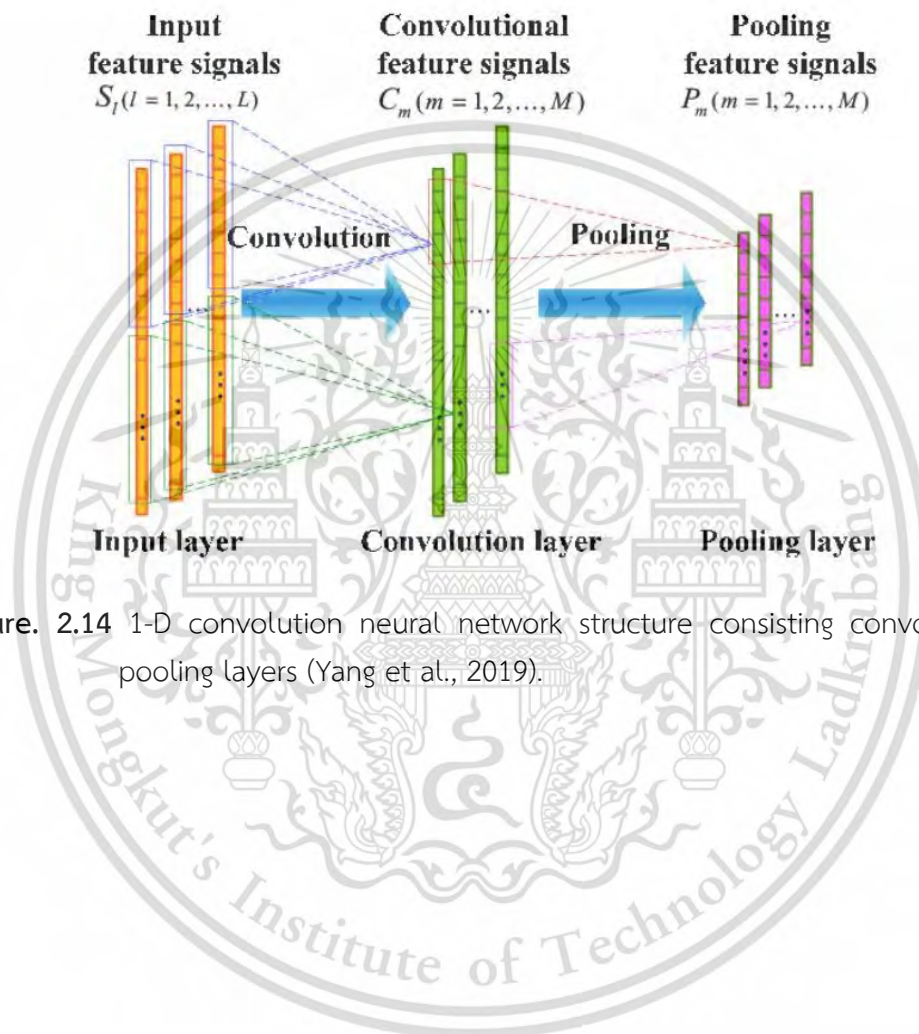


Figure. 2.14 1-D convolution neural network structure consisting convolution and pooling layers (Yang et al., 2019).

Chapter 3

Hyperspectral imaging system for maturity stage classification of durian pulp using Bayesian optimized machine learning algorithms

This chapter describes the study regarding the maturity classification of durian pulp using Bayesian optimization on three machine learning classifiers. The hyperspectral image (HSI) of durian pulp was obtained using a reflectance-based system. The mean raw spectra of the durian pulp were extracted and pre-treated using standard normal variate (SNV). An assessment of maturity stage classification (unripe, ripe, and overripe) on the full wavelength (900 – 1600 nm) was performed. The comparison among the machine learning (ML) algorithms (random forest (RF), support vector machine (SVM), and k Nearest Neighbours (kNN)) was carried out, where the hyperparameters were tuned using Bayesian optimization and the 3-fold cross-validation method. The samples were split into training (70%) and test (30%) set using stratified random sampling. Accuracy assessment was done based on the overall classification accuracy and kappa coefficient of each classifier. The classifiers attained fair result, however, the need to improve the overall accuracy is proposed.

This chapter constituted the international conference article: Sharma, S., K.C. S., and Sirisomboon P. “Hyperspectral imaging system for maturity stage classification of durian pulp using Bayesian optimized machine learning algorithms.” **The 10th Agriculture for life, life for agriculture conference**, 3-5 June 2021 pp.236-242

This material is reserved for educational use only, not allowed for commercial use.

Forbidden to modify the content, and cite the document when use.

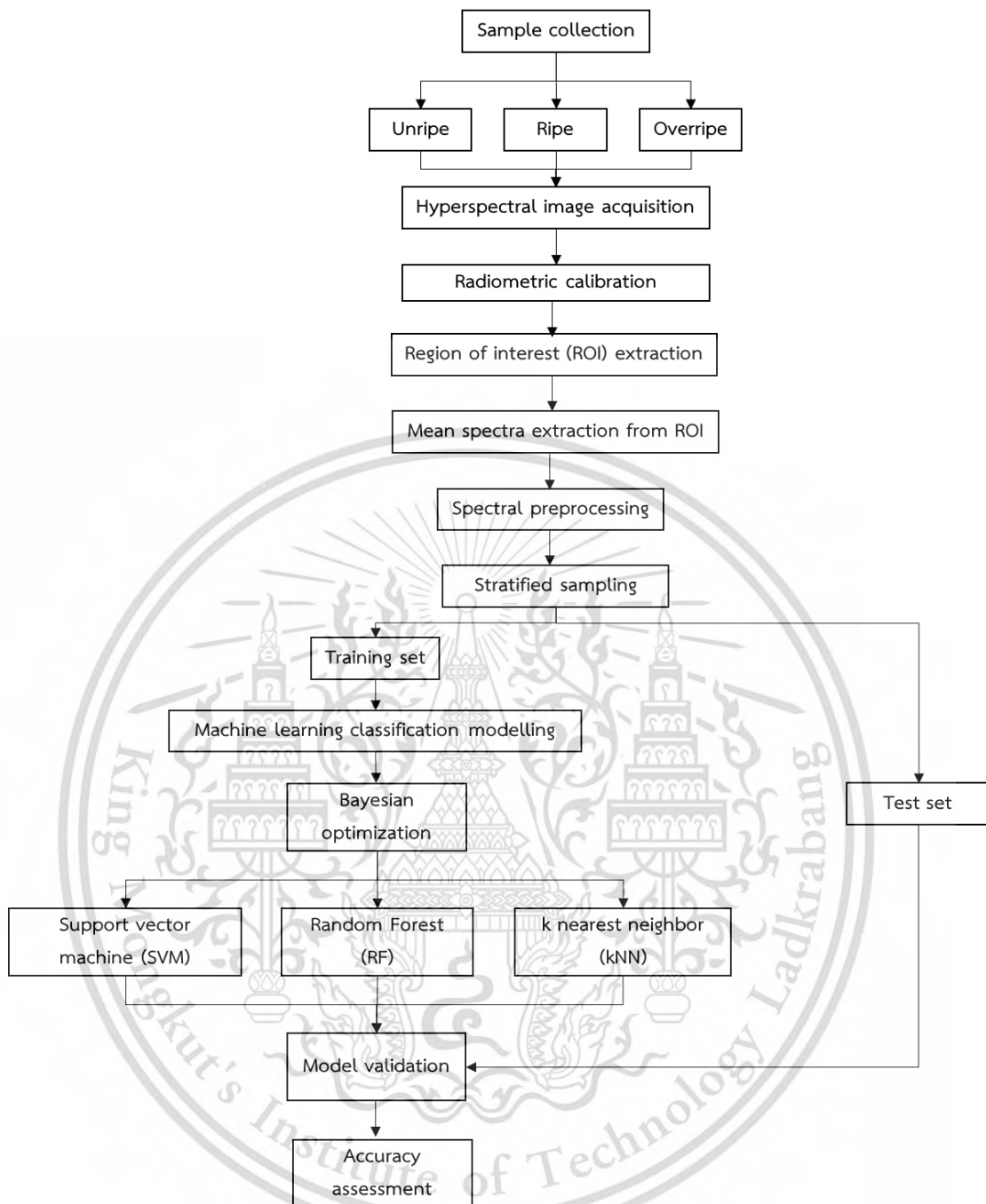


Figure. 3.1 Overall methodology for the durian ripening stage classification model development using Bayesian optimized machine learning algorithms.

3.1 Introduction

In Southeast Asian countries, durian is known as “the king of fruits”. Durian is produced and consumed highly in Malaysia, Indonesia, Singapore, Thailand, the Philippines, and China (Siriphanich, 2011). Durian is popular for its appearance, taste, and distinct odor. Thailand is considered to be one of the largest durian producing country, as well as an exporter to the international market among the countries in the Association of Southeast Asian Nations (ASEAN) (Maninang et al., 2011a; Somton et al., 2015). In some countries such as Malaysia, the fruit is likely to be consumed fully ripe with a soft texture and strong odor, whereas the majority of people from Thailand prefer just ripe fruit with a firm texture and mild odor (Siriphanich, 2011). The traditional methods for identifying the ripeness and maturity of durian before harvesting includes mostly visual inspection and destructive techniques (Ketsa et al., 2020). Uneven ripeness due to harvesting immature fruits develop low eating quality, and even after ripening, the fruit lacks the quality characteristic: aroma and flavour (Ketsa et al., 2020). Identifying the correct maturity is one of the biggest challenges that durian producers are facing currently.

Spectroscopy and imaging techniques have been applied on several fruits and vegetables for quality monitoring. Recently, hyperspectral imaging (HSI) is more in use for quality inspection as it integrates both, spectroscopy and imaging techniques (Park and Lu, 2015a). Application of HSI has been done for decades in several fruits such as strawberry, peach, pear, banana, etc (Cen et al., 2011; Elmasry et al., 2007; Khodabakhshian and Emadi, 2018; Rajkumar et al., 2012b). HSI generates 3-dimensional hypercube where the first two dimensions contains spatial information and the last dimension stores the spectral information. Based on an approach in which the spatial information is acquired, the HSI sensor are classified into point scanning (whiskbroom), line scanning (push broom), and area scanning (tunable filter). In pushbroom system configuration either the object or the imaging unit is moving which gives an advantage to be used in online systems for industrial application (Liu et al., 2007).

Similar to spectroscopic technique, HSI images are first preprocessed and then the classification/regression algorithms are implemented for classification and regression task along with feature extraction and dimensionality reduction. Machine learning algorithms such as support vector machine (SVM), random forest (RF), k nearest neighbor (kNN), discriminant analysis (linear discriminant analysis (LDA), partial least squares discriminant analysis(PLS-DA)) are popular for classification and regression analysis. In machine learning, some parameters control the learning process known as hyperparameters. Hyperparameter optimization can be done manually or with

automatic search methods. One of the famous hyperparameter optimization methods is Bayesian optimization. It combines prior information about the unknown function with sample information, to obtain posterior information of the function distribution by using the Bayesian formula (Wu et al., 2019). Based on this posterior information, the optimal parameters combination can be known where the function outputs the optimal value (Wu et al., 2019). Bayesian optimization was proved to be a promising method to find the best hyperparameters for widely used machine learning models such as RF, SVM, and neural networks (NN) (Jones, 2001). Hyperparameter for SVM such as soft margin constant (C) should not be too high or low. It has to be considered that large values for C lead to few training errors and narrow margin, whereas small values generate a larger margin, at the cost of more errors and more training points situated inside the margin (Eitrich and Lang, 2006). Similarly, the number of estimator trees (n-estimator) is one of the important parameters to be optimized in RF. If the value is too high for n-estimators, the strength can be improved but at the same time the error rate due to high inter tree correlation increases (Wu et al., 2019). If the value is low, the inter tree correlation and strength of individual tree goes down (Wu et al., 2019). Therefore, a proper optimization method plays a critical role in obtaining a good classification model with minimal error in machine learning.

The main objective of this research is to identify the potential of HSI system for the ripeness classification of the durian pulp by using machine learning algorithms: SVM, RF, and kNN. The hyperparameter tuning is performed by using Bayesian optimization for machine learning algorithms.

3.2 Materials and methods

Durian samples were collected from Trat Province, the eastern part of Thailand. The fruits were harvested at 99, 106, 113, 120, 127, and 134 days after anthesis (DAA). The total number of whole fruits harvested was 50 with each fruit consisting of approximately 5 to 6 pulps. In total, 260 pulps were used for the experiment. The experiment was conducted 2 days after the harvesting date. The fruits were divided in terms of ripeness level as unripe (99-106 DAA), ripe (113-120 DAA), and overripe (127-134 DAA).

The image was acquired using a pushbroom HSI system with a wavelength range from 900-1600 nm and the spectral resolution of 3.2 nm. The HSI system configuration is shown in Figure 3.2. The HSI system included an imaging spectrograph (Inspector N17E Specim, Spectral Imaging Ltd., Oulu, Finland) with a CCD camera (Xeva 992, Xenics

Infrared Solutions, Belgium), and two 500 W tungsten–halogen light sources (Lowel Light Inc., New York, United States of America) at an angle of 45 degrees. The system was controlled by Specim’s LUMO Software Suite (Spectral Imaging Ltd., Oulu, Finland). The integration time was set as 6. The pulp was placed on the translation stage moving at the speed of 10 mm s⁻¹ and was guided by the bar on both sides to make it stable during the scan.

After hyperspectral image acquisition, the radiometric calibration was done. The white reference and dark reference acquired for each image in the HSI system were used for the radiometric calibration. To capture the white reference, the spectralon with relative reflectance of 99% was used. In the HSI system, the dark reference image was captured by the system automatically by closing the shutter of a camera.

$$R = \frac{I_o - D}{W - D} \quad (3.1)$$

where **R** is the relative reflectance image, **I_o** is the raw reflectance image, **D** is the dark reference image, and **W** is the white reference image.

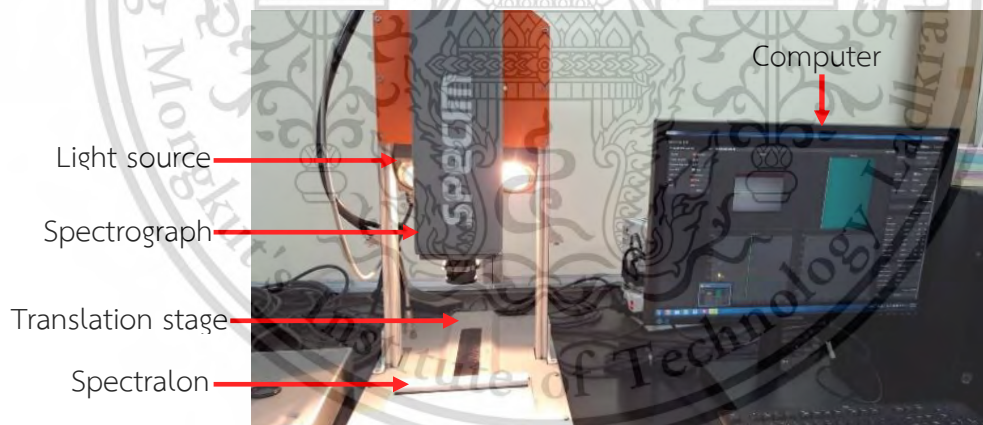


Figure. 3.2 Pushbroom NIR-HSI system configuration for scanning durian pulp.

The area of interest (AOI), pixels representing pulp region, was extracted from each radiometrically corrected image. Since the durian pulp was supported by two guiding bars (Figure 3.3a) while scanning, a normalized difference index (NDR) (Equation 3.2) was computed to separate pulp from the bars and background (translation stage). Two

wavelengths with high reflectance (1205 nm) and low reflectance (1450 nm) were selected for NDR computation.

$$\text{NDR} = \frac{(R_{1075.67} - R_{1450.18})}{(R_{1075.67} + R_{1450.18})} \quad (3.2)$$

The binary threshold operation was then applied to NDR image to separate the pulp from the background as shown in Figure 3.3b. The threshold value was set to 0.5, with values greater than 0.5 representing the pulp. The morphological filters (dilation and erosion) were then applied to the binary image to extract the pulp pixels. From the extracted AOI, the mean spectra were calculated from every pixel within the boundary of the AOI.

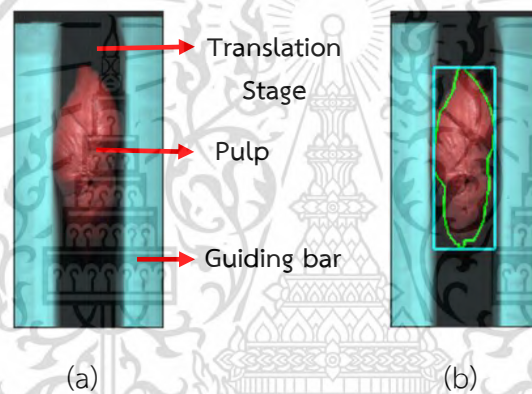


Figure. 3.3 Raw image acquired from hyperspectral imaging (a) Masked image by binary masking and morphological filter.

The obtained mean spectra was then preprocessed using standard normal variate (SNV) technique as it minimizes the effects of scattering, particle size, and the difference in the global intensities of the signals (Barnes et al., 1993; Roger et al., 2020) Supervised machine learning algorithms: SVM, RF, and kNN, were applied on the preprocessed mean spectra of durian pulp. The classification models were developed in Python 3.8 using Scikit-learn machine learning library. The hyperparameters: soft-margin constant (C), and gamma (γ) for SVM, the number of estimators trees in the forest (n-estimator), the number of features to consider for the best split, the maximum depth of the tree for RF, and number of neighbors (n) to calculate the nearest neighbor for kNN, were optimized by Bayesian optimization. In the case of SVM, the radial bias function (RBF) kernel function was used. The distance metrics in kNN was set as

euculidean. The sample set was divided randomly into a training set and the test set in the ratio of 70:30. Overall accuracy (Equation 3.3), precision (Equation 3.4), recall (Equation 3.5), and Kappa coefficient (Equation 3.6) values were used to analyze the performance of each machine learning classifier. The Kappa coefficient measures the actual agreement (indicated by the diagonal elements of the confusion matrix in Figure 3.4) minus chance agreement (indicate by the product of the row and column marginal). It measures how the classification performs as compared to the reference data (Fung and Ledrew, 1988).

$$\text{Overall Accuracy (\%)} = \frac{TP + TN}{TP + TN + FP + FN} \times 100 \quad (3.3)$$

$$\text{Precision} = \frac{TP}{TP + FP} \quad (3.4)$$

$$\text{Recall} = \frac{TP}{TP + FN} \quad (3.5)$$

$$\text{Kappa coefficient} = \frac{p_o - p_e}{1 - p_e} \quad (3.6)$$

		Predicted Class	
		Positive	Negative
Actual Class	Positive	True Positive (TP)	False Negative (FN)
	Negative	False Positive (FP)	True Negative (TN)

Figure. 3.4 Confusion matrix.

Where, TP is true positive, TN is true negative, FP is false positive and FN is false negative, p_o is the empirical probability of agreement on the label assigned to any sample, p_e is the expected agreement when both annotators assign labels randomly.

3.3 Results and discussions

The average raw spectra from the extracted AOI of the pulp are shown in Figure 3.5. With the change in path length due to the different sizes of the sample, the raw spectra showed a baseline shift. Therefore, the SNV preprocessing was applied in the raw spectra to improve the spectral characteristics. The SNV pretreated spectra show a dominant peak of water at the wavelength of 970 nm and 1205 nm (Figure 3.6). This wavelength represents O-H stretching due to the first overtone of water. Also, at 1450 nm there is a significantly lower reflectance band which represents the band of water and starch. Table 3.1 shows the hyperparameter selection for each classifier.

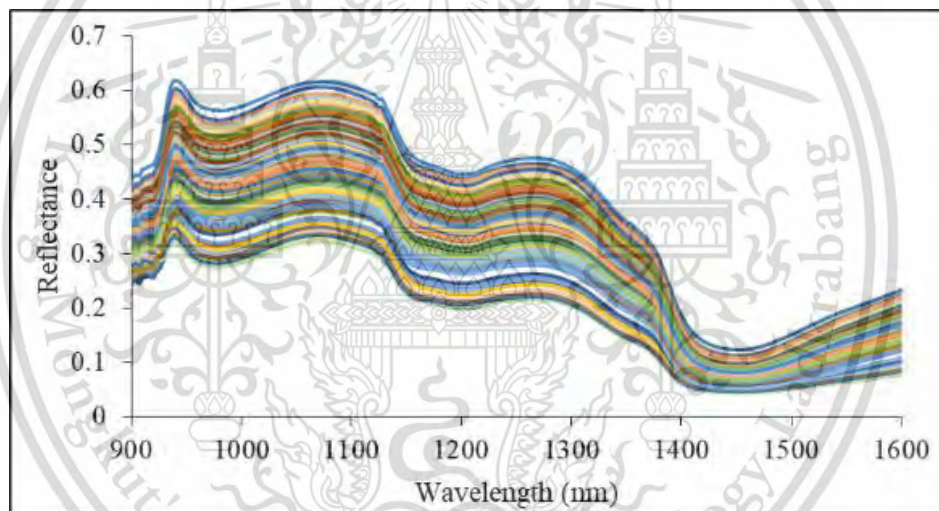


Figure. 3.5 Average raw spectra of durian pulp.

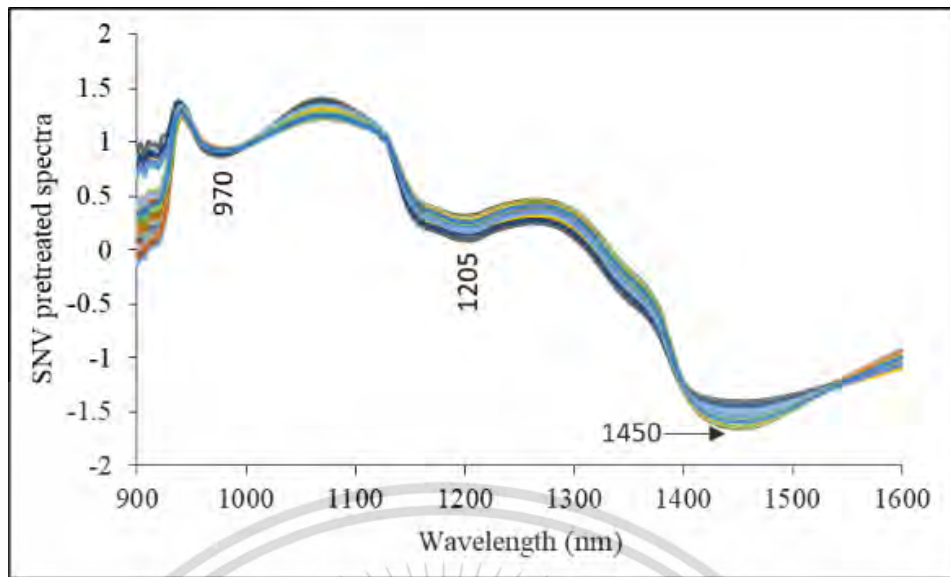


Figure. 3.6 SNV pretreated spectra of durian pulp.

Table. 3.1 Selection of hyperparameters for SVM, RF, and kNN using Bayesian optimization.

Classifiers		Hyperparameter		
Support vector machine	Input	C	gamma	Kernel function
		0.01-1000	0.1-100	Radial base function, Linear, Polynomial
	Output	53	0.4	Radial base function
Random forest		n-estimator	Maximum feature	Maximum depth
	Input	25-500	2-20	2-20
	Output	93	8	14
k nearest neighbor		n- neighbor		Distance
	Input	2-20		Euclidean (default)
	Output	10		Euclidean

The best classification performance from the optimized hyperparameter classification models from SVM, RF, and kNN in terms of training accuracy, cross-validation accuracy, and test accuracy is shown in Table 3.2. SVM showed the highest test accuracy (91.8%) among three machine learning classifiers. The training accuracy of RF was significantly (100%) higher but the 3-fold cross-validation (86.8%) and test accuracy (84.6%) do not show the good performance of the RF model. Meanwhile, kNN obtained the lowest accuracy among all the machine learning classifiers.

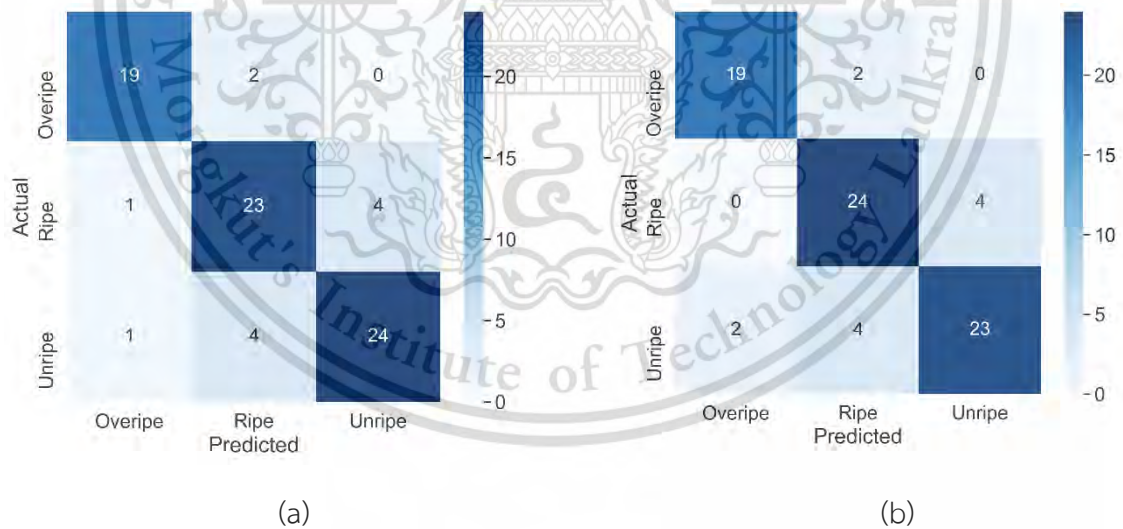
Table. 3.2 Performance of machine learning classifiers using Bayesian optimization.

Classifiers	Training accuracy	3-fold cross validation accuracy	Overall accuracy
Support vector machine	91.8%	87.9%	88.5%
Random forest	100%	86.8	84.6%
k nearest neighbour	84.1%	81.3%	73.1%

Table 3.3 shows the precision, recall and kappa coefficient of test set. Figure 3.7 shows the confusion matrix from each ML classifiers. The number of overripe, ripe and unripe in the test set were 21, 28 and 29, respectively, which is represented in confusion matrix. The precision, recall and kappa coefficient of overripe samples are higher for all classification models. With the advancement of the maturity stage, the moisture content of the pulp decrease. The significant difference in the moisture content between overripe samples and the other samples may have resulted in classification metrics value of overripe samples. The inter-class confusion between ripe and unripe can be seen for all the classification models with more classification error in the case of kNN. The similar spectral characteristics of ripe and unripe sample must have influenced the classification performance of kNN.

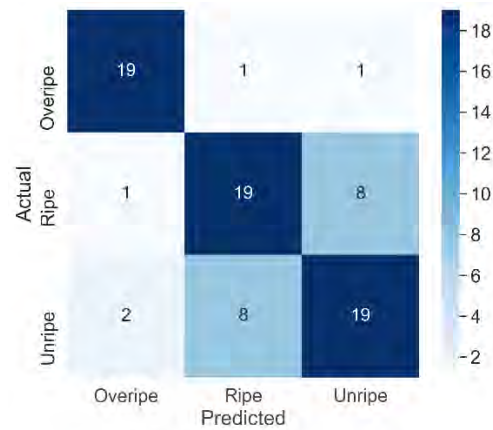
Table. 3.3 Precision, recall and kappa coefficient obtained from the classification model by different machine learning classifiers.

Classifiers		Precision	Recall	kappa coefficient
Support vector machine	Overripe	0.95	0.95	0.83
	Ripe	0.86	0.86	
	Unripe	0.86	0.86	
Random forest	Overripe	0.90	0.90	0.77
	Ripe	0.80	0.86	
	Unripe	0.85	0.79	
k nearest neighbor	Overripe	0.86	0.90	0.59
	Ripe	0.68	0.68	
	Unripe	0.68	0.66	



This material is reserved for educational use only, not allowed for commercial use.

Forbidden to modify the content, and cite the document when use.



(c)

Figure. 3.7 Confusion matrix from classification model of support vector machine (a), random forest (b), and k nearest neighbors (c).

Many supervised and unsupervised classification algorithms have been used for the maturity classification of fruits. The ripeness classification model of pear using short near-infrared (425-1000 nm) by three classification model soft independent modeling of class analogy (SIMCA), LDA, and PLS-DA were compared by Khodabakhshian and Emadi, 2018. The overall classification result showed that PLS-DA attained the best correct classification accuracy of 87.86% for pear ripeness classification (Khodabakhshian and Emadi, 2018). Hyperspectral image of navel oranges was obtained using the diffuse transmittance imaging-based system and a multispectral index was developed to identify the maturity with the hyperspectral technique by Wei et al., 2017. Linear discriminant analysis and kNN were used to classify the three maturity stages of navel orange, among which kNN attained the highest correct classification rate of 96.0%. Classification of maturity stages of cherry fruits by using the HSI system in the NIR region (874-1734 nm) was done by Li et al., 2018. The result showed the best correct classification ratio of 96.4% by the LDA classifier (Xiaoli Li et al., 2018). For different fruits, different machine learning algorithms showed the best results for maturity classification.

Durian maturity was evaluated by minimal destruction based on electrical impedance measurement (Kuson and Terdwongworakul, 2013). According to the findings of Kuson and Terdwongworakul (2013), selected impedance parameters using a stepwise regression could be used to classify durian samples into an immature class and mature class with less accuracy of 83.3%. Similarly, the research done by Timkhum and Terdwongworakul (2012) showed a good result to identify the characteristic changes in the durian spine with maturity using visible spectroscopy. Their result

showed the best accuracy of 94.7% into only four maturity classes from 113-134 DAA. Tantisoparak et al. (2016) identified the potential of natural frequency due to electromagnetic scattering properties of durian to identify the fruit maturity. The findings shows that, the changes in natural frequencies were associated with the maturity of the fruit which resulted in a variation of resonant frequencies for classification of durian according to its maturity stages (Tantisoparak et al., 2016).

Researches have been conducted on durian intact fruit and pulp for maturity identification and internal properties evaluation. However, the research using the HSI system had not been performed for the maturity classification of durian pulp. The results from this research show the potential to use the HSI system for ripeness classification. The result from SVM shows an overall accuracy of 88.5%, which is comparable to other research that have been done.

3.4 Conclusion

The potential of the HSI pushbroom system with a spectral range from 900-1600nm for ripeness classification of durian pulp was evaluated in this research. The mean spectra extracted from the area of interest were preprocessed using SNV. Three machine learning classifiers: SVM, RF, and kNN were used for developing the ripeness classification of durian pulp where Bayesian optimization was used for tuning the the associated hyperparameters. SVM showed best classification with the training, cross-validation, and overall accuracy of 91.8 %, 87.9%, and 88.5%, respectively. The result shows the potential of the HSI system combined with machine learning algorithms for the ripeness classification of durian pulp. However, the overall accuracy should be improved further using more samples and applying other machine learning as well as deep learning approaches. Different wavelength selection algorithms: successive projection algorithm (SPA), genetic algorithm (GA), and competitive adaptive reweighted sampling (CARS), will be applied further for feature extraction and dimensionality reduction for improvement of classification performance.

Chapter 4

Rapid ripening stage classification and dry matter prediction of durian intact fruit and pulp using a pushbroom near infrared hyperspectral imaging system

This chapter examined the potential of a pushbroom near infrared hyperspectral imaging (NIR-HSI) system (900–1600 nm) for ripening stage (unripe, ripe, and overripe) classification based on the days after anthesis (DAA) of durian intact fruit and pulp. In addition, a preliminary study was done by partial least squares regression (PLSR) model development for the dry matter (DM) prediction in durian pulp. The performance of five supervised machine learning classifiers was compared including support vector machines (SVM), random forest (RF), linear discriminant analysis (LDA) partial least squares-discriminant analysis (PLS-DA), and k-nearest neighbors (kNN) for the ripening stage classification and a partial least squares regression (PLSR) model was developed for the DM prediction. The classification and regression models were developed and compared using the full and selected wavelengths by genetic algorithms (GA) and principal component analysis (PCA). The optimum wavelength selected showed effective result to classify the ripeness level. The finding suggests that the approach used can be implemented in the packaging firms to solve the problems related to uneven ripeness and to inspect the quality of durian based on DM content.

* This chapter constituted the publication article: Sharma, S., K.C, S., Sirisomboon P. “Rapid ripening stage classification and dry matter prediction of durian intact fruit and pulp using a pushbroom near infrared hyperspectral imaging system.” **Measurement**, 189(2022), pp. 110464.

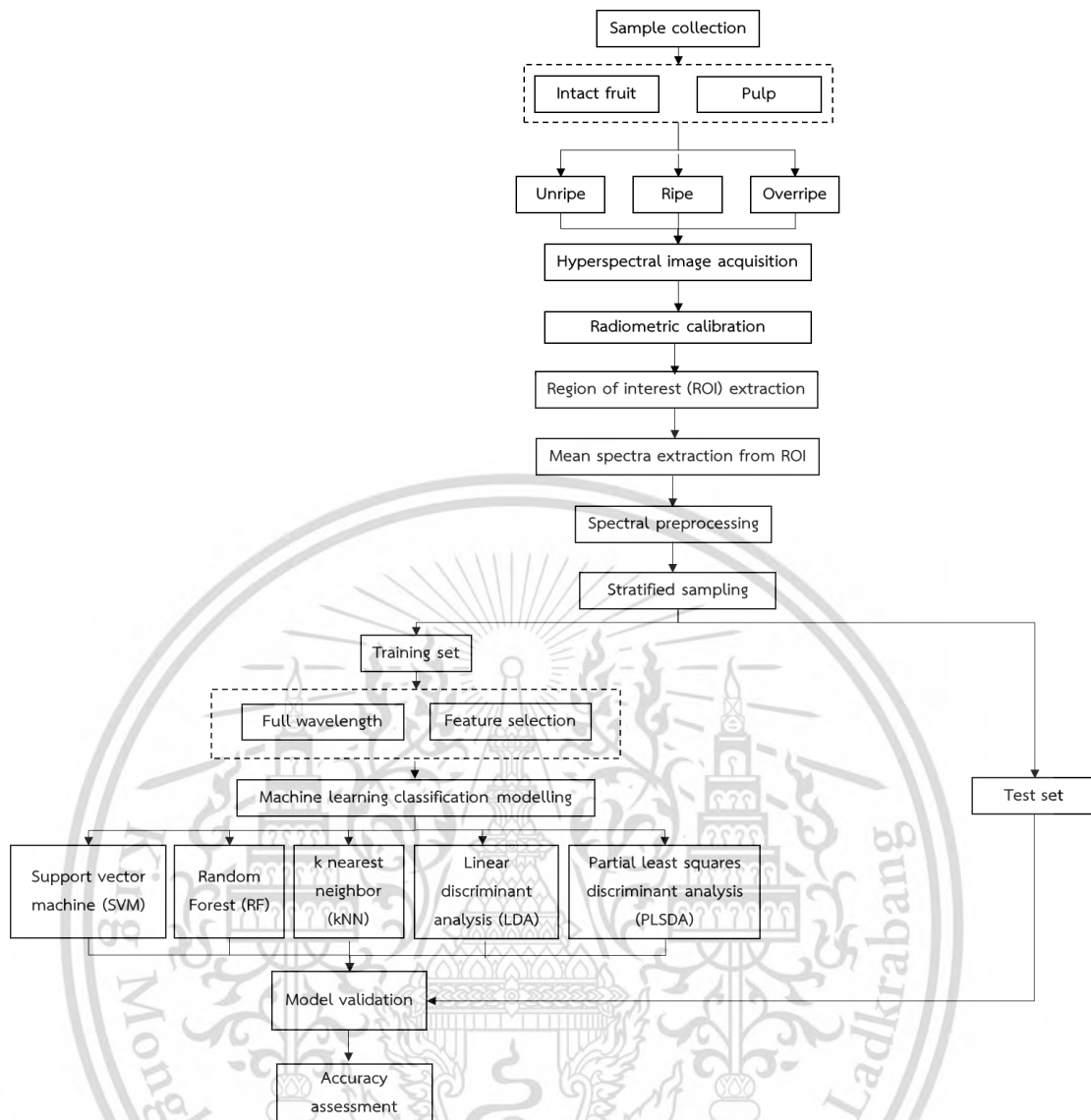


Figure 4. 1 Overall research methodology to classify the ripening level of durian intact fruit and pulp using hyperspectral imaging.

4.1 Introduction

Durian is a unique and expensive tropical fruit usually grown in Southeast Asian countries. Durian is consumed as fresh fruit and in the form of processed products such as ice cream, pasta, and chips. The quality of the fruit is very important, as it directly influences the consumer's demand. Harvesting indices need to be monitored properly, as they are related to the postharvest quality of the fruits. In the case of Thailand, durian harvesting is mostly performed manually, and the harvested fruits are transported to the packaging house for quality inspection. Only the best quality whole fruits, pulps, or fruit products will be transferred to the national and international

This material is reserved for educational use only, not allowed for commercial use.

Forbidden to modify the content, and cite the document when use.

markets. The postharvest storage and eating quality of the fruit are directly influenced by the maturity stages. Maturity refers to the process that leads to the ripeness of fruits, and in climacteric fruits, maturity overlaps with ripeness (Giovannoni, 2001). Generally, durian fruit growth is significant until 90 DAA, after which growth slows down until 112 DAA [2]. In the later stages, the fruit attains full maturity and eventually starts to fall when overripe. Fruits harvested at different maturities also have different respiration rates (Ketsa et al., 2020) and ethylene production, which directly influence the ripening process (Seymour et al., 2013). Some important maturity indices have been used for harvesting durians, such as DAA counting, abscission layer, spines, fruit stalk, grooves, tapping, sap, and dry matter (DM) content (Ketsa et al., 2020; Siriphanich, 2011). Most of these traditional methods depend on the experience of the farmers and are generally done through visual inspection (Kalayanamitra et al., n.d.). Likewise, DM content analysis is a destructive and time-consuming method. Preliminary experimental results on the classification of durian fruit ripening stage by visual inspection, tapping or DAA counting showed low accuracy to discriminate some ripening stages (personal communication with Peerapong Sangwanangkul, Kasetsart University, Kamphaeng San campus). These traditional methods are more likely to have an error caused by the person's inexperience or fatigue while harvesting (Kuson and Terdwongworakul, 2013). The timeline from first flowering and full bloom to fruit set and maturity depends on annual climate conditions, cultivar, and the location (Kalayanamitra et al., n.d.; Subhadrabandhu and Ketsa, 2001). 'Monthong' is one of the popular varieties among Southeast Asian countries, particularly for its aroma and taste. Research by Pakcharoen et al. (Pakcharoen et al., 2013) showed that Monthong fruit harvested at 106 DAA had higher chances of uneven ripening and higher variation within the fruit in terms of pulp firmness and soluble solids concentration than fruit harvested at 113 DAA. Harvesting immature fruits result in inferior eating quality, and even after ripening, the fruit lacks the characteristic aroma and flavor (Ketsa et al., 2020). Ripening stage identification is an important aspect for durian consumers and producers, as it influences the overall quality of fruit and pulp. The DM of the durian pulp was measured as an important maturity index (Kuson and Terdwongworakul, 2013; Siriphanich, 2011). DM is used as an index of the storage reserve, as it accumulates soluble sugar content and starch in the pre-harvest stage, and future soluble solids content, as after ripening the starch is converted into sugar in climacteric fruits such as durian (Walsh et al., 2020). Therefore, the DM of durian at harvest can be related to the future eating quality (Saechua et al., 2021). It would be a great benefit for the producers and the packaging firm to know the quality of the product beforehand, which will eventually save economic loss. Emerging technologies that have been applied for the maturity classification of durian include thermal imaging (Mohd Ali et al., 2018).

This material is reserved for educational use only, not allowed for commercial use.

al., 2020b), spectroscopic techniques (Onsawai et al., 2020; Phuangsombut et al., 2018; Timkhum and Terdwongworakul, 2012), wireless sensor networks (Krairiksh et al., 2011), and natural frequency simulation (Tantisopharak et al., 2016). As noted by Ketsa (2020) (Ketsa et al., 2020), although non-destructive techniques have been carried out intensively for durian maturity determination in research studies, none have been adopted for commercial practice.

The application of spectroscopic (Amodio et al., 2017; de Oliveira et al., 2014; Jha et al., 2012) and imaging techniques (Manickavasagan et al., 2014; Mohammadi et al., 2015; Tan et al., 2010) for determining the quality traits of fruits and vegetables has been successfully implemented for decades. Spectroscopic techniques are suitable for qualitative and quantitative analysis of agricultural product chemical composition and properties, but the exact location or position information throughout the sample cannot be obtained. On the other hand, imaging techniques can provide information based on external parameters such as texture, size, shape, and appearance. However, these techniques lack sufficient information regarding the internal attributes of the products (Du and Sun, 2004; Park and Lu, 2015a). Hyperspectral imaging (HSI) or imaging spectroscopy has been developed as a technique to overcome the limitations of spectroscopic and imaging techniques. The hypercube generated from the HSI image contains both spatial and spectral information, which offers the advantage of developing a spatial map of spectral variation. The application of the NIR-HSI technique is a great area of research for both automatic target detection and characterizing the analytical composition (ElMasry and Sun, 2010). HSI can be generated by point scanning (whiskbroom), line scanning (pushbroom), and area scanning (tunable filter) depending on the method by which spatial information is acquired (Elmasry et al., 2012). The pushbroom system configuration is normally used when either the object or the imaging unit is moving, such as those used in online systems for industrial applications (Liu et al., 2007).

The application of variable selection algorithms is preferable in HSI data for dimensionality reduction and to obtain a more stable model for easier implementation in the subsequent multispectral imaging system (Elmasry et al., 2012; Zhang et al., 2013; Zhu et al., 2017). Machine learning has been successfully applied to high-dimensional datasets for various classification and regression problems. Several types of research in fruit quality and safety evaluation have been carried out in the last two decades using the HSI combined with wavelength selection and machine learning (Pu et al., n.d.). Support vector machine (SVM) was used to develop the classification models based on full spectral data, optimal wavelength selected by principal component analysis (PCA), textural features, and combined datasets for HSI system covering two-wavelength range (Zhang et al., 2016a). SVM provided the strawberry

This material is reserved for educational use only, not allowed for commercial use.

ripening stage classification accuracy higher than 85% for different dataset models (Zhang et al., 2016a). The maturity stages classification of cherry fruit was studied using full spectral bands and selected wavelength by genetic algorithm (GA) and successive projection algorithm (SPA) combined with linear discriminant analysis (LDA). The correct classification ratio of 96.4% was attained by LDA (Li et al., 2018). A comparison was made between two-stage regression algorithm and random forest (RF) to classify the maturity of red and yellow sweet pepper (Harel et al., 2020). The RF algorithm developed a robust model with a classification accuracy of 97.3% and the researchers highly recommended RF for variable agricultural domain (Harel et al., 2020). Three classifiers, k-nearest neighbor (kNN), SVM, and AdaBoost were used to test the performance of the selected bands from HSI to classify blueberry fruit growth stages and background (Yang et al., 2014). Results showed that the overall accuracy of kNN ranged from 96.8% to 98.7%, was comparative and higher than SVM and Adaboost (C. Yang et al., 2014). Similarly, the performance of three classifiers i.e., partial least squares discriminant analysis (PLS-DA), soft independent modeling class analogy (SIMCA), and LDA, were compared for ripeness classification based on the day after the full bloom of pears and among which PLS-DA provided the highest correct classification rate (CCR) of 87.86% (Khodabakhshian and Emadi, 2018). Some other classification algorithms such as decision trees and neural networks have also been implemented successfully for the maturity classification of bananas, dates, and papaya (Garillos-Manliguez and Chiang, 2021; Najeeb and Safar, 2018; Nasiri et al., 2019). Literature shows that different machine learning classifiers has been providing the optimum result based on the sample (fruits). However, to identify the optimum classifier the comparison should be reported. Therefore, in this research, we compared different popular supervised machine learning algorithms: SVM, RF, LDA, PLS-DA, and kNN to classify the ripening stage of durian.

The NIR-HSI system has been implemented on fruits such as mango (Rungpichayapichet et al., 2017), cherry (Li et al., 2018), banana (Rajkumar et al., 2012b), plum (Li et al., 2018) to predict and visualize the spatial distribution of the physicochemical properties. The HSI technique was used to develop partial least squares regression (PLSR) model to predict the soluble solids content (SSC) and firmness of pears (Fan et al., 2015). The correlation coefficient and RMSEP were 0.876 and 0.491 for SSC and 0.867 and 0.721 for firmness (Fan et al., 2015). Li et al. (Li et al., 2018) studied the application of two HSI cameras in visible NIR (600-975 nm) and shortwave NIR (865-1610 nm) for the prediction of the color, SSC, and firmness of plums. The study shows the prediction of quality attributes with a coefficient of determination of prediction (R_p^2) greater than 0.8 for SSC and greater than 0.7 for firmness and color (Li et al., 2018).

This material is reserved for educational use only, not allowed for commercial use.

Forbidden to modify the content, and cite the document when use.

Thailand is one of the largest exporters of durian among the South-East Asian countries. According to the Thailand Customs department, the statistical report from January 2021 to July 2021 shows 668,271,511 kg of fresh durian fruit, worth approximately 250 million USD, was exported from Thailand (*Thai Customs*, n.d.). Durian is exported as fresh fruit, frozen, or processed products (chips, ice-cream, paste). As one of the economically important fruit, the major problem related to durian taste and quality should be considered. NIR-HSI systems have the potential to inspect defects (Ariana et al., 2006), predict internal constituents (Fan et al., 2015; Rungpichayapichet et al., 2017) and classify ripening stages (Chandrasekaran et al., 2019; Rajkumar et al., 2012b) of fruits and vegetables (Pu et al., n.d.) with high accuracy based on the spatial and spectral information that are beyond the capabilities of the human eye. NIR-HSI has been widely used as a non-destructive, robust, and accurate technique compared to the traditional methods. Physicochemical spatial mapping of durian pulp enables the visualization of pulp ripening and variation of important quality parameters which is one of the major advantages of using the HSI system. Furthermore, the implementation of NIR-HSI system in the durian intact fruit and pulp packaging firms can improve the productivity, reduce the time and cost, and can aid in delivering quality product to the consumers. This state-of-the-art has not yet been applied for the ripening stage classification and DM prediction of durian fruit or pulp.

The main objective of this research was to identify the possibility of ripening stage classification (unripe, ripe, and overripe) of durian intact fruit and pulp based on DAA using a pushbroom NIR-HSI system; to select the important features from NIR-HSI high-dimensional data using principal component analysis (PCA) and a genetic algorithm (GA); to compare the classification performance of different machine learning models (SVM, RF, LDA, PLS-DA, and kNN) on full wavelength and selected wavelengths; and to develop the partial least squares regression model for full and selected wavelengths by GA and PCA for dry matter prediction and spatial distribution for visualization.

4.2. Materials and methods

4.2.1 Sample collection

Durian fruit was collected from Trat Province, located in the eastern part of Thailand. The farmers used days after anthesis (DAA) as the key maturity index for harvesting. Thus, in this research, DAA was used as the index for measuring the ripeness of the durian. For the experimental sample collection, the fruits were tagged manually by the farmers under the supervision of a horticulturist from the first flower blooming day. The fruits were harvested at 99, 106, 113, 120, 127, and 134 DAA. Fifty whole fruits were harvested, with each fruit consisting of approximately 5 to 6 pulps. In total, 260 pulps were used for the experiment. The experiment was conducted 2 days after the

This material is reserved for educational use only, not allowed for commercial use.

Forbidden to modify the content, and cite the document when use.

harvesting date. Farmers use the term percent maturity from 70 to 100% (95 to 130 DAA) for their communication to buyers (Siriphanich, 2011). Fruits below 70% maturity have inferior quality, and 100% maturity are ready to drop off from trees and have a very short shelf life (Siriphanich, 2011). The fruits were divided into three ripening stages based on the DAA: unripe (99 to 106 DAA), ripe (113-120 DAA), and overripe (127-134 DAA), which were categorized according to percent maturity (Table 4.1). The samples were kept in a room at a temperature of 25 ± 2 °C before and during the experiment. The intact fruit were peeled out to extract the pulp with minimal damage. The total tested intact fruit were 20 for unripe, 20 for ripe and 10 for overripe; and pulps were 97 for unripe, 94 for ripe, and 69 for overripe.

Table 4.1 Classification of ripening with respect to the DAA and maturity percentage according to Siriphanich (2011) (Siriphanich, 2011)

DAA	Maturity percentage	Ripening stage
99-106	70	Unripe
113-120	80-90	Ripe
127-134	90-100	Overripe

DAA: Days after anthesis

4.2.2 HSI system configuration

In this research, a pushbroom NIR-HSI system was used for image acquisition. The system was equipped with an imaging spectrograph (ImInspector N17E Specim, Spectral Imaging Ltd., Oulu, Finland) and comprised of a linear array of 320 CCD detectors (Xeva 992, Xenics Infrared Solutions, Belgium). Two 500 W tungsten-halogen light sources (Lowel Light Inc., New York, United States of America) were adjusted at an angle of 45 degrees, providing uniform lighting in the field of view (FOV). The system was controlled by Specim's LUMO Software Suite (Spectral Imaging Ltd., Oulu, Finland). The HSI system produces 256 spectral bands (bit depth of 12) between 900-1600 nm with a spectral resolution of 3.2 nm. Each image (band) contains 320 pixels in the x-direction (width) and n pixels (depending upon the length of the pulp and intact fruit) in the y-direction (length). The spectral bands from each acquisition are stacked and stored in band interleaved by line (BIL) format. The focal distance from the sensor to the pulp was approximately 23 cm, resulting a spatial resolution of 30 μ m per pixel. The image of intact fruit was taken first and after cutting the image of pulps was acquired one by one. The focal distance from the sensor to the intact fruit approximately 30 cm. The

This material is reserved for educational use only, not allowed for commercial use.

Forbidden to modify the content, and cite the document when use.

optimized integration time was set to 6 ms. Samples were scanned on a translation stage at the speed of .

4.2.3 HSI radiometric calibration.

Reflectance calibration or radiometric calibration of NIR-HSI was performed to convert the measured digital numbers to percent reflectance values with spectrally flat and spatially homogenous standard known materials (Park and Lu, 2015a). The white reference and dark reference were acquired for each image in the NIR-HSI system for radiometric calibration. To capture the white reference, a spectralon with a relative reflectance of 99% was used. Similarly, the dark reference image was acquired by the system by closing the camera shutter closed automatically.

$$R = \frac{I_o - D}{W - D} \quad (4.1)$$

After image acquisition, the raw hypercube was radiometrically corrected according to Equation 4.1, where R is the relative reflectance image, I_o is the raw reflectance image, D is the dark reference image, and W is the white reference image. After radiometric calibration, the noise due to the background spectral response of the instrument and the dark current within the camera is minimized (Gowen et al., 2007). Figure 4.2 represents the overall methodology starting from the image acquisition to classification model development and validation.

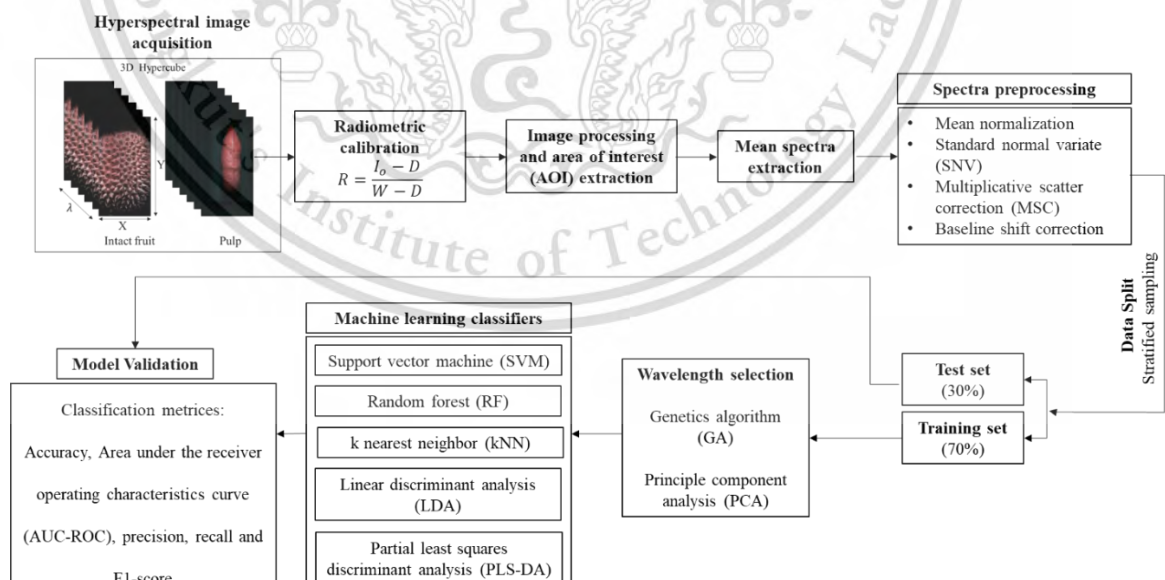


Figure 4.2 Flowchart for the overall methodology from image acquisition to classification model development and validation.

4.2.4 Extracting area of interest (AOI)

The HSI image of the rind was captured by placing the intact fruit samples randomly in a stable position on the translation stage one by one. To acquire an image of pulp, it was guided by two bars from both sides, and the image was captured by placing the pulp in a stable position on the translation stage one by one, as shown in Figure 4.3a. The normalized difference spectral index (NDSI) was computed using the reflectance at two wavelengths, i.e., 1075.67 nm and 1450.18 nm (Equation 4.2), to extract the AOI of rind and pulp. The NDSI value range was from -1 to 1. The translation stage, guiding bars, and shadow area exhibited a lower NDSI value (≤ 0). As shown in Figure 4.3b, the spectral profile was approximately constant throughout the wavelength of the translation stage and guiding bars. However, the NDSI values of rind and pulp were high and positive (close to 1), as the reflectance at a wavelength of 1075.67 nm was high and the reflectance at a wavelength of 1450.18 nm was low.

$$\text{NDSI} = \frac{(R_{1075.67} - R_{1450.18})}{(R_{1075.67} + R_{1450.18})} \quad (4.2)$$

The binary threshold operation was then performed to separate the pulp from the background. The threshold value was set to 0.5, with values greater than 0.5 representing the rind and pulp. Morphological filters (dilation and erosion) were applied to the binary image to extract the durian pixels. First, the erosion filter (filter size of $f \times f$ and n iteration) was applied to the binary image (Figure 5.3c) to avoid the background pixels, and then the dilation filter (filter size of $f \times f$ and n iteration) was applied to fill the gaps within the AOI (Figure 4.3d). Finally, the erosion filter (filter size of $f \times f$ and n iteration) was used again to avoid the pixels around the edge of the rind and pulp (Figure 4.3e). After applying the morphological filters, the contours representing the homogenous pixels were extracted. The AOI was represented by a single big contour. Some of the patches of background pixels remained even after the morphological operation; however, their contour size was very small. Thus, the contour with the largest boundary area was taken as the rind and pulp, as shown in Figure 4.3f. The mean spectra of the rind and pulp were then extracted as the mean value of every pixel at different wavelengths that were within the extracted boundary.

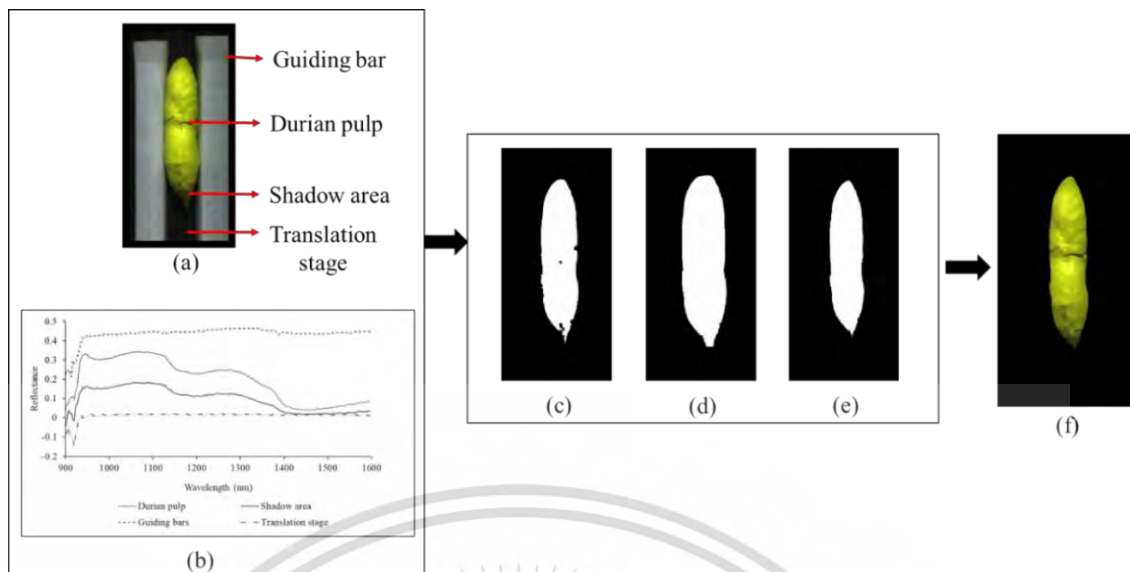


Figure 4.3 Near Infrared hyperspectral image after radiometric calibration pulp (a) and spectral profile of the section of durian pulp, guiding bar, and the translation stage (b), erosion applied to a binary image (c), dilation followed erosion (d), erosion followed dilation (e), contour extracted durian pulp (f).

4.2.5 DM content measurement

DM content measurement was performed by the oven drying method. After acquiring images, the surface of the pulp was cut and chopped finely. Samples were placed in aluminum moisture can with a diameter of 5 cm and a height of 3 cm. Approximately 5 ± 0.05 g of sample was weighed in moisture can by electronic balance with 0.0001 g resolution (Mettler Toledo Model- JS1203C) and kept in a hot air oven (FDA240, Binder, Tuttlingen, Germany) at 60 °C. After 24 h, the dry weight was recorded. The samples were dried and weighed again every 3 h until a constant weight was measured. Two replicate measurements were performed for each sample, and the average DM content was calculated.

The percent DM was calculated using the following equation:

$$DM = 100 \times \frac{W_2}{W_1} \quad (3)$$

where W_1 is the initial weight and W_2 is the final weight.

4.2.6 Spectral preprocessing

This material is reserved for educational use only, not allowed for commercial use.

Forbidden to modify the content, and cite the document when use.

From every pixel of the AOI, the mean spectra for each sample were extracted. Light scattering, which results in path-length variation and varying background signal levels, causes baseline shifts and curvature that might vary greatly within and among the samples (Barnes et al., 1993; Isaksson and Naes, 1988; Zeaiter and Rutledge, 2009). Spectral preprocessing techniques: mean normalization, standard normal variate (SNV), multiplicative scatter correction (MSC), and baseline shift correction were applied in the raw mean spectra. SNV and MSC transformation reduce the effects of scattering, particle size, and the difference in the global intensities of the signals (Barnes et al., 1993; Roger et al., 2020). Normalization also minimizes the effect of factors such as light scattering, variations in radiation penetration, or the size of the samples (Zeaiter and Rutledge, 2009). Similarly, baseline offset correction works best in the case of vertical baseline shifts from spectra and is also useful for reflectance data where signal offset can occur (Zeaiter and Rutledge, 2009).

The data set was divided into training and test set using stratified sampling in a ratio of 70:30 prior to the model development. In this research, a grid search approach (GridSearchCV) from Scikit-learn was implemented for hyperparameter tuning (Bradski, 2000; Pedregosa et al., 2011). The grid search approach implements cross-validation (CV) to find the optimal hyperparameters over a parameter grid for each classification model (Pedregosa et al., 2011). Thus, stratified k-fold CV with $k=5$ was applied where the training set (70%) is split into five groups and each group is used in turn to evaluate the model fitted on the other 4/5 of the training dataset (Pedregosa et al., 2011). The mean accuracy and the standard deviation value were computed from the results of 5-fold CV. Finally, the model with optimal hyperparameters were evaluated on the test dataset (30%).

4.2.7 Classification model development

4.2.7.1 Support vector machine (SVM)

SVM is one of the most powerful and robust classifications and regression algorithms in diverse fields of application (Cervantes et al., 2020). For classifying a group of data, SVM attempts to find the optimal hyperplane that can separate the closest samples of two classes, also known as the support vectors, by maximizing the margin. The SVM uses the kernel function that nonlinearly maps input space to higher-dimensional space (Pal et al., 2016; Yu et al., 2010). The hyperparameters used for SVM were the soft-margin constant (C), gamma (γ), and kernel function (radial basis function (RBF) and polynomial function). Hyperparameter tuning was performed to find the optimum value of these parameters by the grid search approach. The input values for C were 0.01, 0.1, 1, 2, 5, 10, 20, 50, and 100, those for γ were 0.01, 0.05, 0.1, 0.25, 0.5, 2.5, 5, and 10 and kernel function RBF and polynomial with order of 3, 5 and 7.

This material is reserved for educational use only, not allowed for commercial use.

Forbidden to modify the content, and cite the document when use.

4.2.7.2 Random forest (RF)

The RF is an ensemble learning approach that constructs multiple trees based on random bootstrapping samples (samples with replacement) of the training data (Breiman, 2001). It is an improved algorithm compared to the decision tree and can be used in both classification and regression problems. In a classification problem, RF combines a group of decision trees at the training stage, and the output class is determined by majority voting (Cui et al., 2018). In each decision tree of RF, the internal nodes are split using the best split feature from a group of randomly selected features (Liaw and Wiener, 2002). This strategy makes RF robust and avoids overfitting. RF can also handle multiclass problems with many dependent and independent variables (Breiman, 2001). Among the different hyperparameters, the number of trees in the forest ($n_estimator$), the number of features to consider for the best split (maximum features), the maximum depth of the tree, and the function to measure the quality of a split (criterion) were considered when building an RF model. Hyperparameter tuning was performed by the grid search approach for the $n_estimator$ (50, 100, 200, 500), maximum feature (2, 5, 10, 15, 20), maximum depth (2, 5, 10, 15, 20), and criterion (Gini and Entropy).

4.2.7.3 Linear discriminant analysis (LDA)

The LDA, also known as the Fischer discriminant, is a very common technique used mainly for dimensionality reduction and classification (Tharwat et al., 2017). LDA is an effective subspace method that focuses on finding projections of the original higher-dimensional space to a lower-dimensional space. LDA calculates the between-class and within-class variance, and the lower-dimensional space is constructed in such a way that it maximizes the ratio of the between-class variance and the within-class variance (Mohanty et al., 2013). This is also known as Fischer's criteria, which provides class separability by creating the decision boundary. In this research, singular value decomposition was used to transform the higher dimensional dataset to the number of components ($n-1$), where n is the total number of classes. In this research, two LDA components were used to classify three ripening stages.

4.2.7.4 Partial least squares discriminant analysis (PLS-DA)

The PLS-DA was developed as a classification method that combines the properties of PLS regression with the discrimination power of a classification technique (Ballabio and Consonni, 2013). PLS-DA is applicable for the classification and descriptive modeling of higher-dimensional data sets. In PLS-DA, a linear relationship between the dependent matrix Y , which contains the information about the class, and the independent matrix (X) is established. For the binary class, PLS-1 is used with the Y

This material is reserved for educational use only, not allowed for commercial use.

Forbidden to modify the content, and cite the document when use.

($N \times 1$) matrix, where N is several samples that create a value assumed to be 0 or 1, depending on whether or not it belongs to the class represented for that column (Barker and Rayens, 2003). Similarly, for multiple classes, PLS-2 is applied, where the Y ($N \times 1$) matrix is converted into a dummy ($N \times G$), and G is the number of classes (Lee, Liong, Jemain, 2018).

4.2.7.5 k nearest neighbors (kNN)

The kNN classification is one of the simplest algorithms in machine learning. The kNN classifies the sample based on the closest training examples in the feature space. For classification, in the training set, the unlabeled query point is simply assigned to the label of its k nearest neighbor by the majority vote (Kim et al., 2012). For every row of the test set data, the k nearest training set objects are determined and classified based on closest neighbors voting (Vadivambal and Jayas, 2015). The hyperparameters used for kNN are the number of neighbors (2, 5, 10, 15, 20), metrics (Euclidean and Minkowski), and algorithms (ball tree, kd tree, and brute).

Supervised machine learning algorithms: SVM, RF, LDA, PLS-DA, and kNN were applied for the ripeness classification of durian intact fruit and pulp. The classification models were developed separately for raw and pretreated spectra. The accuracy (Equation 4.4), precision (Equation 4.5), recall (sensitivity or CCR) (Equation 4.6), specificity (Equation 4.7), and F1-score (Equation 4.8) were used to compare the results. In addition, the area under the receiver operating characteristics curve (AUC-ROC) score was also compared between the classifiers. AUC-ROC measures the ability of the classifier to differentiate between the classes, therefore, this metric is considered as one of the reliable indicators to compare the performance of the classifier. The range of AUC-ROC is from 0 to 1. AUC-ROC score close to 1 indicates that the classifier can highly distinguish the positive class from the negative class. Table 4.2 shows the confusion matrix representing the true positives (TP), true negatives (TN), false positives (FP), and false negatives (FN). For the three classes (unripe, ripe, and overripe), TP, TN, FP, and FN with respect to class unripe can be explained as: TP is the number of samples that are correctly classified for unripe; TN is the number of samples belonging to ripe and overripe; FN is the number of samples belonging to unripe which are misclassified as ripe and overripe; FP is the number of samples of ripe and overripe that are incorrectly classified as unripe (Azarimdel et al., 2020). The classification algorithms were developed in Python 3.8 using a widely popular machine learning package, Scikit-learn (Pedregosa et al., 2011), and MATLAB R2018a (Mathworks, Natick, MA, USA).

Table 4. 2 Confusion matrix of actual versus predicted classes.

This material is reserved for educational use only, not allowed for commercial use.

Forbidden to modify the content, and cite the document when use.

		Predicted Class	
		Positive	Negative
Reference Class	Positive	True Positive (TP)	False Negative (FN)
	Negative	False Positive (FP)	True Negative (TN)

$$\text{Overall Accuracy (\%)} = \frac{TP + TN}{TP + TN + FP + FN} \times 100 \quad (4.4)$$

$$\text{Precision (\%)} = \frac{TP}{TP + FP} \times 100 \quad (4.5)$$

$$\text{Recall (\%)} = \frac{TP}{TP + FN} \times 100 \quad (4.6)$$

$$\text{Specificity (\%)} = \frac{TN}{TN + FP} \times 100 \quad (4.7)$$

$$\text{F1 score} = 2 \times \frac{\text{Precision} \times \text{Recall}}{\text{Precision} + \text{Recall}} \quad (4.8)$$

4.2.8 Selection of optimal wavelength

4.2.8.1 Principal component analysis (PCA)

Principal component analysis (PCA) is one of the various techniques for solving the problem of multicollinearity and decomposing high-dimensional data into new orthogonal axis, known as principal components (PCs). The original data will be represented by the combination of a few PCs and with minimal loss of information, making PCA a well-established technique for dimensionality reduction and variable selection in HSI. PCA allows the user to select the wavelength based solely on spectral information, which is not influenced by any candidate subset selection and evaluation function. PCA had been applied successfully for identifying: six key wavelengths for apple bruise detection from HSI (Xing and De Baerdemaeker, 2005), five and six wavelengths for HSI system covering two wavelength range for strawberry ripeness evaluation (Zhang et al., 2016a), and five wavelengths for identification of different particle size in milk powder (Khan et al., n.d.). Furthermore, the results from Amanda et al. (Badaró et al., 2020); Kong et al. (Kong et al., 2018); and Chu et al. (Chu et al., 2020) showed the potential and importance of using PCA in comparison to other

This material is reserved for educational use only, not allowed for commercial use.

Forbidden to modify the content, and cite the document when use.

wavelengths selection methods such as competitive adaptive reweighted sampling (CARS), SPA, and second derivative spectra for HSI. PCA was applied to the SNV pretreated spectra, and the loading weight was calculated for the three important PCs that explain most of the variance in the spectra. The loading weights show the importance of corresponding wavelengths or bands in the spectral matrix. The peaks or valleys with the maximum absolute loading weights from the PCs were selected manually as the sensitive wavelengths (Xia et al., 2017). After extracting the feature wavelengths, machine learning classifiers were used to develop the classification and regression model.

4.2.8.2 Genetic Algorithm (GA)

Genetic algorithm is popular feature selection algorithms based on the mechanics of natural selection theory and an evolutionary computing algorithm for solving optimization problem (Hassanat et al., 2019). The basic idea of GA is based on the theory of evolution, the best individuals have a greater chance to survive and there is a greater probability of getting better offspring from the mating of two good individuals. GA performs a random search method to find the optimal solution by simulating the natural selection and evolution processes (Ying and Liu, 2008), which mainly consists of the following five steps (Li et al., 2018): 1) variable coding, 2) creation of the initial chromosome which is a collection of values of the variables to be optimized, the variables themselves are called genes (Ying and Liu, 2008), 3) fitness evaluation (response evaluation), 4) reproduction (crossover) and 5) mutation (Ying and Liu, 2008). After one loop is completed, steps 3 to 5 are executed until the criteria are satisfied (Li et al., 2018). Crossover operations recombine the part of two parental solutions to create a new chromosome which can provide a better solution and the mutation can occur randomly (Shorman and Pitchay, 2015). GA searches a population of points in parallel dimensions not only in a single point, which allows to implicitly evaluate many schemas at once (Gandhi, 2015; Shorman and Pitchay, 2015). GA does not require prior knowledge of the problem, as it can produce the random changes through the crossover and mutation in their solution genes and then use the objective function to determine whether the applied changes are positive or negative to the overall search problem (Gandhi, 2015). Most of the algorithms can only explore the solution area to a problem in trend at a time, if the solution found is suboptimal the whole process must be restarted (Shorman and Pitchay, 2015). However, in GA if one path turns out to be suboptimal, it can change the path and continue to work providing a greater chance in each run to find the optimal solution which in turn saves the computational time. Therefore, it is a well-suited optimization method to interrogate a large search in HSI high dimensional space where many wavelength combinations

This material is reserved for educational use only, not allowed for commercial use.

are possible (Ying and Liu, 2008). The initial population was set to 30, and the probability of mutation and crossover was 0.01 and 0.6, respectively. Considering that, the low crossover rates lead to low rates of exploration the crossover value was chosen from the range (0.1-1) (Hassanat et al., 2019). Similarly, the high mutation rates normally led to random search, and the mutation rates were always lower than the crossover rates, in which the mutation rate was in the range of (0.001–1) (Hassanat et al., 2019). GA was run 100 times, and the importance of variables were calculated as the average number of times that a variable was selected (Mamouei et al., 123 C.E.). The GA selected wavelength was integrated with SVM, RF, LDA, PLS-DA, and kNN for classification and PLSR for regression model development.

4.2.9 DM prediction model and spatial distribution

The methodology for DM prediction model development and spatial distribution is shown in Figure 4.4. A partial least squares regression model has been developed for both full and selected wavelengths. The training set and test set were divided at a ratio of 70:30 by Kennard-Stone (KS) sampling. The KS algorithm selects a representative subset from a pool of N samples, and to ensure a uniform distribution of such a subset along with the X data space, the algorithm follows a stepwise procedure in which new selections are taken in the regions of space located far from the already selected samples using the Euclidean distance (Saporo et al., 2012). From the training set, the PLSR model was developed, and the regression coefficient obtained from the model was used to calculate the DM at each pixel throughout the sample (durian pulp). The PLSR model is given $[Y] = [X][B]$, where Y represents predicted DM, X is the relative reflectance in each pixel, and B is the regression coefficient obtained from the acquired optimum calibration model (Pitak et al., 2021). Each spectrum in the pixel was taken into consideration. The predicted DM was then represented as a 2D array of pixels for each sample.

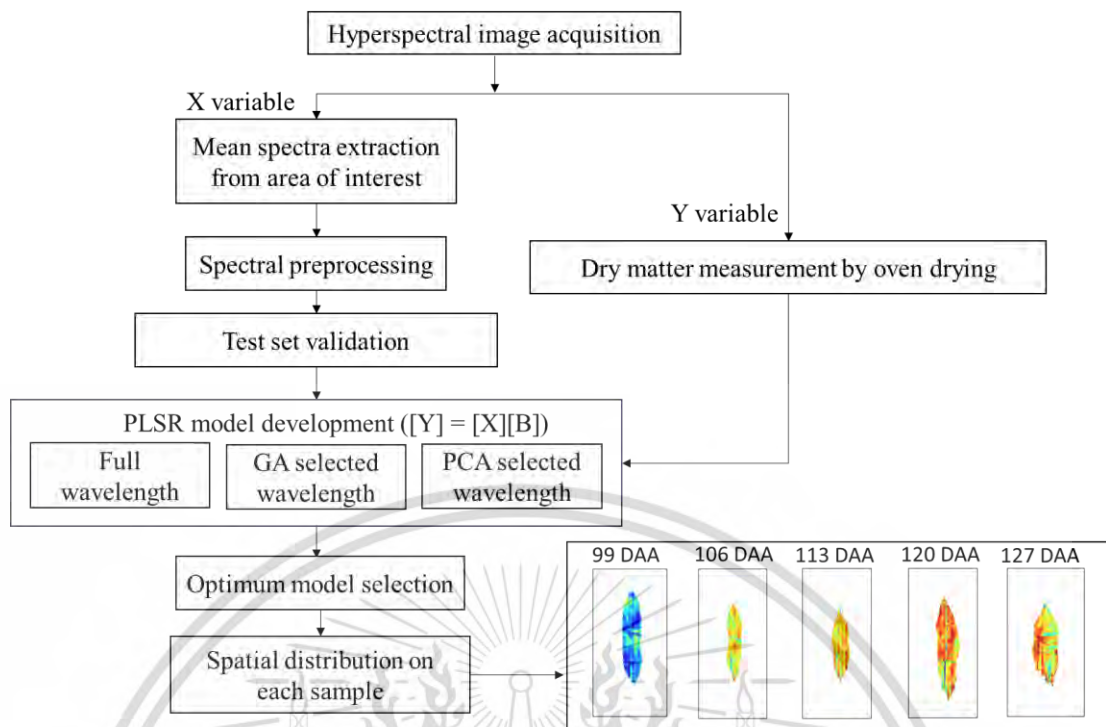


Figure 4.4 Flowchart representing the methodology for the dry matter prediction model and spatial mapping.

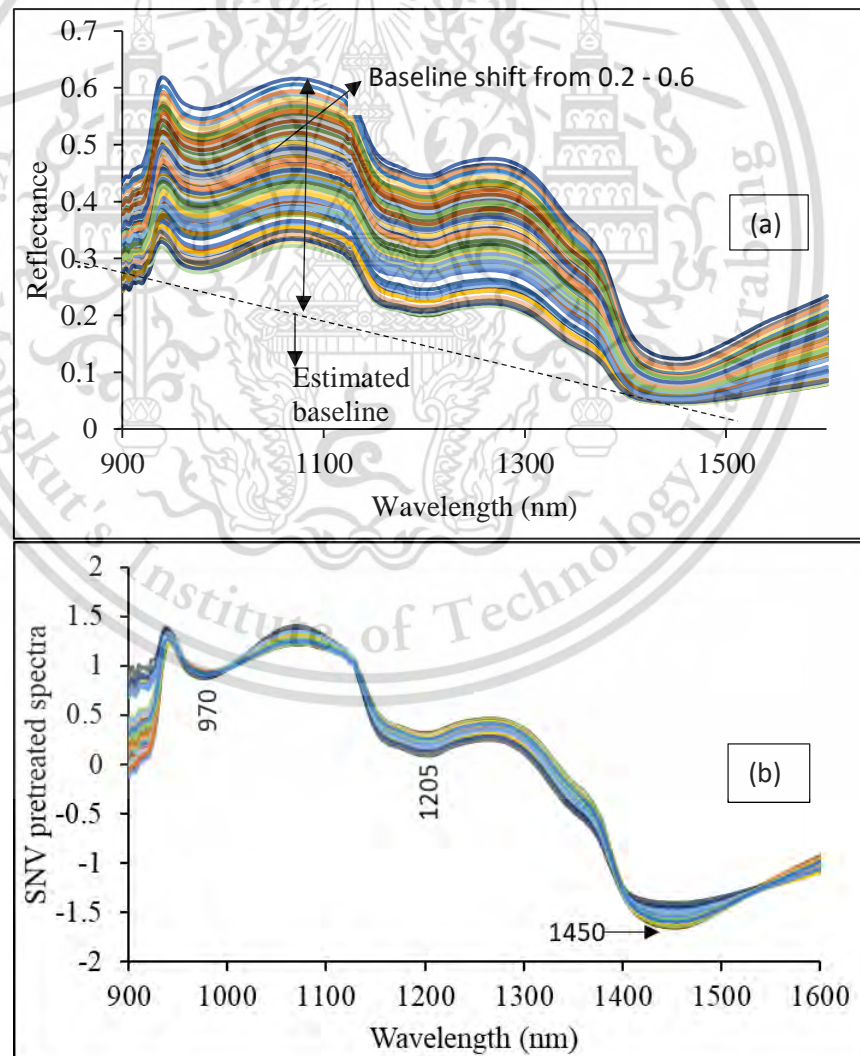
4.3 Results and Discussion

4.3.1 Spectral profile of durian pulp

The raw spectra of durian pulp are shown in Figure 4.5a. The raw spectra show baseline shift and the spread throughout the spectrum which is known as the scatter or scattering effect. The variation on the y-axis (reflectance) is mainly related to the size and composition of durian pulp (Williams and Antoniszyn, 2019). Pretreatments were applied to eliminate those effects on the raw spectra. The SNV pretreated spectra of all samples are shown in Figure 4.5b, and those representing the mean spectra of unripe, ripe, and overripe stages are shown in Figure 4.5c. The spectral characteristics of the rind of the intact fruit and pulp are almost similar as shown in Figure 4.5c and 4.5d, which is in agreement with the report by Somton et al. (2015). The absorbance of rind could be lower than pulp because of the non-uniform surface characteristics of rind which cause light scattering (Somton et al., 2015). It was previously reported by Rutpralom et al., (2002) that during ripening the moisture content of the rind continuously decreased and was inversely correlated to the moisture content of the pulp. The major downward valley was observed at 974, 1205, and 1450 nm, which were shifts of 970 and 1200 nm. The peaks at 970 and 1200 nm represent the absorption bands involving the symmetric and asymmetric stretching modes of the

This material is reserved for educational use only, not allowed for commercial use.

water molecule (Workman and Weyer, 2007). A wavelength of 1450 nm is associated with an O-H stretch first overtone of water and starch (Osborne et al., 1993). In the pulp, the reflectance of overripe samples at 1205 nm was lower than that of the unripe and ripe samples, as shown in Figure 4.5c. According to Timkhum and Terdwongworakul (2012), the DM percentage of the durian pulp increases significantly from 99 to 113 DAA compared with the later ripening stage (from 113 to 134 DAA) as the water content increases significantly from unripe (99 to 106 DAA) to ripe (113 DAA) fruit. This justifies the higher reflectance of unripe pulp at the initial stage in the water band 1200 nm as shown in the Figure 4.5c. As reported by Timkhum and Terdwongworakul (2012), the SNV pretreated spectra were able to show the relationship with DAA. At some wavelengths, such as 900, 1200 nm, and 1450 nm, the spectra can be separated according to the ripening stage defined by DAA, but in many wavelengths range, there are overlapping peaks between the stages, as shown in Figure 4.5c.



This material is reserved for educational use only, not allowed for commercial use.

Forbidden to modify the content, and cite the document when use.

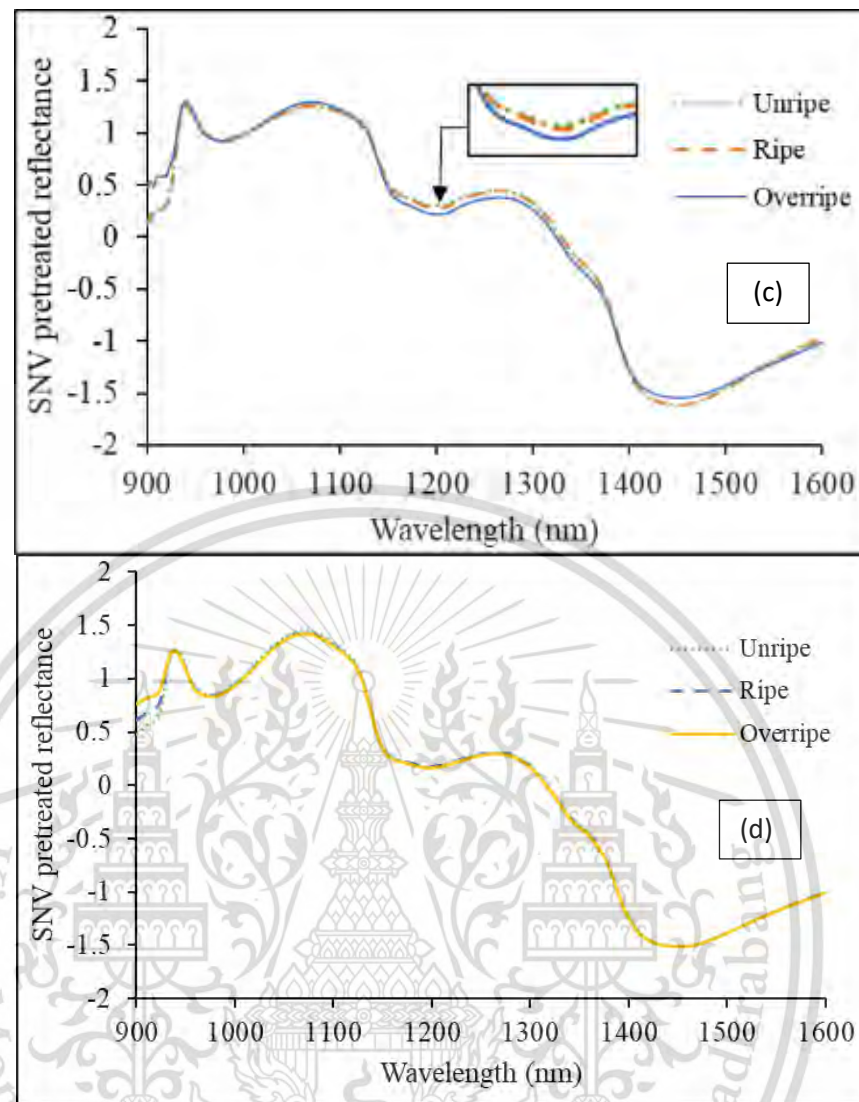


Figure 4. 5 Raw mean spectra of durian pulp (a), standard normal variate pretreated spectra (b), and average spectra of each ripening stage (c), and average spectra of intact durian fruit at each ripening stage.

4.3.2 Classification model performance for durian pulp

4.3.2.1 Full wavelength

The classification models, SVM, RF, LDA, PLS-DA, and kNN, were developed using the full wavelength and selected wavelengths by GA and PCA. Using each classifier, a separate classification model was developed for raw and pretreated spectra. The classification performance was assessed based on training, 5-fold CV, and test accuracy as shown in Table 4.3. The test accuracy shows the reliability of the training model for correctly classifying each group. Among all classifiers, LDA outperformed with the best training, 5-fold CV, and test accuracies of 100%, 98.4%, and 100%, respectively, using raw spectra. The classification accuracy of SVM ranged between 90-95% for the training

This material is reserved for educational use only, not allowed for commercial use.

Forbidden to modify the content, and cite the document when use.

set and 77-89% for the test set. The test accuracy was attained 93.6% from MSC pretreated spectra using SVM with the optimal hyperparameter combination ($C = 20$, $\gamma = 5$ and polynomial kernel of order 3). Using RF on baseline pretreated spectra provided a training accuracy of 100%, but the test accuracy was poor, which shows the overfitting of the training model. RF using the mean normalized spectra achieved the test accuracy of 87.2% with optimal hyperparameter combination (number of estimators= 200, maximum features=10, maximum depth= 5, and criterion= Gini). The optimum model for PLS-DA provided a test accuracy of 87.2% using SNV pretreated spectra. The kNN classifier performed poorly with test accuracies lower than 90%. Figure 4.6 shows the precision, recall, specificity, and F1 score of the test set provided by the optimum model selected for each classifier using raw and preprocessed spectra from Table 5.3. The average AUC-ROC score for the classifiers is in the range of 0.67-1.0. AUC-ROC score of single class against other class for each classifier model is shown in Appendix. The average AUC-ROC score SVM and RF are higher than 0.95 which indicates that the selected model showed good performance in distinguishing the ripening stages. The AUC-ROC score of the LDA model showed the highest value, indicating that the classification performance of LDA models is better than other classifiers.

Table 4.3 Accuracy comparison among the classification models using the full wavelength.

Classifiers	Preprocessing	Full wavelength			AUC-ROC score	
		N	Training accuracy (%)	5-fold CV accuracy (%)		Test accuracy (%)
SVM	Raw	216	77.5	84.1±2.1	74.3	0.87
	Mean Normalized	216	90.7	92.9±2.2	87.2	0.97
	SNV	216	95.1	92.3±2.0	92.3	0.98
	MSC	216	97.1	91.2±2.6	93.6	0.98
	Baseline	216	91.2	85.2±2.1	80.8	0.94
RF	Raw	216	100	64.9±4.9	55.1	0.75
	Mean Normalized	216	96.7	89.0±4.3	87.2	0.97
	SNV	216	100	87.4±4.1	85.9	0.97
	MSC	216	100	87.4±2.8	85.9	0.97
	Baseline	216	100	80.3±5.8	71.8	0.85
LDA	Raw	216	100	96.7±2.1	100	1
	Mean Normalized	216	100	94.5±3.1	89.7	0.97

This material is reserved for educational use only, not allowed for commercial use.

Forbidden to modify the content, and cite the document when use.

	SNV	216	100	96.7±2.1	97.4	0.99
	MSC	216	100	96.1±2.8	94.9	0.99
	Baseline	216	100	96.2±2.7	98.7	1
PLS-DA	Raw	216	84.1	82.4±5.9	79.5	0.92
	Mean Normalized	216	85.7	86.8±1.9	85.9	0.94
	SNV	216	88.5	87.4±3.3	87.2	0.95
	MSC	216	85.7	83.0±5.8	87.2	0.95
	Baseline	216	83.5	81.3±3.3	71.8	0.90
kNN	Raw	216	69.2	59.4±9.3	50.0	0.67
	Mean Normalized	216	87.4	74.4±4.4	74.4	0.88
	SNV	216	93.4	84.1±2.0	76.9	0.85
	MSC	216	93.4	84.1±2.0	78.2	0.86
	Baseline	216	84.1	62.1±5.1	65.4	0.78

CV: Cross-validation; N = Number of wavelengths; SVM: Support vector machine; RF: Random forest; LDA: Linear discriminant analysis; PLS-DA: Partial least squares discriminant analysis; kNN: k nearest neighbor; SNV: Standard normal variate; MSC: Multiplicative scattering correction; AUC-ROC: Area under the receiver operating characteristics curve

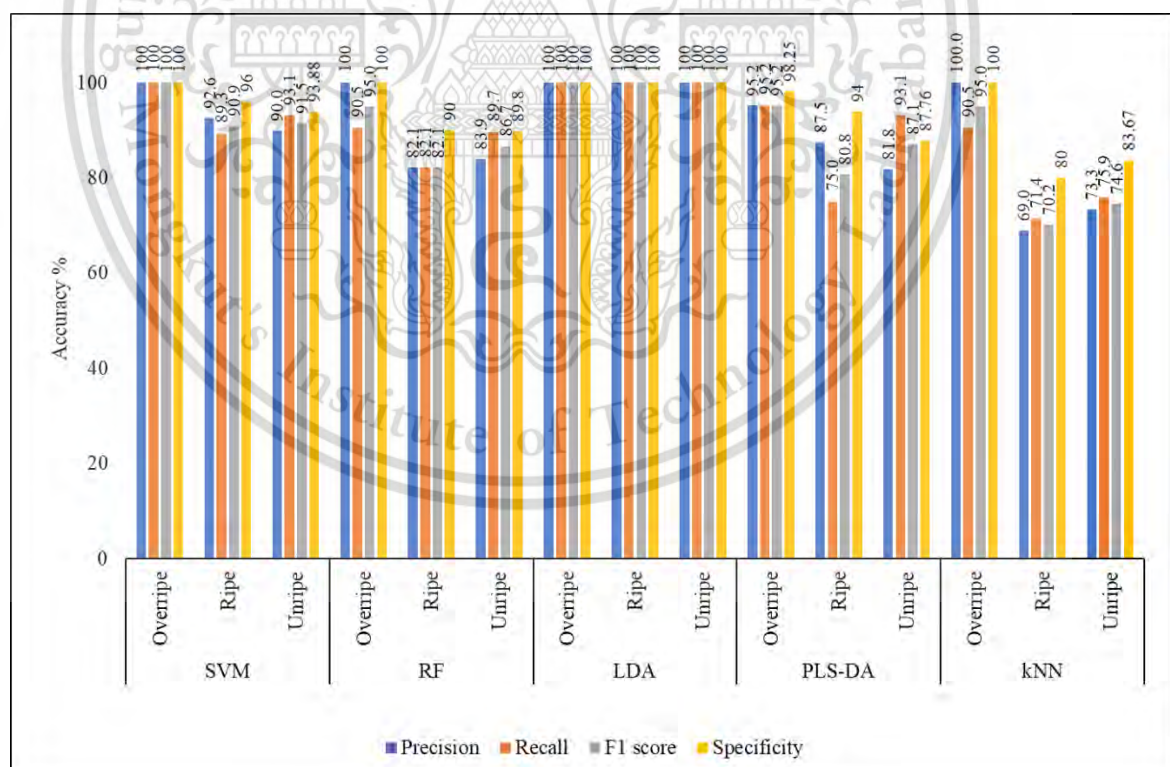


Figure 4.6 Precision, recall, specificity, and F1 score obtained for each ripening stage from the test set using the full wavelength.

4.3.2.2 GA selected wavelength

The performance of classifiers based on a selected wavelength by GA is shown in Table 4.4. The training, CV, and test accuracy were either similar or better after using the selected wavelengths by GA compared to the full wavelength. For the classification by SVM, the best performance was attained by SNV pretreated spectra with training and test accuracies of 96.2% and 88.5%, respectively. The optimal hyperparameter combination of C, γ , and kernel: 2, 0.05, and polynomial function order 7 was able to achieve the test accuracy of 92.3% using 106 optimum selected wavelengths. RF provided similar or improved accuracy using the GA selected wavelength. The number of wavelengths selected for each classifier and pretreatment combination ranged from 101-138 wavelengths by GA. The PLS-DA model developed using SNV-pretreated spectra showed better results than other preprocessing methods. LDA applied to the raw spectra for ripening stage classification attained a training, CV, and test accuracy of 100% with the selected 135 wavelengths. The selected wavelengths are continuous and discrete at 900-916, 932-958, 965, 981-1026, 1039, 1043-1108, 1114, 1121-1143, 1150-1202, 1212-1231, 1241, 1254.63, 1261-1300, 1310-1400, 1410-1473, and 1480-1593 nm. These wavelengths include the important water absorption bands at 970 and 1200 nm, water and starch bands at 1450 nm, sucrose and starch bonds at 1440 nm, and starch and glucose bonds at 1580 nm (Osborne et al., 1993). The performance of the kNN classification model was improved significantly using the GA-selected wavelength for raw and preprocessed spectra. The test accuracy of 84.6% was achieved by the kNN classifier using MSC pretreated spectra with optimal hyperparameters (number of neighbors=5, metric = Euclidean, and algorithm = ball tree).

Figure 4.7 shows the precision, recall, specificity, and F1 score of the test set attained by the optimum model selected for each classifier from Table 4.4. The classification metrics of overripe samples were higher than those of ripe and unripe samples. This implies that the overripe samples can be classified with less error and high precision from ripe and unripe samples. The unripe samples harvested at 99 DAA and 106 DAA are misclassified with the ripe samples harvested at 113 and 120 DAA by most of the classifiers. LDA was able to obtain 100% precision, recall, specificity, and F1 score. The average AUC-ROC score for the classifiers is in the range of 0.5-1.0. The AUC-ROC score of each class is shown in Appendix B.

Table 4.4 Accuracy comparison among the classification models using the GA selected wavelength.

Classifiers	Preprocessing	GA (selected wavelength)			AUC-ROC score	
		N	Training accuracy (%)	5-fold CV accuracy (%)		Test accuracy (%)
SVM	Raw	118	91.2	83.0±5.9	80.8	0.93
	Mean Normalized	122	94.0	93.4±2.8	89.7	0.98
	SNV	106	94.5	90.7±2.7	92.3	0.98
	MSC	138	92.9	89.6±4.1	60.7	0.86
	Baseline	101	93.4	89.0±3.5	84.6	0.95
RF	Raw	131	100	64.9±4.9	53.9	0.76
	Mean Normalized	121	100	89.5±4.3	87.2	0.97
	SNV	121	98.9	86.8±4	85.9	0.97
	MSC	120	100	88.4±2.8	85.9	0.96
	Baseline	124	100	75.9±5.1	68.0	0.86
LDA	Raw	135	100.0	97.2±1.8	100.0	1
	Mean Normalized	117	100.0	91.2±5.3	100.0	1
	SNV	122	100.0	83.5±2.9	100.0	1
	MSC	134	100.0	82.4±7.6	37.2	0.5
	Baseline	127	100.0	94.5±3.4	100.0	1
PLS-DA	Raw	120	85.7	85.7±4.0	85.9	0.95
	Mean Normalized	136	86.3	83.3±6.7	85.9	0.93
	SNV	112	87.9	84.6±5.8	85.9	0.94
	MSC	122	81.9	81.3±4.1	88.5	0.95
	Baseline	125	86.8	84.1±4.9	84.6	0.95
kNN	Raw	103	72.5	61.6±9.2	50.0	0.69
	Mean Normalized	118	87.9	83.0±6.0	83.3	0.94
	SNV	114	94.5	86.3±3.1	79.5	0.88
	MSC	114	89.6	85.2±3.6	84.6	0.95
	Baseline	120	82.4	59.9±4.8	69.2	0.81

GA: Genetic algorithm; CV: Cross-validation; N = no of selected wavelength; SVM: Support vector machine; RF: Random forest; LDA: Linear discriminant analysis; PLS-DA: Partial least squares discriminant analysis; kNN: k nearest neighbor; SNV: Standard normal variate; MSC: Multiplicative scattering correction; AUC-ROC: Area under the receiver operating characteristics curve

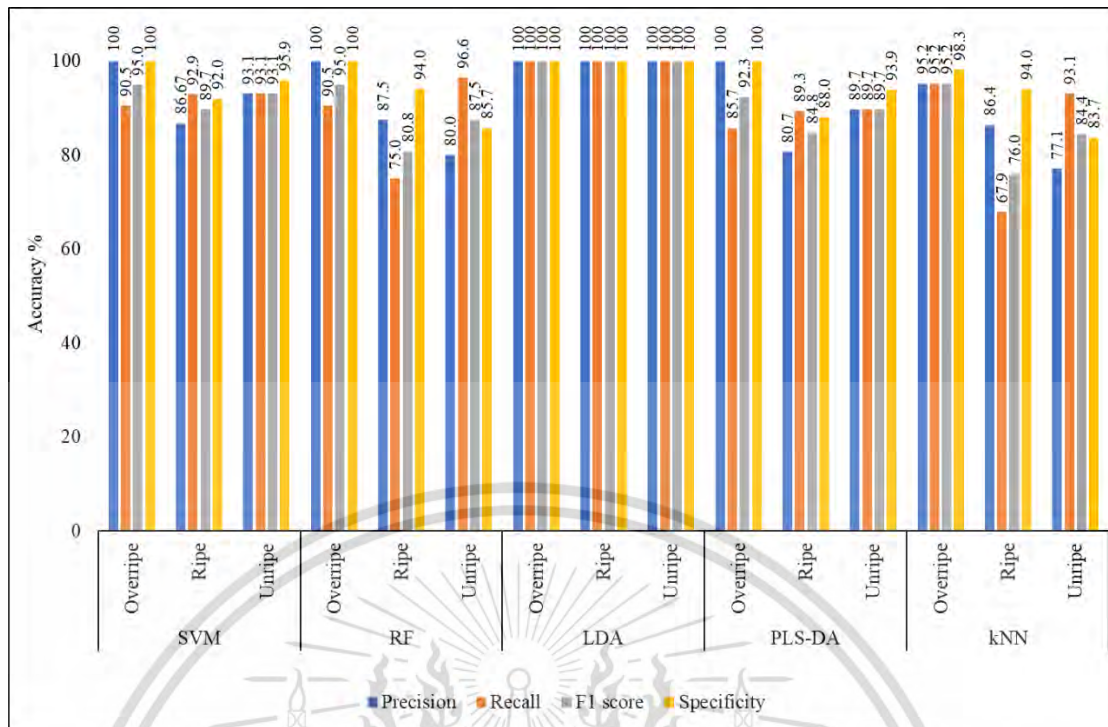


Figure 4.7 Precision, recall, and F1 score obtained for each ripening stage from the test set using the selected wavelength by the genetic algorithm.

4.3.2.3 PCA selected wavelength

Optimal wavelengths were selected from the loading weight of the first three PCs, as shown in Figure 4.8. The first three PCs for pulp explained variance were 99.9%. From the loading weight, a total of 11 wavelengths were selected, i.e., 903, 955, 971, 1052, 1072, 1140, 1205, 1345, 1358, 1391, and 1450 nm. In Figure 4.8, a small peak at 971 nm was observed with a relatively low loading weight, our analysis showed that the results were improved including the peak at 971 nm, since the peak represents the water band, which is important for ripeness classification based on DAA and for dry matter prediction, as reported by Saechua et al. (2021). The loading weight plot of durian pulp at 1205 nm, which represents the vibration band of water molecules, was explained by PC-3, and that at 1450 nm, which represents the vibration band of water and starch, was explained by PC-1 and PC-2. The other wavelengths also include C-H stretching and C-H deformation at 903 (900 nm), 1052 (1053 nm), and 1358 (1360). C-H molecular grouping is common in agricultural food and product analysis because the major constituents, such as starch, cellulose, protein, and oil/fats, are all rich in C-H molecular grouping, for example, CH₂ and CH₃ [54]. At 1391 nm, corresponding to 1395 nm, the loading weights of PC-1 and PC-2 were almost zero, and PC-3 showed the highest loading weight. The peak at 1395 nm represents CH₂, a combination of vibration

This material is reserved for educational use only, not allowed for commercial use.

Forbidden to modify the content, and cite the document when use.

due to C-H stretching + C-H deformation (Osborne et al., 1993). The wavelength 1140 (1142 nm) corresponds to the C-H str. second overtone of aromatic compounds (Osborne et al., 1993).

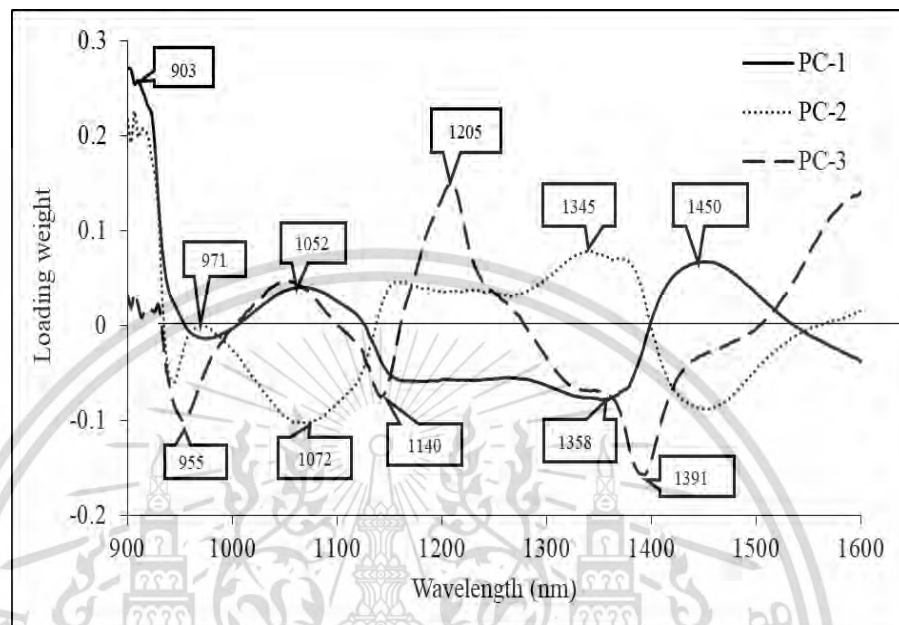


Figure 4.8 Loading weight plot of the first three principal components.

Table 4.5 shows the accuracy, precision, recall, specificity and F1 score obtained from the classifiers based on the selected 11 wavelengths from PCA. The highest test accuracy of 93.6% was attained by LDA among other classifiers. SVM, RF, PLS-DA, and kNN were able to attain a test accuracy greater than 80%. The precision, recall, specificity, and F1-score implied that the overripe pulp was classified more accurately from the ripe and unripe pulp. From the comparison of AUC-ROC score, all classifier models attained a value higher than 0.90. LDA model attained the highest value of 0.98 and the kNN model received the lowest score of 0.91. Full wavelength and selected wavelength by GA and PCA showed similar results in the confusion matrix. There was confusion between the classification of an unripe and ripe durian. The reasons for this misclassification are a similar spectral signature and non-significant biological changes obtained from the pulp of the unripe and ripe stages. Additionally, due to the small size of the test sample, the classification metrics are highly influenced even after single sample misclassification for each stage.

Overall, machine learning models for durian ripening stage classification based on spectral data provided good training and test accuracy. LDA classifier performance using raw and preprocessed spectra showed reliable results for the durian ripening

stage classification. LDA performs dimensionality reduction by mapping from a higher dimensional space to a lower dimensional space in such a way that most discriminant features are preserved during the transformation. LDA tries to find those vectors in the underlying space that can best discriminate among the classes with higher accuracy (Ye et al., 2009). Figure 4.9 shows the LDA score plot of the first two components illustrating the separation of three ripening stages. Using raw spectra from the HSI system with full wavelength, the first two LDA components explained the variance 62.6% and 37.4%, respectively. Similarly, using GA selected 135 key wavelengths two LDA components explained 71.5% and 28.5% variance to classify unripe, ripe and overripe durian pulp. The selected 11 wavelengths from PCA loading weight obtained by pretreated spectra with SNV were used to develop the LDA model. Figure 4.9 shows that the unripe and overripe samples were classified by LDA using PCA selected wavelength, however, the ripe samples were misclassified. Recently, Badaró et al. (Badaró et al., 2020) applied PCA and LDA to classify three groups of orange peel based on the pectin (lower, intermediate, and higher) content. LDA models developed using wavelength selected by PCA loading weight of pretreated NIR spectra provided the highest classification accuracy of 92.78% (Badaró et al., 2020). Discriminant analysis is used to classify observations into two or more different groups, clusters, and populations and it has been proved to be able to distinguish the maturity levels of fruits (Khojastehnazhand et al., 2019; Zhang et al., 2020). In comparison to other machine learning algorithms, LDA is one of the simple techniques with less training time. Therefore, in our research, we found that the LDA model was best suited for the ripeness classification of durian pulp using full wavelength and selected wavelengths.

Table 4.5 Classification metrics obtained from each classifier using the selected wavelength by PCA.

Classifiers (Optimal hyperparameters)	Accuracy (%)			Reference	Predicted			Precision (%)	Recall (%)	Specificity (%)	F1-Score	AUC-ROC Score
	Training	5-fold CV	Test		Overripe	Ripe	Unripe					
SVM (C=5; γ =0.5; kernel =polynomial order 5)	92.9	88.5±4.4	89.7	Overripe	18	3	0	100	85.7	100	92.3	0.97
				Ripe	0	25	3	83.3	89.3	90.0	86.2	
				Unripe	0	2	27	90.0	93.1	93.9	91.5	
RF (n_estimator=500; maximum_feature =5; maximum_depth=2; Criterion=Entropy)	90.1	88.5±3.2	80.8	Overripe	19	2	0	100	90.5	100	95.0	0.96
				Ripe	0	16	12	84.2	57.1	94.0	68.1	
				Unripe	0	1	28	70.0	96.6	75.5	81.2	
LDA	89.6	86.3±5.1	93.6	Overripe	21	0	0	100	100	100	100	0.98
				Ripe	0	24	4	96.0	85.7	98.0	90.6	
				Unripe	0	1	28	87.5	96.6	91.8	91.8	
PLS-DA	86.3	81.9±6.2	89.7	Overripe	20	1	0	100	95.2	100	97.6	0.95
				Ripe	0	23	5	88.5	82.1	94.0	85.2	
				Unripe	0	2	27	84.4	93.1	89.8	88.5	
kNN (n_neighbors = 5; metric = Euclidean; algorithm= ball_tree)	88.5	84.1±5.3	82.1	Overripe	19	2	0	95.0	90.5	98.2	92.7	0.91
				Ripe	1	21	6	75.0	75.0	96.0	75.0	
				Unripe	0	5	24	80.0	82.8	87.8	81.4	

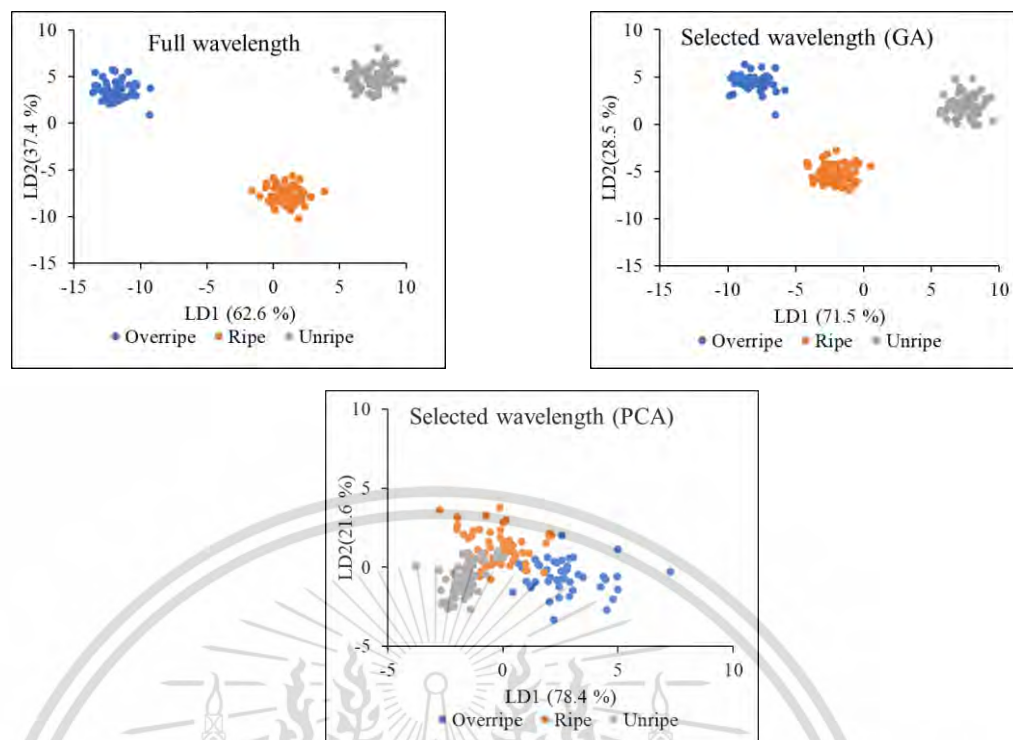


Figure 4.9 Linear discriminant analysis score plot showing two components (LD1 and LD2) with explained variance to classify three ripening stages using full and selected wavelength by genetic algorithm and principal component analysis.

4.3.3 Classification model performance for intact fruit

Table 4.6 shows the performance of the classifiers for the ripeness classification of durian intact fruit and Table 4.7 shows the performance of classifiers based on the wavelength selected by PCA. The 5-fold CV accuracy for the classification of intact fruit was obtained in the range of 82.4 to 100 % by different classifiers using full wavelength. LDA applied on the pretreated SNV pretreated spectra classified the ripening stages by 100% accuracy. The LDA classifier obtained the highest overall accuracy and 5-fold cross-validation accuracy of 100% for intact fruit classification using the full wavelength. The kNN performance was the least accurate among the classifiers. Similarly, using the 11 selected wavelength the 5-fold cross validation classification accuracy of 100% was attained using LDA and PLS-DA. However, classification model by selected wavelength showed the best training and validation accuracy of 100% for intact fruit by LDA. However, due to lower number of samples the robustness of these model has yet to be determined.

Table 4.6 Performance of each classifier for ripeness classification of durian intact fruit.

Classifiers	Pretreatment	Training Accuracy (%)	5-fold CV accuracy (%)	Ripeness ^c	Confusion matrix		
					Overripe	Ripe	Unripe
SVM ^a	SNV	96.0	94.1	Overripe	9	1	0
				Ripe	0	20	0
				Unripe	0	1	19
RF ^a	MSC	100	93.8	Overripe	10	0	0
				Ripe	0	20	0
				Unripe	0	0	20
LDA ^a	SNV	100	100	Overripe	10	0	0
				Ripe	0	20	0
				Unripe	0	0	20
PLS-DA ^a	Raw	84	93.8	Overripe	6	4	0
				Ripe	0	17	3
				Unripe	0	1	19
kNN ^a	SNV	90.0	82.4	Overripe	10	0	0
				Ripe	0	20	0
				Unripe	1	4	15

SVM: Support vector machine; RF: Random forest; LDA: Linear discriminant analysis; PLS-DA: Partial least squares discriminant analysis; kNN: k nearest neighbor; SNV: Standard normal variate; MSC: Multiplicative scattering correction

Table 4.7 Performance of classifiers using PCA selected wavelengths for ripeness classification of durian intact fruit.

Classifiers	Pretreatment	Training Accuracy (%)	5-fold CV accuracy	Confusion matrix			
				Ripeness ^c	Overripe	Ripe	Unripe
SVM	Mean Normalization	96.0	94.1	Overripe	10	0	0
				Ripe	0	20	0
				Unripe	0	2	18
RF	SNV	98.0	93.8	Overripe	10	0	0
				Ripe	0	20	0
				Unripe	0	1	19
LDA	Mean normalized	100	100	Overripe	10	0	0
				Ripe	0	20	0
				Unripe	0	0	20
PLS-DA	MSC	92	100	Overripe	8	2	0
				Ripe	1	18	1
				Unripe	0	0	20
kNN	Mean normalized	84.0	88.2	Overripe	8	2	0
				Ripe	0	20	0
				Unripe	0	6	14

SVM: Support vector machine; RF: Random forest; LDA: Linear discriminant analysis; PLS-DA: Partial least squares discriminant analysis; kNN: k nearest neighbor; SNV: Standard normal variate; MSC: Multiplicative scattering correction

The maturity classification of durian pulp has not been carried out previously, but research has been performed on intact fruit. Timkhum and Terdwongworakul (2012) established the PLS-DA classification model using absorbance spectra from the visible spectroscopy of spines, and transformation by the standard normal variate achieved the best accuracy of classification (94.7%) into four maturity classes ranging from 113 to 134 DAA (Timkhum and Terdwongworakul, 2012). However, the best classification result does not account for immature samples from 99-106 DAA, and the whole wavelength range of 350-750 nm was used by Timkhum and Terdwongworakul (2012)(Timkhum and Terdwongworakul, 2012). Electrical impedance spectroscopy was used to develop the model for dry matter prediction and maturity classification grouped

by the DAA of durian (Kuson and Terdwongworakul, 2013). The results show that the selected impedance parameters using a stepwise regression could be used to classify durian samples into an immature class and mature class with lower accuracy of 83.3%. Phothisonothai (2010) proposed maturity classification by using fractal analysis, which was carried out by automatic knocking, and the knocking sound was analyzed in terms of the fractal dimension (Phothisonothai, 2010). The proposed method achieves an average accuracy rate of 89.94% and 88.20% in classifying immature and mature individuals, respectively, among Monthong durians weighing 3.5-4.0 kg and 4.0-4.5 kg (Phothisonothai, 2010). The non-uniform shape and the thorn-covered peel can cause errors in the sound recording process (Phothisonothai, 2010). The literature has shown that many nondestructive and destructive methods have been applied for the maturity classification of durian for decades. However, focus has been more on maturity indices such as dry matter, color constituents, and total soluble solids to correlate with the maturity of durian. In this research, we are more focused on high-resolution NIR-HSI applications for durian pulp ripening stage classification by spectral signatures. Unlike NIR spectroscopy, which provides information on a sample by scanning at a single point or single line if integrated into the conveying system, NIR-HSI provides information from each pixel within the AOI. The results from our research show the high potential of the NIR-HSI system combined with machine learning for ripening stage classification based on the DAA of durian. Feature selection by GA and PCA to identify the optimum wavelengths on the HSI dataset provided the 135 and 11 important wavelengths, respectively. And the selected wavelengths were able to classify the ripeness of durian pulp by LDA with test accuracies of 100% and 93.6%, respectively. The highest test accuracy was attained with the GA selected wavelength combined with LDA. The classification model using 11 selected wavelengths from PCA also provided good and comparable accuracy. The results shows that the wavelength selected by PCA includes the bands that are important for ripeness classification. Therefore, these optimum 11 wavelengths could be used for the further development of a multispectral imaging system. Multispectral imaging can produce up to dozens of bands by combining different filters for image acquisition (Morales et al., 2020). The use of a multispectral imaging system, which is low cost and portable compared to NIR-HSI could be an easier and more convenient method for farmers and durian packaging firms to use in real-time situations.

In this research, DAA has been used for the ripening stage labeling of durian pulp. The proposed experimental design included the samples from 99-135 DAA and the fruits were tagged in the day of flower bloom under the supervision of the horticulturist. The developed approach can predict the DAA range and classify the

ripening stage, however, it would be more challenging for the developed classification models to predict the ripening stage if the harvested fruits fall outside the selected DAA range. The classification results show that the overripe samples are classified accurately, however, there are still some confusions to classify the unripe and ripe samples. Nevertheless, this classification error can be minimized by increasing the number of samples for model development such that the inter- and intra-class variability of all ripening stage will be covered. Furthermore, the proper supervision of the horticulturist and/or farmers to track the flowering day and tag the fruit with the correct DAA will also be equally important. Though the sample collection could be time consuming and tedious, it could help for reliable model development capable of classifying the ripening stage within a few seconds. This research focused only on the Monthong variety of durian, however, the ripening stages and commercial harvesting DAA of other variety of durian could be different. Therefore, before sample collection, a proper study on the ripening behavior and DAA specific to the cultivar must be conducted.

4.3.4 PLSR model and spatial distribution of DM

The total number of samples used for DM prediction was 90, among which 63 samples were for training and 27 samples were for the test set. The minimum, maximum, average, and standard deviation of DM for the training and test sets are 18.24%, 42.16%, 36.19%, and 4.76% and 26.78%, 40.72%, 36.47%, and 3.57%, respectively. The PLSR model was developed for DM prediction of the durian pulp, and the results are presented for each preprocessing technique in Table 4.8. Among raw spectra and all preprocessed spectra, SNV showed the best result for full wavelength, selected wavelength by GA, and PCA. The coefficients of determination (R^2) for the training set, CV, and test set were 0.863, 0.786, and 0.878, respectively, using 93 selected wavelengths by GA. The selected wavelengths by GA are shown in Figure 4.10. Different wavelengths from 900 to 938 nm represent the bond vibration due to the C-H stretch third overtone of CH_3 (900 nm), protein (910 nm), CH_2 (913 and 938 nm), and oil (928 nm) (Osborne et al., 1993). The wavelength range from 948-965 nm includes a shifted water absorption valley at 970 nm. The wavelength at 984 nm corresponds to 990 nm, which represents the bond vibration due to the O-H stretch second overtone of starch. The range from 1010-1036 nm includes the bond vibration of protein and oil at 1020 and 1037 nm. The wavelength range from 1211-1390 nm represents the bond vibration due to the C-H stretch second overtone and C-H combination. Similarly, the wavelength ranges from 1411-1453, 1502-1535 and 1580-1590 nm include the important wavelengths of the C-H combination bond representing CH_2 at 1415 nm, O-H stretch first overtone representing sucrose and starch at 1440 nm, and starch and water at 1450

nm, and O-H stretch first overtone of starch and glucose at 1580 nm, respectively. Some PCA selected wavelengths, such as 955, 1345, and 1450 nm, were included in the 93 selected wavelengths by GA. Similarly, using the selected 11 wavelengths by PCA, the R^2 values for the training set, CV, and test set obtained were 0.823, 0.731, and 0.827, respectively. The comparison between the PLSR model from the full wavelength and that from the selected wavelength by GA and PCA shows that the best result was attained by GA with 93 selected wavelengths followed by PCA with 11 selected wavelengths. PLSR model comparison with respect to R^2_p , RMSEP, and RPD difference shows that the GA selected wavelengths can provide marginally higher accuracy, but it is more comparable with the 11 PCA selected wavelengths. The RMSEP obtained from the PLSR model using 11 wavelengths is 1.45%, which is lower and comparable to the results from Onsawai et al. (Onsawai et al., 2021) (RMSEP = 3.60%) and Somton et al. (Somton et al., 2015) (RMSEP = 1.65%).

The spatial distribution of DM on pulp harvested at different DAAs from the PLSR model obtained by full wavelength, GA selected wavelengths, and PCA is shown in Figure 4.11. The first row shows the pseudocolor representation of the sample with the RGB band combination (Red = 961.93 nm, Green = 1075.67 nm, and Blue = 1450.18 nm). The DM distribution on each pulp varied from 10% to 50% at different ripening stages depending on the DAA of the samples. Each DAA stage showed DM variation within the pulp and represented the increment in the DM gradually until 120 DAA. The root mean square error (RMSE) calculated for the observed and predicted mean DM was 1.89%, 1.48%, and 3.02% from the full wavelength, selected wavelength (GA), and selected wavelength (PCA), respectively. As seen in Figure 4.11, some parts showed a line with cracks on the surface, which occurred during pulp extraction from the hard outer surface. The pixels representing the cracked portion were excluded as outliers. The mean observed and predicted DMs for each sample are shown in Figure 4.11. The box plot in Figure 4.12 shows the mean DM predicted by the optimum PLSR model developed by the full wavelength and selected wavelengths from GA and PCA of durian pulp at different DAAs. The box plot shows that the DM is increased from 99 to 120 DAA.

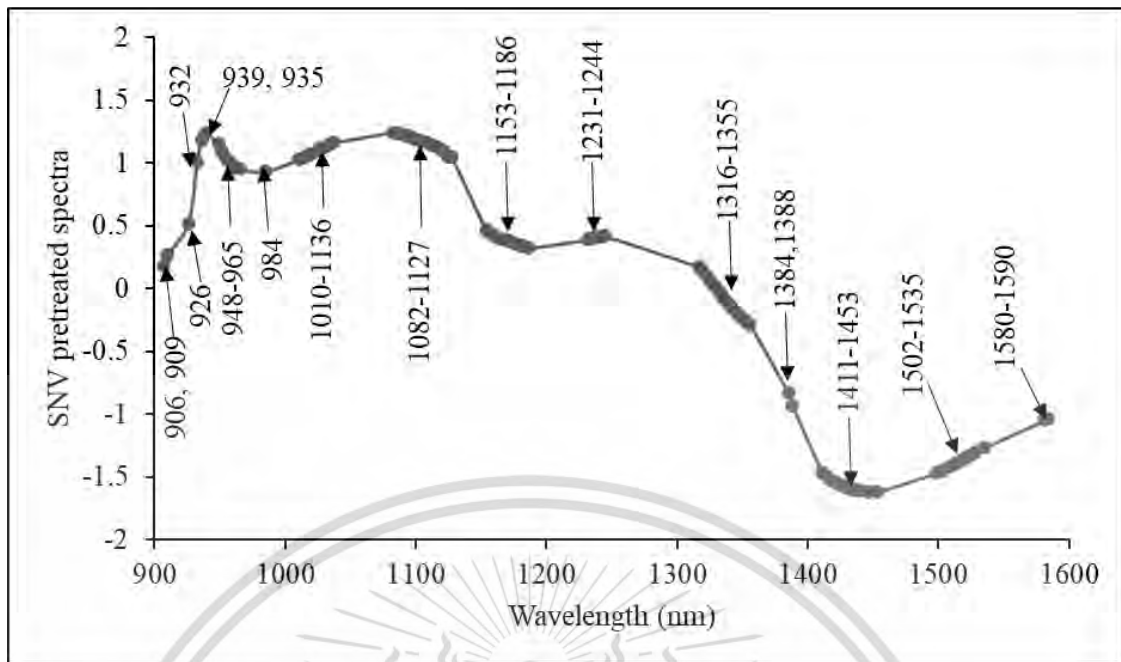


Figure 4.10 Average full wavelength spectra pretreated by standard normal variate and 93 selected wavelengths by genetic algorithm.

Table 4.8 PLSR model results obtained using raw and preprocessed spectra from the full wavelength and selected wavelengths by genetic algorithm and principal component analysis.

Preprocessing		N	LV's	Training set		5-Fold CV		Test set			
				R^2_c	RMSEC (%)	R^2_{cv}	RMSECV	R^2_p (%)	RMSEP	RPD (%)	Bias (%)
Raw	Full	216	5	0.834	1.92	73.49	2.43	0.778	1.65	2.12	0.09
	GA	99	5	0.857	1.79	79.41	2.14	0.813	1.51	2.32	-0.18
	PCA	11	5	0.823	1.99	72.03	2.5	0.780	1.57	2.23	-0.07
Mean Normalized	Full	216	4	0.833	1.93	75.54	2.34	0.798	1.57	2.23	0.25
	GA	95	4	0.845	1.98	77.11	2.26	0.879	1.22	2.87	0.05
	PCA	11	5	0.859	1.96	75.48	2.34	0.813	1.51	2.32	-0.08
SNV	Full	216	4	0.874	1.68	77.19	2.26	0.804	1.55	2.26	-0.39
	GA	93	4	0.863	1.75	78.62	2.18	0.878	1.22	2.87	-0.27
	PCA	11	4	0.823	1.99	73.1	2.45	0.828	1.45	2.45	-0.13
MSC	Full	216	4	0.874	1.68	77.19	2.26	0.802	1.56	2.25	-0.39
	GA	114	5	0.882	1.62	81.74	2.02	0.881	1.21	2.9	0.38
	PCA	11	4	0.824	1.98	73.41	2.44	0.121	3.28	1.07	-2.95
Baseline	Full	216	5	0.855	1.8	75.33	2.35	0.806	1.54	2.28	-0.41
	GA	100	4	0.847	1.85	77.9	2.22	0.844	1.38	2.54	-0.18
	PCA	11	5	0.836	1.91	74.08	2.41	0.814	1.51	2.32	-0.37

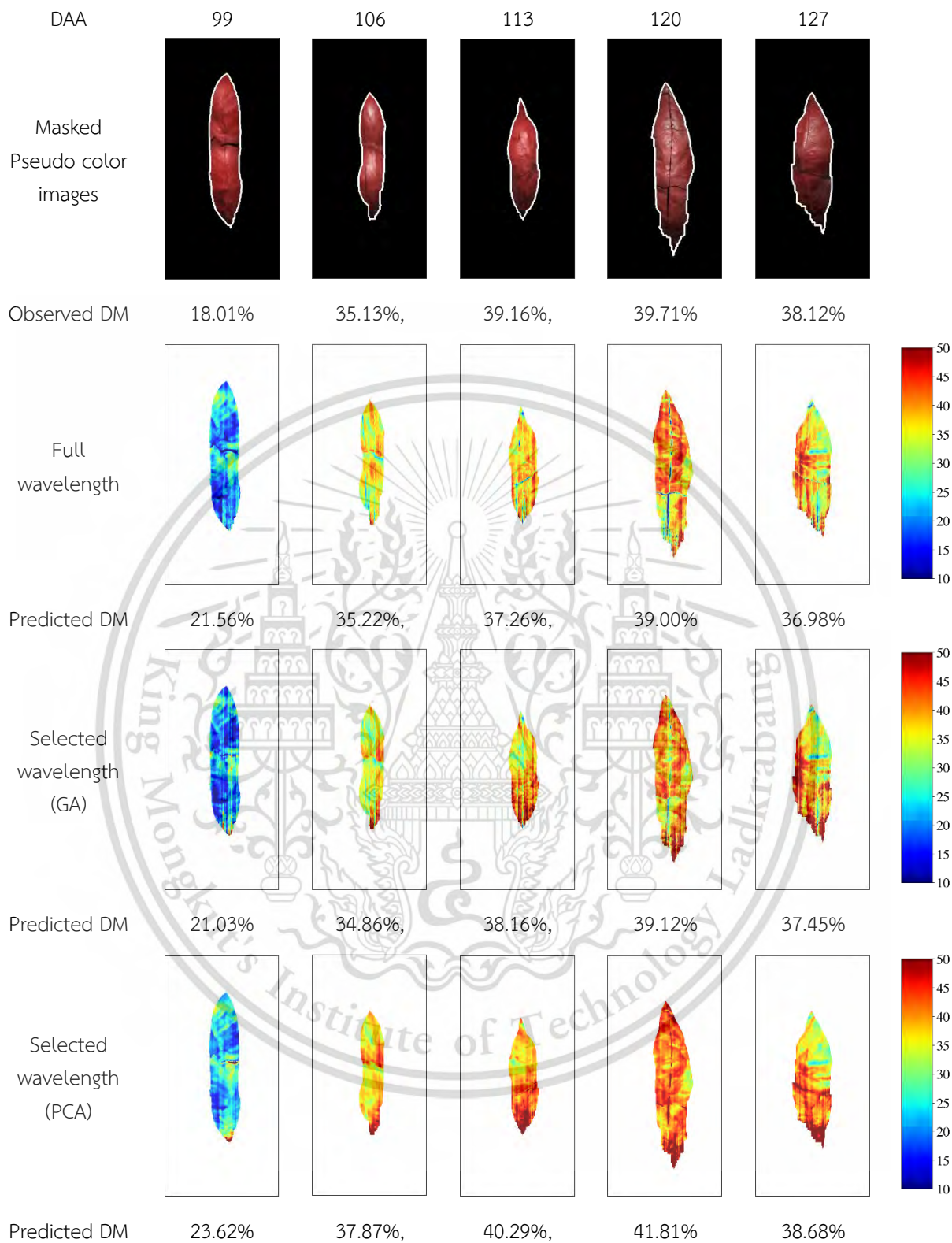


Figure 4.11 Dry matter spatial distribution from the optimum partial least squares regression model developed using the full wavelength and selected wavelengths by genetic algorithm and principal component analysis.

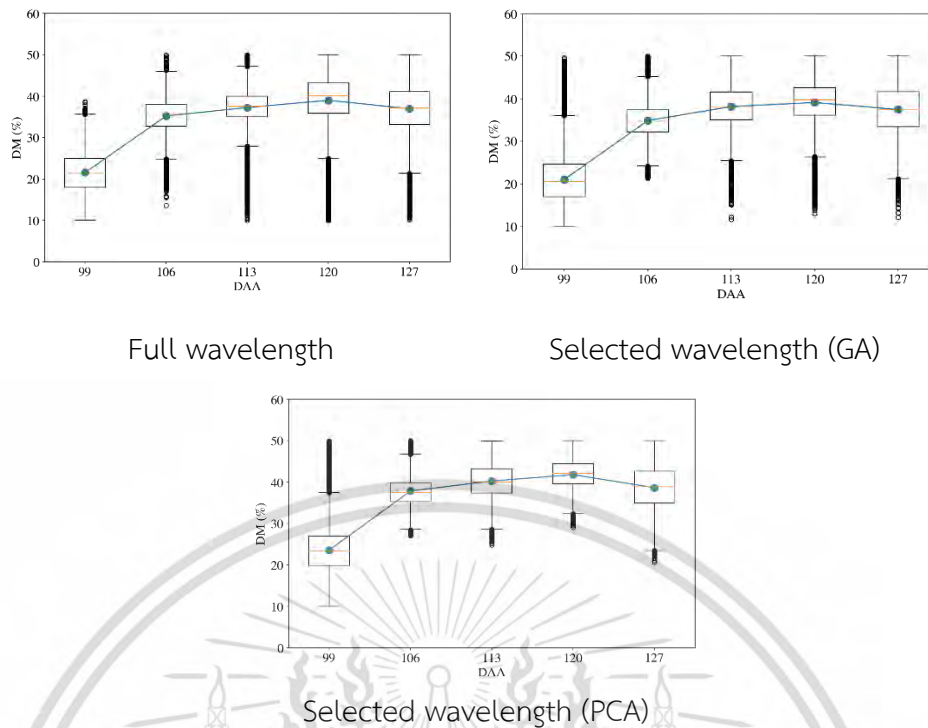


Figure 4.12 Box plot representing a change in dry matter predicted by the optimum partial least squares regression model developed using full and selected wavelengths from 99-127 days after anthesis of the durian pulps.

4.4..Conclusion

This research aims to investigate the potential of the NIR-HSI system for developing a ripening stage classification model based on DAA using SVM, RF, LDA, PLS-DA, and kNN and a PLSR model for DM prediction of durian pulp. A comparison was made according to the classification metrics between the classifiers using full wavelengths (900-1600 nm) and selected wavelengths by GA and PCA. The major findings from this research are:

1. The ripening stage classification accuracies were in the range of 37.2%-100%. LDA models based on full and selected wavelength successfully classified the durian pulp ripeness with 100% test accuracy.
2. The SVM, RF, and PLS-DA provided a fair classification model, however, the kNN classifier model showed low precision, recall, specificity, and F1-score for the unripe and ripe stage.
3. Classification models using full and selected wavelength by PCA showed the CV accuracy of 100% for intact fruit by LDA.

4. The PLSR model for DM prediction provided R^2_p of 0.878, 0.828, and 0.804, respectively, and RMSEP of 1.22%, 1.45%, and 1.55%, respectively using the GA selected 93 wavelengths, PCA selected 11 wavelengths and full wavelength.
5. The spatial distribution of DM from the NIR-HSI prediction map justified the higher accuracy of the PLSR model developed using the average spectra compared to traditional NIR system. The DM prediction map showed the spatial variability within a durian pulp and gradual changes of DM over the ripening stages.
6. The results showed that 11 optimum selected wavelengths: 903, 955, 971, 1052, 1072, 1140, 1205, 1345, 1358, 1391, and 1450 nm can be used for both the classification of ripening stages and DM prediction in durian pulp.

The NIR-HSI system combined with machine learning and wavelength selection successfully classify the ripening stage of durian intact fruit and pulp, and predicted the DM of durian pulp. This approach can improve the durian pulp grading capabilities in the large packaging firms with respect to the ripening stage and DM content. Furthermore, finding the key wavelengths or features that can classify the ripeness stage of pulp and intact fruit and predict DM gives the advantages of developing a low-cost, rapid, and effective multispectral imaging system compared to the NIR-HSI system. The future work will involve the development of the robust model by adding samples from different years and exploration of the deep learning techniques for the wavelength selection and model development.

Chapter 5

Physicochemical properties prediction and spatial mapping of durian pulp C.V Monthong for quality evaluation using near-infrared hyperspectral imaging

This chapter includes the physicochemical properties of dry matter (DM), total soluble solids (TSS), and fat content (FC) prediction of durian pulp using a near-infrared hyperspectral imaging (NIR-HSI) system. Partial least squares regression (PLSR), support vector machine (SVM), random forest (RF), and 1-D convolution neural network (CNN) models: custom, U-Net, and VGG19 models were developed to predict DM, TSS, and FC of durian pulp. Feature wavelengths were selected using a genetic algorithm (GA) and successive projection algorithm (SPA). The selected wavelengths were then validated based on the algorithms for regression model development. The results showed that the pushbroom NIR-HSI system achieved promising results for the estimation of DM, TSS, and FC in durian pulp. This research identified the featured wavelengths which can be used in the future to develop a portable and reliable HSI or multispectral system to be installed at the durian packaging firms for quality inspection and grading.

* This chapter is under preparation to submit to Information processing in Agriculture: Sharma, S., Terdwongworakul, A., Phetpan, K., K.C. S., Kshetri, T.B., Sirisomboon, P. 2022. “Physicochemical properties prediction and spatial mapping of durian pulp C.V Monthong for quality evaluation using near-infrared hyperspectral imaging”

This material is reserved for educational use only, not allowed for commercial use.

Forbidden to modify the content, and cite the document when use.

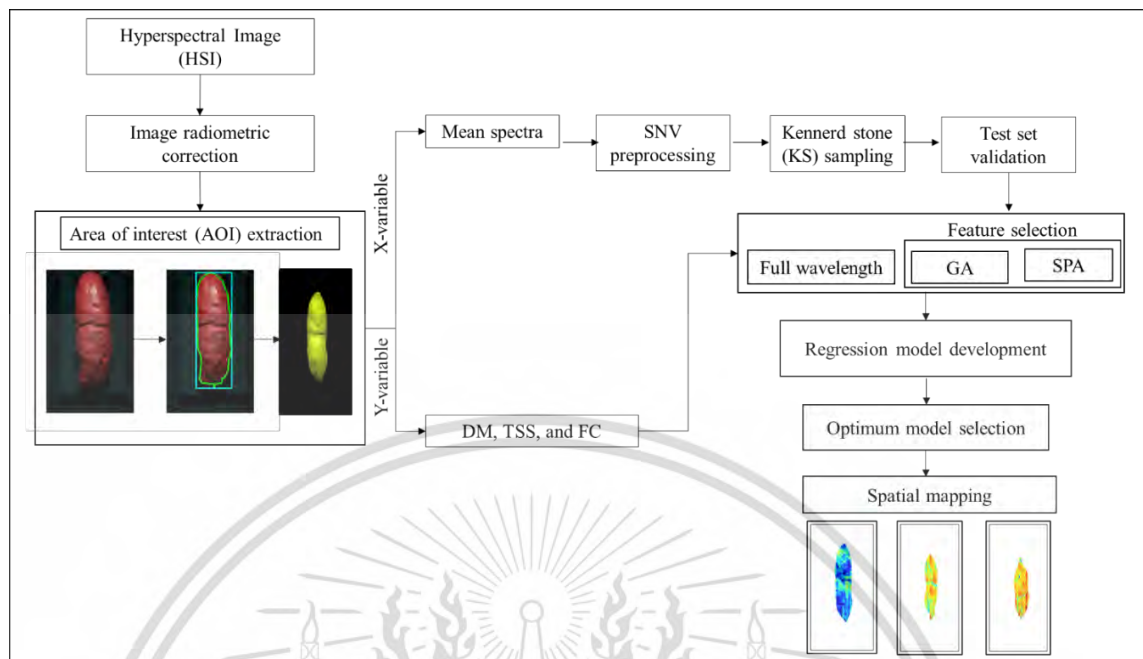


Figure. 5.1 Flowchart demonstrating the methodology used for the regression model development and spatial mapping.

5.1 Introduction

Durian is known as the “King of Fruit” in Southeast Asian countries because of its peculiar taste, appearance, and smell. Thailand, Malaysia, and Indonesia are the top three commercial durian producers and exporters followed by the Philippines and others, with over 1.6 million tons of production globally per year (Zhao et al., 2017; Liu et al., 2020). According to the statistics, from January 2021 to 2022, 52.8 million USD of fresh durian was exported from Thailand (Thai Customs, n.d.). Durian is a climacteric fruit therefore, it is available only in specific periods between May and August. The fruit starts to mature in April after the rainfall and continues until September. Still, the production depends heavily on the type of monsoon in Thailand’s northeast and southeast region (Mohd Ali et al., 2020). Fresh durian and processed products are exported from Thailand globally. Customer preference for durian purchasing depends on the ripeness, appearance, and quality in domestic and international markets. The fruits are harvested and transported professionally to the packaging house. The hard rind and thrones covering the fruit are difficult to cut through without guidance, therefore customer prefers the single or double fresh-cut durian pulp wrapped properly in a transparent film in the market. The peeling and wrapping process is done in the

processing house. Several improvements have been made and are ongoing for predicting the quality index of fresh-cut durians. Nowadays, sensors in the processing line for detecting the quality and ripeness of durian is in high demand as it prevents loss and damage for both farmers and packaging firms.

During the ripening process, the fruit undergoes several internal changes, and thus these physicochemical parameters need to be monitored. The taste and appearance of durian pulp are highly correlated to physicochemical properties such as dry matter (DM), total soluble solids (TSS), and fat content (FC). Visible or near-infrared (NIR) spectroscopy has been widely implemented to predict DM (Somton et al., 2015), and TSS (Onsawai et al., 2021). The NIR spectroscopic technique studies the spectral properties of the samples that are subjected to electromagnetic radiation between 780 and 2500 nm (Pullanagari & Li, 2020). When the NIR radiation hits the sample, the vibrational energy of the chemical bonds such as C-H, N-H, O-H, and O-H changes in forms of stretching and bending (Marten et al., 1984). This change in energy corresponds to specific absorption bands in the NIR region and is affected by the different chemical groups present in the samples. Therefore, each part and location of the fruit sample can correspond differently.

Over the past 15 years, hyperspectral imaging (HSI) has emerged as a new and advanced technology that integrates the significant features of imaging and spectroscopy, thus enabling the acquisition of both spectral and spatial information from an object simultaneously (Lu et al., 2020). HSI allows visualizing the changes in these internal attributes by spatial mapping which is the major advantage of using this system and can be used to analyze and map the distribution of the internal attributes throughout the sample (Du & Sun, 2004). This technology showed promising results for non-destructive sensing of multiple quality attributes of apple fruit (Ma et al., 2017; Zhang et al., 2019), mango (Rungpichayapichet et al., 2017), pears (Fan et al., 2015), strawberry (ElMasry et al., 2012), banana (Rajkumar et al., 2012), and peach (Haiyan Cen, Renfu Lu, Fernando A. Mendoza, 2011). It has been used for the defect and bruise detection of nectarines (Munera et al., 2019) and apples (Lu, 2003). TSS, DM, and FC are important quality attributes of durian pulp. Recent studies have also shown the feasibility of HSI in the spatial mapping of the internal quality as TSS and firmness of blueberries (Leiva-Valenzuela et al., 2013) and plums (Li et al., 2018a). The reflectance mode of image acquisition is widely used for analyzing fruits and vegetables in a HSI system configuration (Gowen et al., 2007; Ravikanth et al., 2017) due to its ease of use (Pullanagari & Li, 2020). According to Su & Sun (2018), flexible and customizable options of the Number and resolution of the spectral wavebands are available from the

manufacturer of the HSI systems. Therefore, the effective wavelength selection techniques can be Na high advantage on HSI data to select the Number of bands to construct the system at an affordable cost.

Several regression algorithms have been developed for analyzing the HSI information. Partial least squares regression (PLSR) has been applied widely for the spectroscopic data to predict the DM, color, SSC, and textural parameters of several fruits including durian (Onsawai et al., 2020). Many advanced non-linear machine learning methods have been introduced with the development of chemometrics methods. Support vector machine (SVM), random forest (RF), artificial neural network (ANN), and convolution neural network (CNN) are among some of the powerful algorithms that show an advantage over linear methods. Sharma et al. (2021) showed the result of the ripeness classification of durian pulp by comparing the performance of several machine learning algorithms. Also, deep learning architectures are widely used in the spectroscopic and imaging datasets. Garillos-Manliguez & Chiang (2021) suggested a novel non-destructive and multimodal classification using deep convolutional neural networks that estimate fruit maturity by feature concatenation of data acquired from two imaging modes: visible-light and HSI imaging systems. The performance of seven CNN pretrained models such as ResNet101, ResNet50, ResNet18, VGG19, VGG16, GoogleNet and AlexNet were compared for the maturity classification of papaya by Behera et al., 2021. Each algorithm has the unique feature, characteristic, advantages, and disadvantages. Several research indicates different machine learning and deep learning algorithms have the potential to predict or classify the parameters of fruits and vegetables. Such state of the art has not been applied for the durian using the HSI dataset. Therefore, the comparative study must be done to find the gaps and uncertainty of these modern algorithms and the optimal algorithm that can be applied for the physicochemical properties' prediction of durian pulp.

Therefore, the aims of this research were (I) to investigate the potential of near-infrared hyperspectral imaging (NIR-HSI) system for predicting DM, TSS, and FC of durian pulp, (II) to identify the featured wavelengths from the HSI data using successive projection algorithm (SPA) and genetic algorithm (GA), (III) to compare the prediction results obtained from the advanced machine learning regression models using full and selected wavelengths, and (IV) to visualize the change in the physicochemical properties according to the ripening level by spatial mapping.

5.2 Materials and methods

5.2.1 Sample preparation

This material is reserved for educational use only, not allowed for commercial use.

Forbidden to modify the content, and cite the document when use.

Durian fruits of the ‘Monthong’ cultivar were collected from the commercial orchards in two regions of Thailand, including the eastern region at Trat and Rayong province, and the southern region at Chumphon Nakhon Si Thammarat province. They were harvested at different ripeness levels randomly from 99 days after anthesis (DAA) to 127 DAA. The fruit classification in terms of ripeness level was the same as the methodology used by Sharma et al., 2021. The fruits were kept in a room at a temperature of 25 ± 2 °C before and during the experiment. The intact fruit was peeled out to extract the pulp with minimal damage (Sharma et al., 2021). 362 durian pulps were obtained and used as the samples in this research.

5.2.2 NIR-HSI image acquisition and radiometric correction

In this research, a pushbroom NIR-HSI system equipped with an imaging spectrograph (Inspector N17E Specim, Spectral Imaging Ltd., Oulu, Finland) and comprised of a linear array of 320 CCD detectors (Xeva 992, Xenics Infrared Solutions, Belgium) was used for image acquisition. The system consists of two 500 W tungsten–halogen light sources (Lowe Light Inc., New York, United States of America) adjusted at an angle of 45° and delivering uniform lighting in the field of view (FOV). Specim’s LUMO Software Suite (Spectral Imaging Ltd., Oulu, Finland) HSI system controlling software was installed on the computer. One HSI image acquired by the system consists of 256 spectral bands (bit depth of 12) between 900 and 1600 nm with a spectral resolution of 3.2 nm. Each image (band) contains 320 pixels in the x-direction (width) and n pixels (depending upon the length of the pulp) in the y-direction (length) (Sharma et al., 2021). Each spectral band and image are stored in band interleaved by line (BIL) format in the system memory. The white reference and dark reference were acquired simultaneously for each image for radiometric correction. To capture the white reference, a spectralon with a relative reflectance of 99% was used, and the dark reference image was acquired by the system automatically by closing the camera shutter. The focal distance from the sensor to the pulp was approximately 30 cm, resulting in a spatial resolution of 30 μ m per pixel, and the optimized integration time was set to 6 ms (Sharma et al., 2021). Samples were scanned on a translation stage at the speed of 10 mm s⁻¹. After image acquisition, the raw hypercube was corrected using equation (5.1) to reduce the noise due to the instruments background spectral response and the camera’s dark current (Gowen et al., 2007).

$$R = \frac{I_o - D}{W - D} \quad (5.1)$$

where R is the relative reflectance image, I_0 is the raw reflectance image, D is the dark reference image, and W is the white reference image.

5.2.3 Extraction of the area of interest (AOI)

The area of interest was extracted using the methodology used in (Sharma et al., 2021). The purpose of this step is to extract durian pulp from the background. The normalized difference spectral index (NSDI) was used to extract the AOI of pulp. Binary thresholding and morphological filters (erosion and dilation) were applied to extract the biggest contour of the pulp. The mean spectra of the pulp were then extracted as the mean value of every pixel at different wavelengths within the extracted boundary (Sharma et al., 2021).

5.2.4 Physicochemical properties measurement

After the image acquisition, the samples were simultaneously transferred for the DM, TSS, and FC determination.

5.2.4.1 DM content

The oven-drying method was used for DM content measurement. Approximately 5 ± 0.05 g samples were cut, chopped finely, and placed in the aluminum moisture can with a diameter and height of 5 cm and 3 cm, respectively. The initial weight of the samples was measured using the electronic balance with 0.0001 resolution (Mettler Toledo Model- JS1203C, Switzerland). After initial weight measurement, the aluminum can with durian pulp sample was placed inside the hot air oven (FDA240, Binder, Tuttlingen, Germany) at 60°C . Weight was recorded after 24 h, placed in the oven, and reweighted every 3 h again until a constant weight (less than 0.003) was recorded. Two replicate measurements were performed for each sample and DM was calculated as an average of two measurement values. Equation (5.2) was used for the DM calculation..

$$\text{DM} = 100 \times \frac{W_2}{W_1} \quad (5.2)$$

where, W_1 is the initial weight and W_2 is the final weight.

5.2.4.2 Total soluble solids (TSS)

TSS was determined by two reference methods. The first method was using a pen refractometer. The SSC of each sample was measured longitudinally throughout the scanning area using a Digital Pen Refractometer (PAL-1 S/No L218454, Atago, Japan), and the distilled water was used to clean the refractometer. Three repeat

measurements at each part (head, middle, and bottom) in the longitudinal axis of the pulp were completed, and the average TSS was recorded as the reference value. TSS of 90 durian pulps were analyzed using this method.

The second method was using the digital refractometer. Durian 5 g was weighed and mixed with distilled water 15 g thorough spinning and refrigerated centrifuged. Thereafter the clear part was filtered and poured into the digital refractometer (Atago, Japan). The reading was noted and the TSS was calculated from the °Brix using equation (5.3). TSS of 270 durian pulps were analyzed using this method.

$$\text{TSS (\%)} = \text{°Brix} \times 4 \quad (5.3)$$

Distilled water was used for the zero setting of the refractometer in both methods, which could be used alternatively for reference test of TSS for future samples.

5.2.4.3 Fat content (FC)

For FC analysis, a 200g sample was sent to the Institution of Nutrition, Mahidol University. For the analysis, AOAC 2016.948.15, 945.16 methods were used. Total fat was measured in percent of 100 gm a sample.

5.2.5 Data analysis

Changes in the physicochemical properties of durian pulp at different harvest dates (DAA) were observed before the modeling steps. The mean comparison was done to observe the changes by one-way ANOVA using SPSS 28.0.1.1.

5.2.5.1. Splitting and preprocessing the dataset

Total samples were divided into a training set and test set in a ratio of 80:20 by Kennard-Stone (KS) sampling. KS sampling initially finds two samples in the dataset with the largest Euclidean distance, later, the points are selected in such a way it maximizes the Euclidean distance from the former two samples (Saporo et al., 2012). Finally, for a given data set and the ratio that is to be separated into the training set samples are selected to smoothly fill the data space and the remaining samples are separated as a test set (Saporo et al., 2012). KS sampling avoids extrapolation when a model developed from the training set is applied to the test set. The stratified k-fold CV with k = 5 was applied where the training set (80%) was split into five groups, and each group was used to evaluate the model fitted on the other 4/5 of the training dataset (Pedregosa et al., 2011). The mean accuracy and the standard deviation value were

computed from the 5-fold cross validation (CV) results. Finally, the model with optimal hyperparameters was evaluated on the test dataset (20%). The test set validation approach was used for model development and validation. The raw spectra were then pretreated by standard normal variate (SNV) preprocessing to minimize the baseline shift due to the scattering effect and change in optical path length. SNV normalizes the spectra by subtracting each spectrum by its average intensity value, and each spectrum is divided by the standard deviation (Sandak et al., 2016). Each spectrum will have an average of 0 and a standard deviation of 1 after SNV (Sandak et al., 2016).

5.2.5.2 Feature selection

This research applied the successive projection algorithm (SPA) and the genetic algorithm (GA) for the feature selection. In SPA, candidate subsets of variables with minimum collinearity are generated by the projection procedure in a vector subspace. These subsets of wavelengths are evaluated by the value of root mean square error (RMSE) obtained from the validation set of multiple linear regression calibration, and then as a final step, the uninformative variables are removed by a variable elimination (SPA-elimination) procedure without significant loss of prediction capability, although this elimination step is optional (Fan et al., 2015; D. Liu et al., 2014). More explanation on the SPA algorithm is provided by Brown et al., 2009. The models were developed using the wavelength selected with and without elimination. For GA, it searches for an optimal value in parallel with a multi-point search focusing on the most promising parts of the solution space and, consequently, near-optimal value can be rapidly and efficiently sought from a very large search space procedure by simulating the biological evolutionary process, based on crossover and mutation (Holland, 1992; Krishnakumar & Goldberg, 1992; Morimoto et al., 1997). The initial population was set to 30, and the probability of mutation and crossover was 0.01 and 0.6, respectively. The details about GA feature selection have been described in Sharma et al. (2021).

5.2.5.3. Model development and evaluation

The preprocessed training set was used to develop the machine learning and deep learning- based models using either full wavelength or selected features. Three machine learning models including partial least squares regression (PLSR), support vector machine (SVM) regression, and random forest (RF) regression, and three deep learning models based on convolution neural network (CNN), including 1-D CNN, VGG19, and U-Net were employed in this research. Note that the features selected by the GA was not implemented with the 1D-CNN because the processing time for GA, when

combined with the CNN model, was high, and the complexity in the model was introduced.

For the model development and analysis, the Python 3.8 with the Scikit learn package was used (Pedregosa et al., 2011). The accuracy assessment of the model was done using the statistical parameters: coefficient of determination of training set (R^2), and test (r^2) set (Eq. 4), root mean squared error of calibration (RMSEC), and prediction (RMSEP) (Eq. 5), bias (Eq. 6), and the ratio of prediction and deviation (RPD) (Eq. 7) (Williams & Antoniszyn, 2019).

$$R^2 = \frac{\sum_{i=1}^n (Y_{\text{actual}} - Y_{\text{predicted}})^2}{\sum_{i=1}^n (Y_{\text{actual}} - Y_{\text{mean}})^2} \quad (5.4)$$

$$\text{RMSE} = \sqrt{\frac{\sum (Y_{\text{actual}} - Y_{\text{predicted}})^2}{N}} \quad (5.5)$$

$$\text{Bias} = \frac{\sum Y_{\text{actual}}}{N} - \frac{\sum Y_{\text{predicted}}}{N} \quad (5.6)$$

$$\text{RPD} = \frac{SD_y}{\text{SEP}} \quad (5.7)$$

where, Y_{actual} is a reference value, $Y_{\text{predicted}}$ is predicted value by the model, N is the number of samples, SD_y is the standard deviation of $Y_{\text{predicted}}$, and SEP is the standard error of prediction.

After selecting the optimum model, the spatial mapping was done on the randomly selected samples. The selected ones were then fitted in each pixel of the durian pulp to obtain the respective values of DM, TSS and FC to visualize the distribution.

5.2.6 Deep learning models

As above mentioned, a convolution neural network (CNN) was applied as an advance deep learning technique based on 3 different models, 1-D CNN (custom), VGG19, and U-Net. This part of the research was provided for more information.

The Custom 1-D CNN model structure is presented in Figure 5.2 (a). The structure consists of one input layer, 3 convolution layers, 1 pooling layer, and 1 dense layer. The flattening step was done to obtain the long vector of the input layer to pass through the dense layer for processing.

The VGG19 model is a very dense with 16 1-D convolution layers, 5 1D maximum-pooling layers, and 3 dense layers, as shown in Figure 5.2 (b). The kernel

initializer mainly rectified linear unit (ReLU), and the linear activation function was used in this model. The main purpose of using ReLU as activation is to introduce nonlinearity, reduce the vanishing gradient problem, and accept models to learn faster and perform better (Hussain et al., 2022). The input dimension of the VGG-19 architecture for our model was 216×1 . The input spectra were passed to a stack of convolution layers with a filter size of 10×10 at the initial convolution layer. After each convolution block, the filter size was increased by 2×2 . For the second convolution block the filter size was 20×20 , similarly, 40×40 in the third convolution block, and 80×80 in the fourth convolution block. The strides of the max-pooling layer were fixed to 2×2 with a pool size of 1. This will help to make the model denser and decrease the width. After applying several convolution blocks, and max pooling, the network was connected to the flatten layer which helps to convert the data into a 1D array. Then the 1D array was passed through the 2 dense layers with ReLU activation and the final dense layer with linear activation. The final dense layer provided one output: the predicted DM, TSS, and FC values.

U-Net model was also initially used for the biometric image segmentation. The U-Net model was modified with 1-D convolution layers consisting of a contraction and expansion path. The contraction path consists of convolution and maximum pooling layer. Initially, there were 64×64 filters and 216×1 input shapes. Later in the contraction path, and the Number of filters was increased by 2. Therefore, the filter size in the second block was 128×128 ; the third block was 256×256 , and so on. The convolution layer uses the ReLU activation function with 2×2 maximum pooling operation and 2 strides for downsampling. After 4 convolution blocks, an expansion path was started. The expansion path was used for up-sampling with deconvolution and layer concatenation series. The final shape from the expansion path was the same as the input shape i.e., 216×1 . Finally, we connected the output from U-Net to the flattened layer. Then the 1D array from the flatten layer was passed through the 2 dense layers with ReLU activation and the final dense layer with a linear activation function. The final dense layer provided one output which was the prediction values. In the VGG 19 and U-Net models, the Adam optimizer with the learning rate of 0.0003 was used. The model was optimized for 1500-3000 epochs for training.

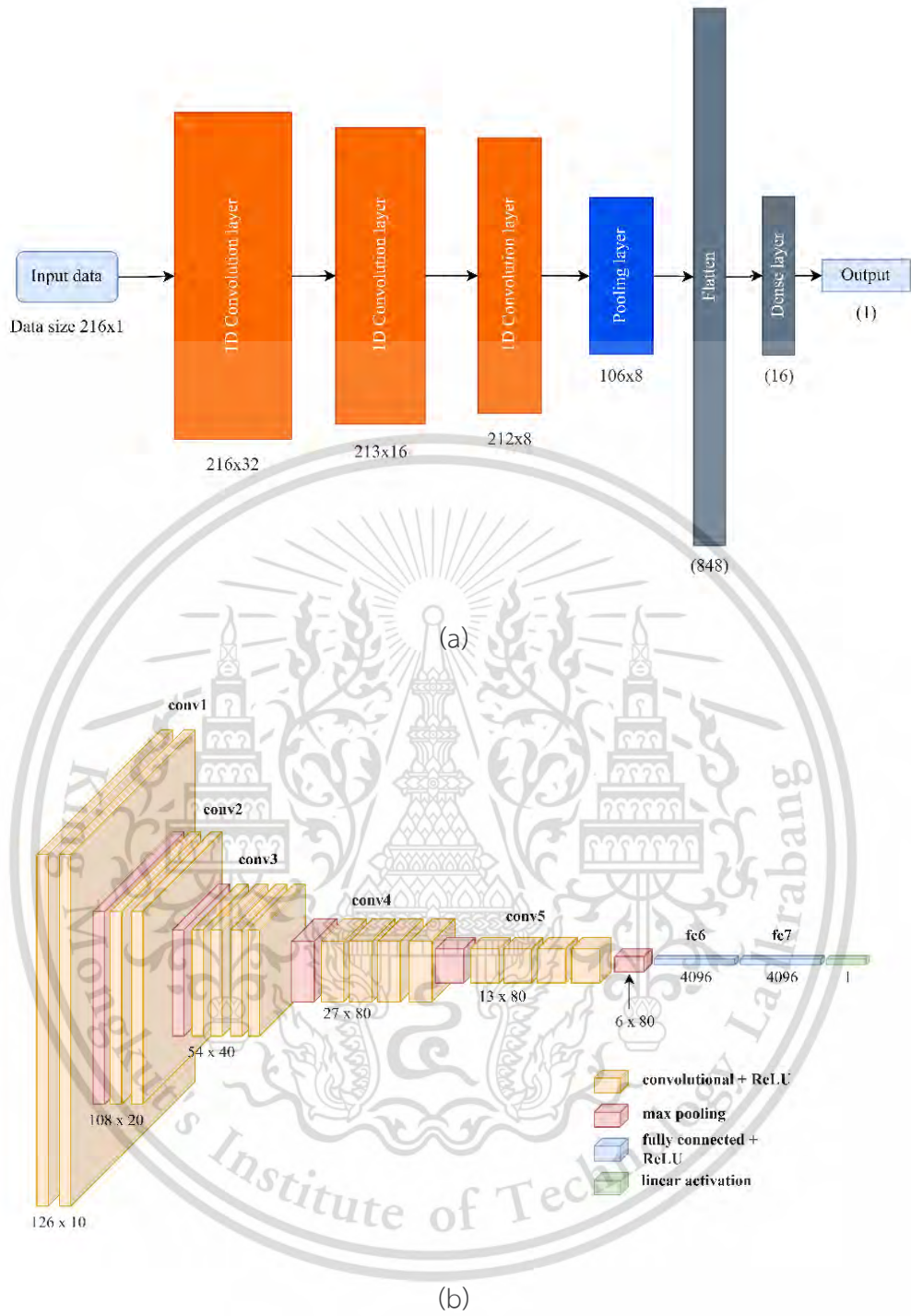


Figure. 5.2 Deep network architecture of 1-D CNN and VGG 19.

5.3 Results and discussion

5.3.1 Spectral profile

This material is reserved for educational use only, not allowed for commercial use.

Forbidden to modify the content, and cite the document when use.

The raw and SNV pretreated average spectra of the durian pulp are shown in Figure 5.3. The raw spectral profile shows the baseline shift throughout the wavelength range. The baseline shift correction can be observed after applying SNV pretreatment in the raw spectra. Three major absorption bands involving the water molecule's symmetric and asymmetric stretching modes were observed at the wavelengths 970, 1205, and 1450 nm (Workman & Weyer, 2007). The wavelength at 1450 nm also represents the O-H first overtone of starch (Osborne et al., 1993). Water content in fruits is higher compared to other quantities; therefore, the absorbance peaks might be dominated by the peak of water (Sahachairungrueng & Teerachaichayut, 2022). The spectral signature from previous research using NIR spectroscopy shows similar characteristics (Onsawai et al., 2020).

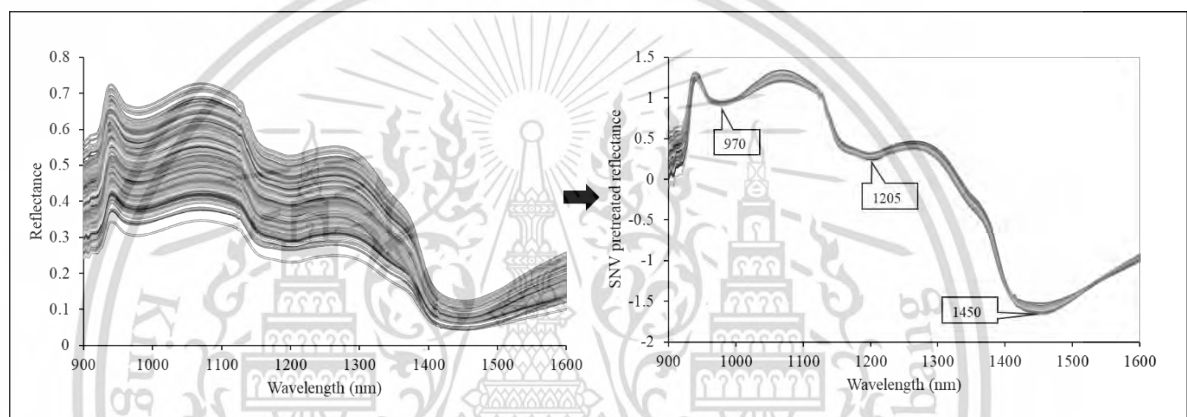


Figure 5.3 Transformation of raw to standard normal variate (SNV) pretreated spectral profile of durian pulp

5.3.2 Statistical analysis of DM, TSS, and FC

Table 1 shows the statistical parameters for each physicochemical property of durian pulp. The minimum, maximum, mean, and standard deviation of the samples divided into a training set and prediction set were calculated.

Table 5.1 Statistical parameters calculated for DM, TSS, and FC.

Physicochemical properties	Set	N	Minimum	Maximum	Average	Standard Deviation
DM (%)	Training	288	8.16	42.70	29.08	8.12

	Test	73	13.96	41.38	31.08	6.26
TSS (%)	Training	288	3.4	40.4	13.9	9.3
	Test	72	4.0	36.9	14.1	8.6
FC (%)	Training	256	0.93	11.46	4.96	1.74
	Test	64	2.14	10.20	5.08	1.49

Note: Dry matter (DM), Total soluble solids (TSS), Fat content (FC), Number of samples (N)

The changes in the physicochemical properties at different harvesting from 99 to 127 DAA are shown in Figure 5.4. The DM increases gradually from the 99 DAA to 113 DAA and decreases thereafter until 127 DAA (Figure 5.4a). DM increased significantly with $\pm 9\%$ from 30.64% at 99 DAA to 39.15% at 113 DAA. After attaining the maximum DM at 113 DAA, the value starts to decrease gradually with $\pm 2\%$. During the starch accumulation process in fruit, the DM also increased owing to the accumulation of plant food. Still, the rate of increase became more gradual at the beginning of ripening. Once the fruit attains maturity, the DM accumulation rate is decreased. This process of DM changes with DAA satisfies the finding from Timkhum & Terdwongworakul (2012). As an important maturity index that directly influences the eating quality, DM content in durian is desirable to be more than 30% while harvesting (Siriphanich & Khurnpoon, 2003). TSS increased significantly every two weeks from 99 DAA to 127 DAA (Figure 5.3 b). TSS risen from 20.27% at 99 DAA to 27.93% at 113 DAA. After 113 DAA the rate of increase in TSS remained slow until 127 DAA. Ketsa & Daengkanit (1998) and Ketsa & Pangkool (1995) reported that the mature and unripe durian aril contains about 23–26% starch that declines rapidly during ripening with a gradual increase in soluble solids and total sugars. This phenomenon can be altered in some cases because of external factors such as humidity, rainfall, and temperature changes during the ripening stage. For FC, the graph shows similar characteristics to TSS. Fat accumulation in durian pulp increased significantly every week from 2.03% at 99 DAA to 4.33% at 120 DAA (Figure 3c). The change in FC is not significant for 120 DAA and 127 DAA..

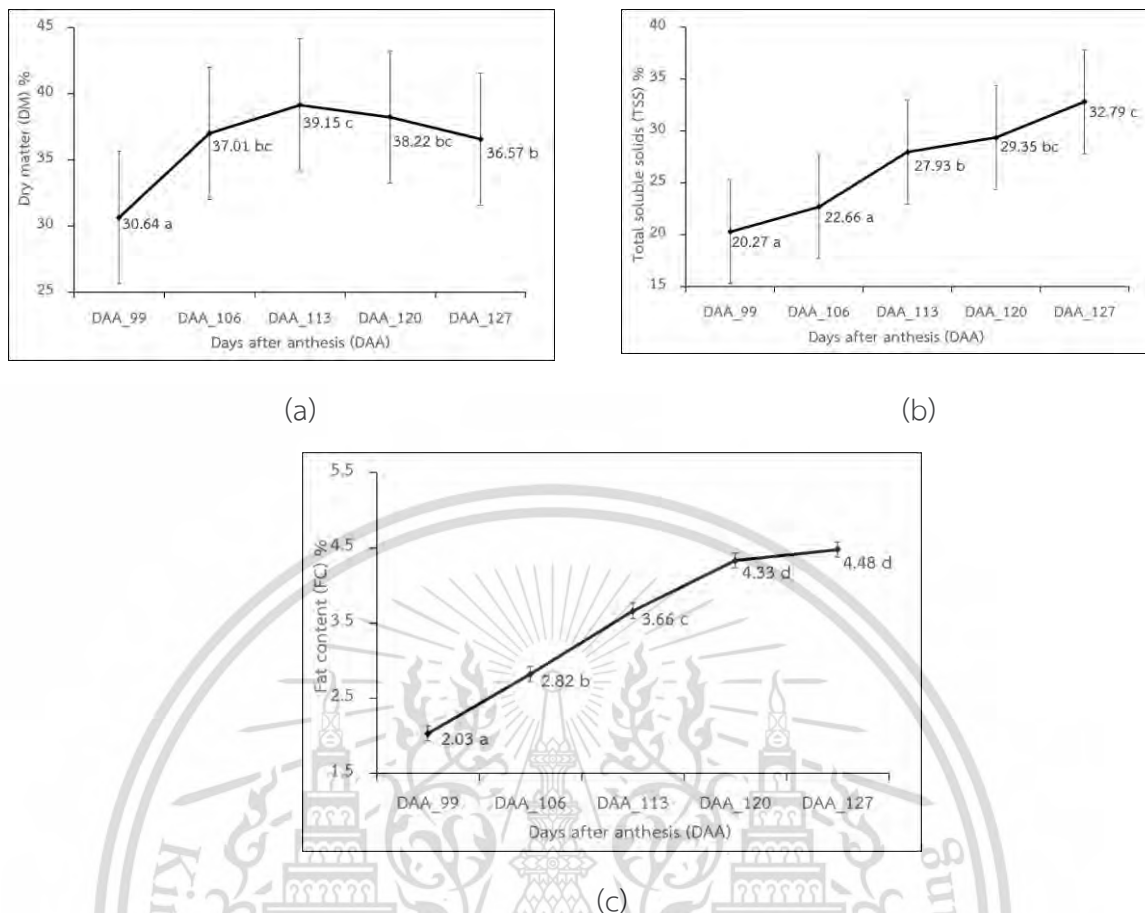


Figure. 5.4 Changes of dry matter (a), total soluble solids (b), and fat content (c) of durian pulp at different DAA.

5.3.3 Training and validating the machine learning models

5.3.3.1 DM prediction models

PLSR, SVM, and RF regression models on full wavelength and featured selected wavelengths by SPA and GA to predict DM are shown in Table 5.2. The best model for DM was attained with GA-PLSR, providing r^2 , RMSEP, and RPD of 0.95, 1.42%, and 4.4, respectively. GA combined with PLSR selected only ninety-seven feature wavelengths for the DM prediction model. The results from the SVM are comparable to PLSR; however, the PLSR model has slightly better results when applied to the test set. GA-SVM model provided RMSEP of 1.65% with RPD of 3.8 using 84 selected features. GA-SVM model used the optimal hyperparameter combination of constant (C), gamma (γ), and kernel: 10, 10, and radial basis function (RBF). SPA-RF model provided the optimal result for DM prediction using 62 feature wavelengths. However, compared to PLSR and SVM, the RF models gave the lowest accuracy for DM prediction. The results presented

in Table 5.2 shows that the overall performance of the PLSR, SVM, and RF models combined with the featured selection showed comparatively better result for DM prediction in durian pulp than full-range spectra.

Table 5.2 Performance of regression model for DM prediction in durian pulp.

Model	N	Training set		5-fold cross-validation		Test Set				
		R ²	RMSEC %	R ² _{cv}	RMSECV %	r ²	RMSEP %	Bias %	RPD	
PLSR	Full	216	0.95	1.8	0.94	2.05	0.93	1.65	0.03	3.8
	SPA	62	0.94	2.04	0.93	2.19	0.92	1.77	0.08	3.5
	SPA- elimination	11	0.94	1.97	0.93	2.15	0.92	1.74	-0.05	3.6
	GA	97	0.95	1.82	0.93	2.02	0.95	1.42	0.01	4.4
SVM	Full	216	0.91	2.46	0.88	2.87	0.89	2.05	0.37	3.0
	SPA	62	0.94	2.05	0.83	3.39	0.89	2.11	0.38	3.0
	SPA- elimination	11	0.93	2.08	0.87	2.89	0.90	2.00	0.4	3.1
	GA	84	0.94	1.98	0.87	2.96	0.93	1.65	0.03	3.8
RF	Full	216	0.98	1.14	0.88	2.92	0.87	2.28	0.56	2.7
	SPA	62	0.98	1.16	0.84	3.29	0.88	2.12	0.30	2.9
	SPA- elimination	11	0.98	1.27	0.84	3.29	0.88	2.18	0.58	2.9
	GA	105	0.98	1.06	0.88	2.84	0.90	1.98	0.55	3.1

PLSR: Partial least squares regression; SVM: Support vector machine; RF: Random Forest; SPA: Successive projection algorithm; GA: Genetic algorithm; R²: Coefficient of determination of training set; r²: Coefficient of determination of training set; R²_{cv}: Coefficient of determination of cross-validation; RMSEC: Root mean square error of calibration; RMSECV: Root mean square error of cross-validation; RMSEP: Root mean square error of prediction; RPD: Ratio of prediction to deviation, N: Number of features selected.

Figure 5.5 shows the selected ninety-seven wavelengths from GA-PLSR. The region from 900-1000 nm contains the feature bands of DM at 965 and 994 nm corresponding to 970 and 990 nm which represents the bond vibration due to O-H str. second overtone of water, and starch, respectively. The second region from 1000-1100 nm consists of the wavelengths corresponding to the bond vibration due to O-H str. second overtone, C-H combination bond, and N-H str. second overtone. The specific characteristics of the 1100-1350 nm region may result from the vibrations caused mainly by C-H str. second overtone and C-H combination bands. The 1400-1500 nm region consists of 1446, 1453,

and 1492 nm corresponding to 1440, 1450, and 1490 nm. This represents the bond vibration due to O-H str. first overtone of starch, water, and cellulose, respectively (Osborne et al., 1993). The final region from 1540-1580 nm consists of the prominent band that is associated with starch at 1548 nm (1540nm), and 1577 nm (1580 nm). The wavelength range selected by GA consists of most of the bands related to water, starch, and cellulose. Similarly, the 11-wavelength selected from the SPA-PLSR with elimination is provided the accuracy of r^2 , RMSEP, and RPD of 0.92, 1.72%, and 3.6. This model is considered to be very good and can be applied for process control (Williams & Antoniszyn, 2019). The 11 wavelengths are 1059, 1072, 1088, 1104, 1117, 1156, 1196, 1290, 1381, 1424, and 1453 nm. The wavelength at 1072, 1196, 1424, and 1453 nm corresponding to the wavelength 1062, 1200, 1440, and 1450 nm represents the absorption band of starch (Osborne et al., 1993; Williams & Antoniszyn, 2019). The wavelength at 1450 nm also represents the absorption band of water (Osborne et al., 1993). The scatter plots showing the actual DM versus the predicted DM from the optimal model (GA-PLSR and SPA-PLSR with elimination) are shown in Figure 5.6.

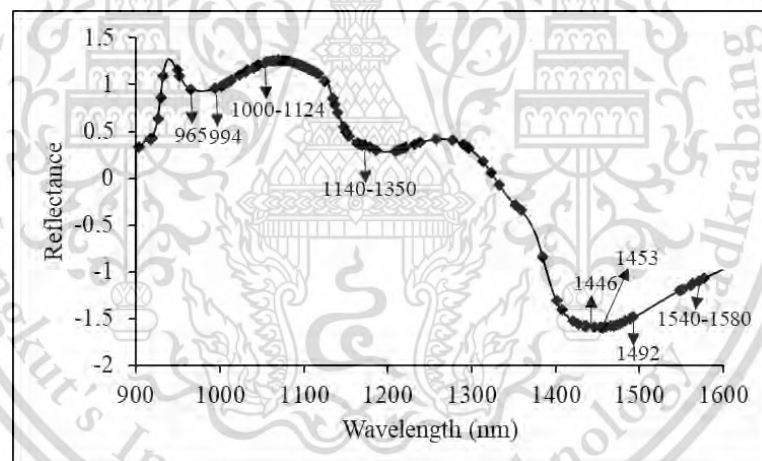


Figure. 5.5 Average spectrum of durian pulp showing selected wavelengths by GA for DM prediction.

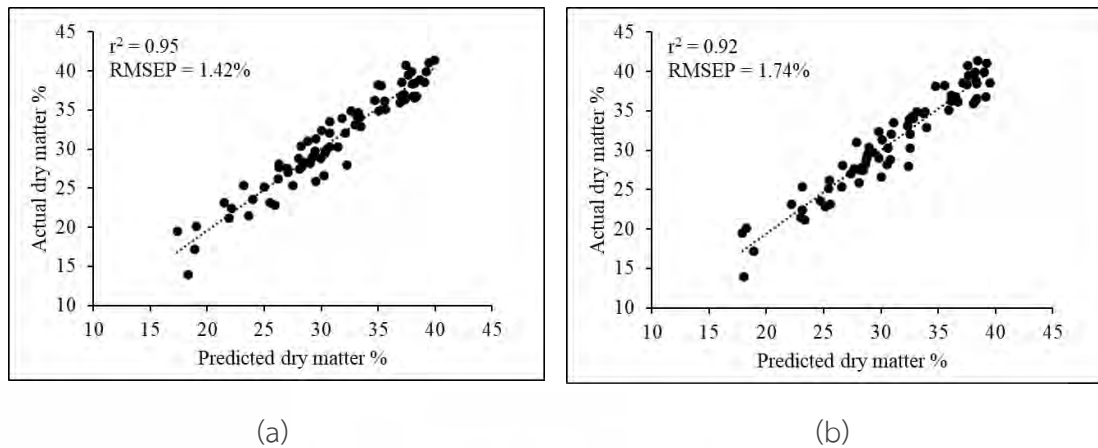


Figure. 5.6 Scatter plot showing the actual versus predicted dry matter from GA-PLSR (a) and SPA-PLSR with elimination (b) regression model.

5.3.3.2 TSS prediction models performance

The GA-SVM achieved the best performance in the prediction of TSS with r^2 , RMSEP, and RPD of 0.87, 3.1%, and 2.8, respectively. The performance of GA-PLSR and GA-SVM produced similar results; however, the GA-SVM model shows slightly better prediction accuracy. The accuracy of the training set was comparatively higher for the RF model; however, the performance on the test data set shows lower accuracy. The overall results show improvement in the TSS prediction model accuracy when applied with the feature selection algorithms. The performance of the PLSR, SVM and RF models shown in Table 5.3 shows fair and comparative results.

Table 5.3 Performance of regression model for TSS prediction in durian pulp.

Model	N	Training set		5-fold CV		Test Set				
		R^2	RMSEC %	R^2_{cv}	RMSECV %	r^2	RMSEP %	Bias %	RPD	
PLSR	Full	216	0.83	3.8	0.81	4.0	0.83	3.5	0.0	2.5
	SPA	39	0.84	3.7	0.82	3.9	0.83	3.4	0.0	2.5
	SPA-elimination	15	0.80	4.1	0.77	4.5	0.79	3.9	-0.3	2.1
	GA	88	0.85	3.5	0.82	3.9	0.87	3.1	0.1	2.8
SVM	Full	216	0.88	3.2	0.74	4.7	0.84	3.3	-0.3	2.6
	SPA	39	0.81	4.0	0.73	4.8	0.83	3.6	-0.8	2.4
	SPA-elimination	15	0.76	4.6	0.50	6.5	0.76	4.2	-0.6	2.0
	GA	94	0.86	3.4	0.78	4.3	0.87	3.1	-0.3	2.8

	Full	216	0.97	1.7	0.77	4.4	0.79	3.9	-0.1	2.2
	SPA	39	0.98	1.4	0.83	3.9	0.84	3.5	-0.2	2.5
RF	SPA- elimination	15	0.94	2.2	0.54	6.3	0.78	4.0	-0.2	2.1
	GA	103	0.97	1.6	0.79	4.2	0.83	3.5	-0.1	2.5

PLSR: Partial least squares regression; SVM: Support vector machine; RF: Random Forest; SPA: Successive projection algorithm; GA: Genetic algorithm; R^2 : Coefficient of determination of training set; r^2 : Coefficient of determination of training set; R^2_{cv} : Coefficient of determination of cross-validation; RMSEC: Root mean square error of calibration; RMSECV: Root mean square error of cross-validation; RMSEP: Root mean square error of prediction; RPD: Ratio of prediction to deviation, N: Number of features selected.

Figure 5.7 shows the ninety-four selected wavelengths used for the TSS prediction using GA-SVM. The first region from 900-1000 nm includes the wavelength at 972 nm related to O-H str. third overtone of sucrose (Workman & Weyer, 2007). Other important bands in the region 1100-1200 nm includes are mainly due to C=O (1160 nm) and C-H (1170 nm, 1194 nm) vibration, and these two chemical bonds are pervasive in soluble sugar, which is a major component of TSS (Burns Donald A., 2008; Li et al., 2018). Wavelengths at 1440, 1480, and 1580 nm represent an important vibration band of sucrose due to O-H str. first overtone, which highly influences the prediction. From SPA-PLSR with elimination, fifteen feature bands were selected, and the model developed using these wavelengths gave the r^2 , RMSEP, and RPD of 0.79, 3.9%, and 2.1, respectively. The result shows that the model was applicable for very rough to rough screening. The fifteen selected features from SPA are: 906, 909, 913, 916, 919, 926, 929, 952, 1179, 1342, 1348, 1381, 1427, 1450, and 1600 nm, respectively. Figure 5.8 shows the scatter plots showing the actual TSS versus the predicted TSS from the optimal model (GA-SVM and SPA-PLSR with elimination).

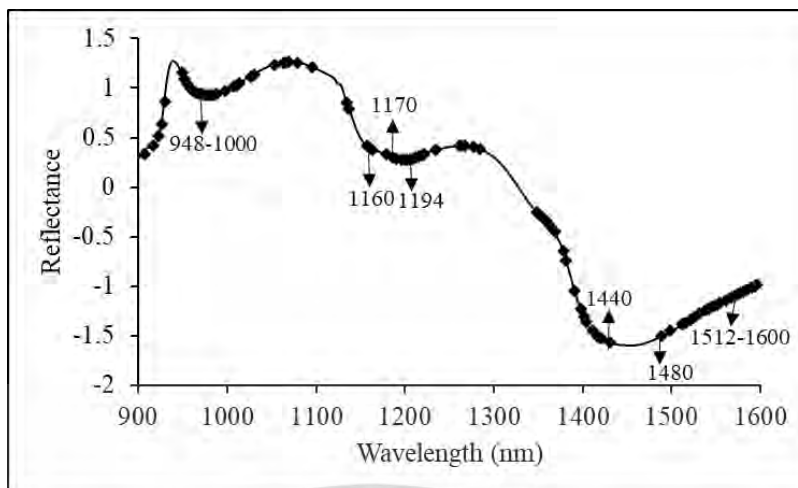


Figure. 5.7 Average spectrum of durian pulp showing selected wavelengths by GA for TSS prediction.

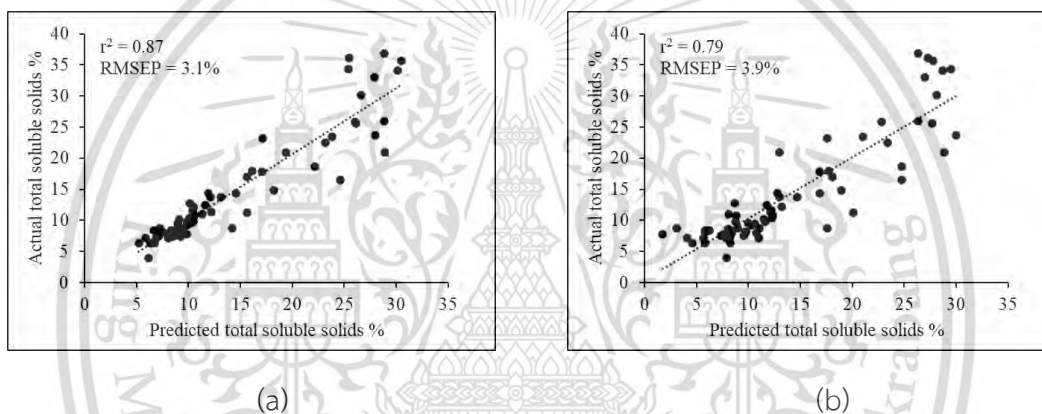


Figure. 5.8 Scatter plot showing the actual versus predicted total soluble solids from GA-SVM (a) and SPA-PLSR with elimination (b) regression models.

5.3.3.3 FC prediction models performance

For FC, the prediction accuracy of GA-PLSR was slightly better than that of SVM and RF. The total Number of latent variables used for GA-PLSR was 7. Ninety-seven bands were selected for the FC model. The model's performance based on selected bands was improved compared with the PLSR, SVM, and RF models using full wavelengths. According to Williams et al. (2019), the model with the ranges of r^2 from 0.66-0.81 and RPD from 2.0-2.4 can be applied for rough screening and approximate calibration. SPA-PLSR with elimination was able to provide the r^2 of 0.60 which suggests that the mode is acceptable for the very rough to rough screening (Williams et al., 2019). However, the performance of FC prediction models was poorer than that of DM and TSS.

Table 5.4 Performance of regression models for FC prediction in durian pulp.

Model	N	Training set		5-fold CV		Test Set				
		R ²	RMSEC %	R ² _{cv}	RMSECV %	r ²	RMSEP %	Bias %	RPD	
PLSR	Full	216	0.76	0.85	0.72	0.91	0.68	0.84	0.15	1.8
	SPA	62	0.77	0.83	0.74	0.88	0.69	0.82	0.2	1.8
	SPA- elimination	21	0.65	1.03	0.60	1.09	0.60	0.94	0.13	1.6
	GA	97	0.82	0.74	0.78	0.82	0.81	0.65	0.16	2.3
SVM	Full	216	0.76	0.86	0.66	1.01	0.66	0.86	0.15	1.7
	SPA	62	0.71	0.93	0.58	1.12	0.61	0.92	0.07	1.6
	SPA- elimination	21	0.58	1.12	0.48	1.24	0.58	0.96	0.07	1.5
	GA	102	0.86	0.66	0.70	0.95	0.78	0.70	0.14	2.1
RF	Full	216	0.94	0.43	0.56	1.15	0.60	0.94	0.15	1.6
	SPA	62	0.94	0.42	0.62	1.07	0.62	0.92	0.15	1.6
	SPA- elimination	21	0.92	0.5	0.47	1.27	0.52	1.03	0.15	1.4
	GA	101	0.95	0.4	0.79	0.4	0.68	0.84	0.14	1.8

PLSR: Partial least squares regression; SVM: Support vector machine; RF: Random Forest; SPA: Successive projection algorithm; GA: Genetic algorithm; R²: Coefficient of determination of training set; r²: Coefficient of determination of training set; R²_{cv}: Coefficient of determination of cross-validation; RMSEC: Root mean square error of calibration; RMSECV: Root mean square error of cross-validation; RMSEP: Root mean square error of prediction; RPD: Ratio of prediction to deviation N: Number of features selected.

The selected wavelength from GA for FC prediction is shown in Figure 5.9. The wavelength ranges from 900-930 nm and consists of the vibrational band of CH₃ (900 nm), protein (910 nm), CH₃ (913 nm), and oil (928 nm) due to C-H str. third overtone. The wavelength at 928 nm corresponds to 930 nm indicating the third overtone C-H stretch vibration of triglyceride (Aernouts et al., 2011; Šašić & Ozaki, 2001; Van der Meer & De Jong, 2011). The range from 950-1100 nm consists of the vibrational band of water (970 nm), starch (990 nm), protein (1020 nm), RNH₂ (1030 and 1053 nm), oil (1037 nm), and benzene (1080 nm). The range from 1100-1300 nm consists of the vibration band due to the second overtone and combination band of C-H stretching CH₂, CH₃, and HC=HC. C-H bonds are assigned to oil or fat; however, it has to be also considered that protein, starch, sugar, and cellulose also contain the same bond (Williams et al., 2019). The wavelength at 1360 and 1395 nm corresponds to the bond vibration due to the C-H combination of CH₂ and CH₃ (Osborne et al., 1993). The wavelength range from 1424-1456 nm and 1510-1600 nm consists of some important feature bands mainly of water

(1450 nm) and starch (1440, 1450, 1528, 1540, and 1580 nm) due to overtone and combination of C-H and O-H stretching (Osborne et al., 1993). The model's performance developed from the wavelengths selected by SPA provided poor prediction results for FC. Hence, only the FC prediction result using the GA-PLSR model is presented, as shown in Figure 5.10.

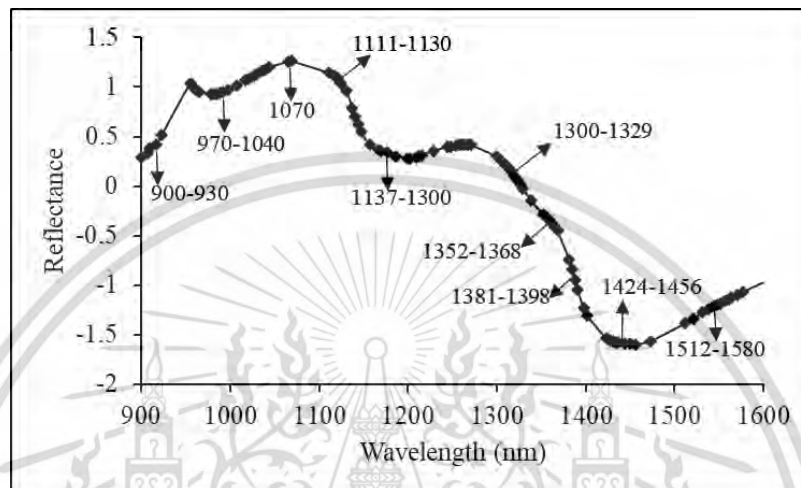


Figure. 5.9 Average spectrum of durian pulp showing selected wavelengths by GA for FC prediction.

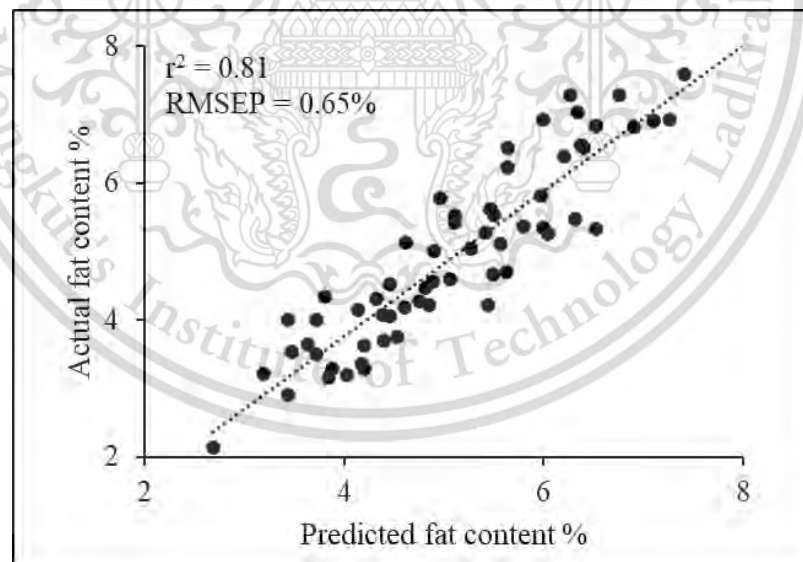


Figure. 5.10 Scatter plot showing the actual versus predicted fat content from the GA-PLSR model.

From the literature, the DM prediction of durian pulp based on the PLSR model using full bands was able to provide the best r^2 , RMSEP, and RPD of 0.89, 3.60%, and

3.27 (Onsawai et al., 2020); 0.83, 4.32%, and 3.52 (Saechua et al., 2021); 0.83, 1.61%, and 1.76 (Somton et al., 2015). TSS/soluble solids content (SSC) prediction models for durian pulp were developed using NIR spectroscopy by scanning online and at-line conditions by Saechua et al. 2021 and Onsawai et al., 2020. The results showed that the maximum r^2 of 0.70 and minimum RMSEP of 1.62 % (at-line) and 4.0 % (online) were attained in previous research. Compared to the previous research, the GA-SVM model with ninety-four wavelengths provided a fair result that it can be applied for the screening and is usable with caution for most applications, including research (Williams et al., 2019). Any ideal prediction models should have r^2 and R^2 above 0.75, RPD index above 2.0, and RMSE lower than its standard deviation (Agussabti et al., 2020). Limited information is available on the fat content of durian pulp. The FC prediction model shows the possibility of further development in the model accuracy. The wavelength selected by SPA with elimination did not show good prediction accuracy. According to Aernouts et al., 2011, the short-wavelength from 400-1000 nm was less informative for FC prediction of raw milk. However, the region from 1660-1730 nm was very effective for FC prediction by the PLSR model. In our research, the NIR-HSI system wavelength range is from 900-1600 nm. The fact that the important absorption bands responsible for the FC prediction were not available in this region might cause the lower FC prediction accuracy.

5.3.4 Deep learning model performance

The results of deep learning model prediction are summarized in Table 5.5. 1D-CNN models: custom, U-Net, and VGG19 obtained fair results for only DM prediction. The best r^2 and RMSEP attained were 0.90 and 1.88% for DM, respectively by the VGG-19 model using the full wavelength range. In the case of TSS, and FC prediction, the performance of those models for was poor compared to the results obtained from the machine learning (PLSR, SVM, and RF) approach. RMSEP for TSS prediction was higher than 4.3%, and the RPD could be in the range of 0.9-1.8, which concludes that the models are not applicable for any purpose. Similarly, the highest r^2 and RPD attained for the FC prediction were 0.67 and 1.4, which was from the U-Net 1-D CNN model, expressing that it is poor and not applicable for the prediction.

CNN robust models can be developed even under challenging conditions and complex data due to the images' background, illumination, different size, orientation, and resolution (Amara et al., 2017; Kamilaris & Prenafeta-Boldú, 2018). The greater advantage is that CNN models can learn and locate the important features while training the dataset (Kamilaris & Prenafeta-Boldú, 2018). However, the CNN model training time is longer than other machine learning models. The fact that the CNN model or any

deep learning model requires large datasets for training. It is one of the major reasons that might have affected the accuracy of the prediction models presented in our research. Collecting a hundred samples in a season for climacteric fruits such as durian is challenging. Also, it will increase the cost and time of the experiment.

Table 5.5 Performance of 1-D CNN models for DM, TSS, and FC prediction.

Parameters	1-D CNN Models			Training set			Test set			
	Method	N		R ²	RMSEC %	r ²	RMSEP %	Bias %	RPD	
DM	Custom	Full	216	0.88	2.88	0.75	2.97	1.51	1.5	
		SPA	62	0.92	2.39	0.86	2	0.07	2.5	
		SPA-elimination	11	0.88	2.7	0.79	2.72	0.46	1.7	
	U-Net	Full	216	0.96	1.68	0.88	2.06	-0.49	2.8	
		SPA	62	0.88	2.83	0.79	2.47	0.22	1.6	
		SPA-elimination	11	0.95	1.89	0.88	2.09	0.06	2.3	
	VGG-19	Full	216	0.96	1.64	0.90	1.88	-0.68	3.1	
		SPA	62	0.92	2.3	0.82	2.24	1.27	2.3	
		SPA-elimination	11	0.94	2.06	0.82	2.54	-1.54	2.3	
	TSS	Custom	Full	216	0.76	4.38	0.68	5.46	1.69	1.2
			SPA	39	0.73	4.7	0.68	5.34	2.02	1.2
			SPA-elimination	15	0.86	3.48	0.74	4.48	-0.54	1.8
U-Net		Full	216	0.9	2.79	0.77	4.6	0.22	1.8	
		SPA	39	0.66	5.22	0.53	6.46	3.22	0.9	
		SPA-elimination	15	0.9	2.94	0.77	4.29	0.32	1.9	
VGG-19	Full	216	0.9	2.88	0.73	5.00	-0.24	1.5		
	SPA	39	0.88	3.13	0.68	5.3	1.95	1.4		
	SPA-elimination	15	0.93	2.47	0.51	6.18	-2.09	1.8		
FC	Custom	Full	216	0.74	0.89	0.49	0.95	-0.06	1.0	

This material is reserved for educational use only, not allowed for commercial use.

Forbidden to modify the content, and cite the document when use.

	SPA	84	0.49	1.21	0.43	1.26	0.25	0.6
	SPA-elimination	21	0.71	0.94	0.52	0.98	0.06	1.3
U-Net	Full	216	0.89	0.58	0.64	0.80	0.11	1.3
	SPA	84	0.68	0.97	0.61	0.94	0.15	1.3
	SPA-elimination	21	0.79	0.8	0.67	0.81	0.29	1.4
VGG-19	Full	216	0.73	0.91	0.34	1.08	0.35	0.8
	SPA	84	0.52	1.2	0.42	1.14	0.02	0.8
	SPA-elimination	21	0.88	0.61	0.54	0.97	0.19	1.3

DM: dry matter; TSS: total soluble solids; FC: fat content; CNN: Convolution neural network; SPA: Successive projection algorithm; R^2 : Coefficient of determination of training set; r^2 : Coefficient of determination of training set; R^2_{cv} : Coefficient of determination of cross-validation; RMSEC: Root mean square error of calibration; RMSECV: Root mean square error of cross-validation; RMSEP: Root mean square error of prediction; RPD: Ratio of prediction to deviation.

5.3.5 Visualization of concentration distribution

One fruit from each DAA starting from 90 DAA-127 DAA was randomly selected to represent the physicochemical properties mapping on the durian pulp. The distribution maps were generated by extracting the feature bands of each pixel and radiometric calibration. Spectra from each pixel were then used to predict DM, TSS, and FC. The original pseudo-colour image with the RGB band combination (Red = 961.93 nm, Green = 1075.67 nm, and Blue = 1450.18 nm) and the distribution map of DM, TSS, and FC are shown in Figure 5.11. The distribution of DM from 99 DAA to 127 DAA shows the changes between the pulps at different stages from 18% to 39%. It must be noted that the TSS concentration within the pulp is denser in the head part than in the tail part. Therefore, the changes between the fruit at different stages are not that significant. The TSS changed from 13% to 15% from the 99 DAA to 127 DAA. The model predicted high TSS mainly at the head part; however, most pixels were predicted as the TSS values in the range of 10% to 15%. However, it must be considered that the samples were selected randomly to avoid bias for the spatial mapping. Like DM, FC has also changed significantly between the ripening stages. FC values have changed from 1% to 5% from the unripe to the ripening stage.

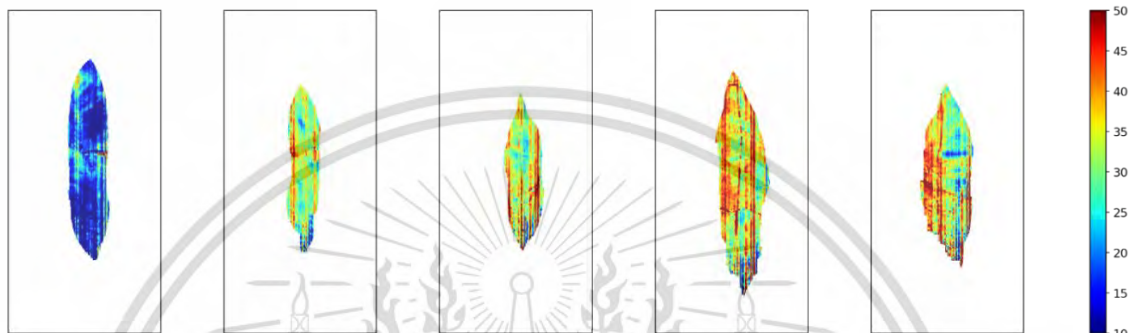
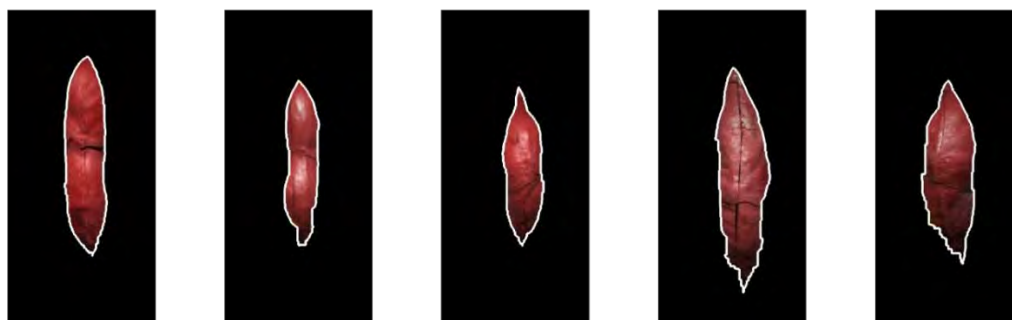
99 DAA

106 DAA

113 DAA

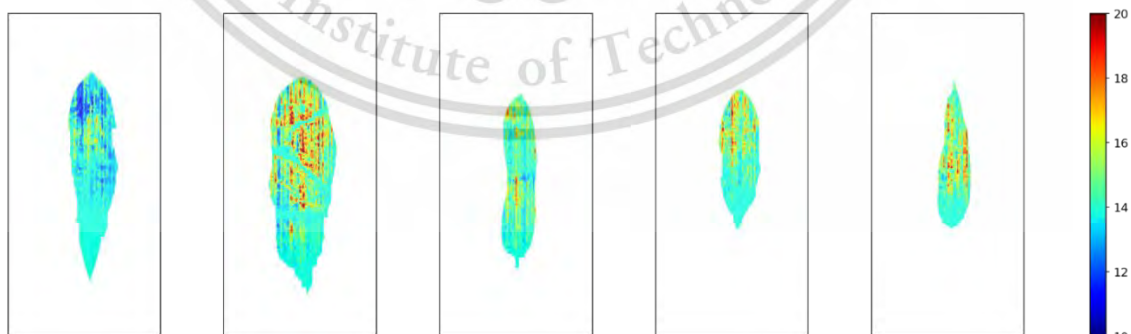
120 DAA

127 DAA



DM distribution on durian pulp.

99 DAA 106 DAA 113 DAA 120 DAA 127 DAA



TSS distribution on durian pulp.

This material is reserved for educational use only, not allowed for commercial use.

Forbidden to modify the content, and cite the document when use.

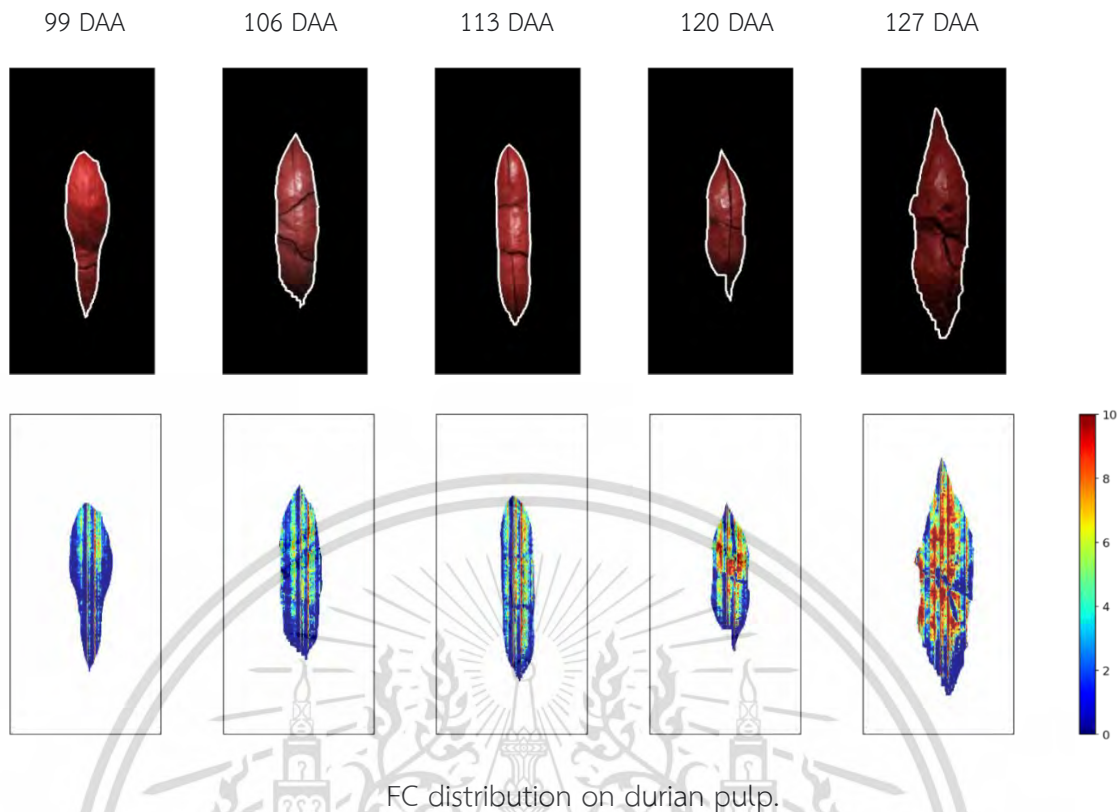


Figure. 5.11 Spatial mapping of dry matter (DM), total soluble solids (TSS), and fat content (FC) in durian pulp on different days after anthesis (DAA).

5.4 Conclusion

The potential of the NIR-HIS system for the DM, TSS, and FC prediction using PLSR, SVM, RF, and 1-D CNN models of durian pulp was investigated in this research. A comparative study was made according to the statistical parameters between the regression model using full wavelength and feature selection by GA and SPA. The significant findings from this research are:

PLSR models with GA selected ninety-seven wavelengths showed a very accurate model for DM prediction with the r^2 , RMSEP, and RPD of 0.95, 1.42%, and 4.4.

DM prediction using SPA selected 11 wavelengths combined with PLSR attained the r^2 , RMSEP, and RPD 0.92, 1.74%, and 3.6, which can be applied for the process control.

SVM model combined with the GA selected wavelength provided the best TSS prediction accuracy for training and test set with R^2 , RMSEC, r^2 , and RMSEP of 0.86, 3.43%, 0.87, and 3.1%, respectively.

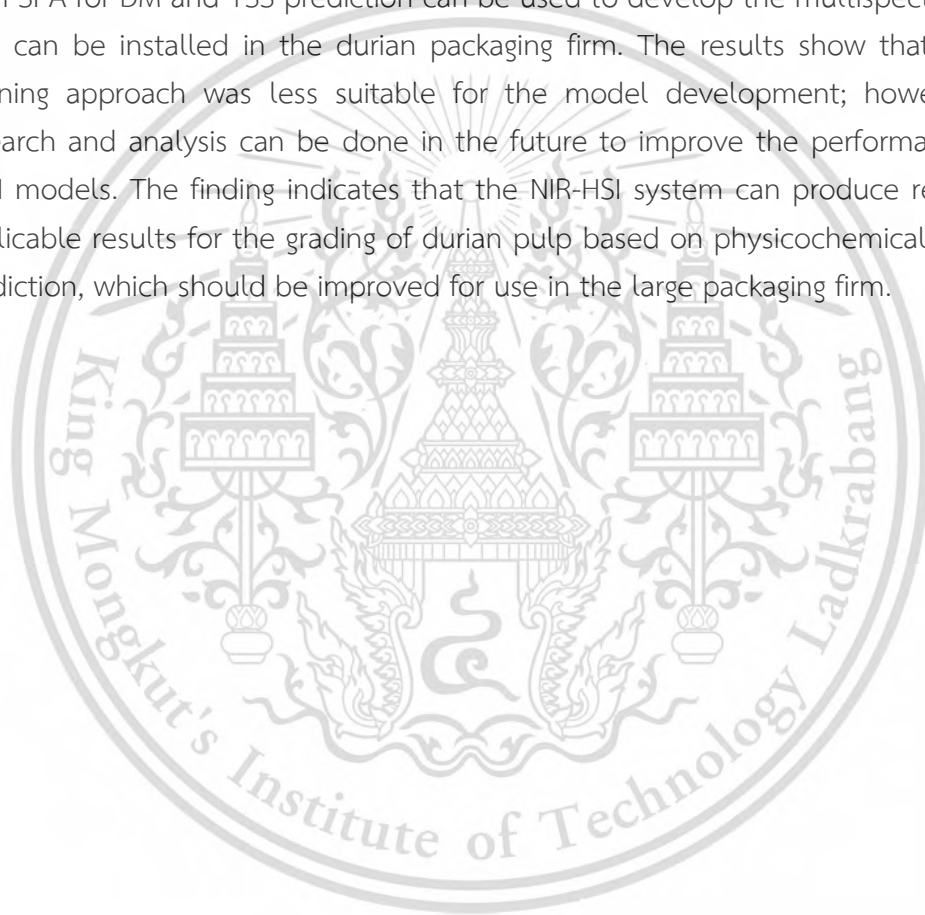
The best accuracy for FC prediction was attained by the PLSR model combined with GA-selected wavelengths with the r^2 , RMSEP, and RPD of 0.81, 0.65%, and 2.3,

respectively.

The 1-D CNN model for the DM, TSS, and FC provided lower accuracy when compared to the PLSR, SVM, and RF model performance.

DM, TSS, and FC spatial distribution shows variability between and within the durian pulp. The gradual change can be observed with the ripening stages.

NIR-HSI approach integrated with multivariate analysis and featured wavelength selection could predict DM, TSS, and FC in durian pulp. The models developed for DM are accurate and applicable for any application. The few feature wavelengths selected from SPA for DM and TSS prediction can be used to develop the multispectral camera that can be installed in the durian packaging firm. The results show that the deep learning approach was less suitable for the model development; however, more research and analysis can be done in the future to improve the performance of 1-D CNN models. The finding indicates that the NIR-HSI system can produce reliable and applicable results for the grading of durian pulp based on physicochemical properties prediction, which should be improved for use in the large packaging firm.



Chapter 6

Conclusion and recommendations

6.1 Conclusion

From the findings of this thesis, it can be confirmed that NIR-HSI technique can be implemented for the ripeness level classification of durian intact fruit and pulp and to predict the physicochemical properties of durian pulp. However, the recommendation is given for the further improvement and implementation of the results obtained.

In chapter 3, the first analysis was conducted for the ripeness level (unripe, ripe and overripe) classification of durian pulp using three machine learning algorithms random forest (RF), support vector machine (SVM), and k Nearest Neighbours (kNN). The hyperparameters were tuned using Bayesian optimization and the 3-fold cross-validation method. In terms of overall classification accuracy and kappa coefficient, SVM (88.5%, 0.83) performed better than RF (84.6%, 0.77) and kNN (73.1%, 0.59). The results show that the classifiers (SVM and RF) can fairly differentiate the ripening stage of durian pulp using NIR-HSI. However, the result shows the possibility for the further improvement in the classification model.

In chapter 4, ripeness level classification of durian intact fruit and pulp was illustrated using different approach. The grid search hyperparameter optimization was used for the classification model development and accuracy assessment of five machine learning classifiers including SVM, RF, and kNN with linear discriminant analysis (LDA) and partial least squares-discriminant analysis (PLS-DA), and kNN. The classification model was developed on the full wavelength and feature wavelengths selected from principal component analysis (PCA) and genetic algorithm (GA). For classification of durian pulp, LDA showed the best result with a test accuracy of 100% for both full wavelength and selected 135 wavelengths by GA. A total of 11 wavelengths selected from PCA achieved a test accuracy of 93.6% by LDA. Among all the classifiers, the performance of LDA classifier was superior for the ripeness level classification of durian intact fruit and pulp. LDA was able to attain the 100% classification accuracy using full and selected wavelengths for intact durian fruit. On the other hand, partial least squares regression (PLSR) model was developed to predict the dry matter (DM) with 90 durian

pulp. Samples were classified into training and test set in the ratio of 70:30. The PLSR models predicted the DM with the coefficient of determination of prediction (R_p^2) greater than 0.80 and a root mean square error of prediction (RMSEP) less than 1.6%. The results concluded that HSI system combined with the machine learning and feature selection algorithms showed the potential to be further implemented to identify the ripeness level of durian intact fruit and pulp in the packaging firms.

Chapter 5 illustrated the approach used for the prediction of physicochemical properties: dry matter (DM), total soluble solids (TSS), and fat content (FC) using NIR-HSI technology. The result showed that, the integration of NIR-HSI data with the multivariate analysis and optimum feature selection can produce an accurate and reliable results for the quality inspection of durian pulp. The DM model was updated by adding a greater number of samples. GA-PLSR model was very powerful to predict the DM, and FC in durian pulp, which obtained the coefficient of determination for the test set (r^2) and root mean square error of prediction (RMSEP) of 0.95 and 1.42% for DM and 0.81 and 0.65% for FC, respectively. Eleven spectral feature wavelengths selected from successive projection algorithm (SPA) when combined with PLSR obtained r^2 and a ratio of prediction to deviation (RPD) of 0.92 and 3.6, respectively for DM measurement. SVM model was more reliable for the TSS prediction, which obtained the r^2 , and RMSEP of 0.87 and 3.05%, respectively. NIR-HSI enabled the visualization of DM, TSS, and DC in durian pulp by physicochemical mapping for the first time by this thesis research. The distribution showed the gradual change and variability between and within the durian pulp.

6.2 Recommendation

In this thesis, NIR-HSI data has been used for the classification and regression model development. However, this technology is expensive and requires special manpower to be installed and to acquire the image. Therefore, in this study the feature wavelengths were selected to reduce the processing complexity. These wavelengths should be utilized to develop the portable multispectral imaging system or to design the single shot imagers with tunable filters which can be easily implemented in the durian orchards and packaging firms. This research was focused on durian cultivar, Monthong, however, the study should be done on other important cultivars as well.

The variation of the samples should be included in the prediction model. The samples from different ripening stage, location, and varieties should be included. Increasing the number of samples can enhance the accuracy and robustness of the prediction model for further implementation. Deep learning models can be improved further by adding more samples. 1D-CNN models can be implemented for feature selection, which can improve the prediction power of the model. Other 1D-CNN models should be explored as well for the classification and prediction model development



References

- Abbott, J. A. (1999). Quality measurement of fruits and vegetables. *Postharvest Biology and Technology*, *15*(3), 207–225. [https://doi.org/10.1016/S0925-5214\(98\)00086-6](https://doi.org/10.1016/S0925-5214(98)00086-6)
- Aernouts, B., Polshin, E., Lammertyn, J., and Saeys, W. (2011). Visible and near-infrared spectroscopic analysis of raw milk for cow health monitoring: Reflectance or transmittance? *Journal of Dairy Science*, *94*(11), 5315–5329. <https://doi.org/10.3168/JDS.2011-4354>
- Agussabti, Rahmaddiansyah, Satriyo, P., and Munawar, A. A. (2020). Data analysis on near infrared spectroscopy as a part of technology adoption for cocoa farmer in Aceh Province, Indonesia. *Data in Brief*, *29*, 105251. <https://doi.org/10.1016/j.dib.2020.105251>

- Ahmad, A., Ali, Z. M., and Zainal, Z. (2013). Effect of 1-methylcyclopropene (1-mcp) treatment on firmness and softening related enzymes of “sekaki” papaya fruit during ripening at ambient. *Sains Malaysiana*, 42(7), 903–909.
- Amara, J., Bouaziz, B., and Algergawy, A. (2017). A deep learning-based approach for banana leaf diseases classification. *Datenbanksysteme Für Business, Technologie Und Web (BTW 2017)-Workshopband*.
- Amodio, M. L., Ceglie, F., Chaudhry, M. M. A., Piazzolla, F., and Colelli, G. (2017). Potential of NIR spectroscopy for predicting internal quality and discriminating among strawberry fruits from different production systems. *Postharvest Biology and Technology*. <https://doi.org/10.1016/j.postharvbio.2016.11.013>
- Anderson, N. T., Subedi, P. P., and Walsh, K. B. (2017). Manipulation of mango fruit dry matter content to improve eating quality. *Scientia Horticulturae*, 226(August), 316–321. <https://doi.org/10.1016/j.scienta.2017.09.001>
- Andrade-Garda, J. (2013). *Basic chemometric techniques in atomic spectroscopy*. Royal Society of Chemistry.
- Andries, J. P. M., and Vander Heyden, Y. (2021). Improved multi-class discrimination by Common-Subset-of-Independent-Variables Partial-Least-Squares Discriminant Analysis. *Talanta*, 234(June), 122595. <https://doi.org/10.1016/j.talanta.2021.122595>
- Arancibia-Avila, P., Toledo, F., Park, Y. S., Jung, S. T., Kang, S. G., Heo, B. G., Lee, S. H., Sajewicz, M., Kowalska, T., and Gorinstein, S. (2008). Antioxidant properties of durian fruit as influenced by ripening. *LWT - Food Science and Technology*, 41(10), 2118–2125. <https://doi.org/10.1016/j.lwt.2007.12.001>
- Araújo, M. C. U., Saldanha, T. C. B., Galvão, R. K. H., Yoneyama, T., Chame, H. C., and Visani, V. (2001). The successive projections algorithm for variable selection in spectroscopic multicomponent analysis. *Chemometrics and Intelligent Laboratory Systems*, 57(2), 65–73. [https://doi.org/10.1016/S0169-7439\(01\)00119-8](https://doi.org/10.1016/S0169-7439(01)00119-8)
- Aredo, V., Velásquez, L., Carranza-Cabrera, J., and Siche, R. (2019). Predicting of the quality attributes of orange fruit using hyperspectral images. *Journal of Food Quality and Hazards Control*, 6(3), 82–92. <https://doi.org/10.18502/jfqhc.6.3.1381>
- Ariana, D., Guyer, D. E., and Shrestha, B. (2006). Integrating multispectral reflectance and fluorescence imaging for defect detection on apples. *Computers and Electronics in Agriculture*, 50(2), 148–161.

<https://doi.org/10.1016/j.compag.2005.10.002>

Artés, F., Minguéz, M. I., and Hornero, D. (2002). Analysing changes in fruit pigments. In *Color in food* (pp. 248–282). Elsevier.

Aspiras, A. B., and Tocino, E. M. (1971). survey of the aroma composition of Philippine fruits. *Philippine Agr.*

Azarmdel, H., Jahanbakhshi, A., Mohtasebi, S. S., and Muñoz, A. R. (2020). Evaluation of image processing technique as an expert system in mulberry fruit grading based on ripeness level using artificial neural networks (ANNs) and support vector machine (SVM). *Postharvest Biology and Technology*, 166(March), 111201. <https://doi.org/10.1016/j.postharvbio.2020.111201>

Aziz, N. A. A., and Jalil, A. M. M. (2019). Bioactive compounds, nutritional value, and potential health benefits of indigenous durian (*Durio zibethinus* Murr.): A review. In *Foods* (Vol. 8, Issue 3). MDPI Multidisciplinary Digital Publishing Institute. <https://doi.org/10.3390/foods8030096>

Badaró, A. T., Garcia-Martin, J. F., López-Barrera, M. del C., Barbin, D. F., and Alvarez-Mateos, P. (2020). Determination of pectin content in orange peels by near infrared hyperspectral imaging. *Food Chemistry*, 323, 126861. <https://doi.org/10.1016/J.FOODCHEM.2020.126861>

Ball, D. W. (2006). Concentration scales for sugar solutions. *Journal of Chemical Education*, 83(10), 1489.

Ballabio, D., and Consonni, V. (2013). Classification tools in chemistry. Part 1: Linear models. PLS-DA. In *Analytical Methods*. <https://doi.org/10.1039/c3ay40582f>

Balram, S. (2003). Manual of Geospatial Science and Technology, edited by John D. Bossler. *Cartography and Geographic Information Science*, 30(2), 231–232. <https://doi.org/10.1559/152304003100011072>

Barker, M., and Rayens, W. (2003). Partial least squares for discrimination. *Journal of Chemometrics*. <https://doi.org/10.1002/cem.785>

Barnes, R. J., Dhanoa, M. S., and Lister, S. J. (1989). Standard normal variate transformation and de-trending of near-infrared diffuse reflectance spectra. *Applied Spectroscopy*, 43(5), 772–777.

Barnes, R. J., Dhanoa, M. S., and Lister, S. J. (1993). Correction to the Description of Standard Normal Variate (SNV) and De-Trend (DT) Transformations in Practical

- Spectroscopy with Applications in Food and Beverage Analysis—2nd Edition .
Journal of Near Infrared Spectroscopy. <https://doi.org/10.1255/jnirs.21>
- Barrett, D., and Gonzalez, C. (1994). Activity of Softening Enzymes during Cherry Maturation. *Journal of Food Science*, 59, 574–577. <https://doi.org/10.1111/j.1365-2621.1994.tb05565.x>
- Basantia, N. C., Nollet, L. M. L., and Kamruzzaman, M. (2018). *Hyperspectral Imaging Analysis and Applications for Food Quality*. CRC Press.
- Behera, S. K., Rath, A. K., and Sethy, P. K. (2021). Maturity status classification of papaya fruits based on machine learning and transfer learning approach. *Information Processing in Agriculture*, 8(2), 244–250. <https://doi.org/10.1016/j.inpa.2020.05.003>
- Berry, S. K. (1981). Fatty acid composition and organoleptic quality of four clones of durian (*Durio zibethinus*, murr.). *Journal of the American Oil Chemists' Society*, 58(6), 716–717.
- Bidlack, W. R. (1998). *Food lipids: chemistry, nutrition and biotechnology*. Taylor and Francis.
- Blankenship, S. M., and Dole, J. M. (2003). 1-Methylcyclopropene: A review. *Postharvest Biology and Technology*, 28(1), 1–25. [https://doi.org/10.1016/S0925-5214\(02\)00246-6](https://doi.org/10.1016/S0925-5214(02)00246-6)
- Bossler, J. D., Campbell, J. B., McMaster, R. B., and Rizos, C. (2010). *Manual of geospatial science and technology*. CRC Press.
- Bradski, G. (2000). *The OpenCV Library*. Dr. Dobb's Journal of Software Tools.
- Breiman, L. (2001). Random forests. *Machine Learning*. <https://doi.org/10.1023/A:1010933404324>
- Brown, S. D., Sarabia, L. A., and Trygg, J. (2009). Comprehensive chemometrics : chemical and biochemical data analysis. *Comprehensive Chemometrics : Chemical and Biochemical Data Analysis*, 1–16. <http://www.sciencedirect.com/science/article/pii/B9780444527011000892>
- Buddenbaum, H., and Steffens, M. (2012). The effects of spectral pretreatments on chemometric analyses of soil profiles using laboratory imaging spectroscopy. *Applied and Environmental Soil Science*, 2012.

- Burns Donald A., C. E. W. (2008). *Handbook_of_Near-Infrared_Analysis_3rd_edition__2008_2.pdf*.
- Campbell, J. B., and Wynne, R. H. (2011). *Introduction to remote sensing*. Guilford Press.
- Castleman, K. R. (1996). *Digital image processing*. Prentice Hall Press.
- Cen, H., Lu, R., Mendoza, F. A., and Ariana, D. . (2011). *Peach maturity / quality assessment using hyperspectral imaging-based spatially-resolved technique ***. 8027, 1–15. <https://doi.org/10.1117/12.883573>
- Cervantes, J., Garcia-Lamont, F., Rodríguez-Mazahua, L., and Lopez, A. (2020). A comprehensive survey on support vector machine classification: Applications, challenges and trends. *Neurocomputing*. <https://doi.org/10.1016/j.neucom.2019.10.118>
- Chandrasekaran, I., Panigrahi, S. S., Ravikanth, L., and Singh, C. B. (2019). Potential of Near-Infrared (NIR) Spectroscopy and Hyperspectral Imaging for Quality and Safety Assessment of Fruits: an Overview. *Food Analytical Methods*, 12(11), 2438–2458. <https://doi.org/10.1007/s12161-019-01609-1>
- Chang, C.-I. (2003). *Hyperspectral imaging: techniques for spectral detection and classification* (Vol. 1). Springer Science and Business Media.
- Chattavongsin, R., and Siriphanich, J. (1990). THE RELATIONSHIP BETWEEN FRUIT-STEM STIFFNESS AND MATURITY OF “MONTHONG” DURIANS (*DURIO ZIBETHINUS* L.). *Acta Horticulturae*, 269, 217–222. <https://doi.org/10.17660/ActaHortic.1990.269.28>
- Chauhan, O. P., Lakshmi, S., Pandey, A. K., Ravi, N., Gopalan, N., and Sharma, R. K. (2017). Non-destructive Quality Monitoring of Fresh Fruits and Vegetables. *Defence Life Science Journal*, 2(2), 103. <https://doi.org/10.14429/dlsj.2.11379>
- Chen, X.-Y., Chen, W.-T., Lv, J.-S., Long, X., and Pang, T. (2017). *Apple Internal Quality Inspection Using Hyperspectral Image Technology*. 44(Wcsn 2016), 768–774. <https://doi.org/10.2991/icwscn-16.2017.155>
- Chen, X., and Ishwaran, H. (2012). Random forests for genomic data analysis. *Genomics*, 99(6), 323–329. <https://doi.org/10.1016/j.ygeno.2012.04.003>
- Chen, Y., and Wang, Z. (2019). Feature selection based convolutional neural network pruning and its application in calibration modeling for NIR spectroscopy.

Chemometrics and Intelligent Laboratory Systems, 191, 103–108.

- Cheng, J. H., Sun, D. W., and Pu, H. (2016). Combining the genetic algorithm and successive projection algorithm for the selection of feature wavelengths to evaluate exudative characteristics in frozen-thawed fish muscle. *Food Chemistry*, 197, 855–863. <https://doi.org/10.1016/j.foodchem.2015.11.019>
- Cheung, N.-M., and Ortega, A. (2009). Distributed compression of hyperspectral imagery. *Distributed Source Coding*, 269–292.
- Chope, G., Terry, L., and White, P. (2006). Effect of controlled atmosphere storage on abscisic acid concentration and other biochemical attributes of onion bulbs. *Postharvest Biology and Technology*, 39, 233–242. <https://doi.org/10.1016/j.postharvbio.2005.10.010>
- Christopher J.C. Burges. (1998). A Tutorial on Support Vector Machines for Pattern Recognition. *Data Mining and Knowledge Discovery*, 2, 121–167.
- Chu, X., Wang, W., Ni, X., Li, C., and Li, Y. (2020). Classifying maize kernels naturally infected by fungi using near-infrared hyperspectral imaging. *Infrared Physics and Technology*, 105, 103242. <https://doi.org/10.1016/j.infrared.2020.103242>
- Chuenatsadongkot, T., Treeamnuk, T., and Treeamnuk, K. (2018). Comparison of the Ability to Evaluation of “Monthong” durian Maturity using Color Value from Spectrometer and Image Processing. In *International Journal of Mechanical And Production Engineering* (Issue 6). <http://iraj.in>
- Comon, P. (1994). Independent component analysis, a new concept? *Signal Processing*, 36(3), 287–314.
- Conzen, J. P. (2006). Multivariate Calibration: A practical guide for developing methods in the quantitative analytical chemistry. *Ettlingen, Germany: BrukerOptik GmbH*.
- Cui, S., Ling, P., Zhu, H., and Keener, H. M. (2018). Plant pest detection using an artificial nose system: A review. In *Sensors (Switzerland)*. <https://doi.org/10.3390/s18020378>
- Cutler, A., and Cutler, D. R. (2012). Ensemble Machine Learning. *Ensemble Machine Learning, January*. <https://doi.org/10.1007/978-1-4419-9326-7>
- Datepumee, N., Sukprasert, P., Jatuporn, C., and Thongkaew, S. (2019). Factors affecting the production of export quality durians by farmers in Chanthaburi Province, Thailand. *Journal of Sustainability Science and Management*, 14(4), 94–

105.

- Daultrey, S. (1976). Concepts and Techniques in Modern Geography - Principal components analysis. *Methods in Molecular Biology (Clifton, N.J.)*, 930. <http://www.ncbi.nlm.nih.gov/pubmed/23086856>
- Davies, E. R. (2009). The application of machine vision to food and agriculture: A review. *Imaging Science Journal*, 57(4), 197–217. <https://doi.org/10.1179/174313109X454756>
- de Oliveira, G. A., de Castilhos, F., Renard, C. M. G. C., and Bureau, S. (2014). Comparison of NIR and MIR spectroscopic methods for determination of individual sugars, organic acids and carotenoids in passion fruit. *Food Research International*. <https://doi.org/10.1016/j.foodres.2013.10.051>
- Deng, L., and Yu, D. (2013). Deep learning: Methods and applications. *Foundations and Trends in Signal Processing*, 7(3–4), 197–387. <https://doi.org/10.1561/20000000039>
- Díaz-Mula, H., Castillo, S., Martínez-Romero, D., Valero, D., Zapata, P., Guillén, F., and Serrano, M. (2009). Sensory, Nutritive and Functional Properties of Sweet Cherry as Affected by Cultivar and Ripening Stage. *Food Science and Technology International - FOOD SCI TECHNOL INT*, 15, 535–543. <https://doi.org/10.1177/1082013209351868>
- Din, S., Rayees Wani, I. A., Ab Waheed Wani, I., Fouzea Nisar, I., Sayeda Farwah, I., Seerat Rizvi, I., Tajamul Farooq Wani, I., Shemoo Nisar, I., Wani, R. A., Waheed Wani, A., Nisar, F., Farwah, S., Rizvi, S., Farooq Wani, T., and Nisar, S. (2019). Fruit set and development: Pre-requisites and enhancement in temperate fruit crops. *Journal of Pharmacognosy and Phytochemistry*, 8(2), 1203–1216.
- Dongare, M. L., Buchade, P. B., Awatade, M. N., and Shaligram, A. D. (2014). Mathematical modeling and simulation of refractive index based Brix measurement system. *Optik*, 125(3), 946–949.
- Du, C. J., and Sun, D. W. (2004). Recent developments in the applications of image processing techniques for food quality evaluation. *Trends in Food Science and Technology*. <https://doi.org/10.1016/j.tifs.2003.10.006>
- Durian Production Guide. (2021). *Department of Agriculture Bureau of Plant*, 53. https://www.buplant.da.gov.ph/images/Production_guide/pdf/DURIAN.pdf
- Echeverria, E., and Ismail, M. (1987). Changes in sugars and acids of citrus fruits during

- storage. *Proc. Fla. State Hortic. Soc.*, 100, 50–52.
- Eismann, M. T. (n.d.). *Hyperspectral Remote Sensing*. SPIE 2012. *PM210*, 748.
- Eitrich, T., and Lang, B. (2006). Efficient optimization of support vector machine learning parameters for unbalanced datasets. *Journal of Computational and Applied Mathematics*. <https://doi.org/10.1016/j.cam.2005.09.009>
- Elmasry, G., Kamruzzaman, M., Sun, D.-W., and Allen, P. (2012). Principles and applications of hyperspectral imaging in quality evaluation of agro-food products: a review. *Critical Reviews in Food Science and Nutrition*, 52(11), 999–1023.
- ElMasry, G., Kamruzzaman, M., Sun, D. W., and Allen, P. (2012). Principles and Applications of Hyperspectral Imaging in Quality Evaluation of Agro-Food Products: A Review. *Critical Reviews in Food Science and Nutrition*, 52(11), 999–1023. <https://doi.org/10.1080/10408398.2010.543495>
- ElMasry, G., and Sun, D. W. (2010). Principles of Hyperspectral Imaging Technology. In *Hyperspectral Imaging for Food Quality Analysis and Control*. <https://doi.org/10.1016/B978-0-12-374753-2.10001-2>
- Elmasry, G., Sun, D. W., and Allen, P. (2012). Near-infrared hyperspectral imaging for predicting color, pH and tenderness of fresh beef. *Journal of Food Engineering*, 110(1), 127–140. <https://doi.org/10.1016/j.jfoodeng.2011.11.028>
- Elmasry, G., Wang, N., Elsayed, A., and Ngadi, M. (2007). *Hyperspectral imaging for nondestructive determination of some quality attributes for strawberry*. 81, 98–107. <https://doi.org/10.1016/j.jfoodeng.2006.10.016>
- Fan, S., Huang, W., and Guo, Z. (2015). *Prediction of Soluble Solids Content and Firmness of Pears Using Hyperspectral Reflectance Imaging*. <https://doi.org/10.1007/s12161-014-0079-1>
- Fukunaga, K. (2013). *Introduction to statistical pattern recognition*. Elsevier.
- Fung, T., and Ledrew, E. (1988). The determination of optimal threshold levels for change detection using various accuracy indices. *Photogrammetric Engineering and Remote Sensing*.
- Gandhi, V. (2015). Interfacing Brain and Machine. *Brain-Computer Interfacing for Assistive Robotics*, 7–63. <https://doi.org/10.1016/B978-0-12-801543-8.00002-8>
- Garillos-Manliguez, C. A., and Chiang, J. Y. (2021). *Multimodal Deep Learning and Visible-Light and Hyperspectral Imaging for Fruit Maturity Estimation*.

<https://doi.org/10.3390/s21041288>

- Gayle Crisosto, G. C., Hasey, J. K., Zegbe, J. A., and Crisosto, C. H. (2012). New quality index based on dry matter and acidity proposed for Hayward kiwifruit. *California Agriculture*, 66(2).
- Giovannoni, J. (2001). Molecular biology of fruit maturation and ripening. *Annual Review of Plant Biology*. <https://doi.org/10.1146/annurev.arplant.52.1.725>
- Gonzalez, R. C., and Woods, R. E. (2008). Digital image processing: Pearson prentice hall. Upper Saddle River, NJ, 1, 376.
- Goulao, L., and Oliveira, C. (2008). Cell wall modifications during fruit ripening: When a fruit is not the fruit. *Trends in Food Science and Technology*, 19, 4–25. <https://doi.org/10.1016/j.tifs.2007.07.002>
- Goutte, C. (1997). Note on free lunches and cross-validation. *Neural Computation*, 9(6), 1245–1249.
- Gowen, A. A., O'Donnell, C. P., Cullen, P. J., Downey, G., and Frias, J. M. (2007). Hyperspectral imaging - an emerging process analytical tool for food quality and safety control. *Trends in Food Science and Technology*, 18(12), 590–598. <https://doi.org/10.1016/j.tifs.2007.06.001>
- Greve, R. (1974). *Phytochemische untersuchungen an der durianfrucht [phytochemical research on the durian fruit]*. Ph. D. Thesis, University of Hamburg.
- Guo, G., Li, S. Z., and Chan, K. (2014). Face Recognition by Support Vector Machines 2 . 1 Basic Theory of Support Vector Machines x x. *Electronic Engineering*.
- Gutiérrez, S., Wendel, A., and Underwood, J. (2019). Spectral filter design based on in-field hyperspectral imaging and machine learning for mango ripeness estimation. *Computers and Electronics in Agriculture*, 164. <https://doi.org/10.1016/J.COMPAG.2019.104890>
- Harel, B., Parmet, Y., and Edan, Y. (2020). Maturity classification of sweet peppers using image datasets acquired in different times. *Computers in Industry*. <https://doi.org/10.1016/j.compind.2020.103274>
- Hart, P. E., Stork, D. G., and Duda, R. O. (2000). *Pattern classification*. Wiley Hoboken.
- Hassan, G. M., and Al-Sager, S. M. (2011). Pecan weevil recognition using support vector machine method. *American Journal of Agricultural and Biological Sciences*, 6(4), 521–526.

- Hassanat, A., Almohammadi, K., Abunawas, E., Hammouri, A., and Surya Prasath, V. B. (2019). *Choosing Mutation and Crossover Ratios for Genetic Algorithms-A Review with a New Dynamic Approach*. 10, 390. <https://doi.org/10.3390/info10120390>
- Holland, J. H. (1992). Genetic algorithms. *Scientific American*, 267(1), 66–72. <https://doi.org/10.1038/scientificamerican0792-66>
- Hruschka, W. R. (1990). Data analysis: wavelength selection methods. *Near Infrared Technology in Agricultural and Food Industries*.
- Hussain, D., Hussain, I., Ismail, M., Alabrah, A., Ullah, S. S., and Alaghbari, H. M. (2022). A Simple and Efficient Deep Learning-Based Framework for Automatic Fruit Recognition. *Computational Intelligence and Neuroscience*, 2022, 6538117. <https://doi.org/10.1155/2022/6538117>
- Isaksson, T., and Naes, T. (1988). Effect of multiplicative scatter correction (MSC) and linearity improvement in NIR spectroscopy. *Applied Spectroscopy*. <https://doi.org/10.1366/0003702884429869>
- Ito, T., Sasaki, K., and Yoshida, Y. (1997). Changes in Respiration Rate, Saccharide and Organic Acid Content during the Development and Ripening of Mango Fruit (*Mangifera indica* L. 'Irwin') Cultured in a Plastic House. *Engei Gakkai Zasshi*, 66, 629–635. <https://doi.org/10.2503/jjshs.66.629>
- Jain, A. K. (1989). *Fundamentals of digital image processing*. Prentice-Hall, Inc.
- Janick, J., and Paull, R. E. (2008). *The encyclopedia of fruit and nuts*. CABI.
- Jaswir, I., CHE MAN, Y. B., Selamat, J., Ahmad, F., and Sugisawa, H. (2008). Retention of volatile components of durian fruit leather during processing and storage. *Journal of Food Processing and Preservation*, 32(5), 740–750.
- Jha, S. N., Jaiswal, P., Narsaiah, K., Gupta, M., Bhardwaj, R., and Singh, A. K. (2012). Non-destructive prediction of sweetness of intact mango using near infrared spectroscopy. *Scientia Horticulturae*. <https://doi.org/10.1016/j.scienta.2012.02.031>
- Jiang, L., Zhu, B., and Tao, Y. (2010). Hyperspectral image classification methods. In *Hyperspectral imaging for food quality analysis and control* (pp. 79–98). Elsevier.
- Jones, D. R. (2001). A Taxonomy of Global Optimization Methods Based on Response Surfaces. *Journal of Global Optimization*. <https://doi.org/10.1023/A:1012771025575>
- Joshi, A., and Bapna, S. (2011). *Comparison Study of Different Pattern Classifiers*. 1–10.

- Julie Caswell, Corinna Noelke, E. M. (2002). Unifying Two Frameworks for Analyzing Quality and Quality Assurance for Food Products. In B. Krissoff, M. Bohman, and J. Caswell (Eds.), *Global Food Trade and Consumer Demand for Quality* (1st ed., pp. 43–61). Springer, Boston, MA. <https://doi.org/https://doi.org/10.1007/978-1-4757-5329-5>
- Kader, A. A. (2008). Flavor quality of fruits and vegetables. *Journal of the Science of Food and Agriculture*, 88(11), 1863–1868.
https://onlinelibrary.wiley.com/doi/pdf/10.1002/jsfa.3293?casa_token=MpLD8m3HJR5AAAAA:gRDL8O7YYfG9C3yc1gvg7qrSAITYq6DaqoFpwzTEHzw1yGp0rEvKClPlmrzwo9JkpVCel07sfbZy
- Kalayanamitra, K., Sornsrivichai, J., and Yantarasri, T. (n.d.). *Model for Evaluation of Maturity Index of Durian Fruit (Durio zibethinus Murray 'Monthong')*.
www.durianpalace.com
- Kamila, N. K. (2015). *Handbook of research on emerging perspectives in intelligent pattern recognition, analysis, and image processing*. IGI Global.
- Kamilaris, A., and Prenafeta-Boldú, F. X. (2018). A review of the use of convolutional neural networks in agriculture. *Journal of Agricultural Science*, 156(3), 312–322.
<https://doi.org/10.1017/S0021859618000436>
- Karichiappan, K., Huat, L. C., and Thai, C. S. (2000). Minimally processed fruits in Singapore. *Preface 11 Opening Address 12*.
- Kasikorn Research Institute. (2021). Kasikorn Research Institute.
<https://kasikornresearch.com/en/analysis/k-econ/business/Pages/Durian-z3233.aspx>
- Kaur, H., and Singh, B. (2013). Classification and Grading Rice Using Multi-Class SVM. *International Journal of Scientific and Research Publications*, 3(4), 1–5.
www.ijsrp.org
- Ketsa, S, and Daengkanit, T. (1998). Changes in softening enzymes of durian fruit ripening. *Acta Horticulturae*, 464(April), 451–454.
<https://doi.org/10.17660/ActaHortic.1998.464.70>
- Ketsa, S, and Pangkool, S. (1995a). Ripening behaviour of durians (*Durio zibethinus* Murray) at different temperatures. *Tropical Agriculture*, 72(2).
- Ketsa, S, and Pangkool, S. (1995b). The effect of temperature and humidity on the

- ripening of durian fruits. *Journal of Horticultural Science*, 70(5), 827–831.
<https://doi.org/10.1080/14620316.1995.11515357>
- Ketsa, S, and Pongkool, S. (2001). Effect of maturity stages and ethylene treatment on ripening of durian fruits. *Proceedings of Australasian Postharvest Horticulture Conference*, 67–72.
- Ketsa, Saichol. (2018a). Durian— Durio zibethinus. In *Exotic Fruits* (pp. 169–180). Elsevier. <https://doi.org/10.1016/b978-0-12-803138-4.00022-8>
- Ketsa, Saichol. (2018b). Durian—Durio zibethinus. In *Exotic Fruits* (pp. 169–180). Elsevier.
- Ketsa, Saichol, and Daengkanit, T. (1998). Physiological changes during postharvest ripening of durian fruit (*Durio zibethinus murray*). *Journal of Horticultural Science and Biotechnology*, 73(5), 575–577.
<https://doi.org/10.1080/14620316.1998.11511017>
- Ketsa, Saichol, and Pangkool, S. (1994). The effect of humidity on ripening of durians. *Postharvest Biology and Technology*, 4, 159–165. [https://doi.org/10.1016/0925-5214\(94\)90017-5](https://doi.org/10.1016/0925-5214(94)90017-5)
- Ketsa, Saichol, Wisutiamonkul, A., Palapol, Y., and Paull, R. E. (2020). The Durian. In *Horticultural Reviews* (pp. 125–211). Wiley.
<https://doi.org/10.1002/9781119625407.ch4>
- Khan, A., Tajammal Munir, M., Yu, W., and Young, B. (n.d.). *Wavelength Selection FOR Rapid Identification of Different Particle Size Fractions of Milk Powder Using Hyperspectral Imaging*. <https://doi.org/10.3390/s20164645>
- Khodabakhshian, R., and Emadi, B. (2018). Application of Vis/SNIR hyperspectral imaging in ripeness classification of pear. *International Journal of Food Properties*, 20(3), S3149–S3163. <https://doi.org/10.1080/10942912.2017.1354022>
- Khojastehnazhand, M., Mohammadi, V., and Minaei, S. (2019). Maturity detection and volume estimation of apricot using image processing technique. *Scientia Horticulturae*, 251(March), 247–251. <https://doi.org/10.1016/j.scienta.2019.03.033>
- Khoo, H. E., Azlan, A., Tang, S. T., and Lim, S. M. (2017). Anthocyanidins and anthocyanins: Colored pigments as food, pharmaceutical ingredients, and the potential health benefits. *Food and Nutrition Research*, 61(1).
<https://doi.org/10.1080/16546628.2017.1361779>

- Kim, J., Kim, B.-S., and Savarese, S. (2012). Comparing Image Classification Methods: K-Nearest-Neighbor and Support-Vector-Machines. *Applied Mathematics in Electrical and Computer Engineering*.
- Koksungnoen, O., and Siriphanich, J. (2008). Anatomical changes during fruit development of durian cvs. Kradum and Monthong. *Agricultural Thai Journal*, 39, 35–44.
- Kong, W., Zhang, C., Cao, F., Liu, F., Luo, S., Tang, Y., and He, Y. (2018). Detection of Sclerotinia stem rot on oilseed rape (*Brassica napus* L.) leaves using hyperspectral imaging. *Sensors (Switzerland)*, 18(6), 1–15. <https://doi.org/10.3390/s18061764>
- Krairiksh, M., Varith, J., and Kanjanavapastit, A. (2011). Wireless Sensor Network for Monitoring Maturity Stage of Fruit. *Wireless Sensor Network*. <https://doi.org/10.4236/wsn.2011.39034>
- Krishnakumar, K., and Goldberg, D. E. (1992). Control system optimization using genetic algorithms. *Journal of Guidance, Control, and Dynamics*, 15(3), 735–740.
- Kuson, P., and Terdwongworakul, A. (2013). Minimally-destructive evaluation of durian maturity based on electrical impedance measurement. *Journal of Food Engineering*, 116(1), 50–56. <https://doi.org/10.1016/j.jfoodeng.2012.11.021>
- Lan, W., Jaillais, B., Renard, C. M. G. C., Leca, A., Chen, S., Le Bourvellec, C., and Bureau, S. (2021). A method using near infrared hyperspectral imaging to highlight the internal quality of apple fruit slices. *Postharvest Biology and Technology*, 175, 111497. <https://doi.org/10.1016/j.postharvbio.2021.111497>
- Landgrebe, D. A. (2003). *Signal theory methods in multispectral remote sensing* (Vol. 24). John Wiley and Sons.
- Lecun, Y., Bengio, Y., and Hinton, G. (2015). Deep learning. *Nature*, 521(7553), 436–444. <https://doi.org/10.1038/nature14539>
- LeCun, Y., Bottou, L., Bengio, Y., and Haffner, P. (1998). Gradient-based learning applied to document recognition. *Proceedings of the IEEE*, 86(11), 2278–2323. <https://doi.org/10.1109/5.726791>
- Lee, L. C., Liong, C. Y., and Jemain, A. A. (2018). Partial least squares-discriminant analysis (PLS-DA) for classification of high-dimensional (HD) data: A review of contemporary practice strategies and knowledge gaps. In *Analyst*. <https://doi.org/10.1039/c8an00599k>

- Leiva-Valenzuela, G. A., Lu, R., and Aguilera, J. M. (2013). Prediction of firmness and soluble solids content of blueberries using hyperspectral reflectance imaging. *Journal of Food Engineering*, 115(1), 91–98. <https://doi.org/10.1016/j.jfoodeng.2012.10.001>
- Li, B., Cobo-medina, M., Lecourt, J., Harrison, N., Harrison, R. J., and Cross, J. V. (2018). *Postharvest Biology and Technology Application of hyperspectral imaging for nondestructive measurement of plum quality attributes*. 141(December 2017), 8–15. <https://doi.org/10.1016/j.postharvbio.2018.03.008>
- Li, J. L., Sun, D. W., and Cheng, J. H. (2016). Recent Advances in Nondestructive Analytical Techniques for Determining the Total Soluble Solids in Fruits: A Review. *Comprehensive Reviews in Food Science and Food Safety*, 15(5), 897–911. <https://doi.org/10.1111/1541-4337.12217>
- Li, Xiaoli, Wei, Y., Xu, J., Feng, X., Wu, F., Zhou, R., Jin, J., Xu, K., Yu, X., and He, Y. (2018). SSC and pH for sweet assessment and maturity classification of harvested cherry fruit based on NIR hyperspectral imaging technology. *Postharvest Biology and Technology*. <https://doi.org/10.1016/j.postharvbio.2018.05.003>
- Li, Xiaona, Wang, M., Liu, Y., Zhang, B., and Zhou, J. (2017). Hyperspectral Imaging and Their Applications in the Nondestructive Quality Assessment of Fruits and Vegetables. *IntechOpen Book Series*, 13. 10.5772/intechopen.72250
- Liaw, A., and Wiener, M. (2002). Classification and Regression with Random Forest. *R News*.
- Lim, M. G., and Chuah, J. H. (2019). Durian types recognition using deep learning techniques. *2018 9th IEEE Control and System Graduate Research Colloquium, ICSGRC 2018 - Proceeding, August 2018*, 183–187. <https://doi.org/10.1109/ICSGRC.2018.8657535>
- Lim, T. ., and Luders, L. (1997). *Boosting Durian Productivity*. Publication No. 97/001W. Northern Territory Department of Primary Industry and Fisheries, Australia.
- Liu, D., Sun, D. W., and Zeng, X. A. (2014). Recent advances in wavelength selection techniques for hyperspectral image processing in the food industry. *Food and Bioprocess Technology*, 7(2), 307–323. <https://doi.org/10.1007/s11947-013-1193-6>
- Liu, D., Zeng, X.-A., and Sun, D.-W. (2015). Recent developments and applications of hyperspectral imaging for quality evaluation of agricultural products: a review. *Critical Reviews in Food Science and Nutrition*, 55(12), 1744–1757.

- Liu, H., Liu, J., Huang, H., Evrendilek, F., Wen, S., and Li, W. (2020). *Optimizing bioenergy and by-product outputs from durian shell pyrolysis*.
<https://doi.org/10.1016/j.renene.2020.09.044>
- Liu, Z., Yu, H., and MacGregor, J. F. (2007). Standardization of line-scan NIR imaging systems. *Journal of Chemometrics*, 21(3–4), 88–95.
<https://doi.org/10.1002/cem.1038>
- Lizada, Ma C Concepcion Ikeda, F., and Chachin, K. (1998). Quality problems in important fruit crops in ASEAN. *Journal of the Japanese Society for Horticultural Science*, 67(6), 1164–1166.
- Lorente, D., Aleixos, N., Gómez-Sanchis, J., Cubero, S., García-Navarrete, O. L., and Blasco, J. (2012). Recent Advances and Applications of Hyperspectral Imaging for Fruit and Vegetable Quality Assessment. *Food Bioprocess Technol*, 5, 1121–1142.
<https://doi.org/10.1007/s11947-011-0725-1>
- Lu, R. (2003). Detection of bruises on apples using near-infrared hyperspectral imaging. *Transactions of the American Society of Agricultural Engineers*, 46(2), 523–530.
<https://doi.org/10.13031/2013.12941>
- Lu, Y., Huang, Y., and Lu, R. (n.d.). *Innovative Hyperspectral Imaging-Based Techniques for Quality Evaluation of Fruits and Vegetables: A Review*.
<https://doi.org/10.3390/app7020189>
- Lu, Y., Saeys, W., Kim, M., Peng, Y., and Lu, R. (2020). Hyperspectral imaging technology for quality and safety evaluation of horticultural products: A review and celebration of the past 20-year progress. *Postharvest Biology and Technology*, 170(July), 111318. <https://doi.org/10.1016/j.postharvbio.2020.111318>
- Ma, T., Li, X., Inagaki, T., Yang, H., and Tsuchikawa, S. (2017). *Noncontact evaluation of soluble solids content in apples by near-infrared hyperspectral imaging*.
<https://doi.org/10.1016/j.jfoodeng.2017.12.028>
- Magwaza, L. S., and Opara, U. L. (2015). Analytical methods for determination of sugars and sweetness of horticultural products-A review. In *Scientia Horticulturae*.
<https://doi.org/10.1016/j.scienta.2015.01.001>
- Mamouei, M., Budidha, K., Baishya, N., Qassem, M., and Kyriacou, P. (2020). Comparison of wavelength selection methods for in-vitro estimation of lactate: a new unconstrained, genetic algorithm-based wavelength selection. *Scientific Reports* |, 10, 16905. <https://doi.org/10.1038/s41598-020-73406-4>

- Manickavasagan, A., Al-Mezeini, N. K., and Al-Shekaili, H. N. (2014). RGB color imaging technique for grading of dates. *Scientia Horticulturae*.
<https://doi.org/10.1016/j.scienta.2014.06.003>
- Maninang, J. S., Wongs-Aree, C., Kanlayanarat, S., Sugaya, S., and Gemma, H. (2011a). Influence of maturity and postharvest treatment on the volatile profile and physiological properties of the durian (*Durio zibethinus* Murray) fruit. *International Food Research Journal*.
- Maninang, J. S., Wongs-Aree, C., Kanlayanarat, S., Sugaya, S., and Gemma, H. (2011b). Influence of maturity and postharvest treatment on the volatile profile and physiological properties of the durian (*Durio zibethinus* Murray) fruit. *International Food Research Journal*, 18(3), 1067–1075.
- Manivel-Chávez, R. A., Garnica-Romo, M. G., Arroyo-Correa, G., and Aranda-Sánchez, J. I. (2011). Optical and mechanical nondestructive tests for measuring tomato fruit firmness. *22nd Congress of the International Commission for Optics: Light for the Development of the World*, 8011(June 2016), 801176.
<https://doi.org/10.1117/12.902157>
- Marquetti, I., Link, J. V., Lemes, A. L. G., Scholz, M. B. dos S., Valderrama, P., and Bona, E. (2016). Partial least square with discriminant analysis and near infrared spectroscopy for evaluation of geographic and genotypic origin of arabica coffee. *Computers and Electronics in Agriculture*.
<https://doi.org/10.1016/j.compag.2015.12.018>
- Marten, G. C., Brink, G. E., Buxton, D. R., Halgerson, J. L., and Hornstein, J. S. (1984). Near Infrared Reflectance Spectroscopy Analysis of Forage Quality in Four Legume Species 1. *Crop Science*, 24(6), 1179–1182.
- Martinsen, P., and Schaare, P. (1998). Measuring soluble solids distribution in kiwifruit using near-infrared imaging spectroscopy. *Postharvest Biology and Technology*, 14(3), 271–281.
- McGlone, V. A., Jordan, R. B., Seelye, R., and Clark, C. J. (2003). Dry-matter—a better predictor of the post-storage soluble solids in apples? *Postharvest Biology and Technology*, 28(3), 431–435.
- Mendoza, F., and Lu, R. (2015). Basics of image analysis. In *Hyperspectral imaging technology in food and agriculture* (pp. 9–56). Springer.
- Mohammadi, V., Kheiralipour, K., and Ghasemi-Varnamkhasti, M. (2015). Detecting

- maturity of persimmon fruit based on image processing technique. *Scientia Horticulturae*. <https://doi.org/10.1016/j.scienta.2014.12.037>
- Mohanty, N., John, A. L. S., Manmatha, R., and Rath, T. M. (2013). Shape-based image classification and retrieval. In *Handbook of Statistics*. <https://doi.org/10.1016/B978-0-444-53859-8.00010-2>
- Mohd Ali, M., Hashim, N., Aziz, S. A., and Lasekan, O. (2020a). Exploring the chemical composition, emerging applications, potential uses, and health benefits of durian: A review. *Food Control*, 113(January), 107189. <https://doi.org/10.1016/j.foodcont.2020.107189>
- Mohd Ali, M., Hashim, N., Aziz, S. A., and Lasekan, O. (2020b). Exploring the chemical composition, emerging applications, potential uses, and health benefits of durian: A review. In *Food Control* (Vol. 113). Elsevier Ltd. <https://doi.org/10.1016/j.foodcont.2020.107189>
- Morales, A., Guerra, R., Horstrand, P., Diaz, M., Jimenez, A., Melian, J., Lopez, S., and Lopez, J. F. (2020). A multispectral camera development: From the prototype assembly until its use in a UAV system. *Sensors (Switzerland)*. <https://doi.org/10.3390/s20216129>
- Moran, M. S., Inoue, Y., and Barnes, E. M. (1997). Opportunities and limitations for image-based remote sensing in precision crop management. *Remote Sensing of Environment*, 61(3), 319–346.
- Morimoto, T., Purwanto, W., Suzuki, J., and Hashimoto, Y. (1997). Optimization of heat treatment for fruit during storage using neural networks and genetic algorithms. *Computers and Electronics in Agriculture*, 19(1), 87–101. [https://doi.org/10.1016/S0168-1699\(97\)00037-9](https://doi.org/10.1016/S0168-1699(97)00037-9)
- Moser, R., Raffaelli, R., and Thilmany-McFadden, D. (2011). Consumer preferences for fruit and vegetables with credence-based attributes: A review. *International Food and Agribusiness Management Review*, 14(2), 121–142. <https://doi.org/10.22004/ag.econ.103990>
- Munera, S., Besada, C., Aleixos, N., Talens, P., Salvador, A., Sun, D. W., Cubero, S., and Blasco, J. (2017). Non-destructive assessment of the internal quality of intact persimmon using color and VIS/NIR hyperspectral imaging. *Lwt*, 77, 241–248. <https://doi.org/10.1016/j.lwt.2016.11.063>
- Munera, S., Blasco, J., Amigo, J. M., Cubero, S., Talens, P., and Aleixos, N. (2019). Use of

- hyperspectral transmittance imaging to evaluate the internal quality of nectarines. *Biosystems Engineering*, 182, 54–64.
<https://doi.org/10.1016/j.biosystemseng.2019.04.001>
- Najeeb, T., and Safar, M. (2018). Dates maturity status and classification using image processing. *2018 International Conference on Computing Sciences and Engineering, ICCSE 2018 - Proceedings*, 1–6.
<https://doi.org/10.1109/ICCSE1.2018.8374209>
- Narendra, V. G., and Hareesha, K. S. (2010). Quality inspection and grading of agricultural and food products by computer vision-a review. *International Journal of Computer Applications*, 2(1), 43–65.
- Nasiri, A., Taheri-Garavand, A., and Zhang, Y. D. (2019). Image-based deep learning automated sorting of date fruit. *Postharvest Biology and Technology*, 153, 133–141. <https://doi.org/10.1016/J.POSTHARVBIO.2019.04.003>
- Ncama, K., Magwaza, L. S., Poblete-Echeverría, C. A., Nieuwoudt, H. H., Tesfay, S. Z., and Mditshwa, A. (2018). On-tree indexing of ‘Hass’ avocado fruit by non-destructive assessment of pulp dry matter and oil content.’ *Biosystems Engineering*, 174, 41–49. <https://doi.org/10.1016/j.biosystemseng.2018.06.011>
- Ngadi, M. O., and Liu, L. (2010). Hyperspectral image processing techniques. In *Hyperspectral imaging for food quality analysis and control* (pp. 99–127). Elsevier.
- Nicolai, B. M., Verlinden, B. E., Desmet, M., Saevels, S., Saeys, W., Theron, K., Cubeddu, R., Pifferi, A., and Torricelli, A. (2008). Time-resolved and continuous wave NIR reflectance spectroscopy to predict soluble solids content and firmness of pear. *Postharvest Biology and Technology*, 47(1), 68–74.
- Onsawai, P., Phetpan, K., Khurnpoon, L., and Sirisomboon, P. (2020). Evaluation of physiological properties and texture trait of durian pulp using pulp and intact fruit spectra by near infrared spectroscopic technique. *Measurement*.
<https://doi.org/10.1016/j.measurement.2020.108684>
- Onsawai, P., Phetpan, K., Khurnpoon, L., and Sirisomboon, P. (2021). Evaluation of physiological properties and texture traits of durian pulp using near-infrared spectra of the pulp and intact fruit. *Measurement*, 174, 108684.
<https://doi.org/10.1016/j.measurement.2020.108684>
- Osborne, B. G., Fearn, T., and Hindle, P. H. (1993). Practical NIR spectroscopy with

- applications in food and beverage analysis. In *Longman Scientific and Technical*.
- Osuna, E., Freund, R., and Girosi, F. (1997). Training support vector machines: An application to face detection. *Proceedings of the IEEE Computer Society Conference on Computer Vision and Pattern Recognition*, 130–136. <https://doi.org/10.1109/cvpr.1997.609310>
- Pakcharoen, A., Tisarum, R., and Siriphanich, J. (2013). Factors affecting uneven fruit ripening in “Mon-Thong” durian. *Acta Horticulturae*. <https://doi.org/10.17660/actahortic.2013.975.40>
- Pal, T., Jaiswal, V., and Chauhan, R. S. (2016). DRPPP: A machine learning based tool for prediction of disease resistance proteins in plants. *Computers in Biology and Medicine*. <https://doi.org/10.1016/j.compbiomed.2016.09.008>
- Palmieri, F., and Fiore, U. (2010). Network anomaly detection through nonlinear analysis. *Computers and Security*, 29(7), 737–755. <https://doi.org/10.1016/J.COSE.2010.05.002>
- Pan, F., Song, G., Gan, X., and Gu, Q. (2014). Consistent feature selection and its application to face recognition. *Journal of Intelligent Information Systems*, 43(2), 307–321.
- Pareek, S. (2016). Postharvest Ripening Physiology of Crops. In *Postharvest Ripening Physiology of Crops*.
- Park, B., and Lu, R. (2015a). Hyperspectral imaging technology in food and agriculture. In *Hyperspectral Imaging Technology in Food and Agriculture*. <https://doi.org/10.1007/978-1-4939-2836-1>
- Park, B., and Lu, R. (2015b). Hyperspectral imaging technology in food and agriculture. In *Hyperspectral Imaging Technology in Food and Agriculture* (Issue January 2015). <https://doi.org/10.1007/978-1-4939-2836-1>
- Pascua, O. C., and Cantila, M. S. (1992). Maturity indices of durian (*Durio zibethinus* Murray). *Philippines Journal of Crop Science*, 17(3), 119–124.
- Paul, V., Pandey, R., and Srivastava, G. C. (n.d.). *The fading distinctions between classical patterns of ripening in climacteric and non-climacteric fruit and the ubiquity of ethylene-An overview*. 2011. <https://doi.org/10.1007/s13197-011-0293-4>
- Paull, R. E., and Ketsa, S. (2014). Durian: postharvest quality-maintenance guidelines.

Fruit, Nut, and Beverage Crops, 1–4.

Pech, J. C., Purgatto, E., Bouzayen, M., and Latché, A. (2012). Ethylene and Fruit Ripening. *The Plant Hormone Ethylene*, 44(January), 275–304.

<https://doi.org/10.1002/9781118223086.ch11>

Pedregosa, F., Varoquaux, G., Gramfort, A., Michel, V., Thirion, B., Grisel, O., Blondel, M., Prettenhofer, P., and Weiss, R., Dubourg, V., Vanderplas, J., Passos, A., Cournapeau, D., Brucher, M., Perrot, M., and Duchesnay, E. (2011). Scikit-learn: Machine Learning in {P}ython. *Journal of Machine Learning Research*, 12, 2825–2830.

Phothisonothai, M. (2010). Nondestructive maturity classification of durian based on fractal features. *10th International Conference on Information Sciences, Signal Processing and Their Applications, ISSPA 2010*.

<https://doi.org/10.1109/ISSPA.2010.5605440>

Phuangsoambut, K., Phuangsoambut, A., Talabnark, A., and Terdwongworakul, A. (2018). Empirical reduction of rind effect on rind and flesh absorbance for evaluation of durian maturity using near infrared spectroscopy. *Postharvest Biology and Technology*, 142, 55–59. <https://doi.org/10.1016/j.postharvbio.2018.04.004>

Pitak, L., Sirisomboon, P., Saengprachatanarug, K., Wongpichet, S., and Posom, J. (2021). Rapid elemental composition measurement of commercial pellets using line-scan hyperspectral imaging analysis. *Energy*, 220, 119698.

<https://doi.org/10.1016/j.energy.2020.119698>

Plaza, A., Benediktsson, J. A., Boardman, J. W., Brazile, J., Bruzzone, L., Camps-Valls, G., Chanussot, J., Fauvel, M., Gamba, P., and Gualtieri, A. (2009). Recent advances in techniques for hyperspectral image processing. *Remote Sensing of Environment*, 113, S110–S122.

Porwal, U., Shi, Z., and Setlur, S. (2013). Machine learning in handwritten arabic text recognition. In *Handbook of Statistics*. <https://doi.org/10.1016/B978-0-444-53859-8.00018-7>

Pouladzadeh, P., Villalobos, G., Almaghrabi, R., and Shirmohammadi, S. (2012). A novel SVM based food recognition method for calorie measurement applications.

Proceedings of the 2012 IEEE International Conference on Multimedia and Expo Workshops, ICMEW 2012, 495–498. <https://doi.org/10.1109/ICMEW.2012.92>

Preedy, V. R. (2008). *Tomatoes and Tomato Products : Nutritional, Medicinal and*

- Therapeutic Properties*. CRC Press.
<http://public.ebookcentral.proquest.com/choice/publicfullrecord.aspx?p=544102>
- Pu, Y.-Y., Feng, Y.-Z., and Sun, D.-W. (n.d.). *Recent Progress of Hyperspectral Imaging on Quality and Safety Inspection of Fruits and Vegetables: A Review*.
<https://doi.org/10.1111/1541-4337.12123>
- Pullanagari, R. R., and Li, M. (2020). Uncertainty assessment for firmness and total soluble solids of sweet cherries using hyperspectral imaging and multivariate statistics. *Journal of Food Engineering*, 289(January 2020).
<https://doi.org/10.1016/j.jfoodeng.2020.110177>
- Qin, J. (2010). Hyperspectral imaging instruments. In *Hyperspectral imaging for food quality analysis and control* (pp. 129–172). Elsevier.
- Qin, J., Chao, K., Kim, M. S., Lu, R., and Burks, T. F. (2013). Hyperspectral and multispectral imaging for evaluating food safety and quality. *Journal of Food Engineering*, 118(2), 157–171. <https://doi.org/10.1016/j.jfoodeng.2013.04.001>
- Rajkumar, P., Wang, N., Elmasry, G., Raghavan, G. S. V., and Garipey, Y. (2012a). Studies on banana fruit quality and maturity stages using hyperspectral imaging. *Journal of Food Engineering*. <https://doi.org/10.1016/j.jfoodeng.2011.05.002>
- Rajkumar, P., Wang, N., Elmasry, G., Raghavan, G. S. V., and Garipey, Y. (2012b). Studies on banana fruit quality and maturity stages using hyperspectral imaging. *Journal of Food Engineering*, 108(1), 194–200.
<https://doi.org/10.1016/j.jfoodeng.2011.05.002>
- RBH, W., and Golding, J. (2016). *Postharvest: An Introduction to the Physiology and Handling of Fruit and Vegetables*. 6th Edition.
- Richards, J. A. (1984). Thematic mapping from multitemporal image data using the principal components transformation. *Remote Sensing of Environment*, 16(1), 35–46.
- Rinnan, Å., Van Den Berg, F., and Engelsen, S. B. (2009). Review of the most common pre-processing techniques for near-infrared spectra. *TrAC Trends in Analytical Chemistry*, 28(10), 1201–1222.
- Roger, J.-M., Boulet, J.-C., Zeaiter, M., and Rutledge, D. N. (2020). Pre-processing Methods. In *Comprehensive Chemometrics*. <https://doi.org/10.1016/b978-0-12-409547-2.14878-4>

- Ruiz-Altisent, M., Ruiz-Garcia, L., Moreda, G. P., Lu, R., Hernandez-Sanchez, N., Correa, E. C., Diezma, B., Nicolaï, B., and García-Ramos, J. (2010). Sensors for product characterization and quality of specialty crops—A review. *Computers and Electronics in Agriculture*, 74(2), 176–194.
- Rungpichayapichet, P., Nagle, M., Yuwanbun, P., Khuwijitjaru, P., Mahayothee, B., and Müller, J. (2017). Prediction mapping of physicochemical properties in mango by hyperspectral imaging. *Biosystems Engineering*, 159(2011), 109–120.
<https://doi.org/10.1016/j.biosystemseng.2017.04.006>
- Rutpralom, T., Kumhom, P., and Chamnongthai, K. (2002). Nondestructive maturity determination of durian by using microwave moisture sensing. *Proceedings of the IEEE International Conference on Industrial Technology*.
<https://doi.org/10.1109/ICIT.2002.1189881>
- Saechua, W., Sharma, S., Nakawajana, N., and Leepaitoon, K. (2021). Postharvest Biology and Technology Integrating Vis-SWNIR spectrometer in a conveyor system for in-line measurement of dry matter content and soluble solids content of durian pulp. *Postharvest Biology and Technology*, 181(June), 111640.
<https://doi.org/10.1016/j.postharvbio.2021.111640>
- Saechua, W., Sharma, S., Nakawajana, N., Leepaitoon, K., Chunsri, R., Posom, J., Roeksukrungrueang, C., Siritechavong, T., Phanomsophon, T., Sirisomboon, P., Lapcharoensuk, R., and Pornchaloempong, P. (2021). Integrating Vis-SWNIR spectrometer in a conveyor system for in-line measurement of dry matter content and soluble solids content of durian pulp. *Postharvest Biology and Technology*, 181, 111640. <https://doi.org/10.1016/j.postharvbio.2021.111640>
- Sahachairungrueng, W., and Teerachaichayut, S. (2022). *Nondestructive quality assessment of longans using near infrared hyperspectral imaging*. 24(1).
- Saini, R. K., Nile, S. H., and Park, S. W. (2015). Carotenoids from fruits and vegetables: Chemistry, analysis, occurrence, bioavailability and biological activities. *Food Research International*, 76(February 2016), 735–750.
<https://doi.org/10.1016/j.foodres.2015.07.047>
- Sandak, J., Sandak, A., and Meder, R. (2016). *Assessing trees, wood and derived products with near infrared spectroscopy: hints and tips*.
<https://doi.org/10.1255/jnirs.1255>
- Sangwanangkul, P. (1998). *Growth and development of durian fruit cv. Monthong and*

the effect of ethephon preharvest treatment.

- Sangwanangkul, P., and Siriphanich, J. (2000). Growth and maturation of durian fruit cv. Monthong. *Thai J. Agric. Sci.*, 33, 75–82.
- Saporo, A., Tadé, M. O., and Vuthaluru, H. (2012). A modified Kennard-Stone algorithm for optimal division of data for developing artificial neural network models. *Chemical Product and Process Modeling*, 7(1). <https://doi.org/10.1515/1934-2659.1645>
- Šašić, S., and Ozaki, Y. (2001). Short-wave near-infrared spectroscopy of biological fluids. 1. Quantitative analysis of fat, protein, and lactose in raw milk by partial least-squares regression and band assignment. *Analytical Chemistry*, 73(1), 64–71. <https://doi.org/10.1021/ac000469c>
- Satti, V., Satya, A., and Sharma, S. (2013). An automatic leaf recognition system for plant identification using machine vision technology. *International Journal of Engineering Science and Technology*, 5(4), 874.
- Schölkopf, B., Smola, A., and Müller, K.-R. (1998). Nonlinear component analysis as a kernel eigenvalue problem. *Neural Computation*, 10(5), 1299–1319.
- Serrano, M., Guillén, F., Martínez-Romero, D., Castillo, S., and Valero, D. (2005). Chemical Constituents and Antioxidant Activity of Sweet Cherry at Different Ripening Stages. *Journal of Agricultural and Food Chemistry*, 53, 2741–2745. <https://doi.org/10.1021/jf0479160>
- Seymour, G. B., Taylor, J. E., and Tucker, G. A. (1993). *Biochemistry of fruit ripening*. Chapman and Hall.
- Seymour, Graham B., Ostergaard, L., Chapman, N. H., Knapp, S., and Martin, C. (2013). Fruit development and ripening. In *Annual Review of Plant Biology*. <https://doi.org/10.1146/annurev-arplant-050312-120057>
- Sharma, S., Sumesh, K. C., and Sirisomboon, P. (2021). Rapid ripening stage classification and dry matter prediction of durian pulp using a pushbroom near infrared hyperspectral imaging system. *Measurement: Journal of the International Measurement Confederation*, October, 110464. <https://doi.org/10.1016/j.measurement.2021.110464>
- Shaw, G., and Manolakis, D. (2002). Signal processing for hyperspectral image exploitation. *IEEE Signal Processing Magazine*, 19(1), 12–16.

- Shijie Tian, H. X. (2022). Mechanical-based and Optical-based Methods for Nondestructive Evaluation of Fruit Firmness. *Food Reviews International*, 1–31. <https://doi.org/https://doi.org/10.1080/87559129.2021.2015376>
- Shorman, S. M., and Pitchay, S. A. (2015). Significance of parameters in genetic algorithm, the strengths, its limitations and challenges in image recovery. *ARPN Journal of Engineering and Applied Sciences*, 10(2), 585–593.
- Siriphanich. (2011). 5 Durian (*Durio zibethinus* Merr.). In *Postharvest biology and technology of tropical and subtropical fruits: Volume 3: Cocona to mango*. <https://doi.org/10.1016/B978-1-84569-735-8.50005-X>
- Siriphanich, J., and Khurnpoon, L. (2003). Dry matter as a possible maturity index of Monthong durians. *Thai Journal of Agricultural Science (Thailand)*.
- Sitts, M. K. (2000). *Handbook for digital projects: a management tool for preservation and access (computer file)*.
- Somton, W., Pathaveerat, S., and Terdwongworakul, A. (2015). Application of near infrared spectroscopy for indirect evaluation of “Monthong” durian maturity. *International Journal of Food Properties*, 18(6), 1155–1168. <https://doi.org/10.1080/10942912.2014.891609>
- Stark, J. A., and Fitzgerald, W. J. (1996). An alternative algorithm for adaptive histogram equalization. *Graphical Models and Image Processing*, 58(2), 180–185.
- Su, W. H., and Sun, D. W. (2018). Multispectral Imaging for Plant Food Quality Analysis and Visualization. *Comprehensive Reviews in Food Science and Food Safety*. <https://doi.org/10.1111/1541-4337.12317>
- Subhadrabandhu, S., and Ketsa, S. (2001). *Durian: King of Tropical Fruit*. D. Brasell. <https://books.google.co.th/books?id=1t1tQgAACAAJ>
- Sun, D.-W. (2010). *Hyperspectral imaging for food quality analysis and control*. Elsevier.
- Sutthaphan, S. (1993). *Postharvest changes in chemical composition of 'Chanee' and 'Monthong' durians pulp*.
- Swinehart, D. F. (1962). The Beer-Lambert law. *Journal of Chemical Education*, 39(7), 333–335. <https://doi.org/10.1021/ed039p333>
- Tadeo, J. L., Ortiz, J. M., and Estelles, A. (1987). Sugar changes in Clementine and orange fruit during ripening. *J. Hort. Sci.*, 62, 531–537.

<https://doi.org/10.1080/14620316.1987.11515817>

- Tan, Y. A., Low, K. W., Lee, C. K., and Low, K. S. (2010). Imaging technique for quantification of oil palm fruit ripeness and oil content. *European Journal of Lipid Science and Technology*. <https://doi.org/10.1002/ejlt.201000020>
- Tantisoparak, T., Moon, H., Youryon, P., Bunya-Athichart, K., Krairiksh, M., and Sarkar, T. K. (2016). Nondestructive Determination of the Maturity of the Durian Fruit in the Frequency Domain Using the Change in the Natural Frequency. *IEEE Transactions on Antennas and Propagation*, 64(5), 1779–1787. <https://doi.org/10.1109/TAP.2016.2533660>
- Teena, M., Manickavasagan, A., Mothershaw, A., El Hadi, S., and Jayas, D. S. (2013). Potential of machine vision techniques for detecting fecal and microbial contamination of food products: A review. *Food and Bioprocess Technology*, 6(7), 1621–1634.
- Thai Agricultural Standard*. (n.d.). October 2003. <https://www.acfs.go.th/standard/download/eng/durians.pdf>
- Thai Customs*. (n.d.). July 2021. http://www.customs.go.th/statistic_report.php?show_search=1ands=COfxRnOQzEo34pVh
- Tharwat, A., Gaber, T., Ibrahim, A., and Hassanien, A. E. (2017). Linear discriminant analysis: A detailed tutorial. *AI Communications*. <https://doi.org/10.3233/AIC-170729>
- Thenkabail, P. S., and Lyon, J. G. (2016). *Hyperspectral remote sensing of vegetation*. CRC press.
- Timberlake, C. . (1981). Anthocyanins in fruits and vegetables. In J. Friend and M. J. C. Rhodes (Eds.), *Recent Advances in the Biochemistry of Fruits and Vegetables* (pp. 221–247). Academic Press.
- Timkhum, P., and Terdwongworakul, A. (2012). Non-destructive classification of durian maturity of “Monthong” cultivar by means of visible spectroscopy of the spine. *Journal of Food Engineering*, 112(4), 263–267. <https://doi.org/10.1016/j.jfoodeng.2012.05.018>
- Titova, T. P., Nachev, V. G., Damyanov, C. I., and Nikovski, P. I. (2013). Intelligent classifiers for non-destructive determination of food quality. *Facta Universitatis*,

Series: Automatic Control and Robotics, 12(1), 19–30.

- Tongdee, S. C., Chayasombat, A., and Neamprem, S. (1988). Effect of harvest maturity on respiration, ethylene production and the composition of internal atmosphere of durian (*Durio zibethinus* Murr.). *Proceedings of a Seminar on Durian. Thailand Institute of Scientific and Technological Research, Bangkok*, 31–36.
- Vadivambal, R., and Jayas, D. S. (2015). Bio-imaging: Principles, techniques, and applications. In *Bio-Imaging: Principles, Techniques, and Applications*. <https://doi.org/10.1201/b18840>
- Valero, D., and Serrano, M. (2010). Postharvest biology and technology for preserving fruit quality. *Postharvest Biology and Technology for Preserving Fruit Quality, May*, 1–271. <https://doi.org/10.1201/9781439802670>
- Van der Meer, F. D., and De Jong, S. M. (2011). *Imaging spectrometry: basic principles and prospective applications* (Vol. 4). Springer Science and Business Media.
- Van Straten, S., De Vrijer, F. L., and De Beauveser, J. C. (1977). Volatile Components in Foods. *Central Institute for Nutrition and Food Research, TNO Zeist, The Netherlands*.
- Vapnik, V. (1999). *The nature of statistical learning theory*. Springer science and business media.
- Varmuza, K., and Filzmoser, P. (2016). *Introduction to multivariate statistical analysis in chemometrics*. CRC press.
- Vega Díaz, J. J., Sandoval Aldana, A. P., and Reina Zuluaga, D. V. (2021). Prediction of dry matter content of recently harvested ‘Hass’ avocado fruits using hyperspectral imaging. *Journal of the Science of Food and Agriculture, 101(3)*, 897–906. <https://doi.org/10.1002/jsfa.10697>
- Walsh, K. B., Blasco, J., Zude-Sasse, M., and Sun, X. (2020). Visible-NIR ‘point’ spectroscopy in postharvest fruit and vegetable assessment: The science behind three decades of commercial use. *Postharvest Biology and Technology, 168*(April 2019), 111246. <https://doi.org/10.1016/j.postharvbio.2020.111246>
- Wardowski, W., Grierson, S. W., and Westbrook, G. (1979). Florida Citrus quality test. *Fla. Coop. Extens. Serv. Bull.*, 188, 3–4.
- Wattanawichian, K., Siangjaew, K., Pongphan, P., and Atthasophonrak, T. (2002). The study of tensile properties of durian stems of different ages. *Proceedings of the*

- 40th Kasetsart University Annual Conference: Engineering, 255–262.
https://kukrdb.lib.ku.ac.th/proceedings/kucon/search_detail/result/8220
- Wei, X., He, J. C., Ye, D. P., and Jie, D. F. (2017). Navel Orange Maturity Classification by Multispectral Indexes Based on Hyperspectral Diffuse Transmittance Imaging. *Journal of Food Quality*. <https://doi.org/10.1155/2017/1023498>
- Welling, M. (2005). *Fisher linear discriminant analysis, vol. 3. department of computer science, university of toronto*. Amsterdam, Netherlands: Elsevier.
- Williams, P., and Antoniszyn, J. (2019). Near-infrared Technology: Getting the best out of light. In *Near-infrared Technology: Getting the best out of light*. <https://doi.org/10.18820/9781928480310>
- Wisutiamonkul, A., Ampomah-Dwamena, C., Allan, A., and Ketsa, S. (2017). Carotenoid accumulation and gene expression during durian (*Durio zibethinus*) fruit growth and ripening. *Scientia Horticulturae*, 220, 233–242. <https://doi.org/10.1016/j.scienta.2017.03.048>
- Wisutiamonkul, A., Promdang, S., Ketsa, S., and Doorn, W. (2015). Carotenoids in durian fruit pulp during growth and postharvest ripening. *Food Chemistry*, 180. <https://doi.org/10.1016/j.foodchem.2015.01.129>
- Wisutiamonkul, A., Promdang, S., Ketsa, S., and Van Doorn, G. (2015). Carotenoids in durian fruit pulp during growth and postharvest ripening. *Food Chemistry*, 180, 301–305. <https://doi.org/10.1016/j.foodchem.2015.01.129>
- Wold, S., Sjöström, M., and Eriksson, L. (2001). PLS-regression: A basic tool of chemometrics. *Chemometrics and Intelligent Laboratory Systems*. [https://doi.org/10.1016/S0169-7439\(01\)00155-1](https://doi.org/10.1016/S0169-7439(01)00155-1)
- Workman, J. . J., and Weyer, L. (2007). Practical Guide to Interpretive Near-Infrared Spectroscopy. In *Practical Guide to Interpretive Near-Infrared Spectroscopy*. <https://doi.org/10.1201/9781420018318>
- Wu, J., Chen, X. Y., Zhang, H., Xiong, L. D., Lei, H., and Deng, S. H. (2019). Hyperparameter optimization for machine learning models based on Bayesian optimization. *Journal of Electronic Science and Technology*. <https://doi.org/10.11989/JEST.1674-862X.80904120>
- Xia, Z., Zhang, C., Weng, H., Nie, P., and He, Y. (2017). Sensitive Wavelengths Selection in Identification of *Ophiopogon japonicus* Based on Near-Infrared Hyperspectral

- Imaging Technology. *International Journal of Analytical Chemistry*, 2017.
<https://doi.org/10.1155/2017/6018769>
- Xie, L. J., Wang, A. C., Xu, H. R., Fu, X. P., and Ying, Y. B. (2016). Applications of Near-infrared systems for quality evaluation of fruits: A review. *Transactions of the ASABE*, 59(2), 399–419. <https://doi.org/10.13031/trans.59.10655>
- Xing, J., and De Baerdemaeker, J. (2005). Bruise detection on ‘Jonagold’ apples using hyperspectral imaging. *Postharvest Biology and Technology*, 37(2), 152–162.
<https://doi.org/10.1016/J.POSTHARVBIO.2005.02.015>
- Yaacob, O. (1983). The growth pattern and nutrient uptake of durian (*Durio zibethinus* Murr.) on an oxisol. *Communications in Soil Science and Plant Analysis*, 14(8), 689–698. <https://doi.org/10.1080/00103628309367400>
- Yahia, E. M. (2011). Postharvest Biology and Technology of Tropical and Subtropical Fruits. In *Postharvest Biology and Technology of Tropical and Subtropical Fruits* (Vol. 2). <https://doi.org/10.1533/9780857092762>
- Yamaguchi, S., Yoshikawa, T., Ikeda, S., and Ninomiya, T. (1970). Studies on the taste of some sweet substances. Part I. Measurement of the relative sweetness. *Agricultural and Biological Chemistry*, 34, 181–186.
<https://doi.org/10.1080/00021369.1970.10859599>
- Yang, C., Lee, W. S., and Gader, P. (2014). Hyperspectral band selection for detecting different blueberry fruit maturity stages. *Computers and Electronics in Agriculture*, 109, 23–31. <https://doi.org/10.1016/J.COMPAG.2014.08.009>
- Yang, K., Huang, Z., Wang, X., and Li, X. (2019). A Blind Spectrum Sensing Method Based on Deep Learning. *Sensors (Basel, Switzerland)*, 19(10).
<https://doi.org/10.3390/s19102270>
- Yang, S.-F., and Hoffman, N. E. (2003). Ethylene Biosynthesis and its Regulation in Higher Plants. *Annual Review of Plant Physiology*, 35, 155–189.
<https://doi.org/10.1146/annurev.pp.35.060184.001103>
- Ye, F., Shi, Z., and Shi, Z. (2009). A comparative study of PCA, LDA and kernel LDA for image classification. *Proceedings - 2009 International Symposium on Ubiquitous Virtual Reality, ISUVR 2009*, 51–54. <https://doi.org/10.1109/ISUVR.2009.26>
- Ying, Y., and Liu, Y. (2008). Nondestructive measurement of internal quality in pear using genetic algorithms and FT-NIR spectroscopy. *Journal of Food Engineering*,

84(2), 206–213.

- Yoon, S.-C., and Park, B. (2015). Hyperspectral image processing methods. In *Hyperspectral Imaging Technology in Food and Agriculture* (pp. 81–101). Springer.
- Yu, W., Liu, T., Valdez, R., Gwinn, M., and Khoury, M. J. (2010). Application of support vector machine modeling for prediction of common diseases: The case of diabetes and pre-diabetes. *BMC Medical Informatics and Decision Making*. <https://doi.org/10.1186/1472-6947-10-16>
- Zaki, M. J., and Meira, Jr, W. (2020). Linear Discriminant Analysis. *Data Mining and Machine Learning*, 501–516. <https://doi.org/10.1017/9781108564175.025>
- Zareef, M., Chen, Q., Hassan, M. M., Arslan, M., Hashim, M. M., Ahmad, W., Kutsanedzie, F. Y. H., and Agyekum, A. A. (2020). An Overview on the Applications of Typical Non-linear Algorithms Coupled With NIR Spectroscopy in Food Analysis. *Food Engineering Reviews*, 12(2), 173–190. <https://doi.org/10.1007/s12393-020-09210-7>
- Zeaiter, M., and Rutledge, D. (2009). Preprocessing Methods. In *Comprehensive Chemometrics*. <https://doi.org/10.1016/B978-044452701-1.00074-0>
- Zhang, B., Huang, W., Li, J., Zhao, C., Fan, S., Wu, J., and Liu, C. (2014). Principles, developments and applications of computer vision for external quality inspection of fruits and vegetables: A review. *Food Research International*, 62, 326–343.
- Zhang, C., Guo, C., Liu, F., Kong, W., He, Y., and Lou, B. (2016a). Hyperspectral imaging analysis for ripeness evaluation of strawberry with support vector machine. *Journal of Food Engineering*, 179, 11–18. <https://doi.org/10.1016/j.jfoodeng.2016.01.002>
- Zhang, C., Guo, C., Liu, F., Kong, W., He, Y., and Lou, B. (2016b). *Hyperspectral imaging analysis for ripeness evaluation of strawberry with support vector machine*. <https://doi.org/10.1016/j.jfoodeng.2016.01.002>
- Zhang, D., Xu, Y., Huang, W., Tian, X., Xia, Y., Xu, L., and Fan, S. (2019). Nondestructive measurement of soluble solids content in apple using near infrared hyperspectral imaging coupled with wavelength selection algorithm. *Infrared Physics and Technology*, 98(December 2018), 297–304. <https://doi.org/10.1016/j.infrared.2019.03.026>
- Zhang, M., Zhang, B., Li, H., Shen, M., Tian, S., Zhang, H., Ren, X., Xing, L., and Zhao, J. (2020). Determination of bagged ‘Fuji’ apple maturity by visible and near-infrared

- spectroscopy combined with a machine learning algorithm. *Infrared Physics and Technology*, 111(August), 103529. <https://doi.org/10.1016/j.infrared.2020.103529>
- Zhang, X., Liu, F., He, Y., and Gong, X. (2013). Detecting macronutrients content and distribution in oilseed rape leaves based on hyperspectral imaging. *Biosystems Engineering*, 115(1), 56–65. <https://doi.org/10.1016/j.biosystemseng.2013.02.007>
- Zhao, C., Cui, X., Liu, Y., Zhang, R., He, Y., Wang, W., Chen, C., and Liu, G. (2017). Maximization of the methane production from durian shell during anaerobic digestion. <https://doi.org/10.1016/j.biortech.2017.03.184>
- Zhu, H., Chu, B., Fan, Y., Tao, X., Yin, W., and He, Y. (2017). Hyperspectral Imaging for Predicting the Internal Quality of Kiwifruits Based on Variable Selection Algorithms and Chemometric Models. *Scientific Reports*, 7(1), 1–13. <https://doi.org/10.1038/s41598-017-08509-6>
- Zuzunaga, M., Serrano, M., Martinez-Romero, D., Valero, D., and Riquelme, F. (2001). Comparative Study of Two Plum (*Prunus salicina* Lindl.) Cultivars during Growth and Ripening. *Food Science and Technology International*, 7(2), 123–130. <https://doi.org/10.1177/108201320100700204>



International Published papers:

This material is reserved for educational use only, not allowed for commercial use.

Forbidden to modify the content, and cite the document when use.

Sharma, S., K.C, S., Sirisomboon P. “Rapid ripening stage classification and dry matter prediction of durian intact fruit and pulp using a pushbroom near infrared hyperspectral imaging system.” **Measurement**, 189(2022), pp. 110464.

Oral presentation:

Sharma, S., K.C. S., and Sirisomboon P. “Hyperspectral imaging system for maturity stage classification of durian pulp using Bayesian optimized machine learning algorithms.” **The 10th Agriculture for life, life for agriculture conference**, 3-5 June 2021 pp.236-242

Sharma, S., K.C, S., Sirisomboon P. “Maturity Classification of Durian Pulp by Hyperspectral Image Processing” **Proceedings of the Seventh Asian NIR Symposium**, February 12-15, 2020, pp. 54-55.



Author biography

Name-Surname

Miss Sneha Sharma

This material is reserved for educational use only, not allowed for commercial use.

Forbidden to modify the content, and cite the document when use.

Date of birth 10 November 1993
Contact address 308/272 Udelight Residence, Pattanakarn, Suan
 Luang, Bangkok, 10250
Email address sharmasneha0725@gmail.com, 61601170@kmitl.ac.th
Contact number 062-8505253

Education background

D.Eng. (Agricultural Engineering) from King Mongkut’s Institute of Technology Ladkrabang, Bangkok, Thailand (2019-2022, GPA: 4.00)

M.Eng. (Agricultural Engineering) from King Mongkut’s Institute of Technology Ladkrabang, Bangkok, Thailand (2017-2018, GPA: 4.00)

B.Eng. (Mechanical Engineering) from Kathmandu University, Dhulikhel, Nepal (2011-2015, GPA: 2.71)

Scholarships and awards:

- **Best oral presentation** on topic “Hyperspectral imaging system for maturity classification of durian pulp using Bayesian optimized machine learning algorithms” at the 10th International Conference Agriculture for Life, Life for Agriculture, Bucharest, Romania (3 – 5 June 2021).
- **KMITL Doctoral Scholarship 2019-2021**
- **KMITL Foreign Student Scholarship for Master’s Degree**

Oral presentation

- Oral presentation on topic “**Hyperspectral imaging system for maturity classification of durian pulp using Bayesian optimized machine learning algorithms**” at the 10th International Conference Agriculture for Life, Life for Agriculture, Bucharest, Romania (3 – 5 June 2021)
- Oral presentation on topic “**Maturity Classification of Durian Pulp by Hyperspectral image processing**” at the 7th Asian NIR Symposium, Avani Hotel, Khon Kaen, Thailand (12 – 15 February 2020).
- Oral presentation on topic “**Feasibility on using NIR spectroscopy for the measurement of the textural parameters in mango**” at the 12th TSAE International Conference (TSAE 2017) held on 13-15 March 2019.
- Oral presentation on topic “**Precision test for spectral characteristic on On-line Vis-NIR versus At-line NIR Spectroscopy for measuring total soluble**”

solids of (*Mangifera Indica* CV Nam Doc Mai)” at 10th TSAE International Conference (TSAE 2017) held in 7-9 September 2017.

International Published papers:

- Sharma, S., K.C., S., Sirisomboon, P. (2021). **Rapid ripening stage classification and dry matter prediction of durian pulp using a pushbroom near infrared hyperspectral imaging system.** Measurement, Available online 14 November 2021, Vol 110464. Impact Factor: 3.927 (2020)
- Sharma, S., K.C., S., Sirisomboon, P. (2021). **Hyperspectral imaging system for maturity classification of durian pulp using Bayesian optimized machine learning algorithms.** Scientific Papers. Series B, Horticulture. Vol. LXV, No. 1, 2021
- Saechua, W., Sharma, S., Nakawajana, N., Leepaitoon, K., Chunsri, R., Posom, J., ... and Pornchaloempong, P. (2021). **Integrating Vis-SWNIR spectrometer in a conveyor system for in-line measurement of dry matter content and soluble solids content of durian pulp.** Postharvest Biology and Technology, 181, 111640. Impact Factor: 5.537 (2020)
- Sirisomboon, P., and Pornchaloempong, P. (2020). **Application of a Vis-NIR Spectroscopic Technique to Measure the Total Soluble Solids Content of Intact Mangoes in Motion on a Belt Conveyor.** The Horticulture Journal, UTD-168. Impact Factor: 0.959 (2020)
- Sharma, S., and Sirisomboon, P. (2019, August). **Feasibility on using NIR spectroscopy for the measurement of the textural parameters in mango.** In IOP Conference Series: Earth and Environmental Science (Vol. 301, No. 1, p. 012064). IOP Publishing.
- Sharma, S., and Sirisomboon, P. (2017). Precision Test for Spectral Characteristic of On-line VisNIR versus At-line NIR Spectroscopy for Measuring Total Soluble Solids of Mango (*Mangifera indica* CV Nam Doc Mai). In the proceeding of The 18th TSAE National Conference and the 10th TSAE International Conference (Vol. 8).

Areas of expertise and interest

- Hyperspectral image processing and analysis of agricultural products

This material is reserved for educational use only, not allowed for commercial use.

Forbidden to modify the content, and cite the document when use.

- Fruits quality inspection using spectroscopy and imaging technologies
- Machine learning and deep learning data analysis
- Monitoring crop health using spectroscopy, multispectral and hyperspectral image

Reference persons

Prof. Dr. Panmanas Sirisomboon (Master and PhD Adviser)

Department of Agricultural Engineering, School of Engineering, KMITL

King Mongkut's Institute of Technology Ladkrabang (KMITL) Bangkok

panmanas.si@kmitl.ac.th

Prof. Dr. Bim Prasad Shrestha (Employer)

Office of External Affairs and Global Engagement, Kathmandu University

Kathmandu, Nepal

shrestha@ku.edu.np

